Observatoire Cantonal de Neuchâtel – Université de Neuchâtel

# APPLICATION OF BACKSCATTER LIDAR TO DETERMINE THE AEROSOL DISTRIBUTION ABOVE COMPLEX TERRAIN

Thèse présentée à la Faculté des Sciences
pour l'obtention du grade de docteur ès sciences
par:

**Max FRIOUD**
Physicien diplômé

acceptée le 26 mars 2003 par le jury:

| | |
|---|---|
| Prof. Associé P.Thomann | Rapporteur |
| Dr. V. Mitev | Co-rapporteur |
| Prof. R. Daendliker | Co-rapporteur |
| Prof. H. Richner | Co-rapporteur |

Neuchâtel, avril 2003

# IMPRIMATUR POUR LA THESE

*APPLICATION OF BACKSCATTER LIDAR TO DETERMINE THE AEROSOL DISTRIBUTION ABOVE COMPLEX TERRAIN*

de M. Max Frioud

---

UNIVERSITE DE NEUCHATEL

FACULTE DES SCIENCES

La Faculté des sciences de l'Université de Neuchâtel, sur le rapport des membres du jury

MM. Pierre Thomann, Valentin Mitev, René Daendliker et Hans Richner (ETHZ),

autorise l'impression de la présente thèse.

Neuchâtel, le 16 avril 2003

Le doyen:

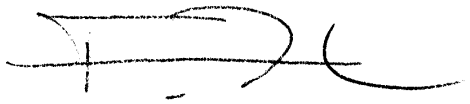

François Zwahlen

# *Contents*

# Foreword

During the last decades, Lidar (Light Detection and Ranging) remote sensing measurements took a growing place in atmospheric research. This trend is associated with the growing interest to monitor the vertical profiles of aerosol particles and trace gases. Improvements in atmospheric modeling following the increasing speed and capacity of computers require increasing experimental datasets for their assessment. The use of the Lidar in air and water pollution monitoring is demonstrated in late 1960s. Today, Lidars are involved in atmospheric measurements routinely in a number of research sites. Lidars also participate in many research campaigns, either as ground based or airborne instruments. The Lidar measurements are also demonstrated from satellite platforms, with more space-borne missions in Earth Observation to follow.

Presently the efforts in the Lidar science are devoted not only to Lidar instruments realization and demonstration, but also to the application of the Backscatter Lidar in the practice of the atmospheric research. In the field of Lidar atmospheric research, the study of the vertical distribution of the aerosol particles in the atmosphere and its temporal variation is one of the primary subjects. The aerosol particles have approximately $1/10^6$ of the atmosphere mass and $1/10^9$ of its volume. But one gram of aerosol particles has in average a surface of 10 $m^2$. Due to this the atmospheric aerosol affects the Earth surface temperature contributing to the climate changes. In a number of cases the atmospheric aerosol offers a surface for efficient heterogeneous chemistry reactions and in this way it influences the trace gases concentration in the atmosphere. The presence of the aerosol particles as condensation nuclei influences the cloud formation, particularly crystal clouds in the upper troposphere. Recently, more and more attention is taken by the fact that the solid aerosol particles in the air pose an important health hazard. In addition to this, the ensemble of aerosol particles is an efficient tracer in indicating the atmospheric dynamics, including the development of the Planetary Boundary Layer (PBL). The last feature is particularly used in the Backscatter Lidar studies of the atmospheric dynamics, where the fact that the aerosol presents a large and spatially distributed backscatter surface helps to follow by the Lidar the airmass movement.

In my thesis work I applied the Backscatter Lidar to specific atmospheric study cases, where the aerosol has a substantial role. In one of these cases the question was: What is the aerosol distribution over a mountain valley (this is the Rhine Valley) during weather conditions convenient for airmass vertical transport? This question is important to understand the role of the mountain in the mixture and the transport of pollutions. In another study case the question was: How this aerosol distribution is modified during the strong Foehn wind? In this study the Lidar detection of the aerosol particles has been used to follow the airmass transport along the valley by this wind. With the third case study my colleagues and I attempt to contribute to the knowledge how the aerosol distribution over Neuchâtel depends on the meteorological conditions, the prevailing wind and also, how far it has traveled before reaching the atmosphere above this town. To make possible the application of the Lidar in these practical studies, I needed to investigate by numerical simulations, how the Backscatter Lidar signal shall be processed in order to represent the aerosol values in the atmosphere and which assumptions and parameters are critical. These case studies are in atmosphere above a terrain containing complex topography features. Those are where the surface is with rapid elevation and albedo changes: mountain valley, steep slopes and lakes. To understand the role of the atmospheric dynamic processes over such terrain is more challenging than over a flat terrain. This motivates the efforts of the researchers active in this field, as well as the efforts in our group. In addition to this general objective, a contribution to my motivation comes from the fact that the country where we leave is predominantly with such complex terrain, so the study of such effects is more important for us.

My PhD work started in the Observatory of Neuchâtel (ON) Lidar group in 1997. After some time of familiarizing with the Lidar field, in particular with the data processing, I was involved in the Lidar numerical simulation and data processing support activity on the project Raman-DIAL in collaboration with the Lidar group from the Laboratory for Air Pollution (LPAS) from the Swiss Federal Institute of Technology of Lausanne (EPFL). Further, my work developed to the practical application of the Backscatter Lidar, realized in the Observatory. During the fall of 1999, I was involved in the Special Observation Period (SOP) of the program FORM (Foehn in the Rhine Valley during Mesoscale Alpine Program). Since May 2000, ON is one of the nineteen participating institutes in the EU-project EARLINET (European Aerosol Research LIdar NETwork). The objective of this research network, operational till February 2003, is the establishment of a database of the aerosol vertical distribution over EUROPE. Within this project, the main activities were the Lidar measurements in ON providing a knowledge of the aerosol distribution above the town.

As you may see, my studies were done as parts of the efforts of the Lidar Group in ON and benefited also from the cooperation with colleagues from other groups and institutions. In the Rhine Valley study this cooperation helped me to see better the necessities for Lidar studies and the importance of the synergy with the

other measurement methods. In the case of the aerosol statistics study over Neuchâtel, this helped us to see better the necessity to cooperate with other groups in Europe, since the aerosol content and its transport above a particular place is more and more international problem and so shall be the efforts for the development of measurement methods and for practical measurements. Part of the presented numerical studies presented here was done in collaboration with our colleagues in EPFL, to verify the information content of a Lidar they have used for ozone and water vapor measurements.

The manuscript of my thesis is organized as follows: In Chapter 1, the atmospheric Backscatter Lidar is introduced, together with basics in atmospheric physics focusing on the aerosol and its properties in the PBL. The techniques for Lidar signal processing applicable to Backscatter Lidars (elastic, Raman and DIAL) are exposed here. In Chapter 2, these signal processing techniques are tested with simulations: we report simulations made in ON and simulation exercises performed in a coordinated way as part of EARLINET activities. The last part of the Chapter reports simulations on ozone and water-vapor retrievals by Raman DIAL Lidar, in the frame of a cooperation with the Lidar group of LPAS-EPFL. In the Chapter 3 and respectively Chapter 4, we report results of Lidar measurements of the aerosol distribution over the Rhine Valley during the SOP of FORM, combined with results from other aerosol research instruments. Parts of these results demonstrate the possibility for a high elevation of the aerosol over the Alps. Other parts of these results show how the aerosol vertical distribution in the Valley atmosphere is modified by the Foehn wind. In Chapter 5, we present a statistical study of the aerosol distribution, based on two years of regular Lidar measurements in Neuchâtel during 2000-2002 performed in the frame of EU project EARLINET. These results show the seasonal variation of the aerosol content in the atmosphere above this town and how far are the main sources of the aerosol over it.

The manuscript is written in English-US.

# Acknowledgments

I convey my gratitude to the following colleagues:

- to my colleagues from the lidar group in ON, Valentin Mitev, Renaud Matthey, Patrick Weibel and Manoj K. Srivastava, for their scientific, technical and personal support.

- to the colleagues from LPAS: Professor H. Van den Bergh, Dr. Bertrand Calpini, Benoît Lazzarotto, Gilles Larchevêque, Philippe Quaglia and Valentin Simeonov.

- to the colleagues in the joint research in FORM: Professor Hans Richner, Christian Haeberli, Markus Furger, Richard Werner, Siegfried Vogt, Stefan Gubser

- to Domenico Bonanni, our guest-stagier from University of L'Aquila, for his efficient support in the lidar measurements during the SOP in the Rhine Valley.

- to many colleagues from the groups participating in EU project EARLINET for the helpful discussions and exchange of results.

I wish to present my acknowledgments to the members of the Jury, for reading this manuscript.

My thanks to my family and to my wife Cynthia, for their patience and personal support.

Thanks to all !

# Chapter 1

# Introduction to Atmospheric Backscatter Lidar

## 1.1 The Backscatter Lidar

### 1.1.1 Introduction

A very common remote sensing instrument is the RADAR ('RAdiowave Detection And Ranging'), largely used in meteorological applications. In a similar way, the term LIDAR is an acronym for 'LIght Detection And Ranging': this means that, in this case, the vector of information for remotely sensing is the light.

Figure 1.1 presents the principle of a monostatic biaxial Lidar. A light beam is produced with a laser. Further, it is directed into the atmosphere. In traveling through the atmosphere, the light is scattered out in all directions by all atmospheric constituents (basic air constituent like molecular $N_2$ and $O_2$, the water-vapor $H_2O$, all other minor molecular constituents, and all constituents like water droplets, dust, ice particles, condensation nuclei, with the generic name Aerosol). In this way, a part of the emitted beam is scattered backward to the Lidar site. From this backscattering process originates the full name of the instrument, namely the 'Backscatter Lidar'. This backscatter light is collected into a telescope and transmitted through an optical system and an interference filter to a detector and post-detector system, named detection chain. Basically, the role of this chain is to transform the backscattered optical beam into an electric signal. Further, this electric signal is digitized through an acquisition system, and the resulting signal is stored on a computer.

A macroscopic description of the interaction of the beam with the atmospheric constituents can be summarized as follow (see [*Measures*, 1984]):

- along its path, the laser beam is progressively attenuated, i.e. its intensity is decreasing with the distance from the Lidar.
- this attenuation is described by a specific optical property of the constituent, namely its extinction. The extinction has two origins: the scattering of light and its molecular absorption.
- the ratio of the backscattered intensities to the forward beam intensities is described by another specific optical property, namely the backscattering coefficient.

The occurrence of scattering processes increases with the density of scatterers. For a given type of scatterers, we then expect that both backscattering and extinction values are increasing function of the scatterers density. This is a first key point of the Lidar principle.

A second key point is that a continuous collection of backscattered beam combined with an adequate pulsing of the emitted beam results in a range-resolved information: considering only simple backscatter processes along

the beam path, the elapsed time from the beam emission to the backscattered beam reception is proportional to the range Lidar-probed volume (i.e. location of the backscatter process).

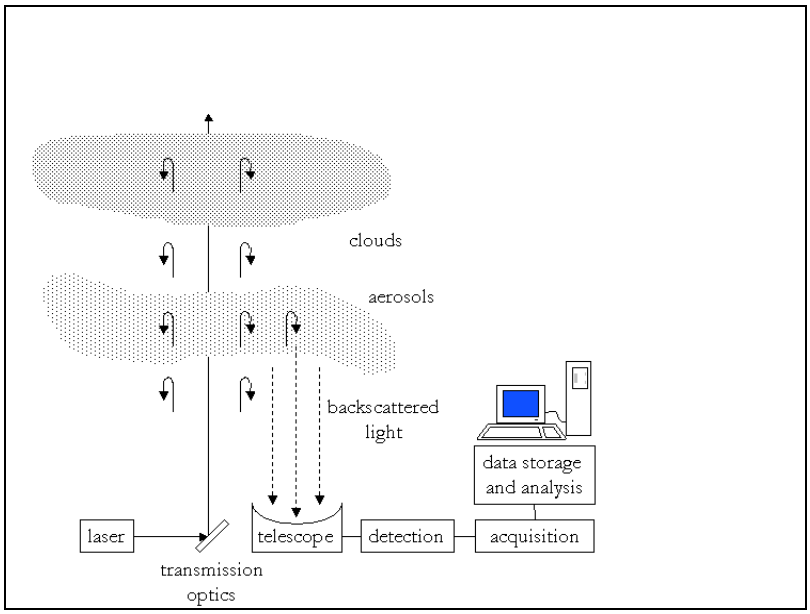


**Figure 1.1.** *Schematic presentation of the principle of the Lidar measurement.*

Based on the above-presented principle, many device and measurement parameters are then adjustable to the specific target and/or to the measurement situation, leading to a large variety among Lidar instruments. Let's consider here just two common general properties of any (monostatic) Lidar:

- the laser beam and the telescope field of view are centered on two parallel axes. These beams are conic, with increasing radii with distance to the Lidar. In this way, the two beams begin to overlap at some distance from the Lidar, and the overlap is full at some greater range. Due only to this simple geometrical consideration, the backscattered signal decreases with range following an inverse range-square law. Furthermore, the signal is attenuated through extinction with increasing range. As a result, above the overlap range, the signal does generally present a very large dynamics along the range scale.
- the detection chain is the source of different noises, altering the optical signal at the receiver. The noise level can be reduced in playing with electronic, optical and thermal properties of the detection devices. Nevertheless, one source of noise, the quantum one, determines a lower limit for the overall noise: the basic reason for the presence of this noise is the involvement of the photoelectric effect when transforming the optical into electrical signal. Considering this effect only, it will be shown that the noise level is proportional to the square root of the signal intensity.

These general characteristics of Backscatter Lidar have the following consequence: the quality of the retrieved information is degraded with increasing of the range. The strategy to overcome this state lies in the reduction of the range resolution with increasing range, or in the reduction of the temporal resolution. In any case, a consensus between range and temporal resolutions has to be found, in order to retrieve information of sufficient quality in suitable range of interest and time period.

Another important consequence for Lidar operation lies in the adaptation of measurements parameters to the atmospheric conditions. Since any acquisition system has an optimal working-domain, any important variation of the aerosol content can significantly alter the quality of the retrieved information, unless an adjustment is made to e.g. the laser power. In extreme cases, like presence of low clouds for operating in zenith position, unsuitable measurements parameters may induce very large signals, leading to significant non-linear effects in the detection chain. In such cases, the single-backscatter processes described above, to which we will limit in this study, are often insufficient to describe properly the relevant scattering processes (multiple scattering).

In the next subsection, the above measurement process is described in a formal way, for the case of single-backscatter processes only.

## 1.1.2 The Lidar equation

The following derivation of the Lidar equation is based on the approach found in [*Measures*, 1984]. Consider a single light pulse of rectangular shape, with energy $E_L$, duration $\tau_L$, emitted at the laser wavelength $\lambda$. At some distance $r$ from the Lidar, the laser beam is spread over an area $A_L(r)$. In the travel to $r$, the light intensity has decreased due to the extinction along the path. The irradiance over the area $A_L(r)$ is expressed as

$$I_\lambda(r) = \frac{E_L T_\lambda(r)}{\tau_L A_L(r)} \qquad \text{(Eq 1.1)}$$

where the factor $T_\lambda(r)$ is named optical transmission and is linked to the optical extinction $\alpha_\lambda(r)$ through the Beer-Lambert law

$$T_\lambda(r) = \exp\left(-\int_0^r \alpha_\lambda(r')dr'\right) \qquad \text{(Eq 1.2)}$$

Restricting to one type of scatterer with number density $n(r)$, and neglecting molecular absorption, $\alpha_\lambda(r)$ take the specific form

$$\alpha_\lambda(r) = n(r)\int \frac{d\sigma_\lambda}{d\Omega}d\Omega \qquad \text{(Eq 1.3a)}$$

where the integrand $\left(\frac{d\sigma_\lambda}{d\Omega}\right)$ is the differential scattering cross-section of the scatterer at given wavelength, and where the integral is over the full unit sphere. Relatively to a spherical coordinate system $(\theta,\varphi)$ with the polar axis in the direction of the incident beam, $d\Omega = \sin(\theta)d\theta d\varphi$. Thus, in (Eq 1.3a), the integral accounts for scattering in all directions. For a mixture of different species of scatterers, a superposition principle applies, and (Eq 1.3a) can be generalized to

$$\alpha_\lambda(r) = \sum_i n^i(r)\int \frac{d\sigma_\lambda^i}{d\Omega}d\Omega \qquad \text{(Eq 1.3b)}$$

where $n^i(r)$ and $\frac{d\sigma_\lambda^i}{d\Omega}$ are respectively the number density and the differential cross-section of the i$^{th}$ scatterer species. Further, if we take into account molecular absorption, i.e. if $\lambda$ lies in the absorption band of some molecular specie, the absorption is accounted for in adding the following term

$$\alpha_\lambda^{abs}(r) = n^{abs}(r)\sigma_\lambda^{abs} \qquad \text{(Eq 1.4)}$$

in which $n^{abs}(r)$ and $\sigma_\lambda^{abs}$ are respectively the number density and the absorption cross-section of the specie at wavelength $\lambda$. Consider further the case, in which the backscatter process is eventually inelastic, i.e. it would not preserve the wavelength of the incident radiation (Raman process, see section 2.3). For such a process, the volume backscatter coefficient is defined as

$$\beta_{\lambda,\lambda'}(r) = n(r)\left[\frac{d\sigma_{\lambda,\lambda'}}{d\Omega}\right]_{\theta=\pi} \qquad \text{(Eq 1.5)}$$

in which the term in the bracket is the differential scattering cross-section for the specific process. If the pulse was emitted at time $t=0$, then at the time $t=r/c$ (c is the light speed), only the volume $V=(A_L c\tau_L)/2$ contributes to the radiation power $I^b$ backscattered in the acceptance solid angle $\Delta\Omega(r)$ of the receiver (telescope) viewed from point $r$

$$I^b_{\lambda,\lambda'} = I_\lambda(r)\beta_{\lambda,\lambda'}(r)V(r)\Delta\Omega(r) \qquad \text{(Eq 1.6)}$$

where $\Delta\Omega(r)$ is proportional to the telescope area $A$

$$\Delta\Omega(r) = \frac{A}{r^2} \qquad \text{(Eq 1.7)}$$

In traveling back to the Lidar telescope, the backscattered beam is again reduced due to the extinction at wavelength $\lambda'$. Let's further assume that the overlap between emitted laser beam and telescope field of view is represented by a function $O(r)$ (with a good optical alignment, $O(r)=0$ for $r<r_0$, $O(r)=1$ for $r>r_{fo}$, $0<O(r)<1$ for $r_0<r<r_{fo}$, for some ranges $r_0$ $r_{fo}$). Then, the optical power received by the telescope is

$$P^{tel}_{\lambda,\lambda'}(r) = O(r)I^b_{\lambda,\lambda'}T_{\lambda'}(r) \qquad \text{(Eq 1.8)}$$

In order to get the (effective) detected power, let's account for overall optical efficiency at the transmitter and receiver, and respectively for the wavelength dependant quantum efficiency of the detector, through additional multiplicative (reducing) factors $K$ respectively $\eta_{\lambda'}$. The detected power is

$$P_{\lambda,\lambda'}(r) = E_L K \eta_{\lambda'} O(r) \frac{A}{r^2} \frac{c}{2} \beta_{\lambda,\lambda'}(r) T_{\lambda}(r) T_{\lambda'}(r) \qquad \text{(Eq 1.9)}$$

During a single-pulse integration time $\tau$, this gives rise to a detected energy

$$E_{\lambda,\lambda'}(r) = E_L K \eta_{\lambda} O(r) \frac{A}{r^2} \frac{c\tau}{2} \beta_{\lambda,\lambda'}(r) T_{\lambda}(r) T_{\lambda'}(r) \qquad \text{(Eq 1.10)}$$

The range $\Delta r = c\tau/2$ is the effective range resolution.
(Eq 1.10) is a general form of the Lidar equation.
For the most common case of elastic backscattering, it takes the traditional form

$$E_{\lambda}(r) = E_L K \eta_{\lambda} O(r) \frac{A}{r^2} \frac{c\tau}{2} \beta_{\lambda}(r) \exp\left( -2 \int_0^r \alpha_{\lambda}(r') dr' \right) \qquad \text{(Eq 1.11)}$$

The integration time $\tau$ cannot be smaller than the temporal resolution of the overall measurement process. This is equivalent to a lower limit for the range resolution

$$\Delta r \geq \frac{c}{2}\left(\tau_L + \tau_D + \tau_P\right) \qquad \text{(Eq 1.12)}$$

where $\tau_D$, and $\tau_P$, are respectively the detection response time and the optical interaction process lifetime. For elastic processes, $\tau_P$ is negligible.

As the intention of the Lidar measurements is the retrieval of information about aerosol concentration, it is of practical interest to reformulate (Eq 1.11) in order to make explicit the appearance of aerosol optical properties. This is made in applying the superposition principle to both extinction and volume backscattering coefficient as in (Eq 1.3b)

$$\alpha_{\lambda}(r) = \alpha_{\lambda}^{mol}(r) + \alpha_{\lambda}^{aer}(r) \qquad \text{(Eq 1.13a)}$$

$$\beta_{\lambda}(r) = \beta_{\lambda}^{mol}(r) + \beta_{\lambda}^{aer}(r) \qquad \text{(Eq 1.13b)}$$

where we have separated the contributions from molecules and from aerosol particles. Such a separation makes a sense since the molecular contributions are generally sufficiently well represented by model values, which will be presented in Chapter 2. It is common to introduce the total scattering ratio as

$$scr_{\lambda}(r) = \frac{\beta_{\lambda}^{mol}(r) + \beta_{\lambda}^{aer}(r)}{\beta_{\lambda}^{mol}(r)} \qquad \text{(Eq 1.14)}$$

We can now rewrite (Eq 1.11) as

$$E_{\lambda}(r) = scr_{\lambda}(r) T_{\lambda}^{aer}(r) E_{\lambda}^{mol}(r) \qquad \text{(Eq 1.15)}$$

in which $E_{\lambda}^{mol}(r)$ is a (virtual) signal from a purely molecular (aerosol free) atmosphere, and $T_{\lambda}^{aer}(r)$ is the aerosol transmission factor.
Further considerations about separation of aerosol optical coefficients out of the Lidar equation are presented in section 1.3.

## 1.1.3 The signal acquisition modes

Once the optical signal is transformed into an electrical one trough the detector (photomultiplier (PMT) or avalanche photo-diode (APD)[*]), it is further "acquired", i.e. its amplitude is measured in function of the time, converted into numbers and stored for further analysis.

When the optical power impinging on the detector is weak enough, the detector output current is a chain of single current pulses corresponding to single arriving photons. These pulses are then counted within successive time intervals. This mode of acquisition is named "photon-counting". By analysis of the amplitude of the current pulses, it is possible to discriminate the pulses caused by photons from the pulses issued from the detector itself. These latter pulses are in average smaller than the former. If the amplitude of a pulse does not exceed a defined threshold, it is not counted. In this way, the acquired signal contains less noise, what is the main advantage of this acquisition mode.

[*] Further, we will restrict consideration to PMT's, since these are the detection units used in all reported measurements

When too many photons arrive, the current pulses pile-up and it is no more possible to count them. In this case, it is better to measure the current itself (or voltage), as it is proportional to the optical power and to convert it into digital form by an analog-to-digital converter (ADC). This acquisition mode is named "analog". It suits to large optical power. However, as it is composed of more electrical circuits, it is intrinsically noisier than the photon-counting mode.

# 1.1.4 Noise sources

As for any remote sensing system, the presence of noise is a common characteristic of any Lidar measurement. In this subsection, we make a brief overview of the main sources of noise, with specific formulae for photon-counting and analog acquisition modes.

## 1.1.4.1 Quantum and shot noises

In (Eq 1.9), we have introduced a quantum efficiency factor $\eta$, expressing the efficiency of photoelectron production. More precisely, when the backscattered light falls onto the photo-cathode, each photon has some probability $\eta$ to free a photoelectron. In usual conditions, we can consider the photons arrivals as independent events. Since $\eta$ is generally of order of some percents, and the number of photons during the integration time $\tau$ is large, the distribution of the number of photoelectrons is well represented by a Poisson statistic (see [*Measures*, 1984], pp 226).
In photon-counting mode, each photoelectron is registered as one unit. During $\tau$, the number of events is proportional to the following incident power (elastic case)

$$P_\lambda(r) = E_L K O(r) \frac{A}{r^2} \frac{c}{2} \beta_\lambda(r) T_\lambda^2(r) \qquad \text{(Eq 1.16)}$$

The corresponding number of detected photons is therefore

$$N_s(r) = P_\lambda(r) \tau \frac{\eta}{h\upsilon} \qquad \text{(Eq 1.17)}$$

where $\upsilon$ is the optical frequency and $h$ is the Planck's constant ($h\upsilon$ is the incident energy per incoming photon). Following Poisson statistic, the variance of this number is the same number, i.e.

$$\sigma_{N_s}^2 = N_s \qquad \text{(Eq 1.18)}$$

The noise associated with these fluctuations is called quantum or photon noise.
In analog detection mode, the power (Eq 1.16) gives rise to an instantaneous value of the current at the PMT output. In that case, the measured signal is proportional to the integrated current. The output momentary current is given by

$$i_s(r) = P_\lambda(r) G \frac{\eta e}{h\upsilon} \qquad \text{(Eq 1.19)}$$

where $G$ is the PMT gain. During this amplification, additional fluctuations arise. This leads to the following variance

$$\sigma_{i_s}^2 = 2eBG\mu i_s \qquad \text{(Eq 1.20)}$$

where $B$=1/(2$\tau$) is the electrical bandwidth and $\mu$ (>1) the excess noise coefficient from the amplification process. The noise associated with these fluctuations of the current is called shot noise.

## 1.1.4.2 Background noise

Any light source other than the backscattered light contributes to the light entering the detector and leads to an additional production of photoelectrons. Potential sources are the scattered light from the sun or the moon, the ambient scattered skylight by other light sources from the surrounding and the “internal sources”, like e.g. the scattered light from the laser flash-lamp. A large part of this radiation can be rejected by a proper mechanical and geometrical setup, and by using adequate optical filters, at the receiver level.

For the natural sources, the power of the received background impinging on the photodectector is

$$b(t) = K_r S_b(\lambda)\Delta\lambda\Omega_r A \quad \text{(Eq 1.21)}$$

where $K_r$ is the optical efficiency of the receiver, $S_b$ (in [$Wm^{-2}sr^{-1}\mu m^{-1}$]) is the sky spectral radiance at the instrument location and instant of measurement $t$, $\Delta\lambda$ (in [μm]) is the optical bandwidth of the receiver, $\Omega_r$ (in [steradian]) the receiver field of view and $A$ (in [$m^2$]), as before, is the effective aperture area of the receiver. The receiver field of view is linked to the full divergence angle $\psi$ of the receiver by

$$\Omega_r = \pi\left(\frac{\psi}{2}\right)^2 \quad \text{(Eq 1.22)}$$

Replacing the incident power (Eq 1.16) by this background radiation in (Eq 1.17) respectively (Eq 1.19) for respectively photon-counting and analog case, we obtain similar formulae for the background counted photons number $N_b$ and the background current $i_b$ at the output of the photo-detector

$$N_b(t,\tau) = b(t)\tau\frac{\eta}{h\upsilon} \quad \text{(Eq 1.23)}$$

$$i_b(t) = b(t)G\frac{\eta e}{h\upsilon} \quad \text{(Eq 1.24)}$$

Let's notice that the natural background can always be considered as constant during the acquisition of a single laser shot Lidar profile, due to the different timescales of evolution. Thus, it appears as a single constant to be subtracted from the measured signal (offset). Nevertheless, its effect is to increase the fluctuations of the electrical signal produced by the detector, following similar formulae than (Eq 1.18) and (Eq 1.20)

$$\sigma^2_{N_b} = N_b \quad \text{(Eq 1.25)}$$

$$\sigma^2_{i_b} = 2eBG\mu i_b \quad \text{(Eq 1.26)}$$

Since the incoming of background light in the telescope is independent of the laser beam backscattering, these fluctuations will be added* to the quantum noise (Eqs 1.18 and 1.25) or shot noise (Eqs 1.19 and 1.26).

### 1.1.4.3 Dark noise

In absence of any incoming radiation, the photo-detector emits electrons through thermal release. The corresponding noise is known as *dark noise*. This noise is a function of the temperature.
In photon-counting mode, any detector is characterized by a (temperature dependant) dark count level $d_l$, such that the number of dark counts in the single-pulse detection period is

$$N_d(t,\tau) = d_l\tau \quad \text{(Eq 1.27)}$$

In analog detection mode, this gives rise to a so-called dark-current $i_d$. Since all currents produced in the dynode chain are integrated, the dark noise is much larger in analog than in photon-counting mode, where the threshold adjustment allows discarding all minor pulses.

As for the natural background noise, the relevant effect of the dark noise is not the additional detected photons/current, but the corresponding additional fluctuations

$$\sigma^2_{N_d} = N_d \quad \text{(Eq 1.28)}$$

$$\sigma^2_{i_d} = 2eBG\mu i_d \quad \text{(Eq 1.29)}$$

### 1.1.4.4 Thermal (Johnson) noise

In analog acquisition mode, the PMT output current is passing through some resistance (impedance) and the output signal is measured as a variable voltage. Thermal agitation of the charge carriers within this resistance leads to an additional fluctuation in the measured signal. The variance of this output current is again function of the temperature

$$\sigma^2_{th} = \frac{4k_B T_{R_{ch}} B}{R_{ch}} \quad \text{(Eq 1.30)}$$

* The variance of the sum of independent random variables is the sum of the individual contributions.

where $k_B$ is the Boltzmann constant, $T_{R_{ch}}$ the absolute temperature of the resistance, $B$ the electrical bandwidth and $R_{ch}$ the equivalent resistance (this value depends on the preamplifier configuration).

## 1.1.4.5 Signal-induced-noise

This noise appears as a complex interaction between the exposure of the photo-cathode, dynodes chain and the electrical network. This noise appears only in presence of signal, justifying its name. It appears at least under two forms. One is known as after-pulse, and appears as an echo of the original pulse shape. Another form is named signal-induced-bias, and appears as a slowly decaying noise-tail, affecting also the upper part of the signal where no atmospheric return occurs. In [*Sunesson et al.*, 1994], a technique for signal-induced-bias correction is presented.

More critical forms of signal-induced-noise occur when the PMT is overexposed, i.e. working in a non-linear domain. For ground-based measurements, typical cases of such occurrence are unexpected appearance of low clouds or fog. The PMT's are saturated and, above the range where saturation occurs, the resulting profile frequently presents a sharp decrease and a spurious tail.

## 1.1.4.6 Other noise

The RF (radio-frequency) electromagnetic fields generated by the laser source or any other device in the Lidar setup, generates other signal fluctuations, which cannot be predicted in a formal way. Theses are noises induced in the detection chain by the laser or by the triggering devices. Usually, these noises affect not only the signal fluctuation but also its shape (i.e. the frequencies involved in such noises are of the same order of magnitude than the acquisition frequency). The usual procedure to cancel such noises in the signal is to proceed to noise measurement (with closed telescope) along with the series of atmospheric measurements. In such case, the first step of the signal processing consists in subtracting this "noise-signal" from the "noisy-atmospheric-signal". This procedure leads again to an increase of the signal fluctuations.

## 1.1.4.7 Signal-to-noise ratio

The signal-to-noise ratio (SNR) is a measure of the quality of the atmospheric signal extracted from the measured (noisy) signal. Formally, it is defined as the following ratio

$$SNR(r) = \frac{S(r)}{\sqrt{\sum_k \sigma_k^2(r)}} \qquad \text{(Eq 1.31)}$$

where $S$ is the atmospheric backscattered signal and the $\sigma_k$ are the standard deviations of the measured signal due to all independent noise sources. For the photon-counting case, this takes the following form

$$SNR(r) = \frac{N_s(r)}{\sqrt{N_s(r) + N_b(r) + N_d(r)}} \qquad \text{(Eq 1.32)}$$

In the analog case, we have to add at least the thermal noise effect, leading to

$$SNR(r) = \frac{i_s(r)}{\sqrt{2eBG\mu(i_s(r) + i_b(r) + i_d(r)) + \frac{4kT_{R_{ch}}B}{R_{ch}}}} \qquad \text{(Eq 1.33)}$$

All above considerations apply for a single pulse. Usually, the signal is averaged over many pulses. In such case, the above *SNR* values have to be amplified by the constant $\sqrt{L}$ and all single pulse values are to be replaced by their average value over the $L$ pulses. Similar considerations apply when averaging the signal versus the range. As example, if we average the signal over $n_{bin}$, successive sample points of the profile, it results a gain factor $\sqrt{n_{bin}}$ on the *SNR*.

The application of formulae such as (Eq 1.33) supposes obviously that we are able to identify the proper constant offset from the measured signal, in order to isolate the signal contribution only. This is a critical point in real cases of Lidar measurements.

# 1.2 The Atmosphere

## 1.2.1 Introduction

Figure 1.2 presents the temperature profile of the standard atmospheric model US-76 till 100 km above sea level (asl). The sign of the temperature lapse rate defines the different parts of the terrestrial atmosphere. The present study is almost entirely limited to the first layer from the surface, the troposphere. It is characterized by a mean temperature lapse rate of about –6.5°C/km, in accordance to the radiative balance and the convective transport of energy. All the water-vapor, clouds and precipitation are confined in this layer. The stratosphere is characterized by an isothermal layer from the tropopause till approximately 20 km. Its temperature structure results exclusively from radiative equilibrium. It plays a relevant role for life, since it contains most of the ozone, acting as UV filter. In contrast with the troposphere, its temperature increase with altitude (temperature inversion) severely inhibits any vertical motion. The mesosphere is a part of upper atmosphere, in which gravity/buoyancy waves, planetary waves, and tides pervade. The temperature distribution in the upper stratosphere and lower mesosphere is mainly controlled by a balance between radiative cooling from $CO_2$ and heating by $O_3$.

## 1.2.2 Constitution of the atmosphere

### 1.2.2.1 The molecular constituents

Table 1.1 summarizes the molecular constituents of the atmosphere, with their respective relative concentration. From the table, we see that $N_2$, $O_2$ and Ar constitute more than 99.99% in volume of the permanent gases. Moreover, their volume ratio is nearly constant up to about 60 km height. One notices that although $CO_2$ is listed as a permanent constituent, its concentration varies as a result of the combustion of fossil fuels, absorption and release by the ocean and the photosynthesis. Actual values are about 370 ppmv and increase of 1.5 ppmv/year. It plays a major role in global warming, since it is quasi transparent to solar radiation, but a strong absorber in the 12-18 μm (terrestrial radiation). Water-vapor's concentration vary greatly both in space and time. Its variation is also extremely important in the radiative absorption and emission processes. Ozone concentration is also highly variable. It is for a large part concentrated in the stratosphere, where it plays a vital role in absorbing harmful ultraviolet solar radiation. During the past 20 years, its concentrations have been threatened by human-made gases released into the atmosphere, including those known as CFC's. These chemical compounds as well as meteorological conditions in the stratosphere affect the concentration of stratospheric ozone. Tropospheric ozone represents 8% of the total ozone column. Its concentration is also of critical importance, since it is harmful for human being and crops. Moreover, tropospheric ozone is chemically very active (oxidant). In Annex 1, tropospheric ozone measurements are presented.

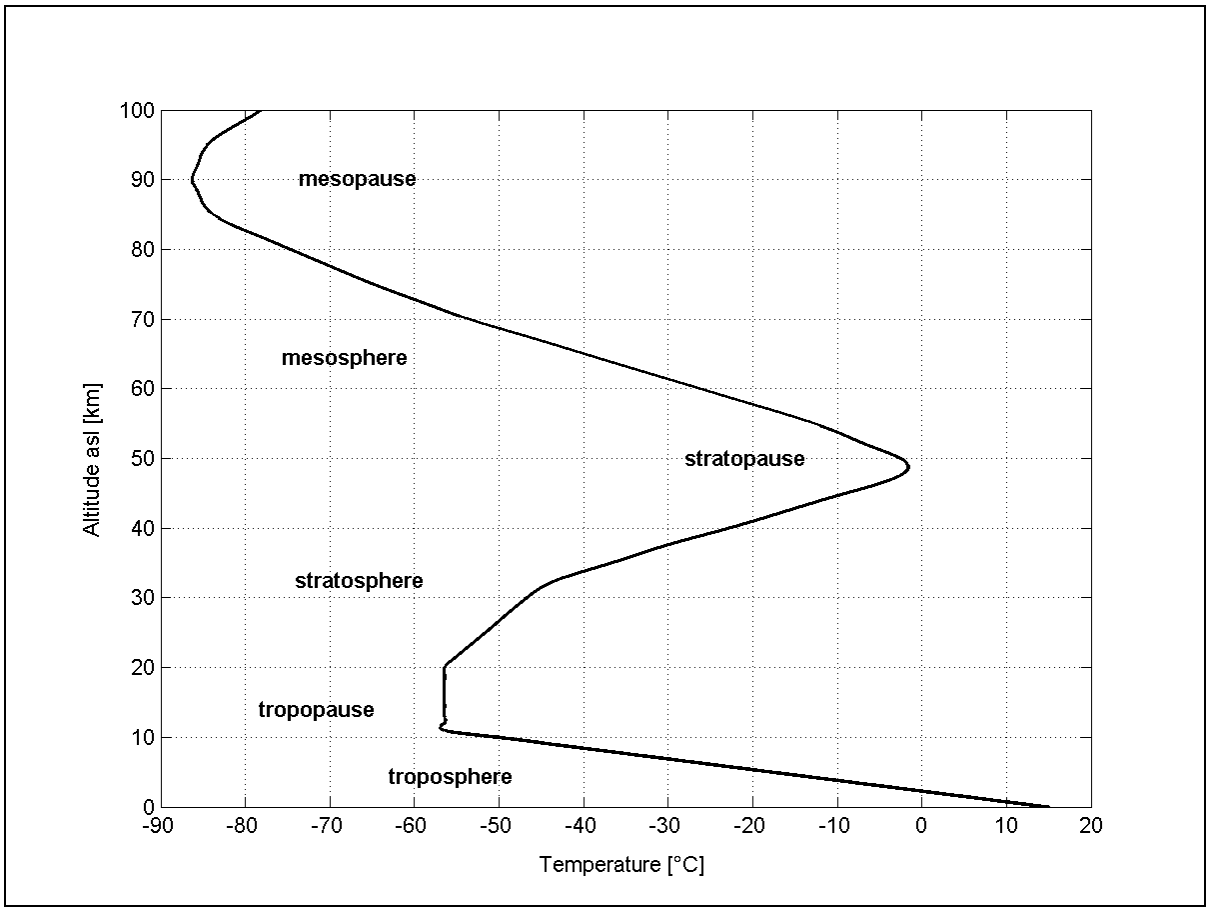


**Figure 1.2.** *Temperature profile of the standard US-76 model.*

**Table 1.1.** *Composition of the atmosphere, following standard US-76.*

| *Permanent Constituents* | *Part per volume [%]* | *Variable Constituents* | *Part per volume [%]* |
|---|---|---|---|
| Nitrogen ($N_2$) | 78.084 | Water-vapor ($H_20$) | 0-0.04 |
| Oxygen ($O_2$) | 20.946 | Ozone ($O_3$) | 0-12 x $10^{-4}$ |
| Argon (Ar) | 0.934 | Sulfur dioxide ($SO_2$) [(a)] | 0.001 x $10^{-4}$ |
| Carbon dioxide ($CO_2$) | 0.033 | Nitrogen dioxide ($NO_2$) [(a)] | 0.001 x $10^{-4)}$ |
| Neon (Ne) | 18.18 x $10^{-4}$ | Ammonia ($NH_3$) [(a)] | 0.004 x $10^{-4}$ |
| Helium (He) | 5.24 x $10^{-4}$ | Nitric oxide (NO) [(a)] | 0.0005 x $10^{-4}$ |
| Methane ($CH_4$) | 1.5 x $10^{-4}$ | Hydrogen sulfide ($H_2S$) [(a)] | 0.00005 x $10^{-4}$ |
| Krypton (Kr) | 1.14 x $10^{-4}$ | Nitric acid vapor ($HNO_3$) | Trace |
| Hydrogen ($H_2$) | 0.5 x $10^{-4}$ | | |
| Nitrous oxide ($N_2O$) [(a)] | 0.27 x $10^{-4}$ | | |
| Carbon monoxide (CO) [(a)] | 0.19 x $10^{-4}$ | | |
| Xenon (Xe) | 0.089 x $10^{-4}$ | | |

[a] Concentration near the earth's surface

### 1.2.2.2 The aerosol particles in the troposphere

Aerosols are tiny particles suspended in the air. Some occur naturally, originating from volcanoes, dust storms, forest and grassland fires, living vegetation, and sea spray. Human activities, such as the burning of fossil fuels and the alteration of natural surface cover, also generate aerosols. Averaged over the globe, aerosols made by human activities currently account for about 10% of the total amount of aerosols in our atmosphere. Most of that 10% is concentrated in the Northern Hemisphere, especially downwind of industrial sites, slash-and-burn agricultural regions, and overgrazed grasslands. A survey of the global aerosol climatology with references about the aerosols radiative characteristics may be found in [*d'Almeida et al.*, 1991]. The aerosol impacts on air quality, human health and vegetation are reported in [*Godish*, 1991].

Anthropogenic aerosol particles are produced in industrial and urban areas (mainly in the Northern Hemisphere) by conversion of gases (e.g., $SO_2$ and $NO_X$) into liquids in chemical reactions, and through emission of graphitic carbon. This pollution spreads over the Northern Hemisphere and takes part in acidification of rain and reduction of visibility. Biomass burning in tropical regions is used to clear land for agriculture. This generates a large fraction of the global flux of aerosol particles as well as trace gases such as $CO_2$, CO, and $CH_4$. Smoke particles have similar effects on visibility, clouds, precipitation, and radiation as industrial and urban aerosol.

Aerosol particles may be solid or liquid; they range in size from 0.01μm to several tens of μm. This range is determined by coagulation for the lower limit and by precipitation for the upper limit (typical cloud drops size is 10 μm). Under normal circumstances, the majority of aerosols form a thin haze in the troposphere, where they are washed out of the air by rain within about one week. Due to their short lifetime and strong interactions, their global concentrations and properties are poorly known. Indeed, they are considered as a major uncertainty in climate forcing. One of the relevant issues is the determination of their size distribution, which is a field of intense actual research.

Aerosols tend to cause cooling of the Earth's surface immediately below them. On one side, through their high scattering power, they contribute significantly to the total solar radiation backscattered to space. On the other side, through their own absorption, they contribute to atmospheric warming. While their direct radiative cooling effect has long been recognized, recent measurements have highlighted the importance of their absorption (surface cooling and atmospheric heating). The net effect of aerosols on the Earth's radiation balance at the top of the atmosphere depends on the relative amounts of light scattered or absorbed by the particles, as well as the surface albedo. Highly absorbing aerosols, such as soot, are so highly efficient as light absorbers that their net radiative impact (scattering plus absorption) usually results in a net warming of the climate system. It is thought that aerosol cooling may partially offset expected global warming that is primarily attributed to increases in the amount of $CO_2$ from human activity.

Aerosols have a relevant effect on climate by changing properties of clouds. Indeed, if there were no aerosols in the atmosphere, there would be no clouds. It is very difficult to form clouds without small aerosol particles acting as condensation nuclei to start the formation of cloud droplets. As aerosol concentration increases within a cloud, the water in the cloud gets spread over many more particles, each of which is correspondingly smaller. Smaller particles fall more slowly in the atmosphere and decrease the amount of rainfall. In this way, changing aerosols in the atmosphere can change the frequency of cloud occurrence, cloud thickness, and rainfall amounts. If there are more aerosols, more cloud drops are expected to form. Since the total amount of condensed water in the clouds is not expected to change much, the average drop must become smaller. This has two consequences: (i) clouds with smaller drops reflect more sunlight, (ii): such clouds last longer, because it takes more time for small drops to coalesce into drops of critical size to precipitate. Both effects increase the amount of sunlight that is reflected to space without reaching the surface.

## 1.2.3 The PBL structure

In the troposphere, the part of the atmosphere next to the surface of the Earth, which is strongly influenced by the structure of the ground, is named planetary boundary layer (PBL). It is distinguished from the upper part, named free atmosphere, which is not affected by ground effects. The PBL is that part of the troposphere, where life exists and where most weather phenomena occur. The PBL is directly influenced by the presence of the earth's surface and responds to surface forcings with a time scale of about an hour or less [*Stull*, 1988]. Its depth is between a few hundred meters and some kilometers according to the latitude, the season, the local topography and the time of the day. The heat transfer from the sun to the ground and from the ground back to the atmosphere is the major motor of air circulation (winds, clouds formation and transport, pollutants mixing, ..). Looking at the

solar radiation absorbed and scattered by atmosphere, clouds and earth, the following picture emerges: below 4 μm wavelength, 47% of the incoming radiation is absorbed by the earth and 19% by the atmosphere, while the rest of 34% is lost to space by reflection from clouds and the earth or by scattering into the atmosphere. The absorbed energy is converted into heat and finally radiated in the IR wavelengths range (4-100 μm). The radiation losses of the earth and the atmosphere equal the amounts absorbed before, so that the sum of 66% is lost to space again. This energy balance means, however, that the global amount of incoming solar radiation has been re-radiated into space, while two thirds have been transformed into long wavelength radiation. The ground radiative heating and cooling change the PBL depth and its inner structure via transport processes, from which turbulence is one of the major sources. Winds mainly transports scalars (like heat, humidity, pollutants) by horizontal advection with typical speeds 2-10 m/s. In the vertical direction, the mean wind velocity generally does not exceed some centimeters per second. Waves are generated, whenever the flow over obstacles produces wind shear. Momentum and energy are effectively transported by waves. The influence of the turbulence on vertical motion grows when approaching the ground, since it is generated by forcings from the ground like frictional drag, evaporation or pollutant emissions. Turbulences arise from an accumulation of irregular swirls of motions, known as eddies or thermals. Their range scale goes from some millimeters to the PBL depth itself.

Buoyancy is a relevant concept for characterizing the PBL structure. As example, heated air parcels near the surface are rising because they are less dense than surrounding cooler air. Applying ideal gas law

$$p = n_{molec} k_B T \qquad \text{(Eq 1.34)}$$

in which $p$ is the pressure, $n_{molec}$ the molecular number density, $k_B$ the Botzmann constant, T the absolute temperature, to a static atmosphere, one obtains the hydrostatic equation

$$p(z) = p_0 \exp\left( -\int_0^z \frac{M_r(z')g(z')}{RT} dz' \right) \qquad \text{(Eq 1.35)}$$

where $z$ is the altitude, $p_0$ is the surface pressure, $R=N_A k_B$ ($N_A$ being the Avogadro's number) is the ideal gas law constant, $M_r$ is the molecular weight, $g$ the acceleration due to gravitation. In the lowest part of the atmosphere, this results in a pressure decrease by a factor 2 pro 5 km altitude increase.

Application of the first law of thermodynamic to the adiabatic vertical motion of an air parcel together with the ideal gas law gives a temperature lapse rate of $-g/c_p \approx -9.8$ °C/km, where $c_p$ is the specific heat of dry air at constant pressure. This value exceeds far real mean values, due to the presence of water-vapor. Water-vapor has a molecular weight of about 18 g/mol, what is much lighter than the dry air value 28.966 g/mol. So, at given temperature and pressure, wet air is more buoyant. The case is different with liquid water-vapor, when the water content exceeds the condensation limit.

In order to quantify the buoyancy by a single parameter, we first release the density variation due to pressure decrease following (Eq 1.35). This leads to the definition of the potential temperature

$$\theta = T\left( \frac{p_0}{p} \right)^{\tilde{R}/c_p} \qquad \text{(Eq 1.36)}$$

where $\tilde{R} = \frac{R}{M_r}$. Conventionally, $p_0$ is taken as 1000 hPa.

Further, accounting for water-vapor leads to the definition of the virtual potential temperature, whose expression is different for unsaturated or saturated case. For unsaturated case, it reads

$$\theta_v = \theta(1 + 0.61r) \qquad \text{(Eq 1.37a)}$$

where $r$ is the water-vapor mass mixing ratio (ratio of the mass of water-vapor to the mass of dry air). For the saturated case, $r$ takes its saturation value corresponding to the saturation water-vapor pressure, and the liquid water content brings a negative contribution, as follow

$$\theta_v = \theta(1 + 0.61r_{sat} - r_L) \qquad \text{(Eq 1.37b)}$$

where $r_L$ is the liquid water mixing ratio (ratio of the mass of liquid water to the mass of dry air).
A detailed derivation is given in [*Stull*, 1988].

Figure 1.3 presents a typical vertical profile of many relevant meteorological parameters. The left panel shows the virtual potential temperature defined above. Due to strong surface heating and surface albedo, $\theta_v$ decreases with height over typically some tenth to hundreds of meters (surface layer). Such unstable conditions are known as super-adiabatic. Correspondingly, the fourth panel shows that the vertical eddy heat flux is increasing when approaching the ground, what is the signature of a net upward heat-flux (strong turbulent activity, mixing through development of thermals). Above that layer, $\theta_v$. is nearly constant, reflecting that the continuous mixing processes have lead to nearly homogeneous partition of the buoyancy. This layer is named (convective) mixed layer (ML). The terms well-mixed and mixing layer are also used. Despite the quasi-

adiabatic conditions, the ML is not statically stable, due to the largest $\theta_v$ values in the surface layer (see also positive values of the vertical eddy heat flux). The ML is capped from above by a zone of increasing $\theta_v$ values, what ensures a global stability (PBL is bounded to earth). Correspondingly, the vertical eddy heat flux becomes negative. This zone is named entrainment zone, since entrainment into the ML occurs there. Let's just add a few comments on other profiles. The specific humidity (second panel) is generally stronger near the ground, since this is a water-vapor source and the radiation induces a large evaporation. Let's notice here that for many cases, the concentration of pollutants presents a similar trend than water-vapor. Near the ground, the wind (third panel) is constraint to get weaker due to the frictional drag. Above the PBL, it tends toward its geostrophic value and direction, which is obtained from the general laws of atmospheric motion by neglecting the frictional terms. Within the mixed layer, wind values are generally smaller than the geostrophic ones, and the wind shear is limited by internal frictions.

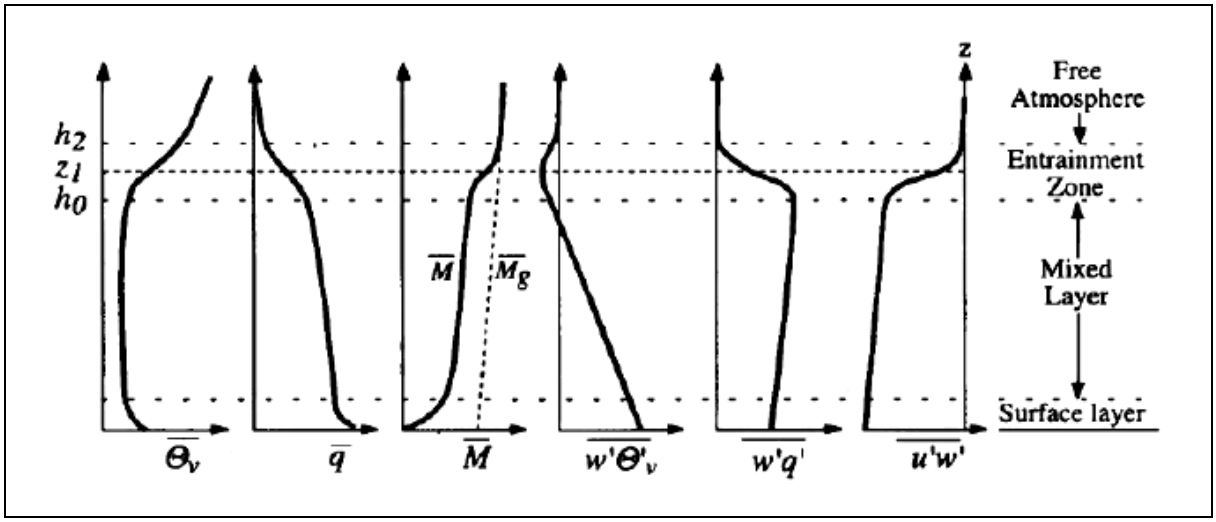


**Figure 1.3.** *Typical daytime PBL profiles of various relevant meteorological parameters. First panel left ($\theta_v$): the virtual temperature; second panel (q): specific humidity; third panel (M): mean horizontal wind speed; fourth panel (w'$\theta_v$'): vertical kinematic eddy heat flux; fifth panel (w'q'): vertical kinematic eddy moisture flux; last panel right (u'w'): vertical kinematic eddy flux of momentum along one horizontal direction. The heights $h_0$ and $h_2$ are the base and top of the entrainment zone; $z_i$ is the mean PBL top (from* [*Hartmann,* 1994]*).*

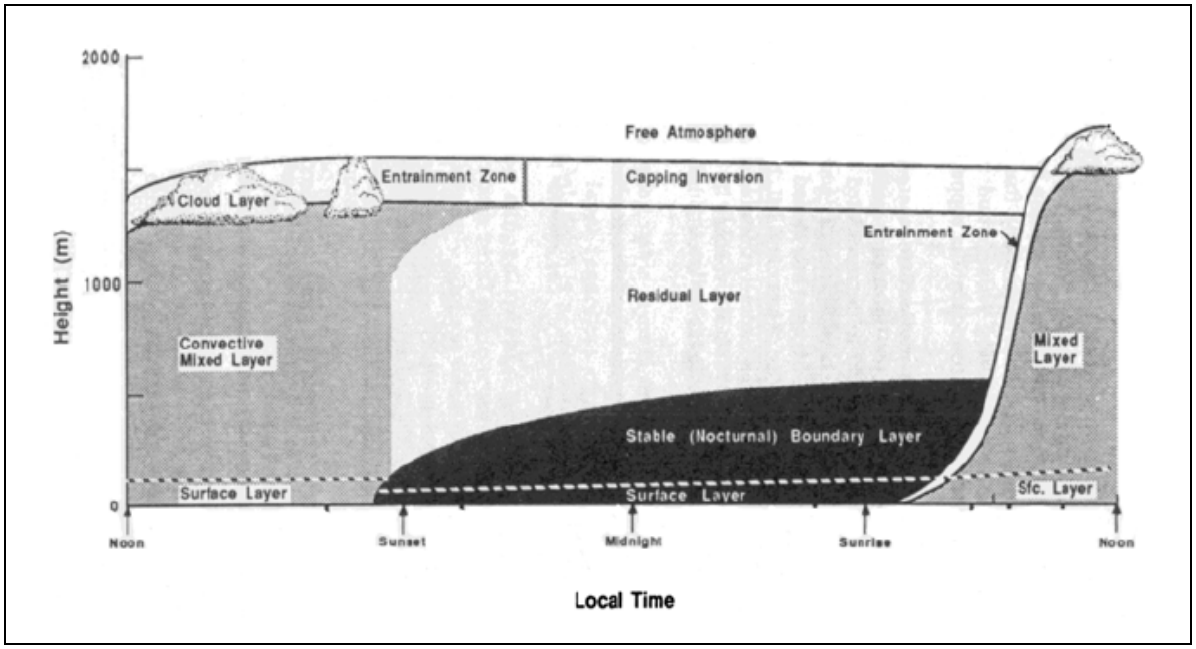


**Figure 1.4.** *Typical diurnal PBL development over land (*[Stull*, 1988*]*). See description in the text.*

Figure 1.4 presents a typical diurnal development of the PBL over land. In almost clear-sky conditions, the mixed layer is essentially driven by convection, as has been noticed above (Fig. 1.3). Its development is linked

with the incoming solar radiation and the consecutive ground heating. About half an hour after sunrise, a turbulent mixed layer starts to grow. This is an unstable situation in which thermals are rising from the ground. Its growth occurs via entraining (or mixing down) of the less turbulent air masses aloft. Typically, the depth of the PBL is maximum at the end of the afternoon. Within the PBL, the turbulence tends to mix heat, moisture, aerosols, tending to a nearly uniform distribution (as in Fig. 1.3). About half an hour after sunset, the turbulence within the mixed layer decreases quickly. Near the ground, and in absence of clouds, the terrestrial IR-radiation induces thermal cooling. This leads to the formation of a statically stable layer, called stable (nocturnal) boundary layer (SBL). Above it, the mixed layer evolves into an almost neutrally stratified layer, named residual layer (RL). Consequently, this results in a relatively low growth speed of the next day's mixed layer till the top of the SBL. Further, the growth is quicker since the RL is nearly neutrally stable (adiabatic). The first tens to hundreds of meters above the surface, named surface layer, presents almost always non-adiabatic lapse rate, with typically super-adiabatic (unstable) during day-time and (stable) temperature inversion night-time. This behavior is naturally linked to the strong influence of the ground radiation heating and cooling. Thus, in presence of clouds, all processes tend to be weaker, since there is less net downward radiation day-time and also less net upward radiation night-time, leading to a reduced PBL depth.

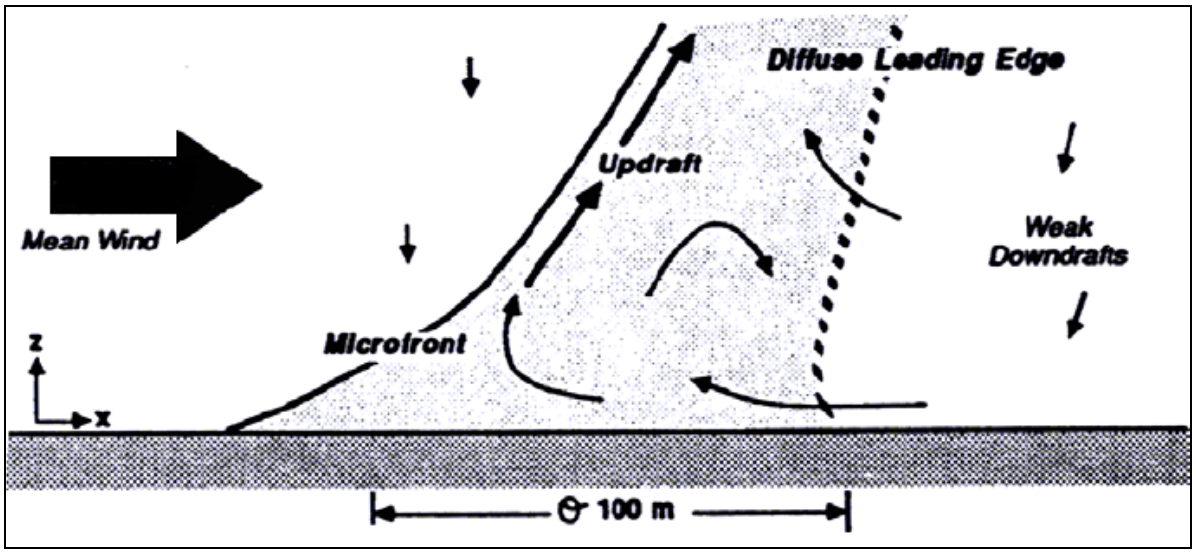


**Figure 1.5.** *Typical structure of a thermal, above ground (from* [*Hartmann,* 1994]*).*

Figure 1.5 shows the typical structure of a thermal above ground. Due to horizontal differential radiation at a micro-scale, an air mass of typical horizontal extent of 100 m, is locally more buoyant than it's surrounding. The upward motion (updraft) creates a micro-front on the side of predominant wind origin. The induced return flow is named downdraft. Updrafts tend to be more organized and cover a smaller area than downdrafts. Such features are the basic elements of the mixing processes trough-out the PBL, in particular in the entrainment zone. Since updrafts are generally more humid and aerosol-rich than downdrafts, their interface is well marked in a Lidar signal. This subject will be developed in the section 1.3.

The aerosol emitted from the Earth's surface from natural and anthropogenic sources are mixed in the PBL unstable layer or accumulate below stable layers. In this way, the aerosols are a tracer showing the development and the dynamics of the PBL.

## 1.2.4 Wind systems in a valley

In the subsection 1.2.3, the typical PBL structure above flat terrain has been presented. This is a case when the PBL growth is nearly horizontally uniform.

As it has been pointed before, the surface layer is the part of the PBL most exposed to radiative forcing. Over hills, mountains or in valleys, the solar exposure is very inhomogeneous. The albedo (ratio of reflecting

radiation to down welling radiation) frequently varies very largely within a few kilometers. The table 1.2 presents some typical albedo values over different landuses*.

Another impact of the complex topography is in the mechanical forcings on the flow, and consecutive enhancement of the generation of eddies. The topography induces flow patterns, like lee waves, rotors, and cavities. Such patterns can last for hours in mountainous areas, and affects significantly the local PBL structure. The differential heating and cooling of air masses at the same altitudes but located either in or above the surface layer induces wind systems. In day-time, the strong heating along slopes leads to anabatic up-slope wind. In night-time, the radiative cooling induces katabatic down-slope wind. Along the valley axis, the terms of valley (or up-valley) wind and mountain (or down-valley) wind are used.

**Table 1.2.** *Typical albedo values.*

| Landuse | Albedo [%] |
|---|---|
| Fresh snow | 95 |
| Permanent ice | 60 |
| Light-colored dry soils | 40 |
| Grass-land / Crops | 20 |
| Deciduous forest | 16 |
| Coniferous forest | 12 |
| Forest swamp | 14 |
| Water | 8 |
| Dark wet soils | 5 |

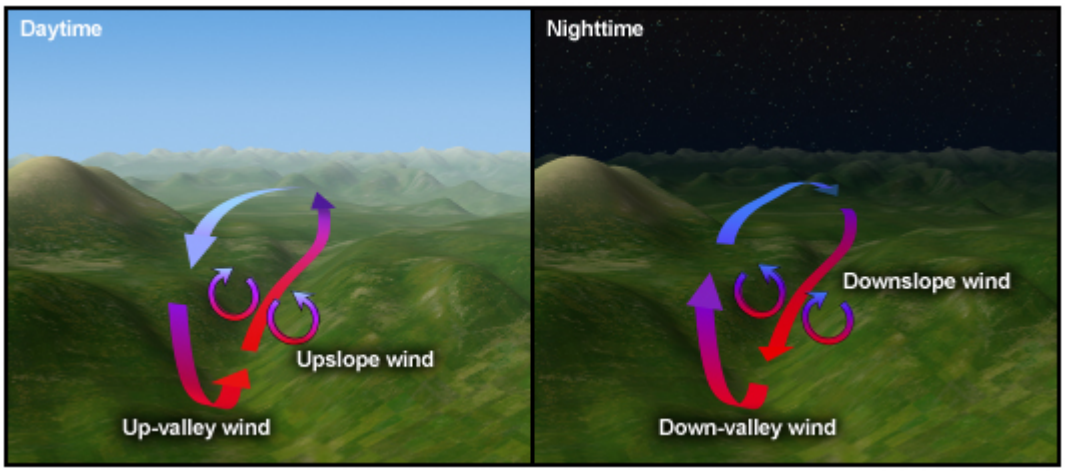


**Figure 1.6.** *Typical wind system in a valley (from http://deved.comet.ucar.edu/mesoprim/mtnval/print.htm).*

Since the valley has a weaker incline than the adjacent slopes, the triggering of along-valley winds is slower than the corresponding slope-winds. Figure 1.6 shows the typical flow pattern in a valley, for day-time (left panel) and night-time (right panel). The conservation laws of the fluid motion induces return (or compensation) flows such a way to close the circulation. Figure 1.7 shows more precisely the typical diurnal cycle of the wind system: as noticed above, the slope winds react in shorter time to the radiative variations, leading to the depicted daily sequence.

* The influence of albedo affects all types of terrain. The concept of thermal internal boundary layer applies to the flow over areas with different surface heat flux. See [*Stull*, 1988]; [*Lyons*, 1975]; [*Garratt*, 1987].

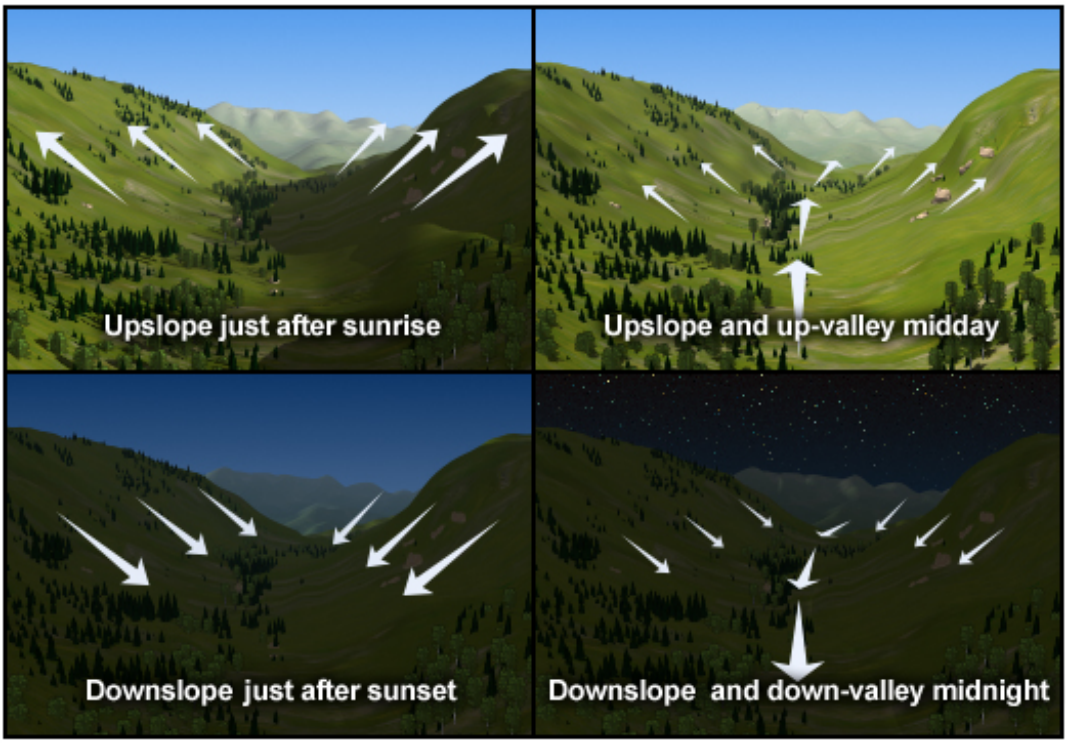


**Figure 1.7.** *Typical diurnal cycle of the wind system (from http://deved.comet.ucar.edu/mesoprim/mtnval/print.htm)*

The development of the nocturnal SBL is also strongly influenced by the topography. In absence of strong advection along the valley axis, the nocturnal down-slopes winds lead to the formation of a cold pool on the valley ground, what evolves into an inversion layer with a depth of the same size as the drop between surrounding crest level and valley floor. Above this layer, the residual layer is relatively warm. During the morning, the new mixed-layer on the valley floor and the upslope wind system erode this inversion core. This procedure last typically for several hours. Under good radiative conditions, a well-mixed layer develops by end of the afternoon. But in absence of strong radiation and advection, the inversion core can persist several days.
Similar wind patterns are observed between a plateau and an adjacent mountainous area. Let's notice that in the countries of Central Europe, the vertical dimension of obstacles (~2000-4000 m) is larger than the typical PBL depth above flat terrain (~1500 m). Thus, it is obviously expected that the PBL structure is deeply influenced by the topography. Examples of such complex terrain influences will be presented in Chapters 3-4**.**

# 1.2.5 Scattering properties of the atmosphere

The Lidar does "see" the aerosols exclusively trough their optical properties, like backscattering coefficient, extinction. In this subsection, we make a short overview of the scattering properties of the atmospheric constituents.

## 1.2.5.1 The meteorological range of visibility

As pointed out in §1.2.2.2, one of the relevant properties of tropospheric aerosols is their high reflectivity to solar radiation. In proper optical terms, this means that their backscattering coefficient is an important part of the total backscattering.

Since the surface is the principle source of aerosols (pollution) and humidity (evaporation), aerosol densities are often maximal near the ground. Common life experience shows that high aerosol concentrations affect significantly the horizontal visibility. This is equivalent to say that, in the visible wavelengths, the mean aerosol extinction is a large part of the total extinction.

Usually, aerosols tend to be spread out in horizontal (through e.g. lofting or fumigation processes). In this way, the naked-eye horizontal visibility is a first measure of the local extinction at 550 nm, where is the peak of human eye sensitivity. The Koschmieder equation allows such a simple evaluation

$$R_m = \frac{1}{\overline{\alpha}} \ln\left(\varepsilon^{-1}\right) \qquad \text{(Eq 1.38)}$$

where $\overline{\alpha}$ is the mean volume extinction coefficient, $\varepsilon$ a threshold contrast of the observer, $R_m$ the meteorological range. $R_m$ is defined as the limit of observation of a black target against the horizon sky in daylight. Typically $\varepsilon$=0.02 (value adopted in LOWTRAN): it is just the (minimum perceptible) optical transmission $T\ (R_m) = \exp\left(-R_m \overline{\alpha}\ \right)$. Table 1.3 gives the meteorological ranges for some typical weather conditions. The comparison of the two last lines demonstrates strikingly the huge impact of aerosols on optical transmission.

**Table 1.3.** *Meteorological ranges for some typical weather conditions.*

| Weather condition | Meteorological range [km] | Extinction coefficient (@550 nm) x$10^{-3}$ $m^{-1}$ |
|---|---|---|
| Thick fog | 0.05 | 78.2 |
| Moderate fog | 0.2 | 19.6 |
| Light fog | 0.5 | 7.82 |
| Thin fog | 1 | 3.91 |
| Haze | 2 | 1.96 |
| Light haze | 4 | 0.954 |
| Clear | 10 | 0.391 |
| Very clear | 20 | 0.196 |
| Exceptionally clear | 50 | 0.078 |
| Pure air [(a)] | 277 | 0.0141 |

[a] Virtual case in the PBL

## 1.2.5.2 Two types of scattering - Overview

Table 1.4 summarizes the responsible particles for atmospheric scattering. Their size ranges over about height orders of magnitude. The scattering of light with these particles depend basically on the size parameter defined as $x = \frac{2\pi r}{\lambda}$, where $r$ is the mean radius of the particle and $\lambda$ the wavelength of the incident light, on their shape and on their composition, which is optically characterized by the refractive index.

For the case of small particle for which $x$<0.1, the scattering type is called “Rayleigh” or “molecular”. In that case, the particles behave almost like electric dipoles, and their shape is nearly negligible. In the next subsection 1.2.5.3, we present the (molecular) Rayleigh scattering properties for the air. For greater values of $x$, which includes a large part of the aerosol constituents at the usual Lidar working wavelength, the scattering type is called “Mie”. This is the subject of the subsection 1.2.5.4.

**Table 1.4.** *Particles contributing to atmospheric scattering.*

| | Radius [μm] | Concentration [$cm^{-3}$] |
|---|---|---|
| Air molecule | $10^{-4}$ | $10^{19}$ |
| Aitken nucleus | $10^{-3}$-$10^{-2}$ | $10^{4}$-$10^{2}$ |
| Haze particle | $10^{-2}$-1 | $10^{3}$-10 |
| Fog droplet | 1-10 | 100-10 |
| Cloud droplet | 1-10 | 300-10 |
| Raindrop | $10^{2}$-$10^{4}$ | $10^{-2}$-$10^{-5}$ |

## 1.2.5.3 Rayleigh scattering

In the air, the scattering term of the extinction coefficient (see (Eq 1.3)) is expressed as the product of the molecular number density $N_{air}$ with the so-called Rayleigh scattering cross-section $\sigma_R$ (per molecule). Let *Oxyz* be a system of coordinates attached to one molecule, and ($\theta$,$\varphi$) the polar coordinate system for the scattered beam direction ($\theta$ is the scattering angle versus *Oz* direction, $\varphi$ the azimuth versus *Ox*). For an incident light beam of wavelength $\lambda$ along the positive z-axis and linearly polarized in the *Ox* direction, the molecular Rayleigh scattering differential cross-section is given by [*Penndorf*, 1957]

$$\frac{d\sigma_R}{d\Omega} = \frac{9\pi^2(n_{air}^2-1)^2}{N_{air}^2\lambda^4(n_{air}^2+2)^2}\frac{6+3\rho}{6-7\rho}(\cos^2\varphi\cos^2\theta+\sin^2\varphi) \qquad \text{(Eq 1.39)}$$

where $n_{air}$ is the air refractive index and $\rho$ is the depolarization ratio. This gives the scattering cross-section

$$\sigma_R = \frac{24\pi^3(n_{air}^2-1)^2}{N_{air}^2\lambda^4(n_{air}^2+2)^2}\frac{6+3\rho}{6-7\rho} \qquad \text{(Eq 1.40)}$$

The backscattering (differential) cross-section is

$$\sigma_R^{\pi} = \left[\frac{d\sigma_R}{d\Omega}\right]_{\theta=\pi} = \frac{9\pi^2(n_{air}^2-1)^2}{N_{air}^2\lambda^4(n_{air}^2+2)^2}\frac{6+3\rho}{6-7\rho} \qquad \text{(Eq 1.41)}$$

Let's notice that, if we neglect molecular absorption, the ratio of extinction to backscatter is $\frac{8\pi}{3}$ sr.

The main behavior of $\sigma_R$ concerns the $\lambda^{-4}$ dependency, which is a first good approximation. Notice that the air refractive index also depends on wavelength [*Eltermann*, 1968]. Anyhow, the largest uncertainty in the evaluation of the Rayleigh scattering cross-section comes from the depolarization term (also named King factor),

$$F(air) = \frac{6+3\rho}{6-7\rho} \qquad \text{(Eq 1.42)}$$

which accounts for anisotropy in molecular polarizability. Following [*Young*, 1981], the recommended value for dry air is 1.0481 ($\rho$ = 0.0279). But it depends also on the wavelength. Following the recommendation found in [*Bodhaine et al.*, 1999], it is sufficient to consider the wavelength dependency of $N_2$ and $O_2$. Such relations have been provided in [*Bates*, 1984]

$$F(N_2) = 1.034 + \left(3.17\times10^{-4}\frac{1}{\lambda^2}\right) \qquad \text{(Eq 1.43a)}$$

$$F(O_2) = 1.096 + \left(1.385\times10^{-3}\frac{1}{\lambda^2} + 1.448\times10^{-4}\frac{1}{\lambda^4}\right) \qquad \text{(Eq 1.43b)}$$

where $\lambda$ is the wavelength in µm. Bates recommended to assume $F(Ar)=1$, $F(CO_2)=1.15$ and to ignore other minor air constituents. In order to adapt the evaluation to the continuous increase of the $CO_2$ concentration, he proposed the following expression

$$F(air) = \frac{78.084F(N_2)+20.946F(O_2)+0.934+C_{CO_2}\times1.15}{78.084+20.946+0.934+C_{CO_2}} \qquad \text{(Eq 1.44)}$$

in which $C_{CO_2}$ is the $CO_2$ concentration in part per volume by percent (i.e. 0.03 stands for 300 ppmv).

In (Eq 1.40), both molecular density $N_{air}$ and the refractive index $n_{air}$ are dependent of pressure and temperature. $N_{air}$ is given by the Avogadro's law, which states that $N_A$ = 6.0221367x10$^{23}$ molecules (Avogadro's number) occupy a volume of 22.414 dm$^3$ at 273.15 K and 1013.25 hPa. Formulae for the evaluation of $n_{air}$ have been proposed by [*Penndorf*, 1957], [*Edlen*, 1966], [*Peck and Reeders*, 1972]. Let's notice first that $n_{air}$ values depart very few from 1: for dry air, a typical value at 532 nm is 1.000278. It depends significantly on the water-vapor content and on $CO_2$ concentration [*Edlen*, 1966]. For dry air, the $CO_2$ concentration dependency is well represented by following correction formula

$$\frac{(n_{air}^{C_{CO_2}}-1)}{(n_{air}^{0.03}-1)} = 1+0.0054\left(C_{CO_2}-0.03\right) \qquad \text{(Eq 1.45)}$$

Further, we again follow the recommendation found in [*Bodhaine et al.*, 1999]. We use the formula proposed by [*Peck and Reeders*, 1972], which is valid for dry air, with $C_{CO_2} = 0.03$ (typical value at that time) at 288.15 K and 1013.25 hPa

$$(n_{air}^{0.03} - 1) \times 10^8 = 8060.51 + \frac{2480990}{132.274 - \lambda^{-2}} + \frac{17455.7}{39.32957 - \lambda^{-2}} \qquad \text{(Eq 1.46)}$$

where, as before, $\lambda$ is the wavelength expressed in μm. With $C_{CO_2} = 0.036$, a similar formula holds

$$(n_{air}^{0.036} - 1) \times 10^8 = 8060.77 + \frac{2481070}{132.274 - \lambda^{-2}} + \frac{17456.3}{39.32957 - \lambda^{-2}} \qquad \text{(Eq 1.47)}$$

At the same pressure and temperature, $N_{air}$ is obtained from Avogadro's law, with an ideal gas correction for the temperature, yielding

$$N_{air} = 2.546899 \times 10^{25} \text{ [molecules/m}^3\text{]} \qquad \text{(Eq 1.48)}$$

Tables 1.5 and 1.6 show some Rayleigh scattering cross-section respectively King factor, deduced from (Eqs 1.43-1.48), for some useful wavelengths and recent average tropospheric values of $CO_2$ concentrations.

**Table 1.5.** *Rayleigh cross-sections of dry air.*

| $\sigma_R$ [x10$^{-26}$ cm$^2$] | 266 nm | 355 nm | 532 nm | 1064 nm |
|---|---|---|---|---|
| [$CO_2$] = 360 ppmv | 9.5597679 | 2.7588526 | 0.51672738 | 0.031269352 |
| [$CO_2$] = 365 ppmv | 9.5598236 | 2.7588752 | 0.51673042 | 0.031269537 |
| [$CO_2$] = 370 ppmv | 9.5598792 | 2.7588849 | 0.51673346 | 0.031269721 |

**Table 1.6.** *King factors for dry air.*

| *F(air)* | 266 nm | 355 nm | 532 nm | 1064 nm |
|---|---|---|---|---|
| [$CO_2$] = 360 ppmv | 1.0603673 | 1.0528864 | 1.0489889 | 1.0472093 |
| [$CO_2$] = 365 ppmv | 1.0603677 | 1.0528869 | 1.0489894 | 1.0472098 |
| [$CO_2$] = 370 ppmv | 1.0603682 | 1.0528873 | 1.0489900 | 1.0472104 |

For further comparison with the Mie scattering type, let's see how the scattered intensity is distributed in function of the angles ($\theta$,$\varphi$). Figure 1.8 presents the angular distribution of the scattered intensity in function of the scattering angle $\theta$ for three values of $\varphi$ ($\varphi$=0 ('parallel'), $\varphi$=π/2 ('perpendicular'), $\varphi$=π/4 ('unpolarized')). The term 'unpolarized' is used here, since the angular distribution (versus $\theta$) of the scattered intensity measured in the plane $\varphi$=π/4 is the same as the one from an incident unpolarized light (for which there is no $\varphi$ dependency). In Fig. 1.8, the radial scale gives the values of the volume scattering coefficient $N_{air}\left[\frac{d\sigma_R}{d\Omega}\right]_{\theta,\varphi}$ with the angular dependency as in (Eq 1.33), for dry air at 287.15 K and 1013.25 hPa, and at a wavelength of 532 nm. First, lets notice that, although the particles shape does not enter in (Eq 1.33), the scattering process is obviously not isotropic. Secondly, the most relevant feature of the Rayleigh scattering (not specifically molecular) is the symmetric behavior between forward and backward directions. Moreover, in the plane parallel to the incident beam polarization, the scattered intensity at 90° vanishes: this behavior is known as Tyndall effect.

## 1.2.5.4 Mie scattering

When the size parameter exceeds approximately 0.1, the qualitative scattering pattern of light deviates from the Rayleigh one. In such cases, the particle constitution (i.e. shape and chemical compositions) is relevant (i.e. the dipolar approximation is insufficient). This makes the calculation of scattering by real atmospheric aerosols a very difficult task. Whenever the particle number density is not too high, what we will always assume (single-scattering approximation), the scattering on each particle can be considered as independent from the other, and the scattering processes may be divided following e.g. the particle size or composition (superposition principle).

Further, let's restrict our consideration to monodispersion of homogeneous spherical particles: monodispersion means that we consider only identical particles. The homogeneity refers to the composition, and

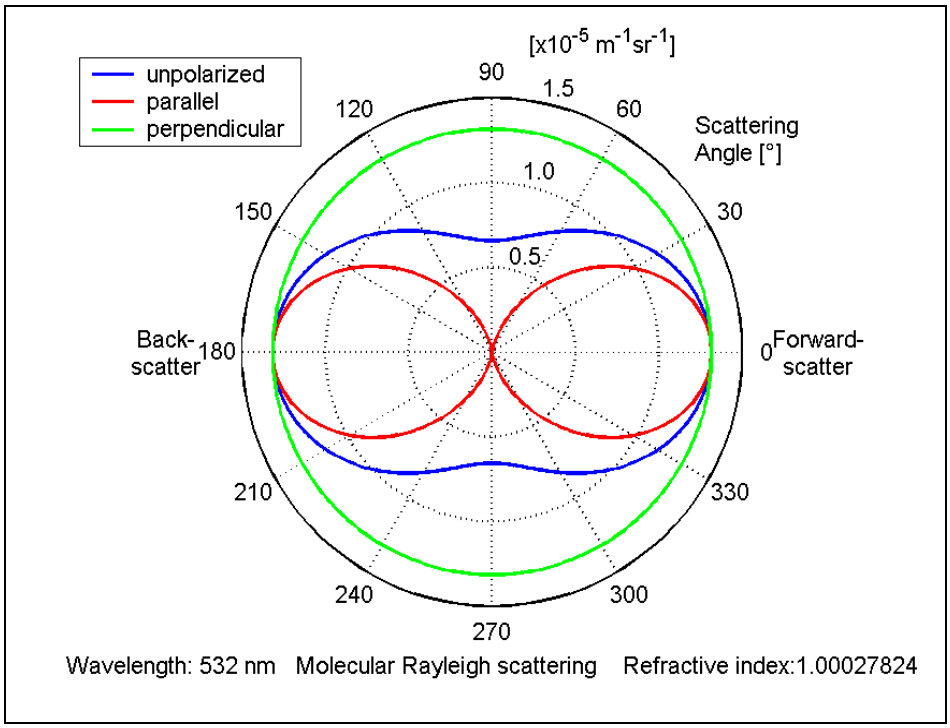


**Figure 1.8.** *Angular distribution of the volume scattering coefficient for a linearly polarized beam at 532 nm, in dry air at 288.15 K, 1013.25 hPa.*

thus to the refractive index. This is the frame of the Mie theory, which gives an analytical solution for the scattering of homogeneous spherical particles. The only input parameters are the size parameter $x$ and the complex (relative) refractive index $m$ of the particle, i.e. the ratio of the particle refractive index (in vacuum) and the one of the background medium (usually, $n_{air}$=1 is assumed). The plane-wave propagation theory shows that the imaginary part of $m$ is associated to the (volumic) absorption coefficient (see (Eq 1.4)), as follow

$\alpha^{abs} = \frac{4\pi|\mathrm{Im}(m)|}{\lambda}$. Also, the energy conservation law in a non-absorbing medium leads automatically to the separation of extinction into scattering and absorption (see [*Bohren and Huffman*, 1983], p. 70). Since Mie theory is an independent particles model, we can express this separation in terms of (particle) cross-sections

$$\sigma^{sca}=\sigma^{ext}+\sigma^{abs} \qquad \text{(Eq 1.49a)}$$

With a classical view, we expect these cross-sections to be proportional to the particle cross-sectional area (as seen along the incident beam direction). Within the Mie model, this is simply $\pi r^2$, where $r$ is the radius of the particles. This leads to the definition of the corresponding efficiencies $Q = \frac{\sigma}{\pi r^2}$, satisfying obviously

$$Q^{sca}=Q^{ext}+Q^{abs} \qquad \text{(Eq 1.49b)}$$

The (differential) backscatter cross-section is defined as

$$\sigma^{back} = 4\pi\left[\frac{d\sigma^{sca}}{d\Omega}\right]_{\theta=\pi} \qquad \text{(Eq 1.50a)}$$

and the corresponding backscatter efficiency is

$$Q^{back} = \frac{\sigma^{back}}{\pi r^2} = \frac{4}{r^2}\left[\frac{d\sigma^{sca}}{d\Omega}\right]_{\theta=\pi} \qquad \text{(Eq 1.50b)}$$

Note that the presence of the factor $4\pi$ in (Eq 1.50a), not included in (Eq 1.5), leads to the following link with the volume backscattering coefficient

$$\beta = N\frac{Q^{back}\pi r^2}{4\pi} \qquad \text{(Eq 1.50c)}$$

where $N$ is the particle number density of the dispersion.

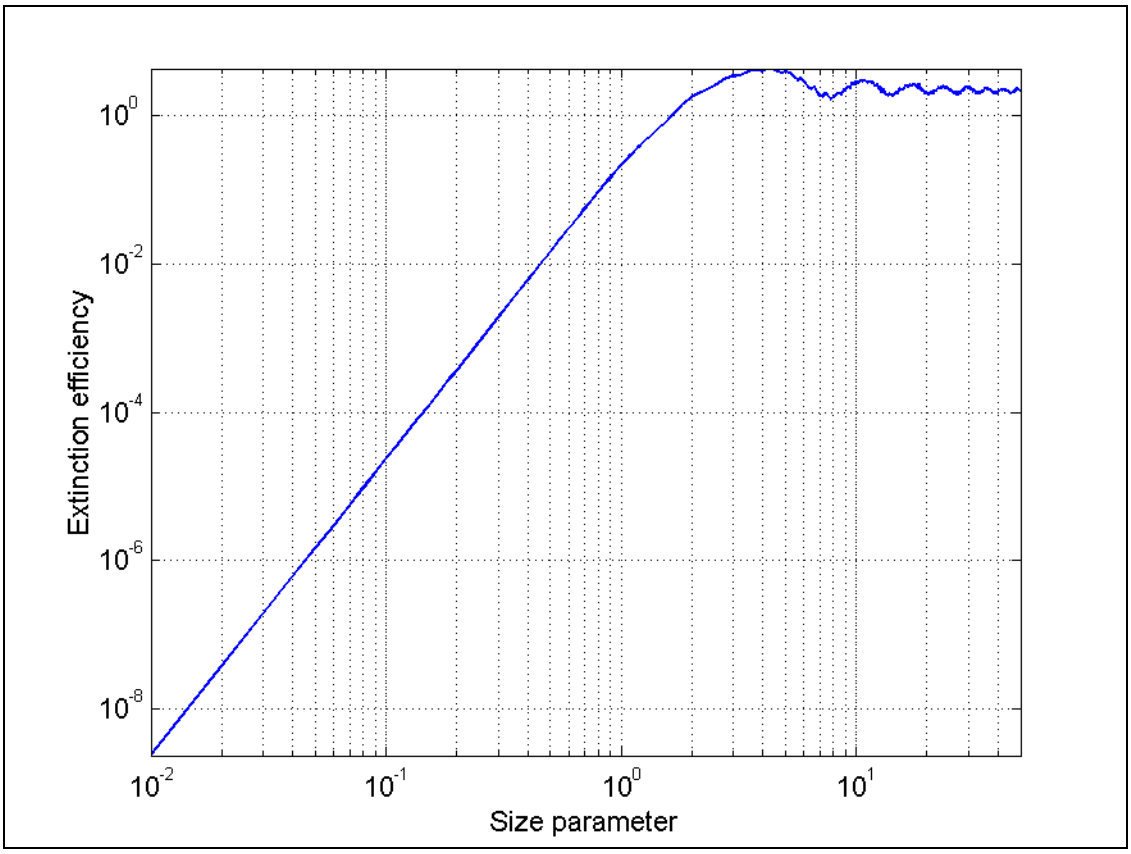


**Figure 1.9.** *Extinction efficiency versus size parameter from Mie routine calculation, with a refractive index of 1.5.*

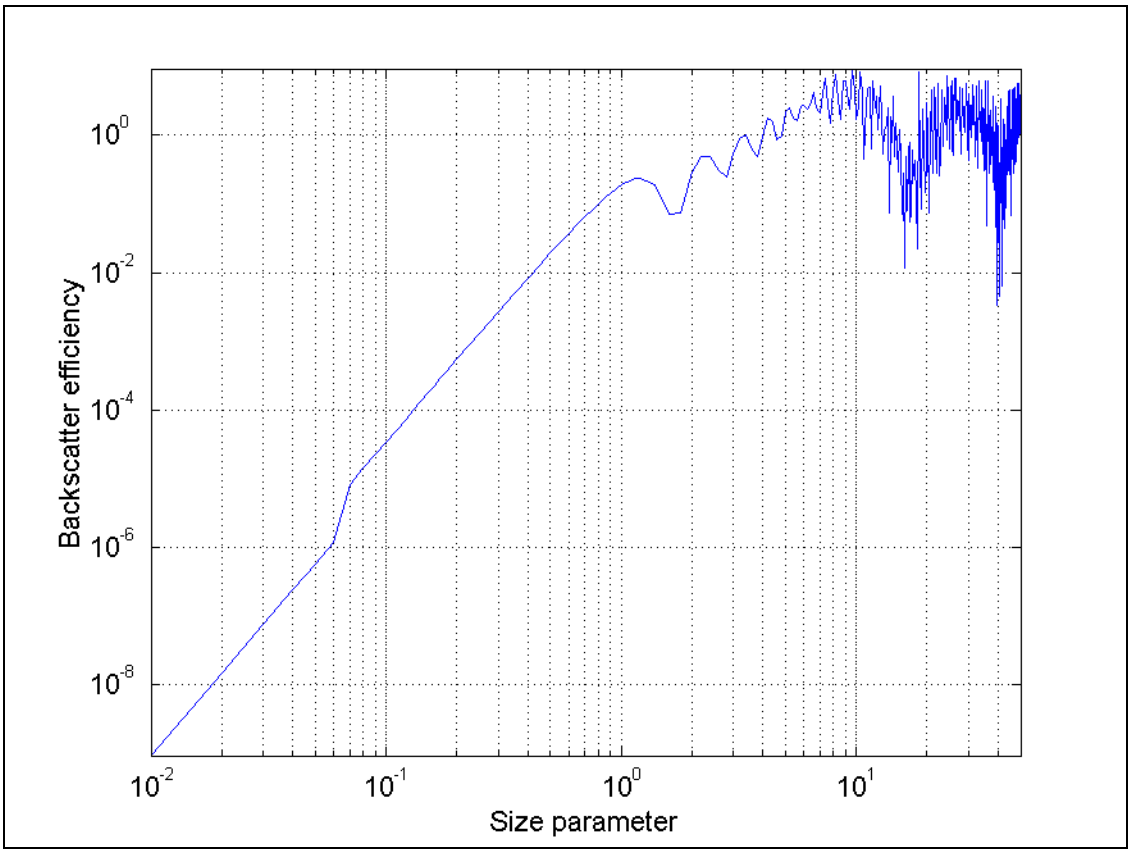


**Figure 1.10.** *Backscatter efficiency versus size parameter from Mie routine calculation, with a refractive index of 1.5.*

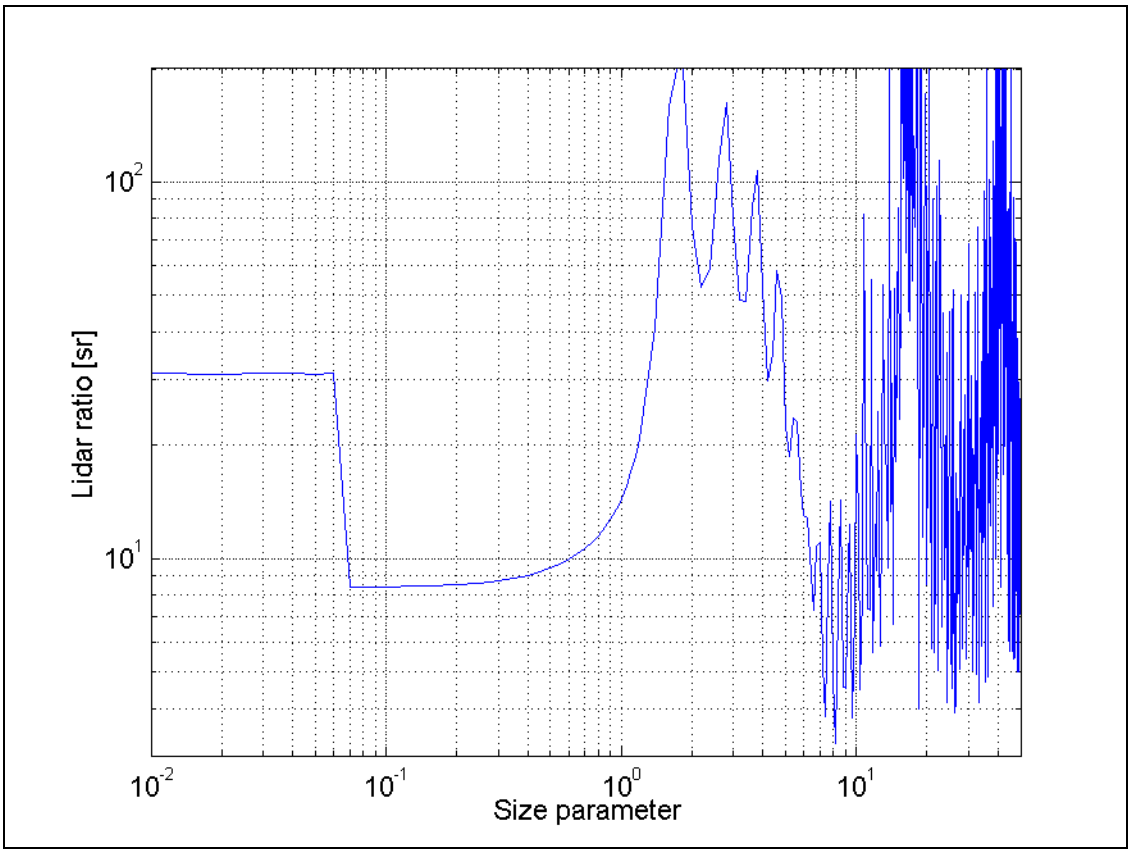


**Figure 1.11.** *Lidar ratio versus size parameter from Mie routine calculation, with a refractive index of 1.5.*

Figures 1.9 and 1.10 show the extinction efficiency respectively the backscatter efficiency versus the size parameter for a particle refractive index of 1.5, obtained by a Mie routine. The increment in size parameter is 0.2 above 1. Both graphs present a fine structure (Ripple structure) over a broader structure (interference structure). Figure 1.9 shows surprisingly the asymptotic value of 2 for the extinction efficiency (geometrical optics predicts 1).

Finally, Fig. 1.11 shows the corresponding extinction-to-backscatter ratio (or Lidar ratio)

$$lr = \frac{\alpha}{\beta} = 4\pi \frac{Q^{ext}}{Q^{back}} \qquad \text{(Eq 1.51)}$$

As a comparison, Fig. 1.12 reports the Lidar ratio from [*Ackermann*, 1998], based on Mie calculations for an aerosol mixture of continental type, versus relative humidity. The components of this mixture consist of three types: soot, insoluble and water-soluble. The real part of their refractive indexes at 532 nm ranges from 1.53 to 1.75. The relative humidity dependency is associated with an increase of the median radius of the water-soluble component.

From such behavior, it can be concluded that, for some real polydispersion of particles (averaging of monodispersions weighted with the size distribution), the scattering coefficient (or extinction coefficient when absorption is negligible) and backscatter coefficient behaves nearly as follow (Angstroem's law):

- $x<0.1$ $\alpha \sim \lambda^{-4}$ $\beta \sim \lambda^{-4}$ [Rayleigh regime]
- $x\sim1$ $\alpha \sim \lambda^{-k}$ with $k \in [0.5\text{-}2]$ $\beta \sim \lambda^{-k}$ with $k \in [0.7\text{-}1.5]$ [Mie regime]
- $x>>1$ $\alpha \sim \lambda^{-0}$ $\beta \sim \lambda^{-0}$ [Mie regime]

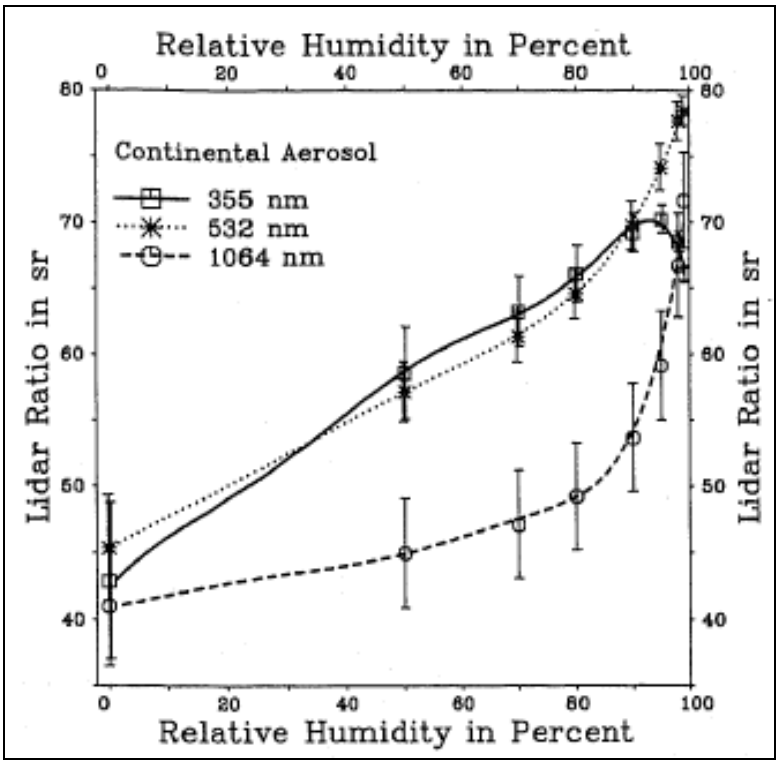


**Figure 1.12.** *Variation of the Lidar ratio based on Mie calculations for an aerosol mixture of continental type, versus relative humidity (from* [*Ackermann, 1998*]*).*

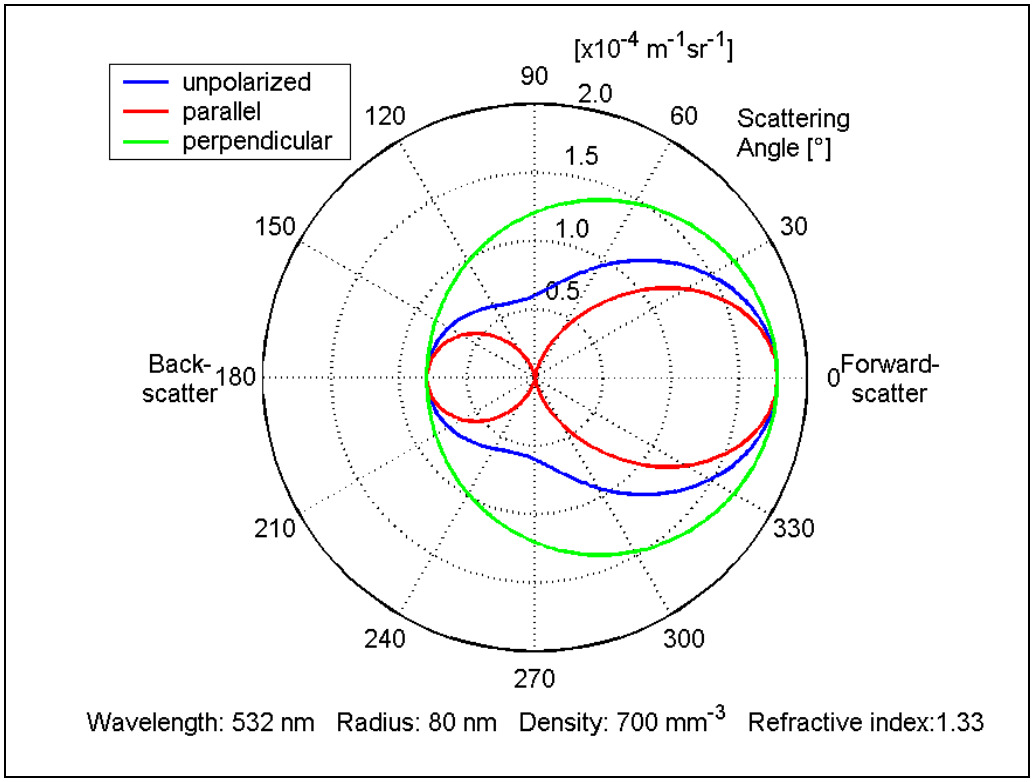


**Figure 1.13.** *Angular distribution of the volume scattering coefficient for a linearly polarized beam at 532 nm, for a monodispersion of particles, with radius 80 nm, density 700 mm*$^{-3}$ *and refractive index 1.33 (Mie routine calculation).*

Coming back to a monodispersion, Fig. 1.13 shows the angular distribution of the scattered intensity with a size parameter $x$=0.945. The striking difference with the Rayleigh case (Fig. 1.8) is the asymmetry between forward and backward scattering. This forward scattering predominance becomes extremely strong when $x$>>1. Secondly, with increasing size parameter appear a growing angular mode structure (succession of peaks and holes at large scattering angles): this appears on Fig. 1.14, what presents a zoomed view of the scattering pattern for a case with a size parameter of about 7.

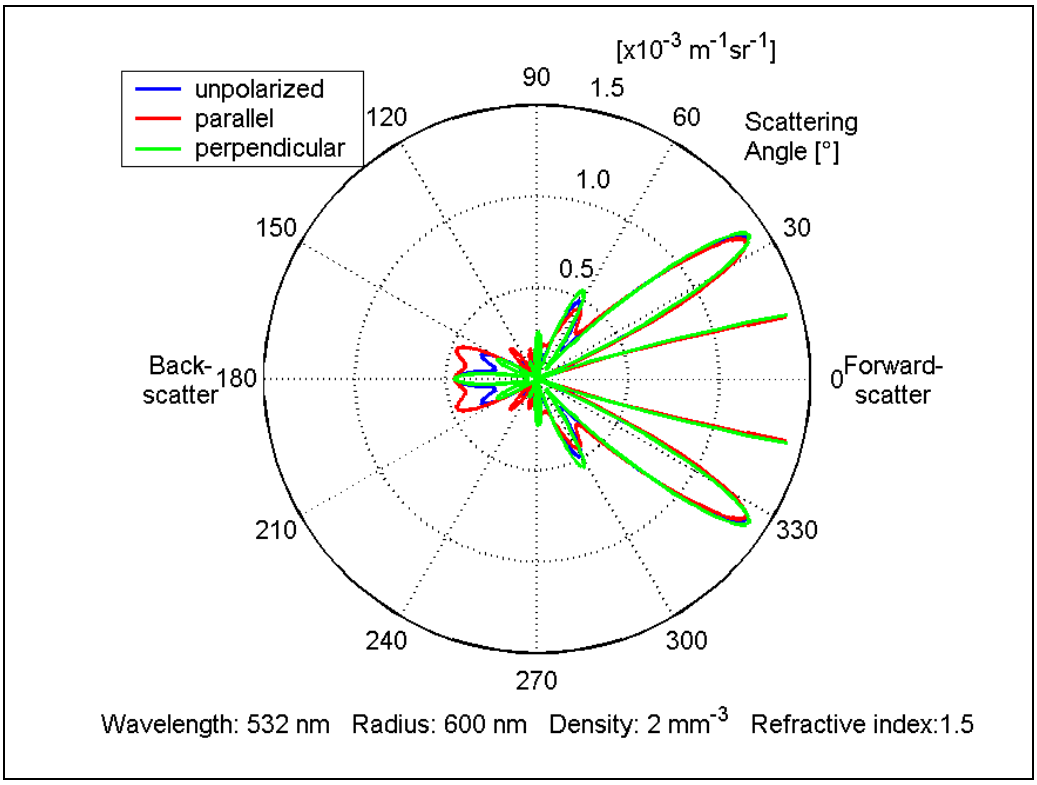


**Figure 1.14.** *Angular distribution of the volume scattering coefficient for a linearly polarized beam at 532 nm, for a monodispersion of particles of radius 600 nm, density 2 $mm^{-3}$ and refractive index 1.5 (Mie routine calculation). The forward lobe (hidden) extends up to 8x10$^{-3}$ $m^{-1}sr^{-1}$.*

# 1.3 The signal processing methods for the Backscatter Lidar

## 1.3.1 From the measured signal to the Range-Corrected Signal (RCS)

As has been pointed out in the subsection 1.1.3, the measured signal differs from the backscatter or atmospheric signal by the presence of noise. So, before beginning any processing, the first step is to account the contribution of all possible sources of noise. The contribution of the electronic noise is accounted by measurement of the "signal" with a closed telescope, when both atmospheric and background are absent. With open telescope and stopped laser beam, the measurements include also the background noise. The first step in the signal processing consists in subtracting this "noise signal" from the (atmospheric) measured signal. In photon-counting case, the measured signal consists usually of three terms, as follow

$$P_m(r) = P_s^{'}(r) + P_b(r) + P_n(r) \qquad \text{(Eq 1.52)}$$

where $P_s^{'}(r)$ is the atmospheric backscattered signal, $P_b$ is the background signal and $P_n$ a noise term from the detection chain. $P_b$ is always flat because the variation of background light during the acquisition of a single profile (one shot) is negligible. If $P_n$ is nearly flat (it is the case of the dark noise as example), then the atmospheric signal is at best approximated by an offset subtraction from $P_m$

$$P_s^{'}(r) \cong P_s(r) = P_m(r) - \left\langle P_b(r) + P_n(r) \right\rangle \qquad \text{(Eq 1.53)}$$

where the average is evaluated out of "atmospheric signal domain", i.e. either before the laser pulse or on the signal tail, where the atmospheric signal contribution is negligible. The approximation of $P_s^{'}(r)$ by $P_s(r)$ is excellent in regions of high signal-to-noise ratios, but become poor as this ratio is of some units only (see [*Bösenberg*, 1998]). Notice that $P_s(r)$ assumes negative values in the region of low signal-to-noise ratio. Thus, $P_s(r)$ is the effective Lidar signal used in the processing. In all subsequent references to Lidar signal, which shall be usually referred as $P(r)$, unless stated otherwise, it shall be understood that we refer to $P_s(r)$.

More relevant than the Lidar signal itself is its range-corrected form

$$RCS(r) = P_s(r) \cdot r^2 \qquad \text{(Eq 1.54)}$$

canceling out the range dependency in $P_s(r)$ of purely geometrical origin (see (Eq 1.7)).

$RCS(r)$ is extremely sensitive to offset shifts as performed in (Eq 1.53), in regions of low signal-to-noise ratio. Since any average evaluation is affected by some uncertainty, it is important to care about the corresponding uncertainties in $RCS(r)$. Another approach is to evaluate such offsets on the range-corrected signal instead of the signal itself (e.g., in fitting the $RCS$ to an expected distribution).

## 1.3.2 The inversion procedure of the Lidar equation

The Backscatter Lidar equation (Eq 1.11) is not sufficient to determine the backscatter coefficient. It contains also the atmospheric extinction, with unknown relation between the extinction and the backscatter coefficients. To solve the equation for $\beta^{aer}$ or $\alpha^{aer}$, it is necessary to assume a priori knowledge for their relation (e.g., guess of the aerosol lidar ratio).

Hereafter we report the solution of [*Klett*, 1981] and [*Fernald*, 1984], which deal with elastic backscatter. The Lidar equation (see (Eq 1.11)) is first put in a simplified form, and restricted above* the full overlap range ($O(r) \equiv 1$)

* The language used here is adequate for Lidar operating in zenith position, but the content is independent of such assumption

$$RCS(r) = C \cdot \beta(r) \cdot e^{-2\int_0^r dr'\alpha(r')} \quad \text{(Eq 1.55)}$$

where $C$ is a constant including laser power, overall optical efficiencies, quantum efficiency, PMT gain. Obviously, the solution of the inversion procedure must be independent of any device constant (i.e., the signal $P_m(r)$ may be expressed in photon number or as a voltage, depending on the acquisition mode). (Eq 1.55) is further put into a differential form as

$$\frac{dS(r)}{dr} = \frac{1}{\beta(r)}\frac{d\beta(r)}{dr} - 2\alpha(r) \quad \text{(Eq 1.56)}$$

where $S(r) = \log(RCS(r))$ **. Any further development requires a specific relation between $\alpha$ and $\beta$.

## 1.3.2.1 The Klett's solution form

A widely accepted relation is

$$\beta(r) = C'(\alpha(r))^k \quad \text{(Eq 1.57)}$$

where $C'$ is a constant and $k$ is another constant with values in the range 0.67-1 (see [*Fenn*, 1966] and [*Twomey et al*, 1965]). This applies only in region where aerosol backscattering dominates the molecular one. Under such simple assumption, (Eq 1.56) becomes a non-linear Bernouilli equation for $\alpha$. A stable solution form is

$$\alpha(r) = \frac{\exp\left(k^{-1}(S(r) - S_f)\right)}{\alpha_f^{-1} + 2\int_{r_f}^{r} dr' \exp\left(k^{-1}(S(r') - S_f)\right)} \quad \text{(Eq 1.58)}$$

where $r_f$ is a reference range, $\alpha_f = \alpha(r_f)$, $S_f = S(r_f)$. In choosing $r_f$ to be the top of the range domain on which we are looking for the solution, (Eq 1.58) gives a stable result versus variation of $\alpha_f$. A generalization of this solution with variable $C'$ is found in [*Klett*, 1985]. The choice of $r_f$ and the evaluation of $\alpha_f$ will be discussed further. Obviously, the solutions for the aerosol contributions $\alpha^{aer}$ and $\beta^{aer}$ are further obtained in subtracting the molecular contributions from the above solution (see (Eq 1.13)). More details for the evaluation of these latter contributions are given in §1.3.2.3.

## 1.3.2.2 The Fernald's solution form

Another approach is given by [*Fernald et al.*, 1972] and further discussed in [*Fernald*, 1984]. It is assumed that the Lidar ratio (see (Eq 1.51)) for the aerosol contribution is a constant $lr$. As has been pointed out in §1.2.5.3, the corresponding ratio for the molecular contribution is the constant $lr0 = \frac{8\pi}{3}$ sr. Under such assumption, the following solution is found

$$\beta(r) = \frac{RCS(r)\exp\left(-2(lr - lr0)\int_{rf}^{r} dr'\beta^{mol}(r')\right)}{\frac{RCS(r_f)}{\beta(r_f)} - 2lr\int_{r_f}^{r} dr' RCS(r')\exp\left(-2(lr - lr0)\int_{r_f}^{r} dr''\beta^{mol}(r'')\right)} \quad \text{(Eq 1.59)}$$

in which $r_f$ is again a reference (or calibration) range. As for the Klett's case, it is recommended to take it in the far range. Anyhow, integration can proceed forward or backward from the reference point. Numerically, this gives rise to a simple recurrence scheme for the evaluation of either $\alpha^{aer}$ or $\beta^{aer}$. It applies as well in regions of low aerosol content where the molecular contributions are dominant. Moreover, it is a relatively simple matter to

** Here and further, "log" stands for natural logarithm

generalize this scheme in order to deal with a variable Lidar ratio, what makes this solution more applicable to real atmospheric situations (i.e., existence of layers with different types of aerosol).

### 1.3.2.3 The contribution of the molecular component

Any inversion scheme requires the evaluation of the molecular contributions $\alpha^{mol}$ or $\beta^{mol}$. As discussed in §1.2.5.3, the molecular extinction is given by the product of the molecular (number) density and the Rayleigh cross-section $\sigma_R$ . The number density is given by (Eq 1.48) at 288.15 K and 1013.25 hPa. For other values, we assume just an ideal gas law correction.

When no specific temperature or pressure are available for the period and location of the Lidar measurement, we assume values from models given in [*Anderson et al.*, 1986]. Six models are given: tropical, mid-latitude summer, mid-latitude winter, subarctic summer, subarctic winter, and the US standard 76. In Central Europe, the midlatitude summer and midlatitude winter models are well suited for most cases.

Let's just add here that a precise knowledge of temperature is required when working with low wavelength, as in the UV: there, the molecular contributions are so large versus the aerosol ones, that it causes huge relative errors in aerosol contributions.

### 1.3.2.4 The choice of the reference values

It is generally accepted that the determination of the reference value is the key point of the Lidar data inversion. In fact, the solution (Eq 1.59) is the exact when the guess Lidar ratio and the boundary value are known. In Chapter 2, we will see that the influence of a wrong Lidar ratio is less critical than a wrong boundary value. The difficulty in guessing the reference value stems from the lack of precise a priori information and of the noisy character of the signal.

Speaking for ground based vertically pointing Lidar profiles, we expect that the aerosol content far above PBL tends to vanish. This is by no way true in detail, since tropospheric and even stratospheric aerosols can stay at any level. As example, in the troposphere, even in visually clear sky condition, sub-visible clouds extending over some hundreds of meters are very common.

The usual hypothesis used for guessing the reference values is the homogeneity of the total aerosol content over some range. With this assumption, the gradient term in the right side of (Eq 1.51) is small compared with the second term, and the mean value of the total extinction over such range is then

$$\alpha_{\text{hom}} = -\frac{1}{2}\left\langle \frac{dS}{dr} \right\rangle \qquad \text{(Eq 1.60)}$$

where the average indicates the mean value over the range of interest. This is the well-known slope method. The difficulty in applying (Eq 1.55) is to find the best linear fit of the *S*-function out of the noisy signal. In [*Kunz et al.*, 1993], [*Rocadenbosch et al.*, 1998] and [*Rocadenbosch et al.*, 2000], the slope method is applied on homogeneous atmosphere and the influence of the noises are presented. For such "ideal atmosphere", [*Kunz et al.*, 1993] found that the extinction values of about $1\text{x}10^{-3}$ $\text{m}^{-1}$ can be retrieved with less than 10% accuracy for a maximum signal-to-noise ratio of some thousands (typically values estimated above the full overlap height). Very large uncertainties occur for extinction values of order $1\text{x}10^{-4}$ $\text{m}^{-1}$ in the same conditions. In [*Rocadenbosch et al.*, 2000], a comparison of the above linear fit and an exponential fit procedure is presented: the latter is based on following local approximation

$$RCS(r) \cong C'(r)\beta_{\text{hom}} \exp(-\alpha_{\text{hom}} r) \qquad \text{(Eq 1.61)}$$

for some (range dependant) constant $C'$ on some range of interest. A method for evaluating the optimal fitting interval for the linear fit method is also presented. It is concluded that the two methods have nearly the same precisions at the limit of low signal-to-noise ratio.

For the inversion of real signal made in analog acquisition mode, the experience shows that applicability of these methods is reduced to a few exceptional cases: the unpredictable atmospheric inhomogeneities, the presence of other noises and the subsequent uncertainty in the offset evaluation (Eq 1.53) make the above assumptions of little usefulness in most practical cases. That's why a "manual approach" has been preferred in which the reference range, the reference value and the signal offset are adjustable in order that following criteria are fulfilled:

1. the RCS signal conforms to the molecular in regions where no significant aerosol load are expected
2. the offset of the signal keeps within an acceptable domain
3. in case of many wavelengths measurement, the relative behavior of the different solutions for the aerosol backscattering coefficient falls into the expected domain values in regions of high signal-to-noise ratios

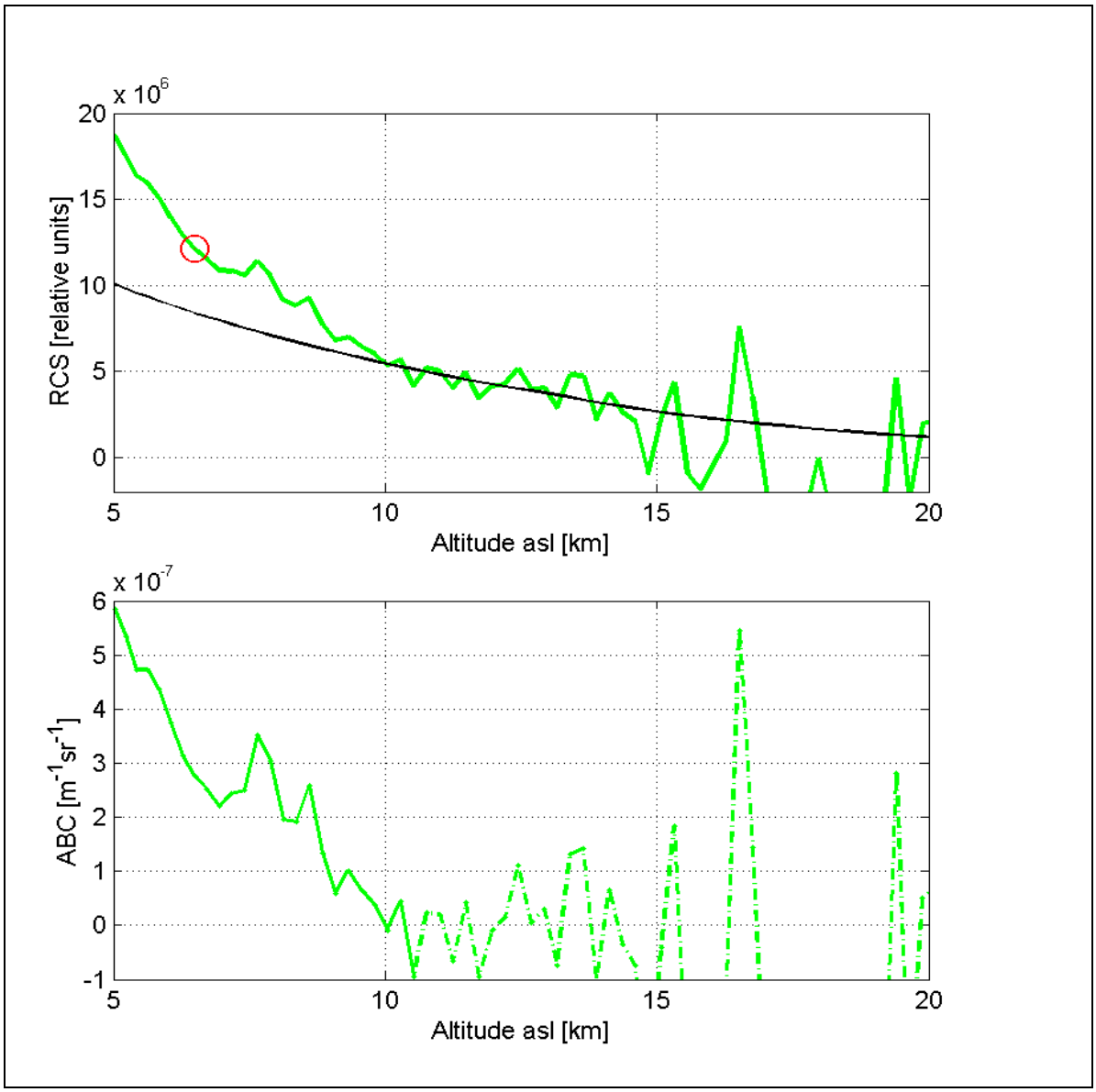


**Figure 1.15.** *Inversion case for the measurement performed in Observatory of Neuchâtel, on 13/08/2001 18h00-19h00 (58000 shots) at 532 nm, truncated below 5000 m. The top panel shows the range-corrected signals (RCS) with the corresponding molecular fit (black line). The circle indicates the reference range (altitude). The bottom panel shows the retrieved aerosol backscattering coefficient (ABC): the solid part of the curve has been retained for contributing to the statistical database (EARLINET). The assumed Lidar ratio was 60 sr.*

Although not systematic, such approach seems to be more appropriate for real applications. Figure 1.15 shows an inversion example for measurements performed in Observatory of Neuchâtel (ON) on the evening of August 13, 2001. The signal is truncated below 5000 m. The filtered signal range resolution was increasing from 30 m at 600 m to 240 m at 8000 m, and constant above. The domain between approximately 10-14 km conforms well to the molecular model signal, which is based on the mid-latitude summer model. Here the reference point (red circle) has been chosen far below this range for practical convenience.

### 1.3.3 Overview of the Backscatter Lidar methods for PBL top determination

As pointed out in section 1.2.2, the PBL top or mean PBL height is located in the entrainment zone, which acts globally as a lid above the mixed layer. Also, in determining the stratification of the PBL by Backscatter Lidar, the aerosols are a tracer showing the altitudes of turbulent mixing, accumulations and mixing with the free troposphere. The entrainment zone is a very turbulent layer, in which aerosol rich positively buoyant (and likely humid) air parcels are mixed with aerosol poor negatively buoyant (and likely dry) air parcels entrained downward (see Fig. 1.5). Numerous definitions of the mixed layer height (MLH) are found in the literature ([*Stull*, 1988], [*Garratt*, 1992], [*Seibert et al*., 1998]). A widely accepted definition is given in [*Seibert et al.*, 2000]: the mixed layer height is that height of the layer adjacent to the ground over which pollutants or any constituents emitted within this layer or entrained into it become vertically dispersed by convection or mechanical turbulence within a timescale of about one hour. The Lidar allows the measurement of aerosol or trace gas concentrations profiles and may therefore be considered to provide direct measurement of the MLH. However, interpreting data from aerosol Lidar is often not straightforward, because the detected aerosol layers are not always the result of ongoing vertical mixing, but may originate from advective transport or past accumulation processes (see [*Russell et al.*, 1974], [*Coulter*, 1979], [*Baxter*, 1991]).

A definition of MLH has been proposed in several studies (see [*Flamant et al.*, 1997], [*Menut et al.*, 1999], [EARLINET*]): it is considered as the lowest layer where turbulent mixing process establishes an exchange between the surface layer and the atmosphere above. When aerosol is used as a tracer, as is the case with a Backscatter Lidar, the top of this layer can be identified by the lowest minimum of the gradient of the range-corrected signal. This is the essence of the gradient method, when the MLH is understood as "aerosol mixed layer height". It should be added that the existence of mixing process can only be verified when time series of profiles are measured. Moreover, it is requested that the absolute value of the backscatter coefficient in the mixed layer is larger than a wavelength dependent minimum value ($3x10^{-7}$ $m^{-1}sr^{-1}$ at 355 nm, $2x10^{-7}$ $m^{-1}sr^{-1}$ at 532 nm, $1x10^{-7}$ $m^{-1}sr^{-1}$ at 1064 nm): such additional constraint allows clarifying ambiguous cases that are common above complex terrain.

Generally, it is accepted that the instantaneous interface between the mixed layer and the free troposphere (i.e. the entrainment zone) does not exceed some tens of meters (see [*Readings et al*., 1973]). More representative is the average horizontal value of the interface depth: this is typically some hundreds of meters. Therefore, Lidar measurement provides in principle a way to determine the base and the top of the entrainment zone, in looking the temporal fluctuations of the successive minima of the RCS gradient. This requires a sufficiently powerful signal in order to work in relatively short times; else the height determined by a Lidar profile represents already the average value of these fluctuations during the accumulation period (in strong advective conditions, the averaging is essentially a spatial one).

Following [*Deardorff et al*., 1980], an adequate method for determining the entrainment zone thickness is to perform the cumulative distribution of the occurrence of the instantaneous unstable boundary layer height (IUBLH) versus height: the median of this distribution may be considered as the mean PBL height (PBL top), and the base and top of the entrainment zone are located respectively at 4% and 98% of that distribution.

Let's have a closer look at the gradient method as applied in [*Flamant et al.*, 1997]. Figure 1.16 exemplifies the gradient method used for the determination of the IUBLH. The top and bottom panels present respectively the Lidar (range-corrected) signal (left panels) and its derivative (right panels) for an updraft respectively a downdraft. The selection of the IUBLH proceeds as follow: a first selection occurs in applying a threshold value in the derivative domain, whose role is to exclude noise fluctuations. The threshold (see thick vertical lines) has been set at three times the standard deviation of the signal gradient evaluated in the free troposphere, below the corresponding mean value (see thin vertical lines). The height corresponding to one time the standard deviation below this mean value is considered as the top of the entrainment zone. Then, a second selection is applied on all points below the threshold: only altitude domains with a minimum vertical extent are considered (in the present case, this minimum extent is 75 m). Within the remaining domain(s), the selected height(s) is (are) the one of the local gradient minimum. When more than one minimum is present, the one with lowest altitude is considered as the IUBLH. Further, the authors report that they add a maximum IUBLH height difference between two consecutive profiles, which has been estimated on the basis of the analysis of a model of an idealized disturbance (thermal). For the case of airborne Lidar time series measurement, they estimated this maximum height difference to be about 200 m for 40 m horizontal displacement.

* see http://Lidarb.dkrz.de/earlinet/mirrors/Lidarb.dkrz.de/earlinet_intern/rules/pblheights.htm

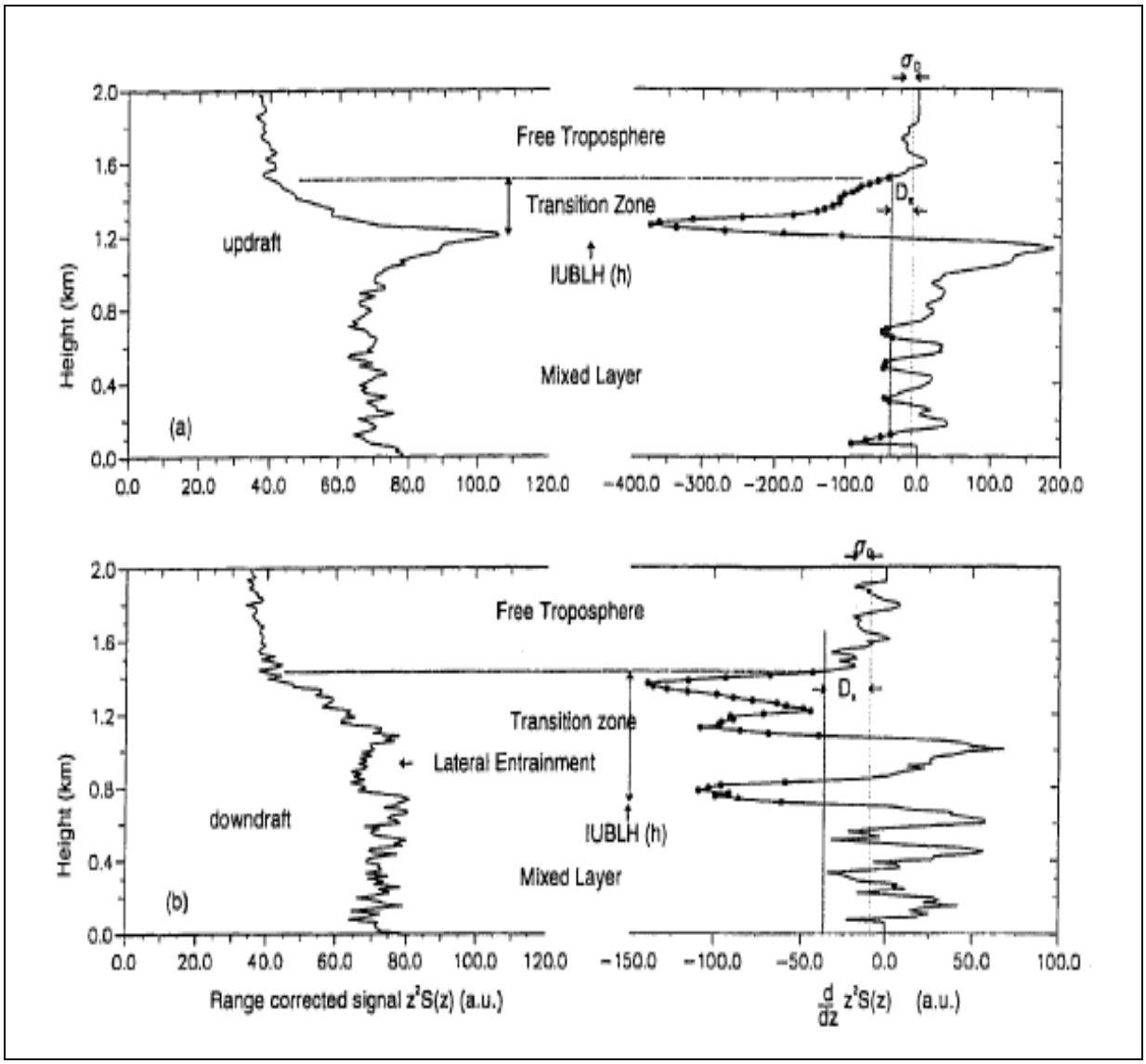


**Figure 1.16.** *Determination of the instantaneous unstable boundary layer height by the gradient method, from* [*Flamant et al.,* 1997]. *Here (unlike in the text) S(z) is used for the Lidar signal versus altitude z. Left panels show the range-corrected signal in arbitrary units, right panels show their derivative (vertical gradient). Top panels: updraft case. Bottom panels: downdraft case.*

In [*Hooper and* Eloranta, 1986] and [*Menut et al.*, 1999], another method is proposed. Since turbulent activity in the entrainment zone viewed at a given location (as the Lidar probes) gives rise to consecutive updrafts and downdrafts, the range-corrected Lidar signal presents in this area large temporal fluctuations. On one side, fluctuations in the mixed layer are comparatively small, since the mixing processes tend to a nearly homogeneous and relatively stable aerosol distribution. On the other side, in the free troposphere, the very poor aerosol content guarantees a high signal stability. Therefore, it is expected that the temporal fluctuation of the range-corrected signal at given altitude presents a maximum at the mean PBL height. This method of detecting the PBL top is known as "centroid" or "variance" method.

In [*Steyn et al.*,1998], a new method is presented. The measured signal (RCS) is fitted by a four parameters model profile, in the form of a superposition of the signals in the mixed-layer and in the layer above the entrainment zone. The entrainment zone is then identified as the one in which the mixing ratio values of the boundary layer and the free atmosphere layer immediately above the transition zone fall in the range 5-95%.

### 1.3.4 Implementation of the gradient and centroid methods for a multi-layers structure in the PBL and low troposphere

Above complex terrain, the PBL structure is rarely looking like the model one presented in Fig. 1.4, due to the contribution of mixed and uplifting from several surfaces (slopes, valley floor,…) as well as to advection processes. The vertical structure of the aerosol in the PBL and low troposphere may consist of more than one nearly well-mixed layers with decreasing aerosol concentration with height. The transition layers between these nearly well-mixed layers are frequently characterized by temperature inversions and are looking like the entrainment zone at the PBL top, as discussed previously.

Here, we present a routine that allows to reconstruct such complex structure as described above, without caring about the PBL top determination. That's why we also include low troposphere in this task. Further, we restrict our talk to the case of Lidar time-series measurements from a ground based Lidar operating in zenith position.

Since a purely molecular return gives rise to a range-corrected signal decreasing of a factor 2 from 0 m to 5000 m due to the molecular density decrease, and since we are looking only for the aerosol structure, it is convenient to normalize the range-corrected signal with the molecular return. This is done in defining a "corrected signal" as follow

$$CS(r) = \frac{RCS(r)}{\beta^{mol}(r)T^{mol}(r)} \qquad \text{(Eq 1.62)}$$

where $T^{mol}$ is the molecular transmission. Since we are looking simultaneously at different levels, it is of interest to define a variable as homogeneous as possible before taking its gradient. A simple way to get this is to take the logarithm of *CS*. Thus, we define the "corrected signal gradient" as

$$CSG(r) = \frac{d(\log(CS))}{dr} \cong \frac{1}{scr}\frac{d(scr)}{dr} - 2\alpha^{aer} \qquad \text{(Eq 1.63)}$$

where *scr* is the total scattering ratio defined in (Eq 1.14). The *CSG* differs by the gradient of *RCS* by the factor $scr \cdot T^{aer}$, which is typically decreasing by a factor 3 along the profile at 532 nm. Additionally, the logarithm cancel out any remaining variation of the signal due to temporal fluctuation of the laser power or of any other device transmission factor. Within the error in guessing the molecular contribution, the *CSG* has a simple constant mean value in the aerosol free regions, namely zero. These different characteristics make the *CSG* a better variable than the *RCS* gradient for our purpose.

Formally, the gradient and centroid methods are similar in the sense that they follow the local extrema of some function: the gradient method looks for the minima of the *CSG*, the centroid method looks for maxima of the temporal fluctuation of the *CS*). Moreover, the height of these extrema must satisfy a certain temporal continuity, as pointed out in the previous subsection ([*Flamant et al.*, 1997]). Therefore, we restrict the discussion to the gradient method only.

The small fluctuations of the *CSG* are discarded in applying a unique negative threshold value to all *CSG* profiles. Then necessary conditions for local minimum are added (sign change of the average CSG derivative with altitude). On the two dimensional domain of interest (altitude x time), these conditions give rise to a set of subsets, where each subset is a connected domain (i.e. all its grid points have at least one neighbor in the same domain). The subsets are further sorted by decreasing size. In the first subset, the routine looks for the strongest minimum. This serves as starting point of a filament. The routine runs in the forward and backward temporal direction from this point. At each step, it looks for the strongest minimum in the part of the profile located at a given maximum height difference from the last selected point (continuity condition). Further, a band around the constructed filament is eliminated for the all additional filaments, avoiding occurrence of multiple filaments at short height difference. The above process is repeated till a chosen number of filaments is achieved.

In the case of the gradient method, this process has been tested in comparing the retrieved structure with the one obtained using a fully (manual) visual determination profile by profile. We concluded that the routine detects properly the main features. In the Chapters 3 and 4, retrieved multi-layers structures above complex terrain are presented.

# Chapter 2

# Numerical Simulations of Atmospheric Backscatter Lidar

## 2.1 Introduction

The numerical simulations exercises of Lidar measurements consist of the following steps:

1. Create numerically a Lidar signal from a set of atmospheric parameters and a set of Lidar performance parameters. The atmospheric parameters are the vertical profiles of the molecular and aerosol components contributing to the backscatter and extinction processes (scattering and absorption). The Lidar performance parameters include the performances of the Lidar subsystems as: laser, telescope, detector, etc. Here also we include the parameters of the measurements as altitude (range) resolution and integration time, noise components.
2. Process the numerically obtained Lidar signal with the processing algorithms and programs used to process the real signal, to obtain the atmospheric parameters used in the numerical simulated Lidar signal.
3. Compare the values of the atmospheric parameters used in the numerical creation of the Lidar signal with the values obtained as a result of the processing of the numerically created signal.

The numerical simulations of Lidar signal allow to investigate how the Lidar signal and the processing methods are affected by atmospheric parameters (the aerosol distribution, presence of background light), by device related parameters (laser power, optical efficiencies, quantum efficiency, telescope area, …) and by the processing parameters (signal filtering, molecular model, guessed reference value).

In section 2.2, we investigate first elastic Backscatter Lidar performances: in the subsection 2.2.1, we report first simulations made in ON, allowing to test the sensitivity of the inversion algorithm of Fernald and the gradient method on different parameters. In the subsection 2.2.2, we report simulation results in joint exercises made in the frame of EARLINET activities. The cooperative Lidar measurements of aerosol profiles of about twenty Lidar groups participating in EARLINET and operating at as many different stations in Europe require such quality insurance tests. For us, this is an additional opportunity to improve and test our processing algorithm.

In section 2.3, we report cases of simulation of Raman Lidar backscatter, also performed in the frame of EARLINET activities. Although Raman measurements are not yet performed with the present surface station status in Neuchâtel, ON participated to this cooperative algorithm test activity. The section begins with a short theoretical background of the Raman Lidar backscatter extinction retrieval.

In section 2.4, we report simulations on Raman differential absorption Lidar (Raman-DIAL) for ozone and water-vapor measurements. This work was performed as a joint study with the Laboratory for Air Pollution at the Swiss Federal Institute of Technology of Lausanne (LPAS / EPFL). In this collaboration, ON was involved only in the part devoted to numerical simulations of a Raman-DIAL Lidar for water-vapor and ozone measurements in

the PBL. These simulations helped to understand better the errors and the sensitivity of the equipment, realized in EPFL. The fruit of this collaboration is a joint paper, reported as Annex 1 of the thesis.

The conclusions of the sections 2.2, 2.3 and 2.4 are grouped at the end of the Chapter (section 2.5).

# 2.2 Elastic Backscatter Lidar simulations

## 2.2.1 Examples for "internal" simulations

### 2.2.1.1 Objectives

The aim of the simulation exercises presented in this sub-section is to show the influence of the following factors on the results from the inversion procedure:

1. the influence of the algorithm, when the Lidar ratio and the reference values are known
2. the influence of the choice of the molecular reference (profile of molecular backscatter coefficient)
3. the influence of the choice of reference value for the aerosol backscatter coefficient
4. the influence of the Lidar ratio uncertainty
5. the influence of the noise and noisy signal filtering

Our aim is to see what is the influence of the above factor on the error for the aerosol backscatter coefficient (ABC*). This will be shown in evaluating the difference

$$\Delta(ABC) = ABC_{RETRIEVED} - ABC_{MODEL} \qquad \text{(Eq 2.1)}$$

and the relative error

$$\delta(ABC) = \frac{\Delta(ABC)}{ABC_{MODEL}} \qquad \text{(Eq 2.2)}$$

Since this last value spans over orders of magnitude along the Lidar profile, it's found to be more convenient to show its absolute value on a logarithmic scale. Thus, after each figure presenting a simulation exercise, an additional figure will present the profiles of $\Delta(ABC)$ on a linear scale and of $|\delta(ABC)|$ on a logarithmic scale.

### 2.2.1.2 General conditions

***The ABC model***

For all reported simulations, a single model of aerosol backscatter profile has been conveniently chosen to represent a measurement above complex terrain: it consists of three successive nearly well-mixed aerosol layer, and aerosol free conditions above approximately 5500 m asl. In view of the measurement reported in Chapters 3 to 5, the Lidar station altitude has been chosen at 490 m and the Lidar is operating in zenith position.

***The inclusion of signal fluctuations (shot noise)***

In photon-counting acquisition mode, the fluctuations due to quantum noise from the backscattered signal and from the background, and due to the dark counts, are simulated in the following way: the profile of counted photons number is evaluated with the equations presented in Chapter 1. As seen in (Eq 1.32), the total number of photons obeys the Poisson statistics. With the chosen atmospheric and device parameters, the profiles of the signal backscatter photons number $N_s$ (see (Eq 1.17)) and of the total photons number

* For convenience of notation, the aerosol backscatter coefficient is symbolized by *ABC*. It is equal to $\beta^{aer}$ (see Chapter 1, Eq. 1.13).

$N_t = N_s + N_b + N_d$ contributing to fluctuations, are first evaluated. $N_t$ is then considered as the average value of a Poisson distribution, in which a random process allows to select a new number $\widetilde{N}_t$. The noisy backscattered signal is evaluated as

$$\widetilde{N}_s = N_s + (\widetilde{N}_t - N_t) \quad \text{(Eq 2.3)}$$

This formula is also valid for an arbitrary shots number, as long as the above numbers are the sums over all shots.

In analog acquisition mode, the inclusion of the noise in the measured current is done as follow: from (Eq 1.17) and (Eq 1.19), the backscattered signal current at the PMT output and the number of photoelectrons from backscattered signal are linked through

$$i_s = K_s N_s \quad \text{(Eq 2.4)}$$

where $K_s = \frac{Ge}{\tau}$.

In the expression for the signal-to-noise ratio (SNR) (Eq 1.33), we group the thermal noise contribution with the other contributions in defining a "thermal current" as

$$i_{th} = \frac{4kT_{Rch}B}{R_{ch}} \frac{1}{2eBG\mu} \quad \text{(Eq 2.5)}$$

Thus, (Eq 1.33) can be put in a form similar to the photon-counting expression

$$SNR = \frac{N_s}{\sqrt{N_{eq}}} \quad \text{(Eq 2.6)}$$

where $N_{eq} = 2eBG\mu \frac{(i_s + i_b + i_d + i_{th})}{K_s^2}$. As above, the noise is then introduced in replacing the $N_{eq}$ by $\widetilde{N}_{eq}$, following the Poisson statistic. The noisy backscattered current is then

$$\widetilde{i}_s = \frac{K_s^2}{2eBG\mu} \widetilde{N}_{eq} - (i_b + i_d + i_{th}) \quad \text{(Eq 2.7)}$$

This formula is valid for one shot. Over $L$ shots, $\widetilde{N}_{eq}$ must be replaced by $\frac{\widetilde{M}_{eq}}{L}$, where $M_{eq} = L \cdot N_{eq}$.

The expressions for the SNR (Eq 1.17) and (Eq 2.6) are strictly valid when the number of photons are much bigger than one (approximation of the binomial law by the Poisson statistic).

Anyhow, we will extend these formulae also below one count. When very low signal level is reached (typically, a SNR below 2), fluctuations due to the electronic noise of the acquisition chain (digitizer), generally much bigger than fluctuations corresponding to some counts, not discussed here, can anyhow no more be ignored.

### *The signal filtering*

As shown by (Eq 1.10), the backscattered signal decreases with the square of the height. Following (Eqs 1.32-1.33), the SNR is also decreasing with increasing height. In order to increase the SNR, the noisy signal will be filtered. Here, the applied filter has been chosen to be a binning, and does operate on the signal as follow: the signal values are averaged over some number of adjacent points, such that each point of the unfiltered signal is used exactly once in the filtered signal. A way to compensate the SNR decrease with increasing height is to increase the number of points (or binning number) to be averaged in the binning process (for a binning number $nbin$, the gain in SNR is $\sqrt{nbin}$). Correspondingly, this leads to a degradation of the resolution with increasing height. We refer to this condition as an optimal from the SNR point of view.

In situations for signal processing and actual signal processing, the filtering also shall take into account other requirements, like the necessity for the temporal and altitude resolution, so there may be a discrepancy from the above optimal SNR condition. As example, in many real cases, the domain for fitting to the molecular atmosphere is limited by the presence of high clouds or by the presence of other noises affecting strongly the signal quality in its upper part. In such cases, it is necessary to keep also a higher resolution, at the expense of SNR. Thus, in all further presented simulations where noise is considered, we will first apply on the noisy signal a binning with increasing binning number with height. This filtered signal will be the input for the inversion procedure and for the evaluation of the corrected signal gradient.

### *The device parameters*

All here reported simulations are done with 532 nm (second harmonic of a Nd:Yag laser). We first present a series of simulations of measurement performed in photon-counting acquisition mode. The device parameters used in these exercises are listed in Table 2.1. They are quite typical of a Lidar performing aerosol measurements in the PBL and low troposphere. The geometrical parameters are such that the overlap between laser beam and telescope field of view is full above 300 m agl, i.e. approximately 800 m asl. In all presented simulations, the part of the profiles below that range will not be shown.

**Table 2.1.** *Device specifications for the simulations in photon-counting acquisition mode.*

| | |
|---|---|
| Laser pulse energy | 20 mJ |
| Pulse repetition rate | 20 Hz |
| Telescope diameter | 15 cm |
| Transmitter efficiency | 65% |
| Laser beam full divergence | 0.8 mrad |
| Laser beam diameter | 11 mm |
| Beam to telescope axes distance | 16 cm |
| Beam to telescope axes inclination | 0 mrad |
| Receiver efficiency | 15% |
| Quantum efficiency | 11% |

Further, some simulation exercises with analog acquisition mode will be presented. The device specifications will be the one listed in Table 2.2. They describe a Lidar with the same geometrical parameters as the one in Table 2.1 (full overlap above approximately 300 m agl), but with a higher laser power.

**Table 2.2.** *Device specifications for the simulations in analog acquisition mode.*

| | |
|---|---|
| Laser pulse energy | 120 mJ |
| Pulse repetition rate | 20 Hz |
| Telescope diameter | 15 cm |
| Transmitter efficiency | 65% |
| Laser beam full divergence | 0.8 mrad |
| Laser beam diameter | 11 mm |
| Beam to telescope axes distance | 16 cm |
| Beam to telescope axes inclination | 0 mrad |
| Receiver efficiency | 15% |
| Quantum efficiency | 11% |
| Receiver full opening angle | 1.4 mrad |
| PMT gain | 100000 |
| PMT excess noise factor | 2 |
| Equivalent resistance output circuit | 50 Ω |

#### 2.2.1.3 Effect of the algorithm (known ABC reference value and Lidar ratio)

Let's consider first a simulation exercise in which we know the exact ABC reference value at some reference height and the exact Lidar ratio. The noise is restricted to the quantum noise, from the backscattered signal only. Here, the Lidar ratio was supposed to be constant (50 sr). The filtering is a variable binning with a resolution of 15 m at 200 m agl to 180 m at 6000 m agl and constant above. The reference height was 9000 m agl, and the corresponding reference ABC vanishes (exact value used for the inversion procedure).

Figure 2.1 presents the result of this simulation exercise. The signal, shown here in its range-corrected form (central panel, bottom scale), is the cumulative number of counts for 50000 shots: this corresponds to approximately 45 min of accumulation with the device parameters of Table 2.2.

In this case, the difference between retrieved and model ABC values is seen to be very small on the presented scale, and is therefore presented separately in Fig. 2.2. On that figure, we see that relative errors do not exceed 1% below 3800 m, and 10% below 5000 m.

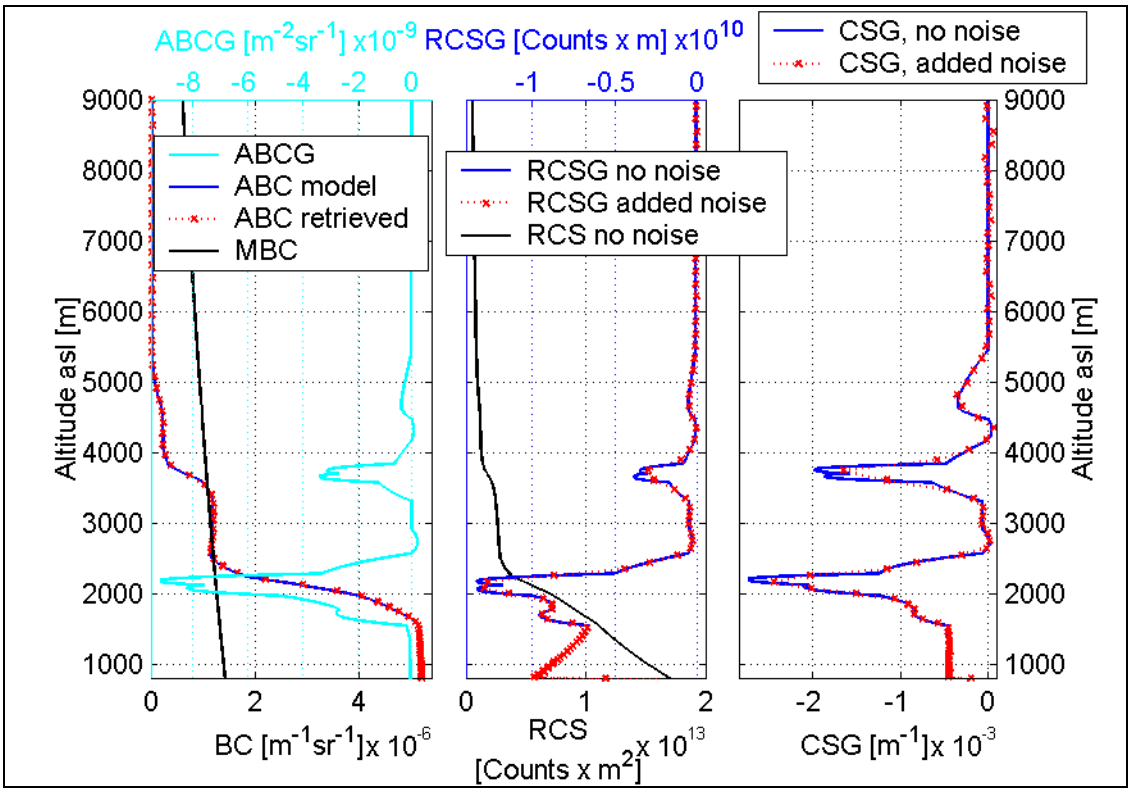


**Figure 2.1.** *Simulation showing the effect of the algorithm in presence of quantum noise from the backscattered signal and the relative behavior of the gradient of the range-corrected signal (RCSG) and the corrected signal gradient (CSG). The signal represents the cumulative counts number during 45 min for a Lidar system with specifications of Table 2.1. The acquisition resolution is 3 m. Left panel, lower scale: backscatter coefficients (BC); molecular backscatter coefficients (MBC) and aerosol backscatter coefficients (ABC): the blue line shows the model profile, while the red line shows the retrieved profile from the noisy (quantum noise) and filtered signal. The difference between these profiles is shown in Fig. 2.2. Left panel, upper scale: aerosol backscatter coefficient gradient (ABCG) from the model profile. Central panel, lower scale: range-corrected signal (RCS), from MBC, model ABC and model of Lidar ratio (constant of 50 sr). Central panel, upper scale: range-corrected signal gradient (RCSG) without noise (blue line) and with quantum noise addition and data filtering (red line). Right panel: corrected signal gradient (CSG) using the exact molecular reference, for the same two cases. Exact values of the Lidar ratio and reference value for the inversion procedure were assumed. The filtering is a variable binning with a resolution of 15 m at 200 m agl to 180 m at 6000 m, and constant above.*

## 2.2.1.4 Gradient of RCS and CSG

In Fig. 2.1, the comparison of the aerosol backscatter gradient (ABCG), the gradient of the range-corrected signal (RCSG) and the correct signal gradient (CSG) shows that the CSG shape is closer to the ABCG one, than the RCSG is. This is particularly marked in the lower part of the PBL, where the molecular density gradient contribution to the total gradient is maximum (see below 1500 m, where the CSG profile is nearly constant as the ABCG is, while the RCSG is well decreasing (a zoom of ABCG, not seen on that scale, shows even a small ABCG increase). Moreover, the CSG asymptotic value is exactly zero, independently of the system (in Fig. 2.5, we will see that the departure from this value due to the use of a suitable guess molecular model instead of the exact molecular reference, is negligible). This CSG property is advantageous when considering time series, where, even in the aerosol free range, the RCS and RCSG values fluctuate due to the variable aerosol transmission and to the laser power fluctuations.

Therefore, the CSG will be preferred in the applications reported in Chapter 3 and 4. Although its value cannot be directly interpreted (see (Eq 1.63)), it is a good indicator for the ABCG (i.e., the locations of CSG extrema correspond to the locations of similar extrema of ABCG).

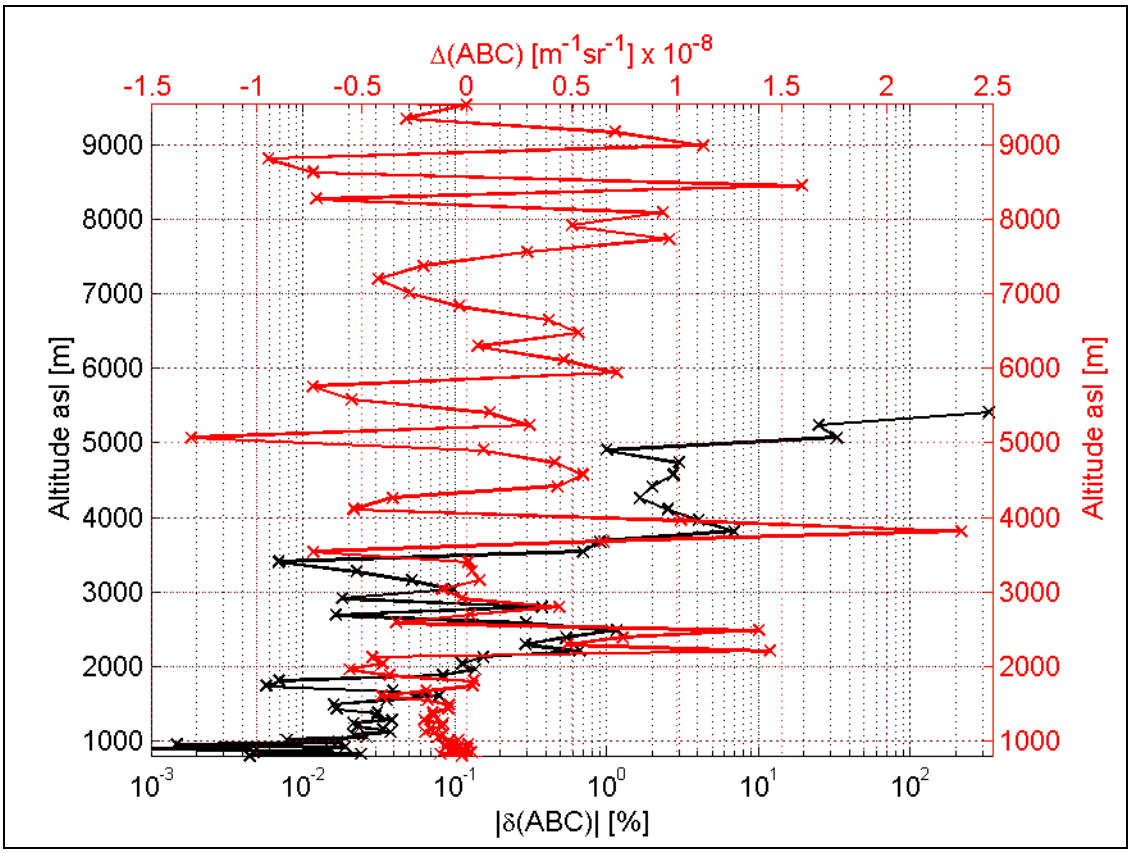


**Figure 2.2.** *Difference between retrieved ABC and model ABC for the simulation exercise presented in Fig. 2.1. The red line (upper scale) shows the difference between the retrieved profile and the model one. The black line (bottom scale) shows the ratio of the absolute values of that difference to the model values, in the range where these last values do not vanish.*

## 2.2.1.5 RCS and ABC similarity

In Fig. 2.1 we see that the range-corrected signal (RCS) profile presents some similarity with the aerosol backscatter coefficient (ABC) profile. This is expected since the RCS is proportional to the total backscattering and that the ABC gradient at the transition zones between the different aerosol well-mixed layers is larger than the gradient of the molecular backscatter coefficient. Figure 2.3 provides a better view of the same profiles. The similarity is the clearest above 2500 m, where the two layers between approximately 2500 m-3500 m and 4000 m-4500 m can be well identified. The case is less obvious for the lowest layer: its top at approximately 1600 m is seen in the RCS as a breaking point (larger slope above than below that point). But there, the signal is strongly influenced by the transmission factor. This is due to the large absolute value of the aerosol extinction coefficient, which is proportional to ABC in this simulation, since the Lidar ratio is constant.

The ABC retrieval depends on the conditions for inversion. In case of very small altitude domain over which simultaneously the signal is high enough and where the nearly aerosol free conditions can be assumed (typically in presence of clouds), the reference value for ABC is very poorly determined. In such case, the above similarity is extremely useful to follow the relative temporal evolution of the ABC, looking at the RCS in a time series. At a given altitude, the matching between ABC and RCS temporal evolutions is good as long as variation of the transmission below the domain of interest can be neglected.

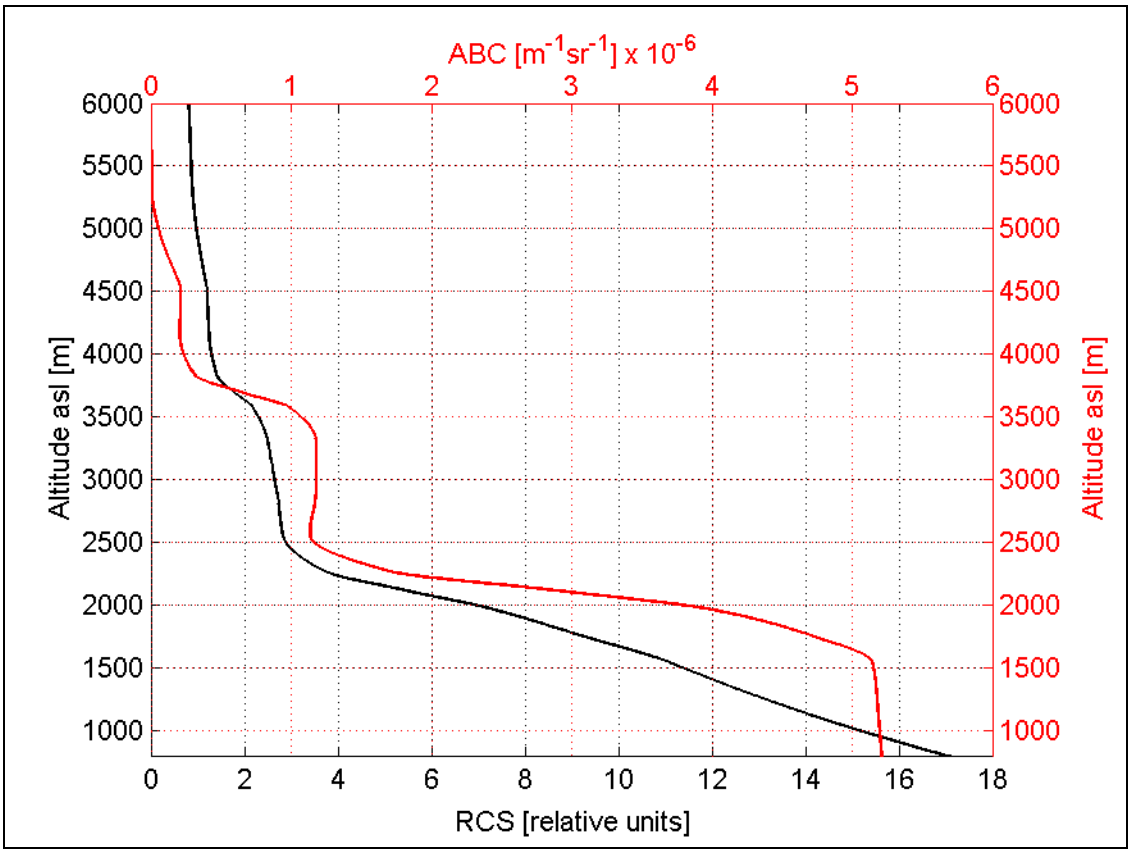


**Figure 2.3.** *Comparison between the range-corrected signal (RCS, lower scale) and the aerosol backscatter coefficient (ABC, upper scale) for the simulation presented in Fig. 2.1.*

### 2.2.1.6 Effect of the choice of an inadequate molecular backscatter coefficient reference

Figure 2.4 presents the profiles of temperature and pressure from the US standard atmospheric model "mid-latitude summer", which is used in most of the presented simulations. As a comparison, real measured profiles from the MeteoSwiss station of Payerne on July 21, 2001 (noon sounding) are reported. Figure 2.5 presents the corresponding relative shifts in absolute temperatures and in the molecular backscatter coefficient (MBC). Here, the correction for both temperature and pressure is assumed to follow an ideal gas law for the density. We see that in that case, these shifts do not exceed some percents in the troposphere. Additionally, we see how absolute temperature and MBC shifts anti-correlate.

Since Lidar measurements are performed at any time, it is of interest to look at the influence of the use of the model instead of real measurements. In absence of radiosonde measurements in the Lidar target area, as will be the case reported in Chapter 3, the use of an atmospheric model is a necessity.

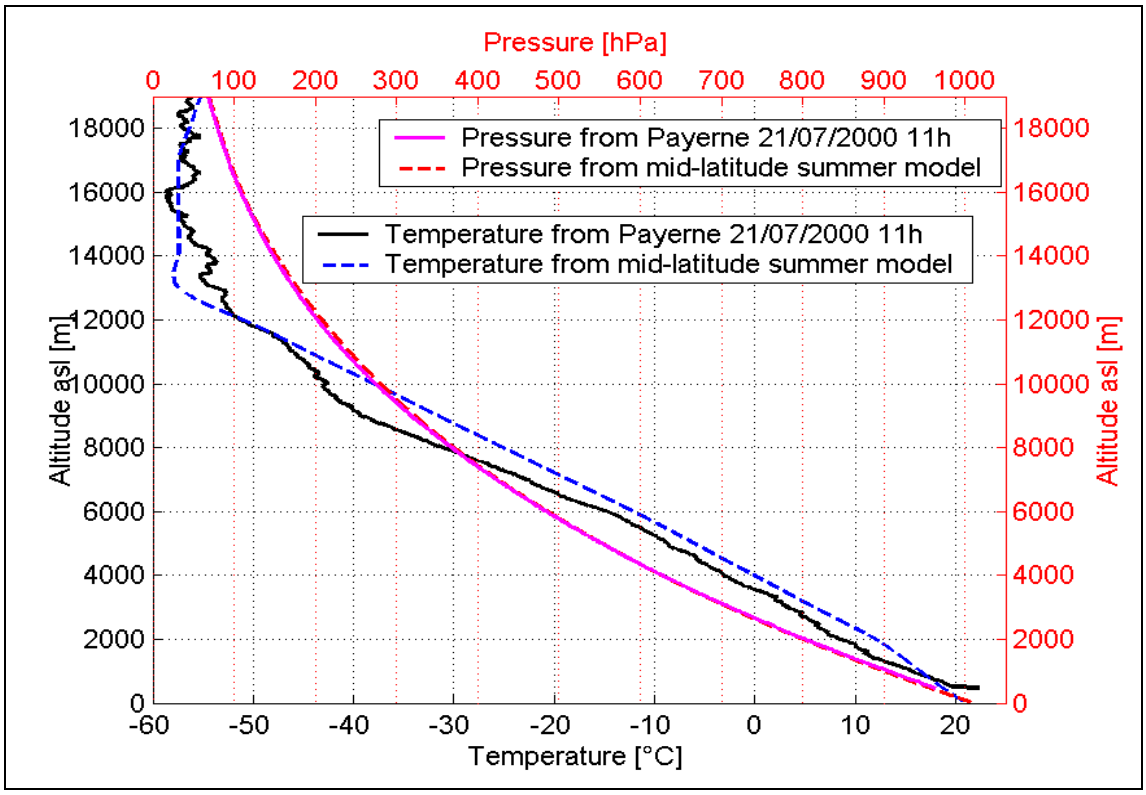


**Figure 2.4.** *Standard mid-latitude summer model of temperature and pressure, together with radiosonde data from Payerne on 21/07/2001 (11h UTC).*

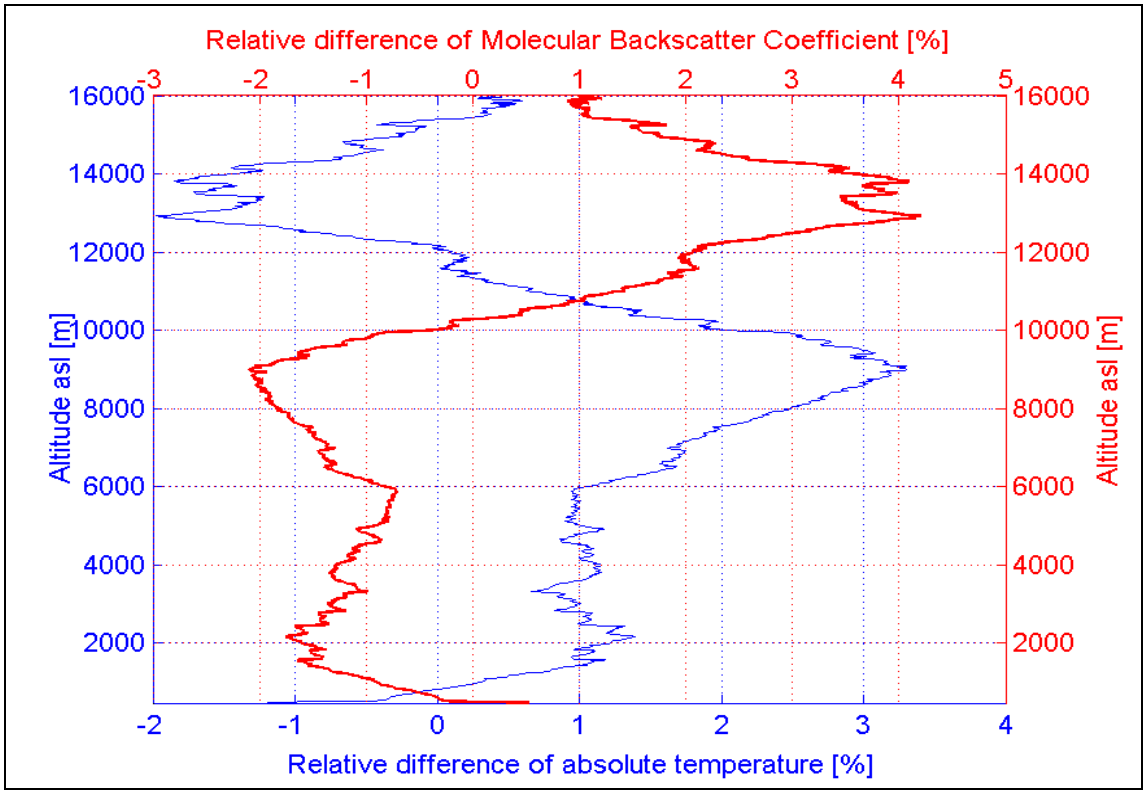


**Figure 2.5.** *Relative differences between the values from the standard mid-latitude model and the radiosonde values, from the temperature and pressure profiles shown in Fig. 2.4: absolute temperatures (blue line, bottom scale) and molecular backscatter coefficient (red line, upper scale). Each relative difference is the ratio of the difference between the mid-latitude model value and the radiosonde value, to the radiosonde value.*

Figure 2.6 presents the results of a simulation in which the molecular atmosphere is based on the real measured profiles from Payerne, reported in Fig. 2.4. In order to isolate just the effect of the molecular reference, exact Lidar ratio, exact reference ABC and no added noise were assumed. For the processing, the guessed (assumed) temperature and pressure profiles are the one from the mid-latitude summer model.

Figure 2.7 shows the corresponding error in ABC: it is seen that the absolute error is increasing downward from the reference point (approximately 12500 m) to 9000 m, and again from 6000 m to 2000 m, where MBC shifts (Fig. 2.5) have the opposite trend (i.e., underestimate of MBC leads to an overestimate of ABC). But Fig. 2.7 also shows that the relative error is nearly a monotone decreasing function with decreasing height. These relative errors do not exceed 3% below 3500 m and 10% below 4500 m. On the right panel of Fig. 2.6 (CSG evaluation), the influence of the guessed MBC profile is seen to be negligible, in the sense that it does practically not affect the position of the CSG minima or maxima. Also, the asymptotic value in the aerosol free region till 12000 m is practically not affected.

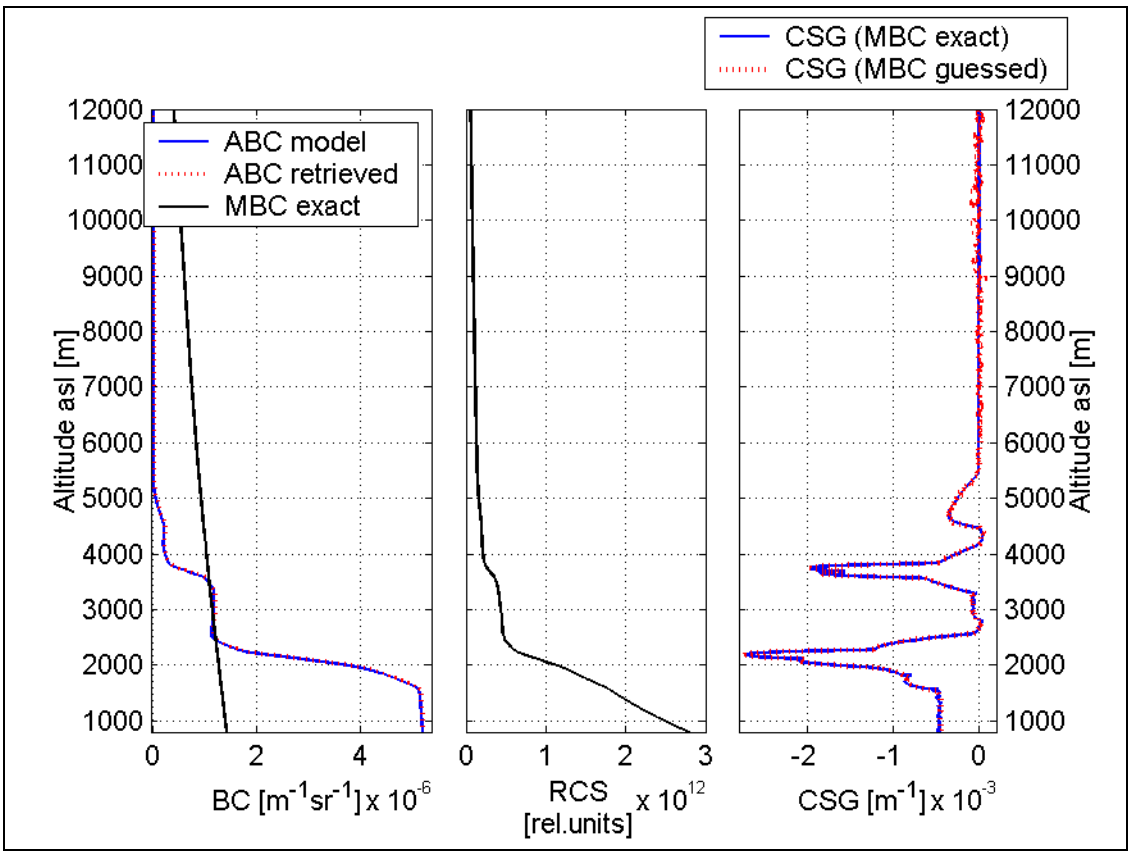


**Figure 2.6.** *Impact of an inadequate choice of molecular reference, using real temperature and pressure profiles (from Payerne radiosonde data reported in Fig. 2.4, on 21/07/2001 11h UTC, here called "exact") for the signal creation and using the here called "guessed" molecular profile (mid-latitude summer model) for processing of the retrieved aerosol backscatter (Fernald inversion algorithm) and for the evaluation of the corrected signal gradient. Left panel: backscatter coefficients (BC); molecular backscatter coefficients (MBC) from radiosonde data and aerosol backscatter coefficients (ABC): model profile (blue); retrieved profile (red) using the guessed MBC values. The difference between these profiles is shown in Fig. 2.7. Central panel: range-corrected signal (RCS), constructed with the exact MBC, the ABC model and the Lidar ratio model (constant of 50 sr). Right panel: corrected signal gradient using the RCS for the two molecular references. No added noise in the signal and exact values of the reference ABC (aerosol free condition at 12000 m agl) and exact Lidar ratio (50 sr) for the inversion procedure, are assumed.*

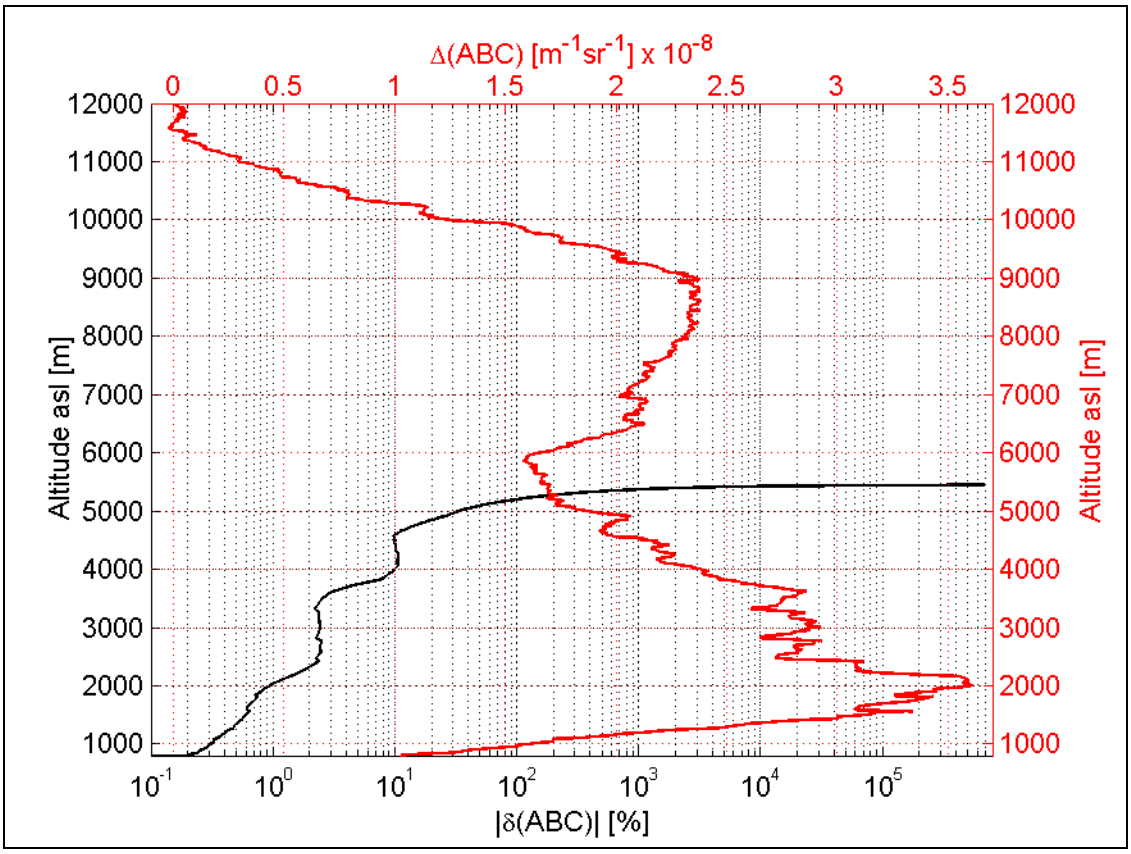


**Figure 2.7.** *Difference between retrieved ABC and model ABC for the simulation exercise presented in Fig. 2.6. The red line (upper scale) shows the difference between the retrieved profile and the model one. The black line (bottom scale) shows the ratio of the absolute values of this difference to the model ABC values, in the range where model ABC does not vanish.*

## 2.2.1.7 Effect of the choice of an inadequate ABC reference

Figure 2.8 presents the impact of an overestimated value of the reference aerosol backscatter coefficient. In order to isolate this effect only, the Lidar ratio and reference molecular were assumed exact and no quantum noise was included. Inclusion of such error (over or under estimate) is the rule in real cases: on one side, residual aerosol may exist even in the upper troposphere; on the other side, the RCS of a noisy signal automatically has an oscillating behavior, especially pronounced in regions of low signal-to-noise ratio. Such uncertainty may also originate from the signal-offset uncertainty, in case of analog measurement.

In this case, such an overestimate is seen to propagate downward from the reference point, in the way shown on Fig. 2.9. The error is increasing in the range domains with (downward) increasing ABC. But, here again, the relative error is nearly monotonically decreasing with decreasing height: these values do not exceed 20% below 4500 m, 5% below 3500 and 1% below 1000 m.

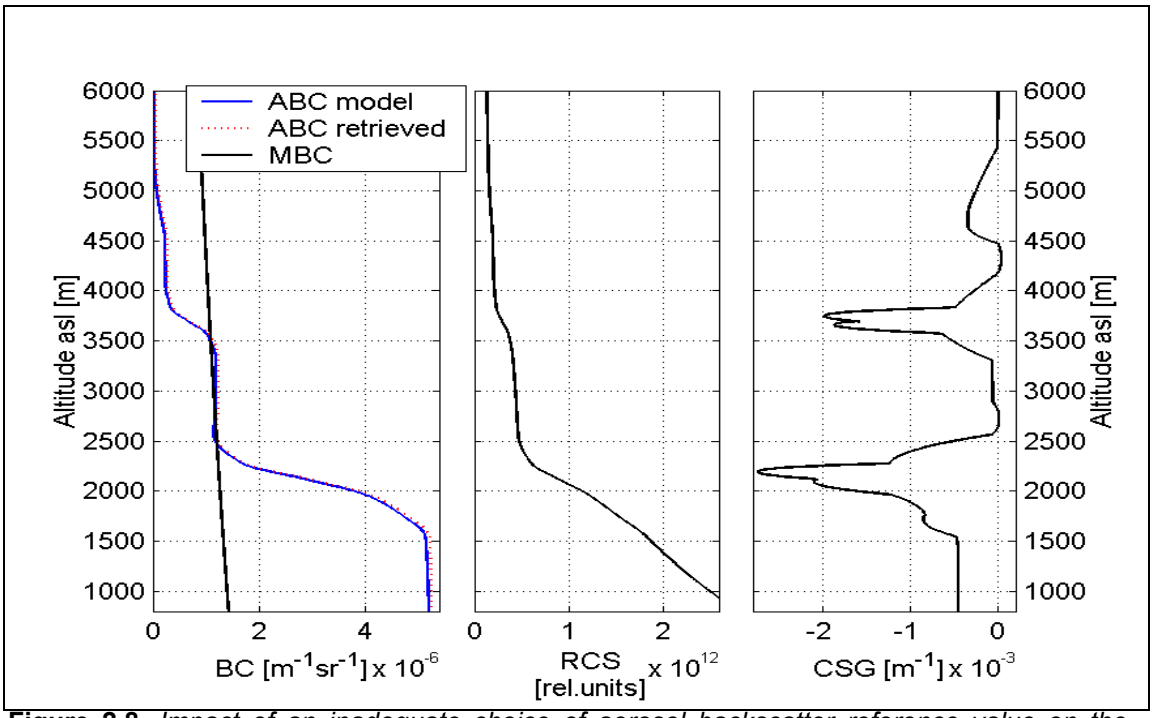


**Figure 2.8.** *Impact of an inadequate choice of aerosol backscatter reference value on the results of the inversion procedure. Midlatitude summer model used as molecular reference for signal creation and signal processing. Since no noise is considered here, the signal is in arbitrary units. The retrieved aerosol is based on a guessed reference aerosol backscatter (scattering ratio = 1.05 at 9000 m agl) instead of the aerosol free value in the model. The difference between these profiles is shown in Fig. 2.9. Left panel: backscatter coefficients (BC); molecular backscatter coefficients (MBC, from the mid-latitude summer model) and aerosol backscatter coefficients (ABC model (blue) and retrieved ABC profile (red), using the guessed ABC reference). Central panel: range-corrected signal (RCS), constructed with the molecular and aerosol models. Right panel: corrected signal gradient (CSG), using the exact molecular reference. No added noise in the signal and exact values of the Lidar ratio (constant of 50 sr) for the inversion procedure, are assumed.*

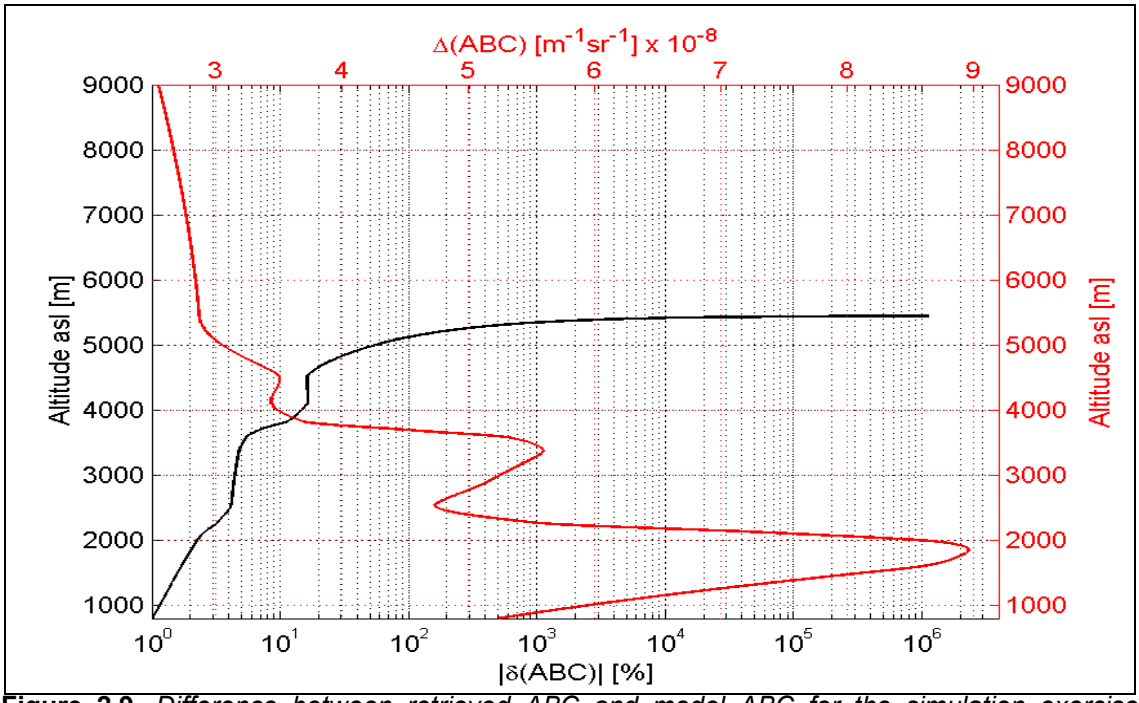


**Figure 2.9.** *Difference between retrieved ABC and model ABC for the simulation exercise presented in Fig. 2.8. The red line (upper scale) shows the difference between the retrieved profile and the model one. The black line (bottom scale) shows the ratio of the absolute values of this difference to the model ABC values, in the range where model ABC does not vanish.*

### 2.2.1.8 Effect of the choice of an inadequate Lidar ratio

Figure 2.10 presents the impact of an inadequate choice of the Lidar ratio value for the inversion procedure. In order to isolate this effect only, all reference parameters were the exact values and no quantum noise was included. Inclusion of such approximation is also the rule in all real cases of elastic Backscatter Lidar measurements: in the PBL and at 532 nm, the Lidar ratio for continental aerosols typically varies from 40 sr (dry conditions) to 80 sr (water-vapor saturated conditions). Thus, we created a model Lidar ratio covering all this range. In this example, we used a guessed value of 60 sr for the inversion procedure.

Looking at the ABC difference in Fig. 2.11, it's seen that the Lidar ratio underestimate between 3500 m and 4000 m gives rise to an ABC overestimate. This relation is obviously not local, as it is seen to propagate further down (e.g. between 2800 m and 3400 m). Below 2500 m, the conjunction of strong Lidar ratio underestimate and high ABC values leads to a strong ABC overestimate below 1700 m. In the region of lower aerosol backscatter values (from 2500 m to 5000 m), the impact of the inadequate Lidar ratio appears to be also weaker. Let's notice that to an overestimates (respectively an underestimate) of ABC corresponds an underestimate (respectively an overestimate) in the aerosol extinction coefficient. This leads to similar errors in aerosol optical depth and aerosol transmission factor evaluations.

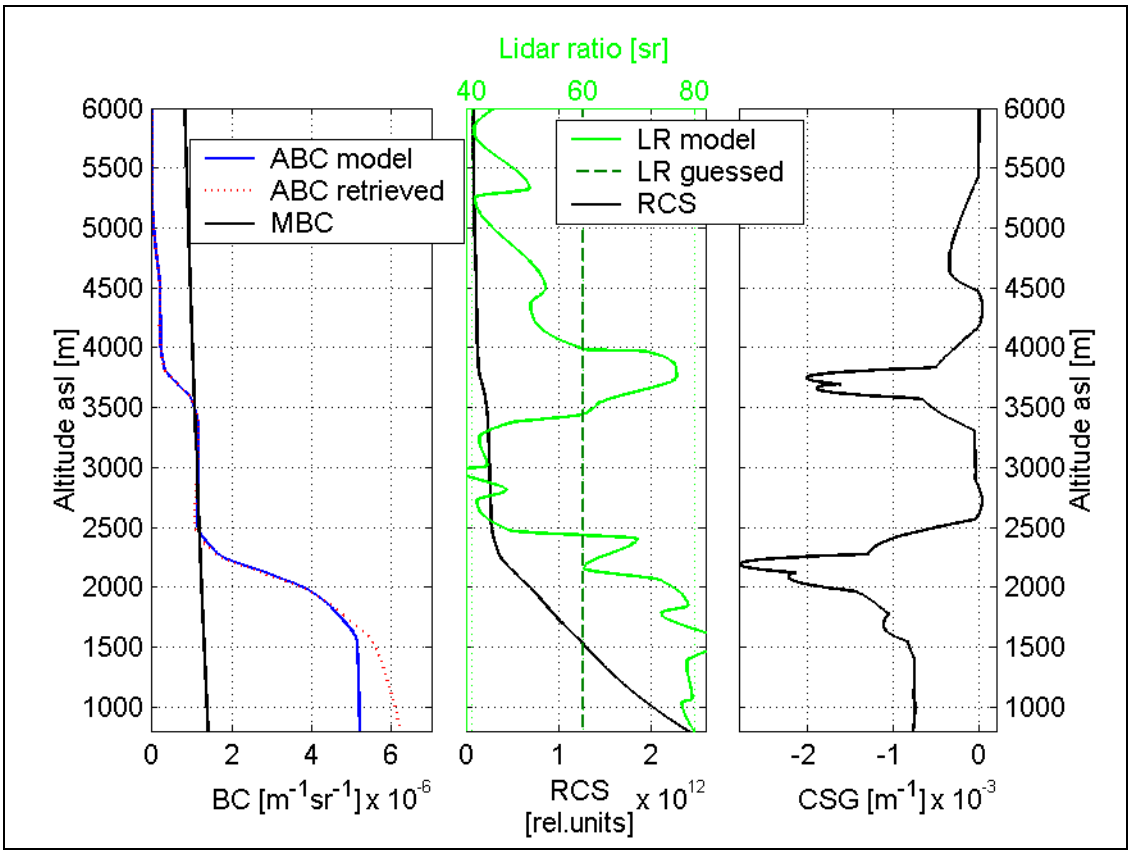


**Figure 2.10.** *Impact of an inadequate Lidar ratio value on the results of the inversion procedure. Midlatitude summer model used as molecular reference for signal creation and processing. No noise is included (the signal is in arbitrary units). The retrieved aerosol is based on a guessed constant Lidar ratio of 60 sr instead of the model values (variable in the range 40 to 80 sr). Left panel: backscatter coefficients (BC); molecular backscatter coefficients (MBC, from the mid-latitude summer model) and aerosol backscatter coefficients (ABC model (blue); retrieved ABC profile (red), using the guessed Lidar ratio). The difference between these profiles is shown in Fig. 2.11. Central panel: range-corrected signal (RCS, bottom scale), constructed with the molecular and aerosol models; Lidar ratio profiles (green lines, top scale). Right panel: corrected signal gradient (CSG) using the exact molecular reference. No added noise in the signal and exact value of reference backscatter for the inversion procedure, are assumed.*

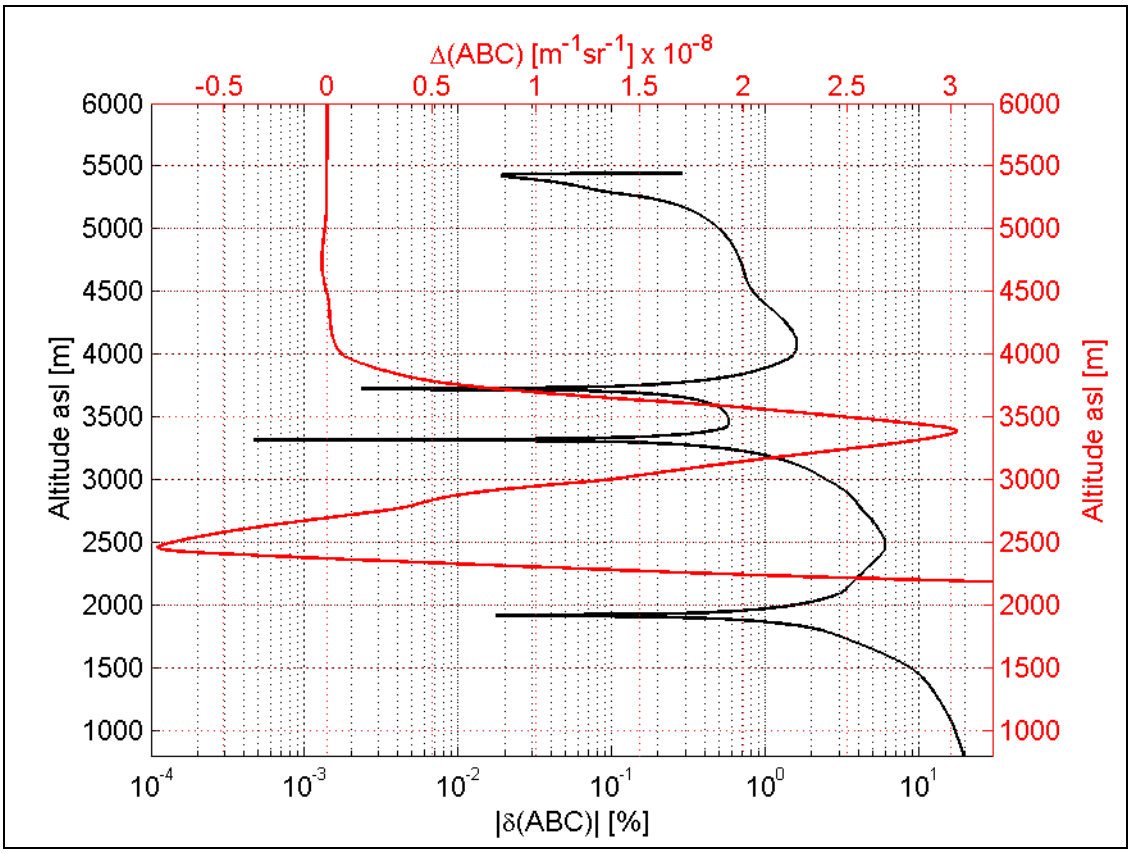


**Figure 2.11.** *Difference between retrieved ABC and model ABC for the simulation exercise presented in Fig. 2.10. The red line (upper scale) shows the difference between the retrieved profile and the model one. The black line (bottom scale) shows the ratio of the absolute values of that difference to the model values, in the range where these last values do not vanish.*

## 2.2.1.9 Effect of the signal shot noise

Figures 2.12 and 2.14 show the effect of quantum noise only for a measurement in photon-counting acquisition mode, for two different accumulation periods. The signal levels are the one obtained by accumulation of 5000 shots (250 sec) and respectively 50 shots (2.5 sec) for a Lidar with the specifications listed in Table 2.1. The ABC differences are shown in Fig. 2.13 for 5000 shots and in Fig. 2.15 for 50 shots accumulation.

In both figures, the signal-to-noise ratio is also reported in dark green for the unfiltered signal (with 3 m resolution) and in light green for the filtered signal. Here, the filtering is a binning with increasing binning number with range (from 15 m at 200 m agl to 180 m at 6000 m agl, and constant above). On each figure, the effect of the filtering on the SNR gain is shown. The comparison of the two figures shows the dependencies on the accumulation time of the SNR and of the fluctuations in the RCS, CSG and retrieved ABC.

In Figs. 2.12-2.13, it's seen that the filtering is such that it allows a rather good recovery of the aerosol backscatter up to about 4500 m, as well as a well-defined PBL structure with the gradient method (CSG minima identification). This is no more the case in Figs. 2.14-2.15, for which an additional resolution degradation would be necessary.

The comparison shows that the values and the variances of the retrieved ABC are nearly one order of magnitude lower for the first case, despite of the rather not optimal choice of reference range for the first case (this range corresponds to a positive peak in the noise). The difference is somewhat less pronounced toward lower range.

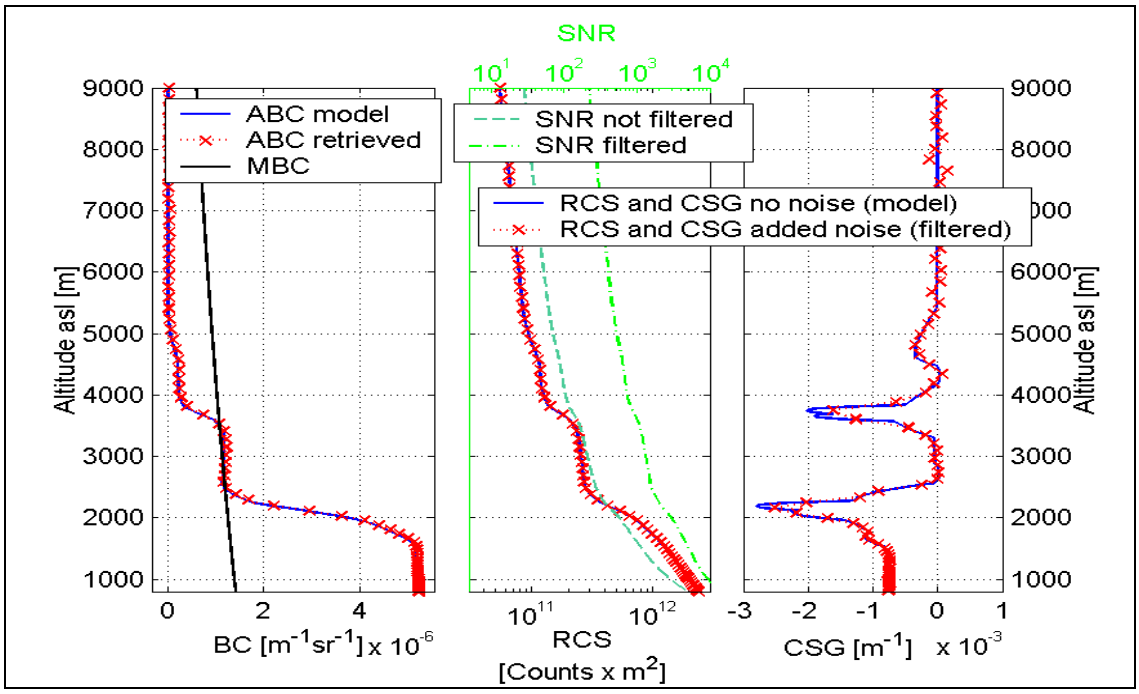


**Figure 2.12.** *Impact of the quantum noise and data filtering in the signal processing. Midlatitude summer model used as molecular reference for signal creation and processing. Acquisition resolution is 3 m. Left panel: backscatter coefficients (BC): molecular backscatter coefficients (MBC) and aerosol backscatter coefficients (ABC model, and ABC retrieved from the noisy and filtered data). The difference between these ABC profiles is shown in Fig. 2.13. Central panel: range-corrected signals (RCS, bottom scale) without noise addition (blue) and with noise addition and signal filtering (red); signal-to-noise ratio (SNR) profiles (green lines, top scale) with and without filtering. Right panel: corrected signal gradient (CSG) using the exact molecular reference, for the same two cases. For the inversion procedure, exact values of molecular reference, Lidar ratio profile (same model as in Fig. 2.10) and reference ABC (aerosol free at 9000 m agl), are assumed. Acquisition mode is photon-counting. The number of counts is the cumulated count during 250 sec (5000 shots), with the system parameters specified in Table 2.1. The filtering is a variable binning with a resolution of 15 m at 200 m agl to 180 m at 6000 m agl and constant above.*

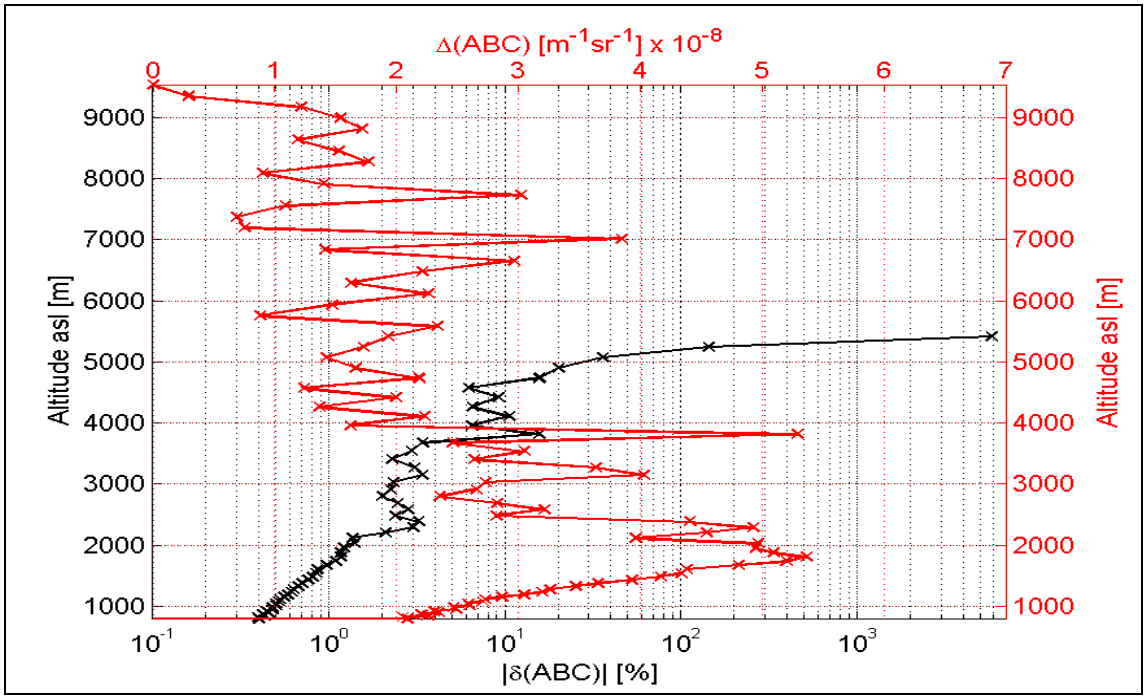


**Figure 2.13.** *Difference between retrieved ABC and model ABC for the simulation exercise presented in Fig. 2.12. The red line (upper scale) shows the difference between the retrieved profile and the model one. The black line (bottom scale) shows the ratio of the absolute values of this difference to the model ABC values, in the range where model ABC does not vanish.*

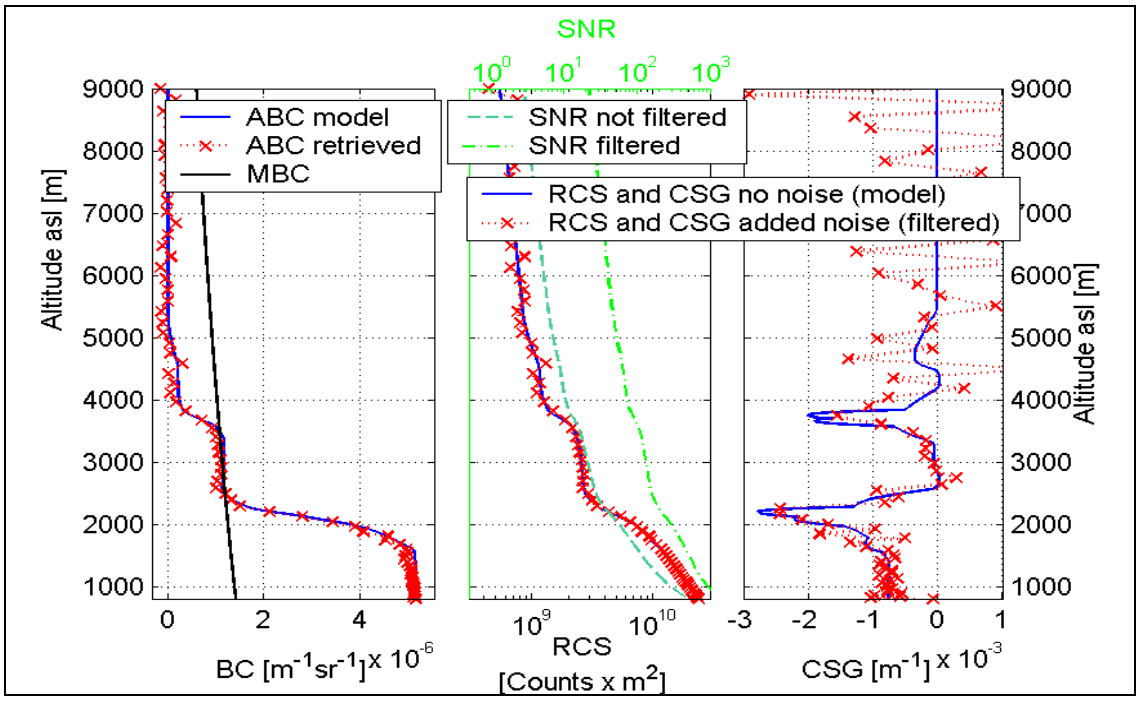


**Figure 2.14.** *Impact of the quantum noise and signal filtering in the signal processing. Midlatitude summer model used as molecular reference for signal creation and processing. Acquisition resolution is 3 m. Left panel: backscatter coefficients (BC): molecular backscatter coefficients (MBC) and aerosol backscatter coefficients (ABC model, and ABC retrieved from the noisy and filtered data). The difference between these ABC profiles is shown in Fig. 2.15. Central panel: range-corrected signals (RCS, bottom scale) without noise addition (blue) and with noise addition and signal filtering (red); signal-to-noise ratio (SNR) profiles (green lines, top scale) with and without filtering. Right panel: corrected signal gradient (CSG) using the exact molecular reference, for the same two cases. For the inversion procedure, exact values of molecular reference, Lidar ratio profile (same model as in Fig. 2.10) and reference ABC (aerosol free at 9000 m agl), are assumed. Acquisition mode is photon-counting. The number of counts is the cumulated count during 2.5 sec (50 shots), with the system parameters specified in Table 2.1. The filtering is a variable binning with a resolution of 15 m at 200 m agl to 180 m at 6000 m agl and constant above.*

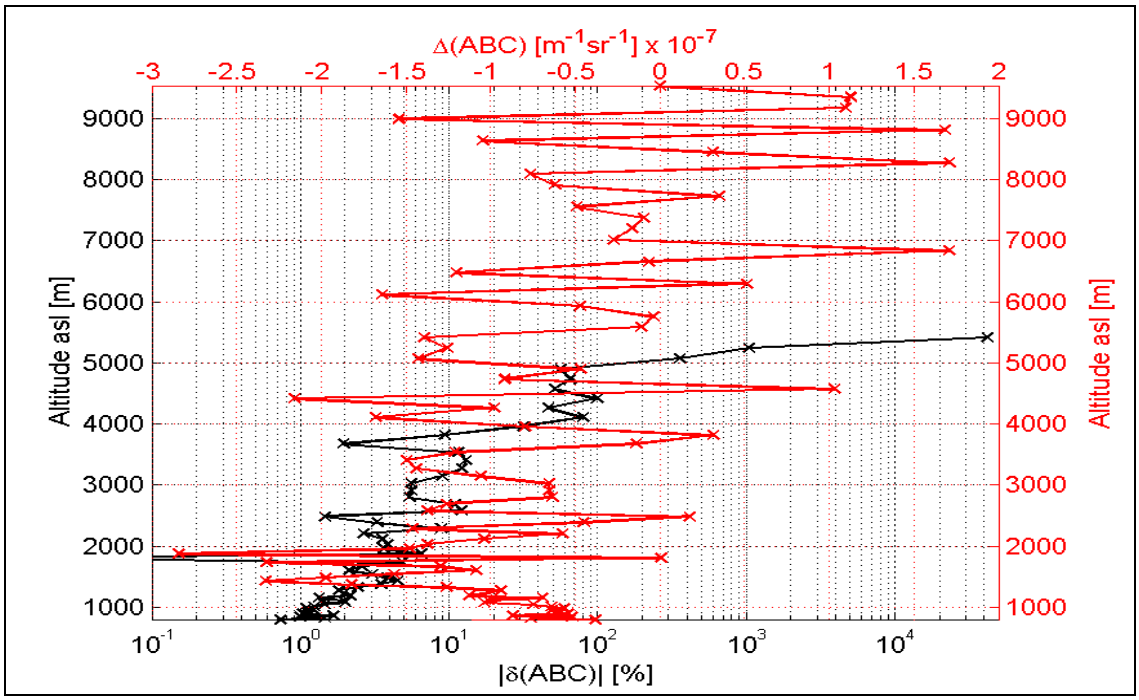


**Figure 2.15.** *Difference between retrieved ABC and model ABC for the simulation exercise presented in Fig. 2.14. The red line (upper scale) shows the difference between the retrieved profile and the model one. The black line (bottom scale) shows the ratio of the absolute values of this difference to the model ABC values, in the range where model ABC does not vanish.*

## 2.2.1.10 Effect of the shot noise of the solar background on the SNR

Figure 2.16 shows a simulation exercise in analog mode, for the shown aerosol backscatter profile and a variable Lidar ratio profile (from 40 sr to 80 sr, as in Fig. 2.10). The acquisition resolution is 15 m. Only backscattered signal shot noise has been included here. Such signal level corresponds to 500 sec of acquisition (10000 shots) for the system specifications listed in Table 2.2.

Let's now add the solar background. As has been pointed in Chapter 1, the main effect of such noise is to increase the signal fluctuations, as the constant background level (i.e. the mean value of the background light signal) can be subtracted (offset evaluation, as in (Eq 2.3)).

At 532 nm, the diffuse solar spectral irradiance on a horizontal surface is about 250 W/($m^2$ x μm) (see [*Iqbal*, 1983]). Applying (Eqs 1.21-1.26) with the device specifications of Table 2.2, we get a background current at the PMT anode of about $2x10^{-6}$A. Figure 2.18 shows the contributions of the backscatter signal and of the background to the anode current. Since the background signal is higher than the backscatter above 5000 m, the total signal fluctuations are enhanced correspondingly, resulting in a degradation of the signal quality in this range domain.

Figure 2.19 shows the effect of the solar background on the fluctuations of the RCS. The signal affected by the background has been exactly offseted for the constant background.

Figure 2.20, reports the signal-to-noise ratio profiles for these simulation exercises, with and without background. Again, we show the SNR for the original signal (resolution 15 m) and for the filtered one. The filtering is again a variable binning, with a resolution of 30 m at 200 m agl to 180 m at 6000 m agl, and constant above. The oscillatory behavior of the filtered SNR is an artefact due to large relative jumps of the resolution (effect of the binning).

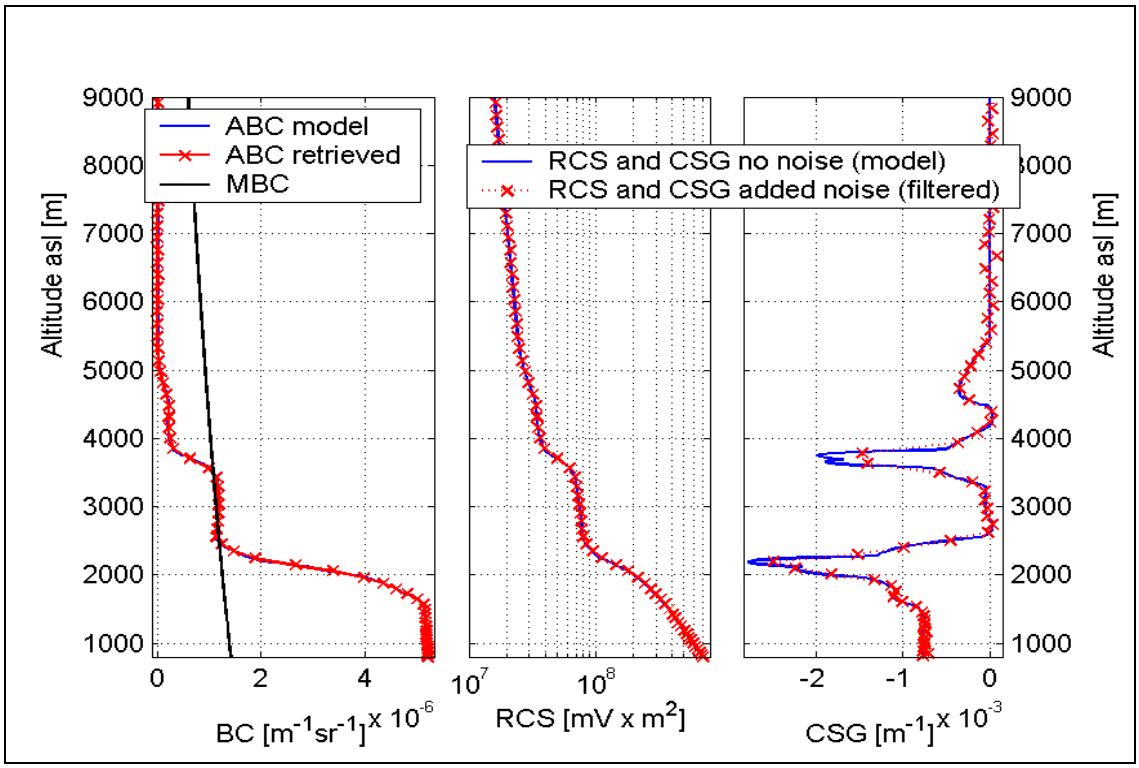


**Figure 2.16.** *Impact of the shot noise and data filtering in the signal processing. Midlatitude summer model used as molecular reference for signal creation and processing. Acquisition resolution is 15 m. Left panel: backscatter coefficients (BC): molecular backscatter coefficients (MBC) and aerosol backscatter coefficients (ABC model; and retrieved ABC, from the noisy and filtered signal). Central panel: range-corrected signals (RCS) without noise neither range filtering (blue) and with noise addition and range filtering (red); right panel: corrected signal gradient (CSG) for the same two indicated cases. No other added noise in the signal and exact values of the Lidar ratio (same model as in Fig. 2.10) and reference ABC for the inversion procedure, are assumed. Acquisition mode is analog. Device specifications are in Table 2.2. The signal voltage is the average over 10000 shots. The filtering is a variable binning with a resolution of 30 m at 200 m agl to 180 m at 6000 m agl, and constant above.*

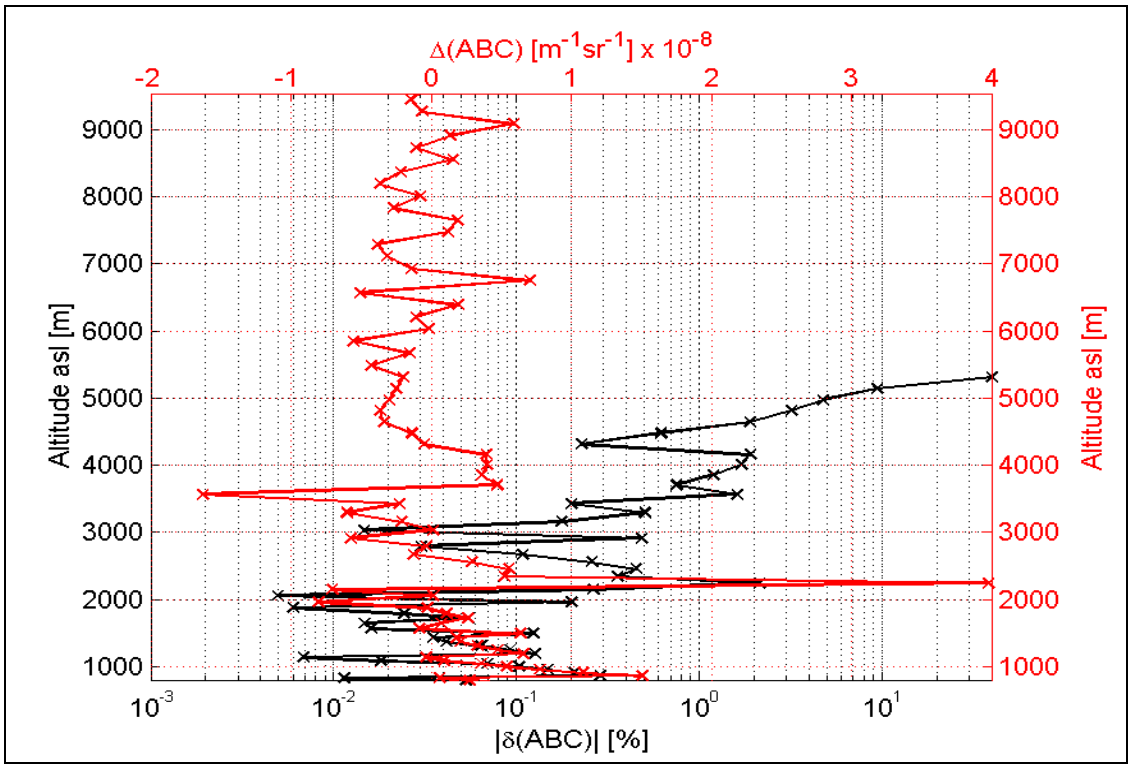


**Figure 2.17.** *Difference between retrieved ABC and model ABC for the simulation exercise presented in Fig. 2.16. The red line (upper scale) shows the difference between the retrieved profile and the model one. The black line (bottom scale) shows the ratio of the absolute values of this difference to the model ABC values, in the range where model ABC does not vanish.*

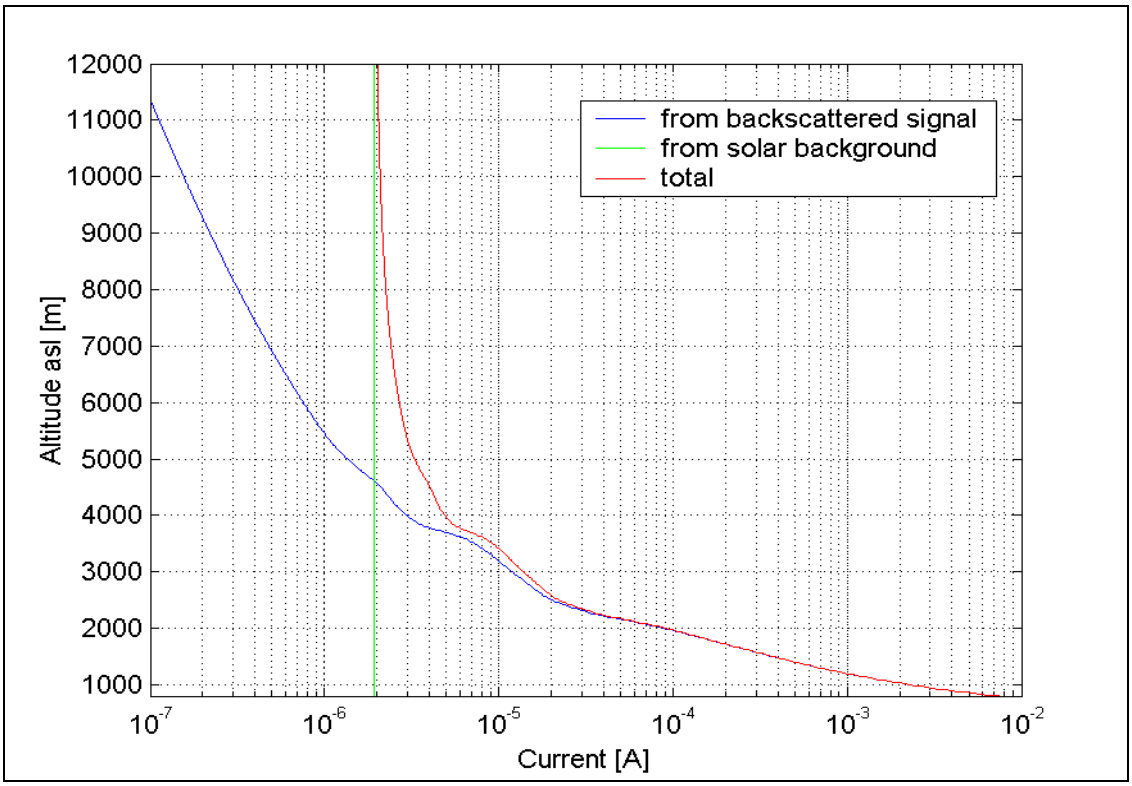


**Figure 2.18.** *Anode current at the PMT output for the analog mode measurement presented in Fig. 2.16, in presence of the solar background (noise). Resolution is 15 m. Device specifications are found in Table 2.2.*

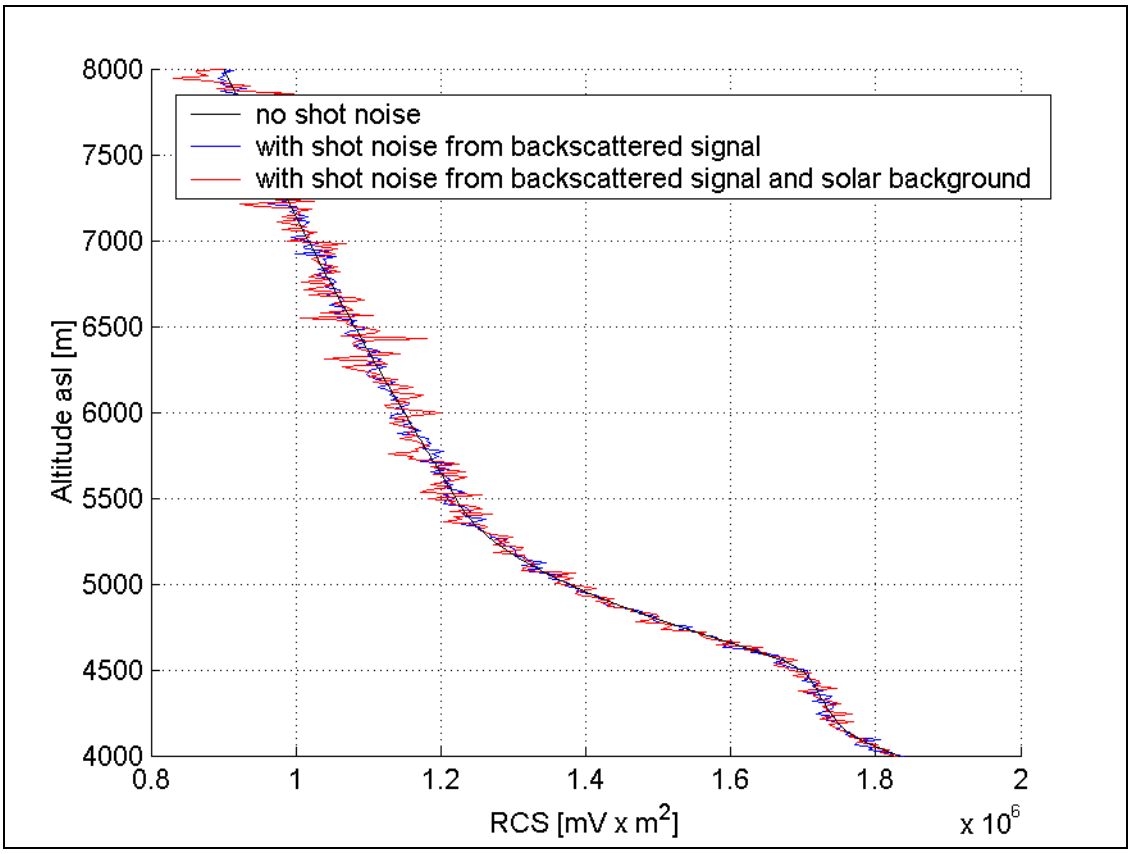


**Figure 2.19.** *Range and background corrected signal for the simulation exercise presented in Fig. 2.16, showing the effect of the background on the signal fluctuation. Resolution is 15 m.*

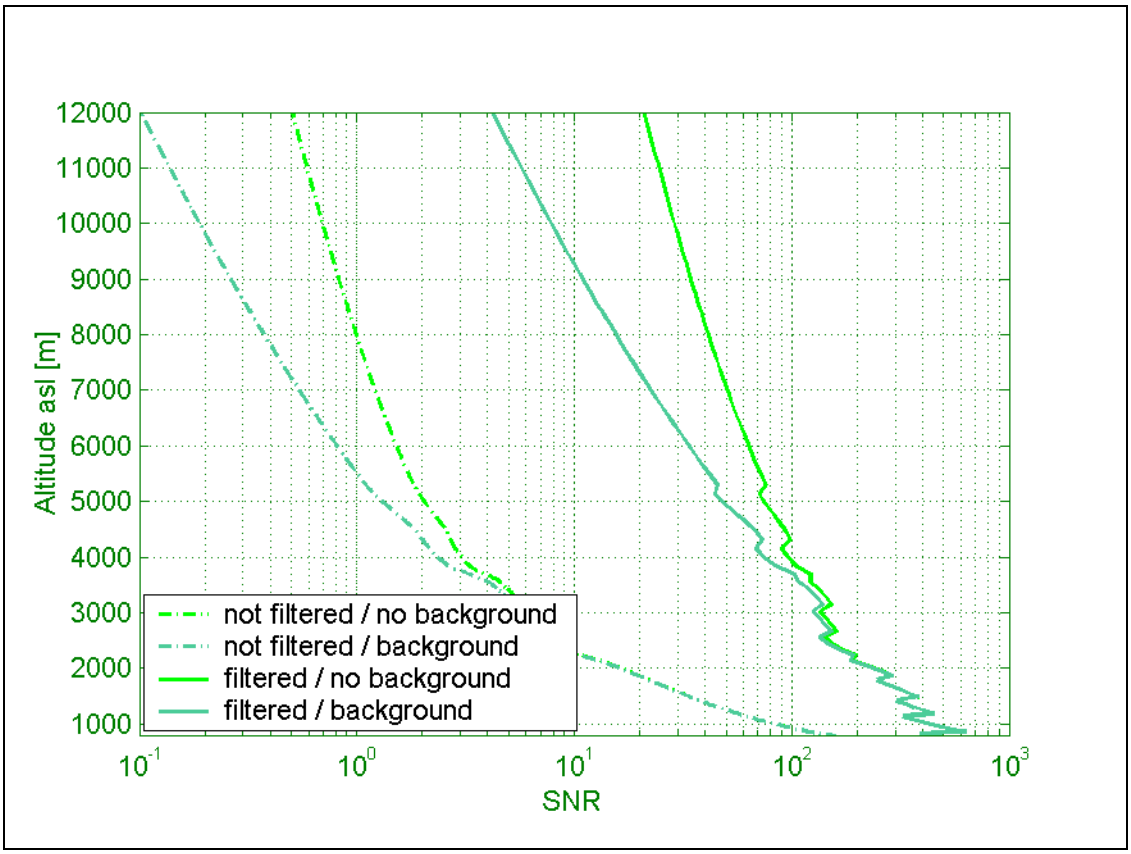


**Figure 2.20.** *Signal-to-noise ratio for the analog mode measurement presented in Fig. 2.16, showing the impact of the presence of a background noise and of a filtering. Resolution is 15 m. Device specifications are found in Table 2.2.*

#### 2.2.1.11 Effect of the dark current and thermal noises on SNR

The dark noise in analog mode depends on anode dark current at the PMT output: a typical value for it is $10^{-9}$ A.

The contribution to fluctuations due to the thermal noise follows from (Eq 2.5). With the device specifications of Table 2.2, this gives approximately $5x10^{-9}$ A. Comparing these values with those in Fig. 2.18, we see that these two noise sources are negligible versus the background effect. With the present system, these noises would become relevant only by night-time measurement and at much higher altitude (the simulation shows that the backscattered signal would reach such small values at about 30 km, with aerosol free conditions above 10 km).

### 2.2.2 Elastic Backscatter Lidar simulations done in EARLINET

#### 2.2.2.1 Introduction

The task of the EU project EARLINET (European Aerosol Research LIdar NETwork) is to start the creation of an aerosol database over Europe. From this point of view, an important part of the activities was devoted to homogenize and test the measurement and the processing algorithm in the various participating groups.

For the signal processing, the test was done with a numerically simulated signal, created by one of the participant and distributed to all partners. The aerosol model profiles have been distributed only after the end of the exercises.

Results on our participation in these exercises are published together with results from other groups in [*Böckmann et al.*, 2001] and [*Matthias et al.*, 2002].

Since most of the groups involved in the EARLINET community, are operating simultaneously at several wavelengths, the following simulations are done with the three most commonly used wavelengths, i.e. at 355 nm, 532 nm and 1064 nm: these are respectively the third, second and first harmonics of a Nd:YAG laser.

The simulation exercises were organized in three successive steps, called here stages. Each stage applies on the same data, but with increasing number of informations:

- stage 1: data were delivered together with a model of temperature and pressure.
- stage 2: the profile of Lidar ratio was given.
- stage 3: an aerosol backscatter reference value was supplied.

The data do not include noise. The processing for the first stage was based on Klett's inversion algorithm. The processing for the second stage was done with Fernald's algorithm with constant Lidar ratio. The third stage was done using Fernald's algorithm with variable Lidar ratio with height.

#### 2.2.2.2 A training exercise with known reference values

Figures 2.21 and 2.22 show the result of a training exercise, processed here with the last version of the inversion routine. The Lidar ratios were respectively 28 sr, 39 sr and 77 sr , and the aerosol backscatter reference values (at 10000 m) were $5x10^{-10}$ $m^{-1}sr^{-1}$, $2.5641 \times 10^{-10}$ $m^{-1}sr^{-1}$, $7.5324 \times 10^{-11} m^{-1}sr^{-1}$ at respectively 355 nm, 532 nm and 1064 nm. Figures 2.21 and 2.22 show only the last stage. No signal filtering was applied, thus the resolution for the retrieved aerosol backscatter is also of 15 m.

This confirms that the Fernald procedure is working properly. Although data did not include any noise, the unknown exact values of the Rayleigh profiles explain the oscillatory behavior of the solutions. This is particularly marked at 355 nm, due to the smaller ratio of aerosol to molecular backscattering coefficient.

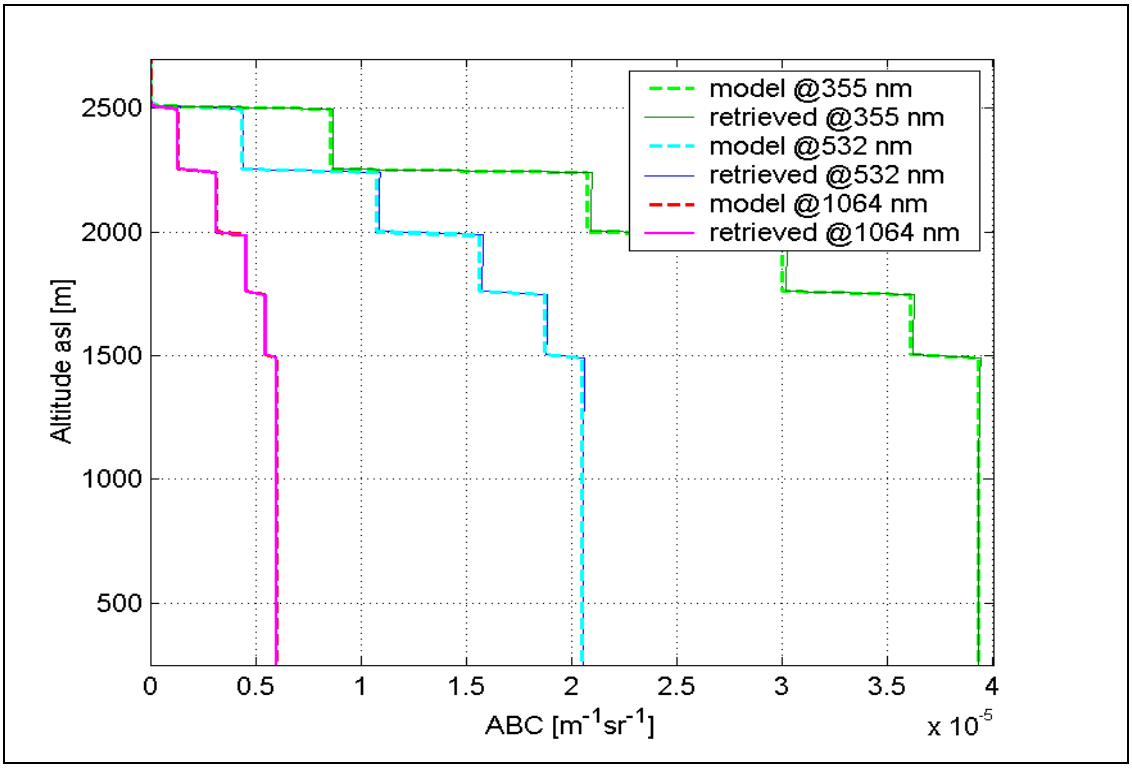


**Figure 2.21.** *EARLINET simulation training exercise at three wavelengths. Zoom on the lower range. Exact reference value for the aerosol backscatter and exact Lidar ratio were assumed (see values in the text).*

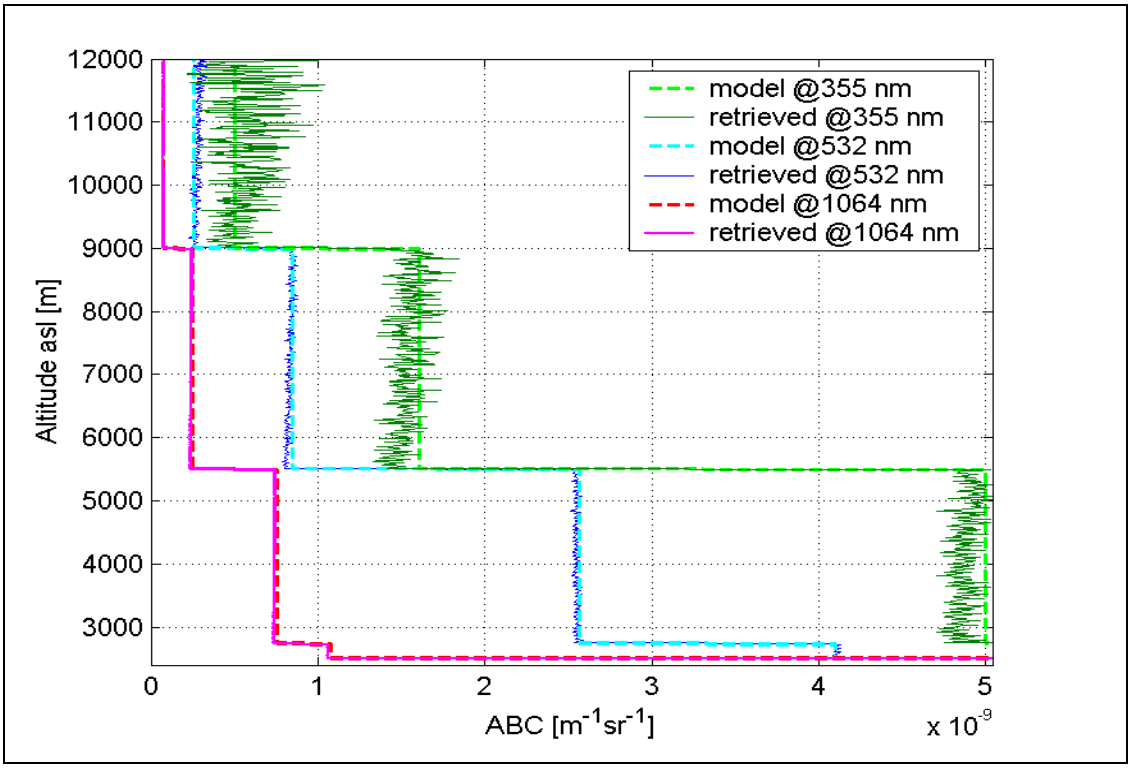


**Figure 2.22.** *EARLINET simulation training exercise at three wavelengths. Zoom on the upper range. Exact reference value for the aerosol backscatter and exact Lidar ratio were assumed (see values in the text).*

### 2.2.2.3 Example of simulation exercise with the three stages

Figures 2.23 to 2.26 show the result of an EARLINET simulation exercise (reported as "example 2" in [*Matthias et al.*, 2002]). Here the results of the three stages described above are reported. This simulation is relatively realistic, in the sense that the extinction profiles and Lidar ratios took wavelength dependent values: Lidar ratios are constant up to 4500 m, with the respective values of 64 sr, 62 sr, 42 sr for respectively 355 nm, 532 nm and 1064 nm.

Figures 2.23 to 2.25 present the solution for three stages at respectively 355 nm, 532 nm and 1064 nm. Figure 2.26 presents an overview of the results for the three wavelengths for backscatter and extinction on a same scale.

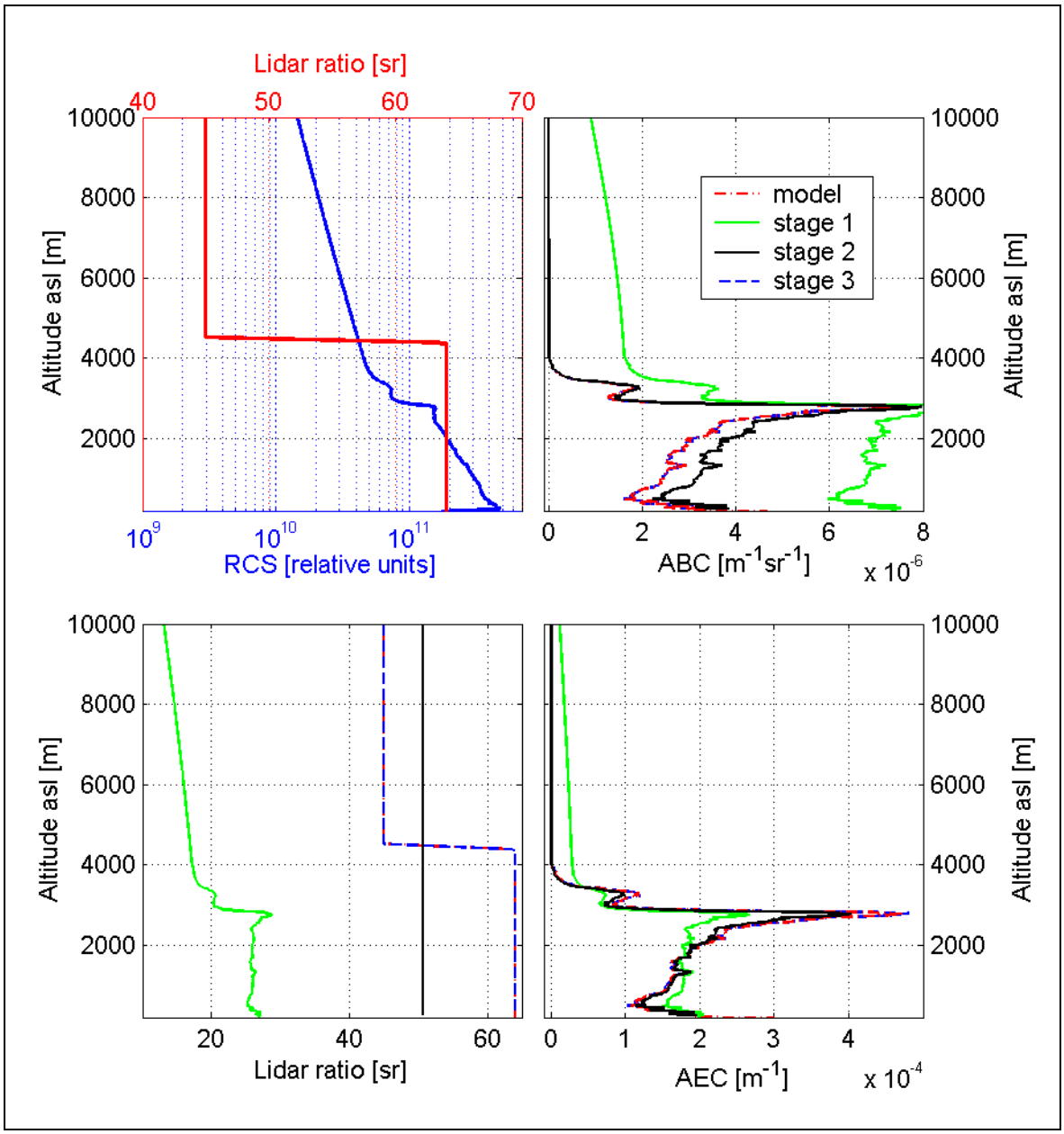


**Figure 2.23.** *EARLINET simulation exercise ("example 2") at 355 nm. Upper left panel shows the input range-corrected signal (RCS, lower scale) and the input Lidar ratio profile (upper scale). Upper right panel shows the aerosol backscatter coefficients (ABC). Lower left panel show the Lidar ratios. Lower right panel shows the aerosol extinction coefficients (AEC). The legend in the ABC panel applies also to the two bottom panels.*

The first stage was achieved with a simple Klett's assumption (see Eqs 1.57-1.58), with an exponent of 0.8. For the three wavelengths, we see that such assumption leads only to a good order of magnitude for the retrieval of both aerosol extinction and backscatter coefficients, and only in the lower part of the profiles. Moreover, the calibration constant (see (Eq 1.57)) was largely overestimated, leading to a large underestimate of the Lidar ratio. The relative errors are seen to be higher at lower wavelength.

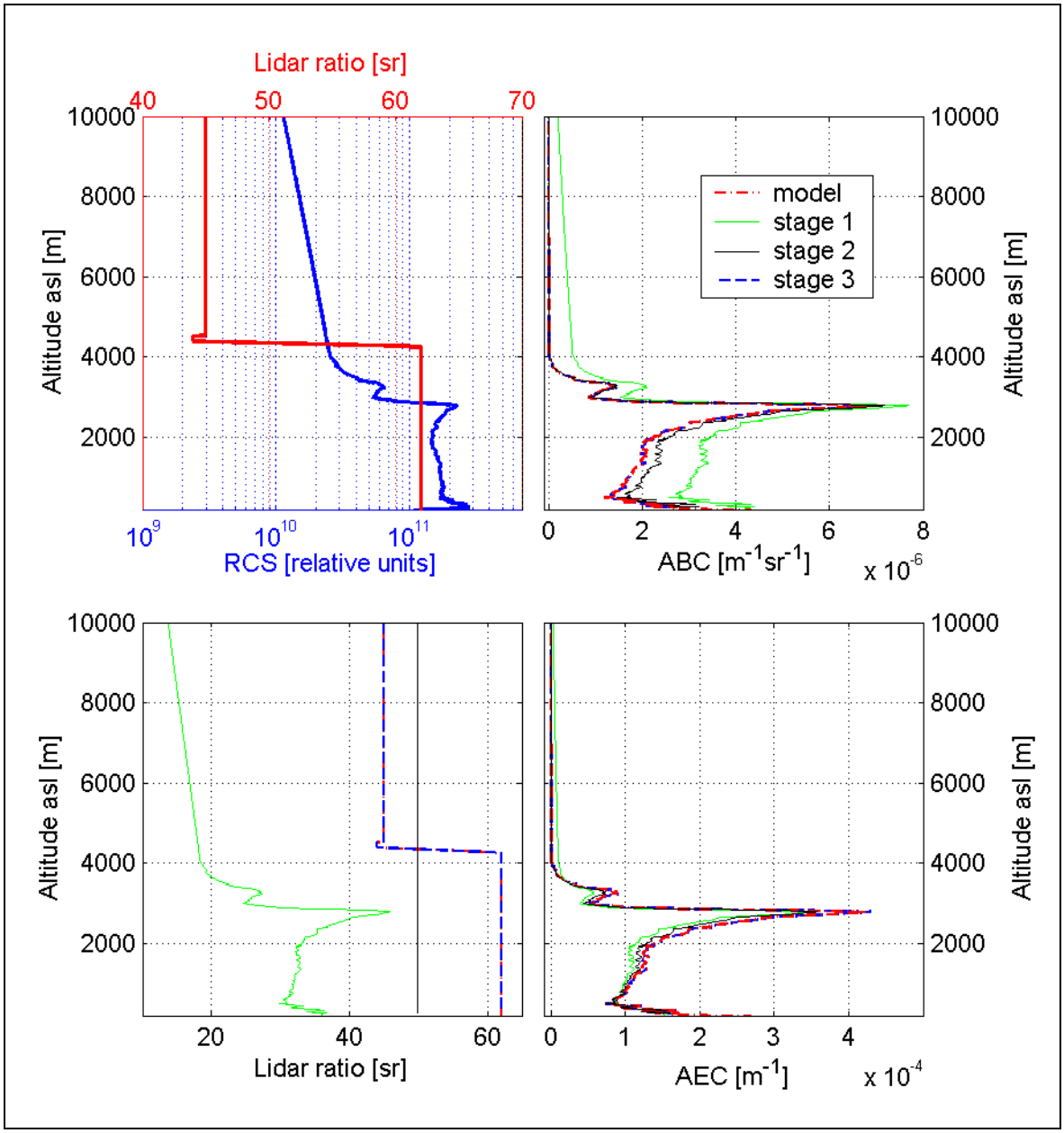


**Figure 2.24.** *EARLINET simulation exercise ("example 2") at 532 nm. Upper left panel shows the input range-corrected signal (RCS, lower scale) and the input Lidar ratio profile (upper scale). Upper right panel shows the aerosol backscatter coefficients (ABC). Lower left panel show the Lidar ratios. Lower right panel shows the aerosol extinction coefficients (AEC). The legend in the ABC panel applies also to the two bottom panels.*

The second stage was achieved with a Fernald's algorithm, without the option for variable Lidar ratio with height. Since the Lidar ratio was supplied, an average value has been chosen. Although the backscatter reference value was typically one order of magnitude too high (see at around 10000 m on Fig. 2.26), in such way that negative values were avoided along the whole profile, the errors below 4000 m are largely due to the approximation in Lidar ratio (see Fig. 2.10). Again, the retrieval at longer wavelength is more precise.

At the third stage, i.e. with known reference values, the results are excellent along the whole profile (see Fig. 2.26). This ensures that, although the Rayleigh reference is not exactly known, the inversion procedure is working properly.

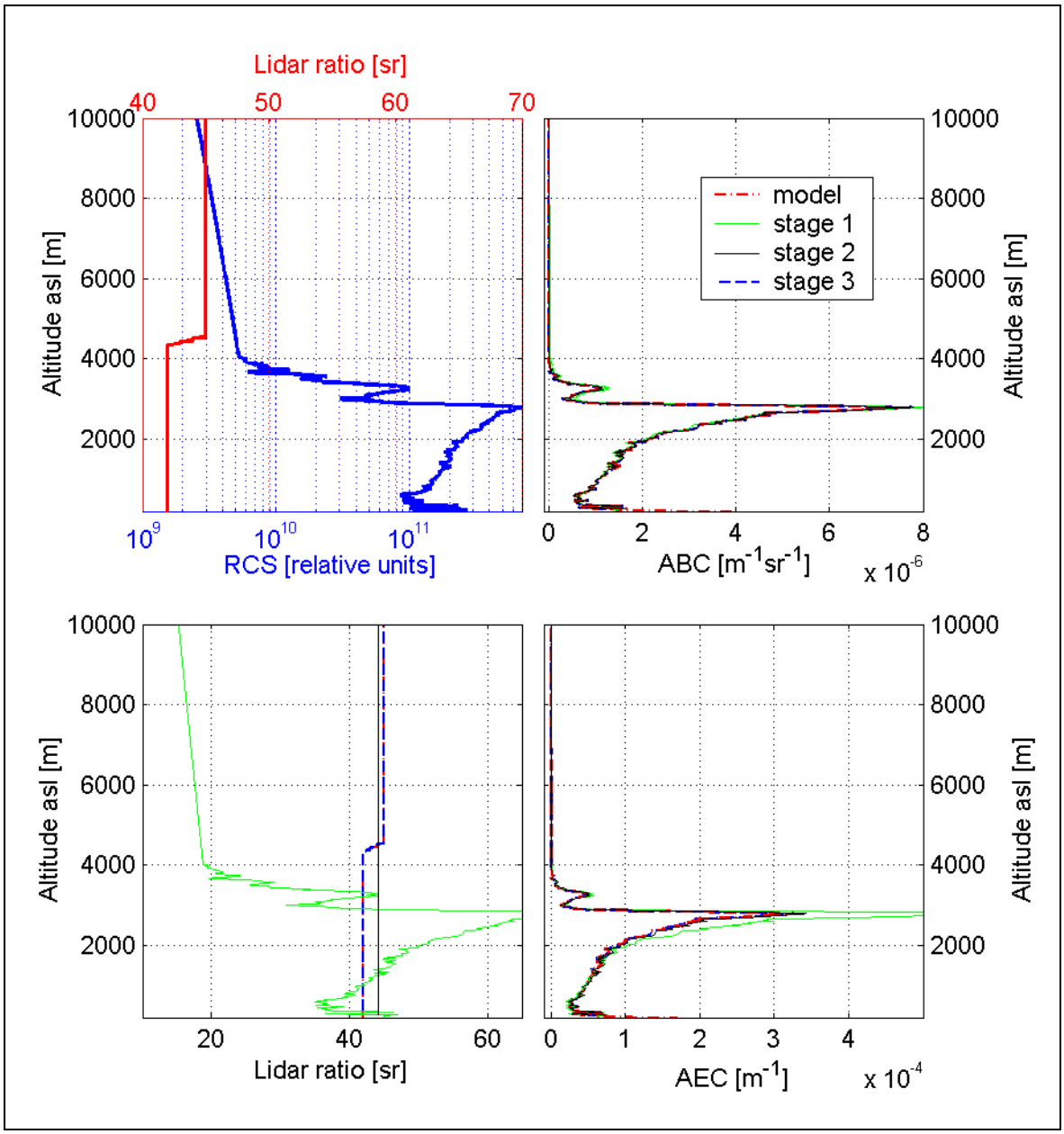


**Figure 2.25.** *EARLINET simulation exercise ("example 2") at 1064 nm. Upper left panel shows the input range-corrected signal (RCS, lower scale) and the input Lidar ratio profile (upper scale). Upper right panel shows the aerosol backscatter coefficients (ABC). Lower left panel show the Lidar ratios. Lower right panel shows the aerosol extinction coefficients (AEC). The legend in the ABC panel applies also to the two bottom panels.*

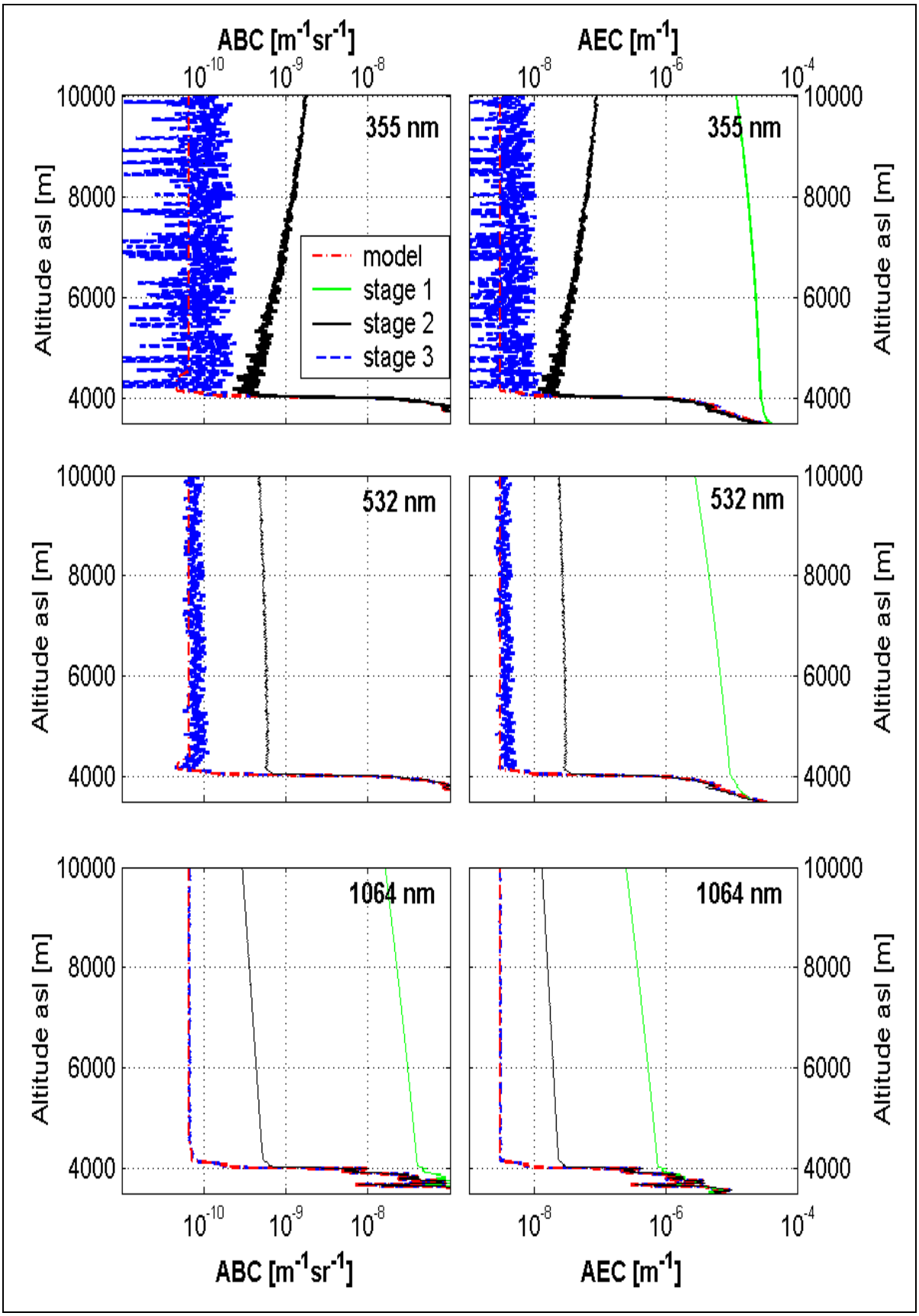


**Figure 2.26.** *EARLINET simulation exercise ("example 2"). Overview of the solutions presented in Figs. 2.23-2.25, zoomed on the upper range. The same scale is used for the three wavelengths. Left panels show the aerosol backscatter coefficients (ABC). Right panels show the aerosol extinction coefficients (AEC). The legend in the upper panel left applies to all panels.*

### 2.2.2.4 Simulation exercise with "realistic" ABC profile

Figures 2.27–2.29 show some results another simulation exercise (reported as "example 3" in [*Matthias et al.*, 2002]). This case can be considered as realistic, in the sense that it contains height-dependent aerosol backscatter coefficients and Lidar ratios. The Lidar ratio was variable below 3600 m, with values between 24 sr and 69 sr, but independent of the wavelength.

Figure 2.27 shows all solutions for the second stage of this simulation exercise, at 355 nm, obtained by 15 groups participating to this exercise.

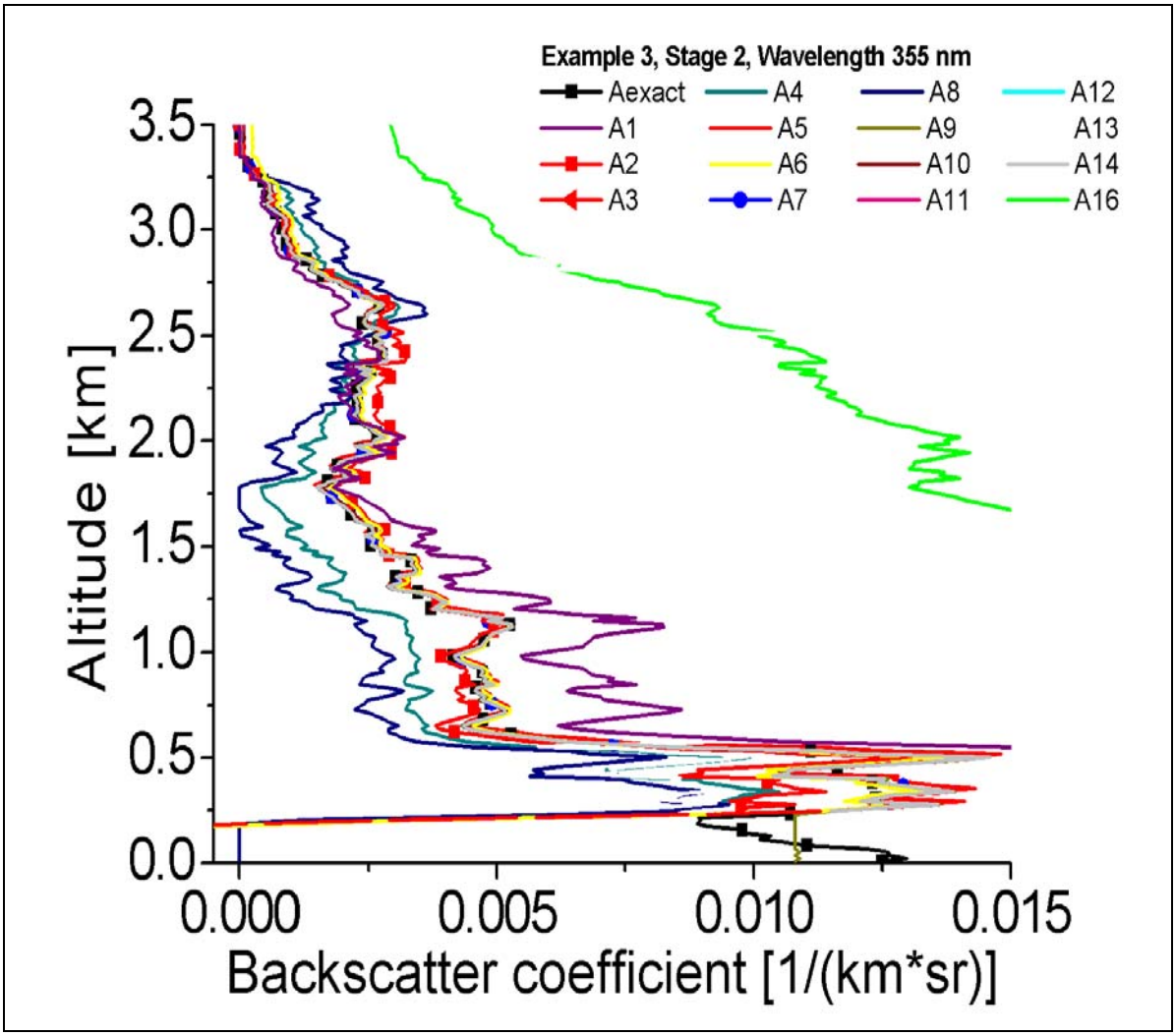


**Figure 2.27.** *EARLINET simulation exercise ("example 3"), stage 2, at 355 nm. Results for 15 EARLINET groups participating to this exercise. Our solution is the line labeled "A2".*

Figures 2.28 and 2.29 show the results of the third stage for the three wavelengths. As before, no filtering was applied, i.e. the retrieved profiles have the same resolution than the input data (15 m). Figure 2.28 shows again that the inversion routine works properly. Figure 2.29 shows a zoom on the upper part of the profiles, where very low constant and wavelength independent aerosol content was simulated. As before, we see that longer wavelengths are less sensitive to the error due to the unknown (exact) Rayleigh profile.

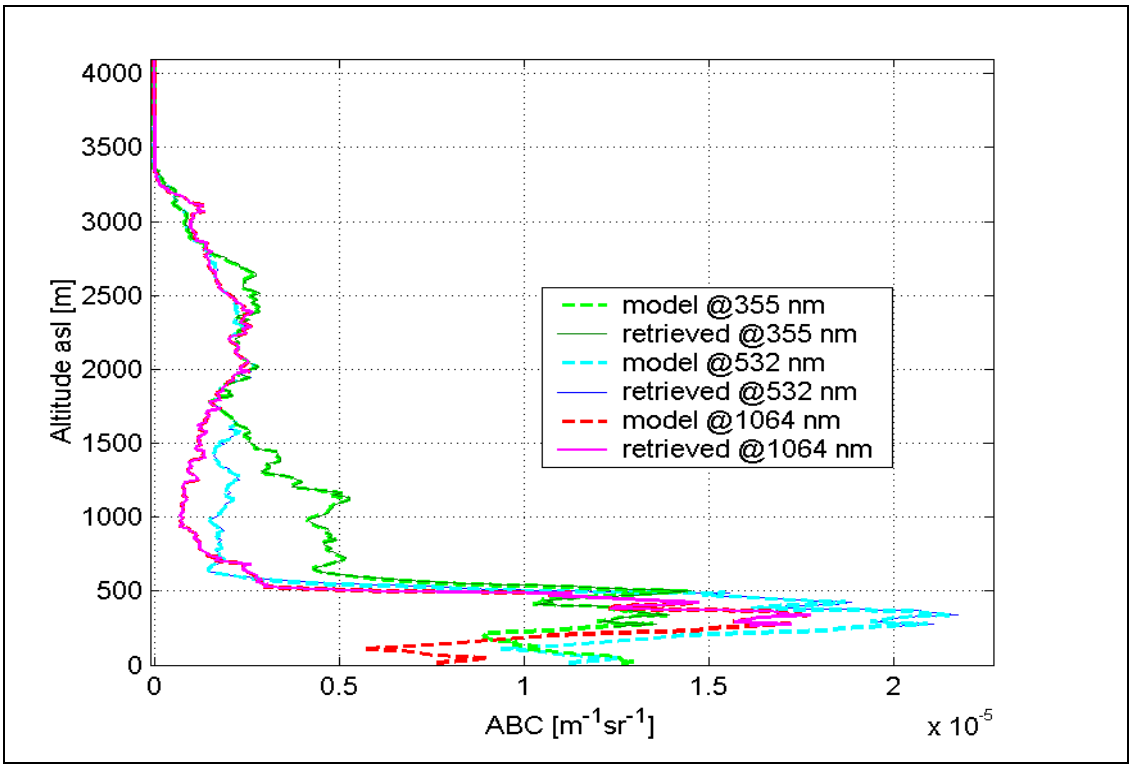


**Figure 2.28.** *EARLINET simulation exercise ("example 3"), stage 3 (known profiles of reference aerosol backscatter coefficients and Lidar ratio), for the three wavelengths. Zoom on the lower range.*

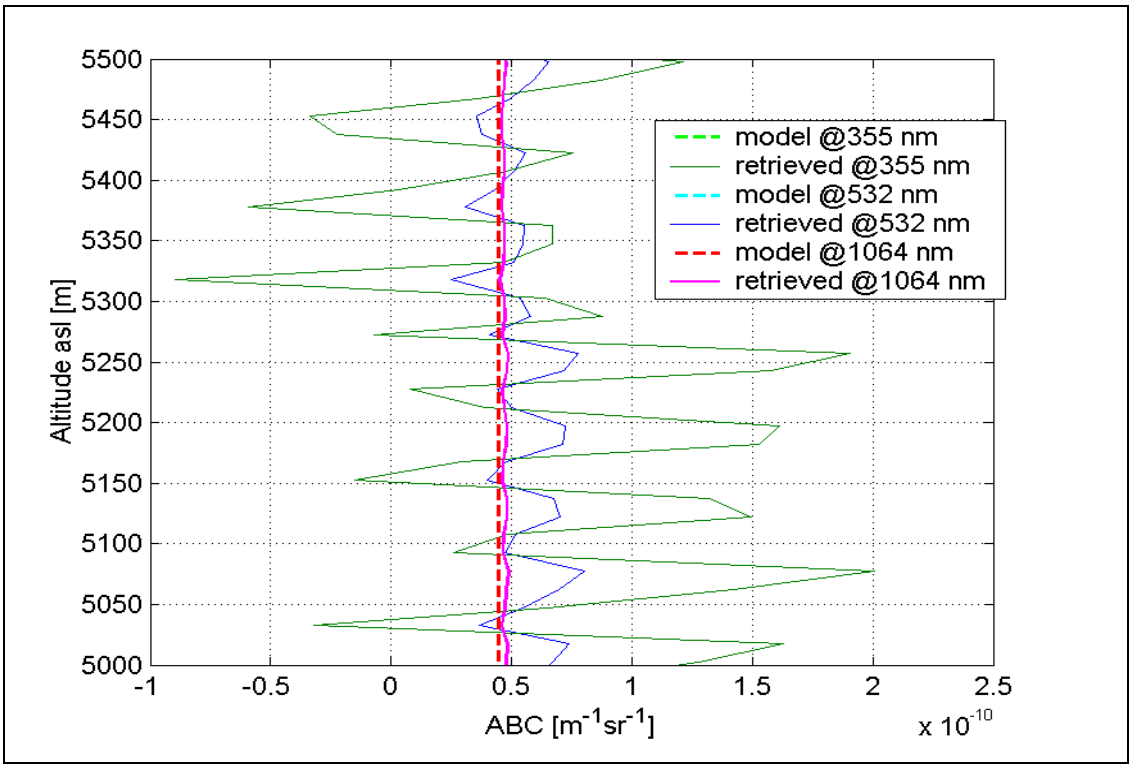


**Figure 2.29.** *EARLINET simulation exercise ("example 3"), stage 3, for the three wavelengths. Zoom on part of the upper range. On this range, the model values for the three wavelengths are the same.*

# 2.3 Raman Backscatter Lidar simulations

## 2.3.1 Introduction to determination of aerosol extinction coefficient by Raman Backscatter Lidar

The Raman scattering processes involve a transition between two rotational or vibrational energy levels of a molecule, just as absorption and emission spectra do (see [*Measures*, 1984]). Absorption and emission spectroscopies directly probe the difference in energy between two energy levels using a single photon. The energy of that photon is the energy difference for the transition between levels. In the Raman process, the molecule interacts with the photon in an inelastic scattering event. During the scattering event, the molecule takes the energy of the incident photon, and can add or subtract from the photon energy by the energy level differences within the molecule. The energy of the incident photon is not required to be in resonance with an energy level difference in the molecule as there is only a "virtual state" at the energy of the incident photon. This scattering process yields a resulting photon whose energy differs from that of the initial photon by the energy differences within the molecule.

Raman processes are of high interest for Backscatter Lidar applications, because a specific wavelength shift is a signature of a particular molecule. The differential backscattering cross-section of Raman processes are smaller than the elastic one by several orders of magnitude. This can be compensated by using the most abundant scatterers in the atmosphere, like the $N_2$ or $O_2$ molecules, and by adapting the device parameters (typically, larger laser power and larger telescope area than in elastic case, are used).

Let's consider the Raman backscatter from some molecular specie $X$ with number density $n_X$. Let $\beta_X^{Raman}$ be the molecular Raman differential backscattering cross-section of the Raman process with incident wavelength $\lambda_0$ and backscattered wavelength $\lambda_R$. Following (Eq 1.10), the backscattered signal at the Raman shifted wavelength is given by

$$P(r) = \frac{K}{r^2} n_X(r) \beta_X^{Raman} T_{\lambda_0}(r) T_{\lambda_R}(r) \qquad \text{(Eq 2.8)}$$

above full overlap, where $K$ is a device constant and $T_{\lambda_0}(r)$ respectively $T_{\lambda_R}(r)$ are the optical transmissions on the forward laser beam path respectively on the backward light path.

Due to their very low value, the Raman signals are often measured in photon-counting mode.
Assuming an Angstroem law for the aerosol extinction around the laser wavelength (see §1.2.5.4),

$$\alpha_\lambda^{aer} \cong \lambda^{-k} \qquad \text{(Eq 2.9)}$$

we obtain the following

$$\alpha_{\lambda_0}^{aer}(r) = \frac{\frac{d}{dr}\left\{\log\left[\frac{n_X(r)}{r^2 P(r)}\right]\right\} - \alpha_{\lambda_0}^{mol}(r) - \alpha_{\lambda_R}^{mol}(r)}{1 + \left(\frac{\lambda_0}{\lambda_R}\right)^k} \qquad \text{(Eq 2.10)}$$

Thus, we got a direct evaluation of the extinction profile. If the elastic backscatter signal is also measured, then the corresponding Lidar equation gives, after a suitable calibration (reference value for the aerosol backscatter), the backscatter profile. In this way, the combined elastic and Raman measurements delivered the simultaneous retrievals of extinction and backscatter. Thus, Lidar ratios can be deduced.
The application of (Eq 2.10) is not straightforward. The following error sources must be considered (see [*Theopold and Bösenberg*, 1988], [*Ansmann et al.*, 1992], [*Whiteman*, 2000] and [*Bösenberg*, 1998]):

(a) ***The statistical error due to signal shot noise***

(b) ***The systematic error associated with the estimate of temperature and pressure profiles***

(c) ***The systematic error associated with the wavelength dependence parameter k***

(d) ***The error introduced by operational procedures such as signal averaging during varying atmospheric extinction and scattering conditions***

Let's here discuss briefly the above points:

(a) ***Statistical error due to signal quantum or shot noise***

Taking into account the random errors that are due to signal quantum or shot noise, the uncertainty on the aerosol extinction coefficient from (Eq 2.10) is deduced

$$\Delta\alpha_{\lambda_0}^{aer} = \frac{\Delta P(r)\ \dfrac{dP(r)}{dr}}{\left(1+\left(\dfrac{\lambda_0}{\lambda_R}\right)^{k}\right)P^2(r)} \qquad \text{(Eq 2.11)}$$

where $\Delta P(r)$ is the error due to the signal quantum or shot noise. This signal error can be taken as the noise term in the expressions for the signal-to-noise ratio. When the filtering is a simple binning, the signal error in photon-counting mode becomes

$$\Delta P(r) = \sqrt{\frac{P(r)}{nbin(r)}} \qquad \text{(Eq 2.12)}$$

where $P$ is the filtered signal (in counts) and $nbin$ the binning number (number of points on the altitude profile).

(b) ***Systematic error associated with the estimate of temperature and pressure profiles***

The use of standard pressure and temperature profiles instead of the real ones lead to an error in the presence of gradient's estimation. While pressure gradients are always limited, temperature gradients are large especially in the case of strong inversion layers. In (Eq 2.10), the computation of the term containing the derivative is directly affected by the temperature gradient, as follow

$$\frac{d}{dr}\left\{\log\left[n_X(r)\right]\right\} = \frac{1}{n_X}\frac{dn_X}{dr} \cong \frac{1}{T}\frac{dT}{dr} \qquad \text{(Eq 2.13)}$$

where $T$ is the absolute temperature. Thus, a significant systematic uncertainty can result from an error in the estimate of strong temperature gradients. In order to reduce this source of error, the use of simultaneous radiosonde temperature profile instead of a standard atmosphere profile is recommended.

(c) ***Systematic error associated with the Angstroem exponent k***

As pointed in Chapter 1, this exponent depends on the wavelength and on the particle size distribution. Thus, it is never known a priori. The corresponding error in (Eq 2.10) depends also on the relative wavelength shift. Letting $k$ vary in the range [0 2], typical relative errors of 6%-8% are observed (see [*Whiteman*, 2000]).

(d) ***Errors introduced by operational procedures***

Due to the non-linearity for the signal in (Eq 2.10), extinction retrieval and time averaging are not commutable. When the atmospheric conditions evolve quickly, and as long as the signal quality allows it, it is recommended to apply (Eq 2.10) on sub-periods with nearly constant aerosol load, and to take the temporal average of these retrieved aerosol extinction profiles. This effect will be exemplified.

## 2.3.2 Raman Backscatter Lidar simulations done in EARLINET

### 2.3.2.1 General conditions and objective

As in the elastic case, the simulations for Raman Backscatter Lidar are intended to test the different algorithm of the EARLINET participating groups. Although Raman measurements were not performed at ON in the frame of EARLINET activities, we participated to some of the proposed simulation exercises. Results on our participation in these exercises are published together with results from other groups in [*Matthias et al.*, 2002].

In order to test the algorithm, the conditions for all Raman exercises were as follow: the profiles of temperature and pressure have been provided as well as the Angstroem exponent for aerosol extinction ($k$=1.5) by the partner controlling the exercise. The laser wavelength and the Raman shifted wavelength on $N_2$ were respectively 532 nm and 607 nm. Unlike the elastic simulations, all Raman signals were contaminated by the signal quantum noise.

The objective of the exercices was to achieve the AEC retrieval with given maximum extinction error due to quantum noise, in given altitude-range. The model extinction values have been delivered only at the end of the exercises. is done by plotting in the same plot the model value and the value obtained in the simulation.

### 2.3.2.2 Impact of the accumulation time: an example

The series of EARLINET Raman exercise began with a training case (reported as "case 1" in [*Matthias et al.*, 2002]). Although we did not participate to this exercise, here we use the provided simulated signals to exemplify the impact of the accumulation time.

Two Raman signals have been simulated in the same conditions, but with assumed different accumulation times. Data were simulated for a simple step-wise profile with realistic values of aerosol extinction coefficient (AEC) below 2500 m and a sharp drop to very low values above.

The AEC retrievals have been performed on filtered and unfiltered signals. The filtering was a variable binning (the resolution of the filtered signal ranges from 75m at 250 m to 240 m at 4000 m). Figure 2.30 reports the profiles of signal-to-noise ratio of the input Raman signals (which, in that case, is just the square root of the total number of counts) and the retrieved AEC from the filtered signals. The most striking feature is the large discrepancy between the amplitudes of the fluctuations of the AEC above 2500 m. It demonstrates the high sensitivity of the retrieval process on the SNR determined by the signal level.

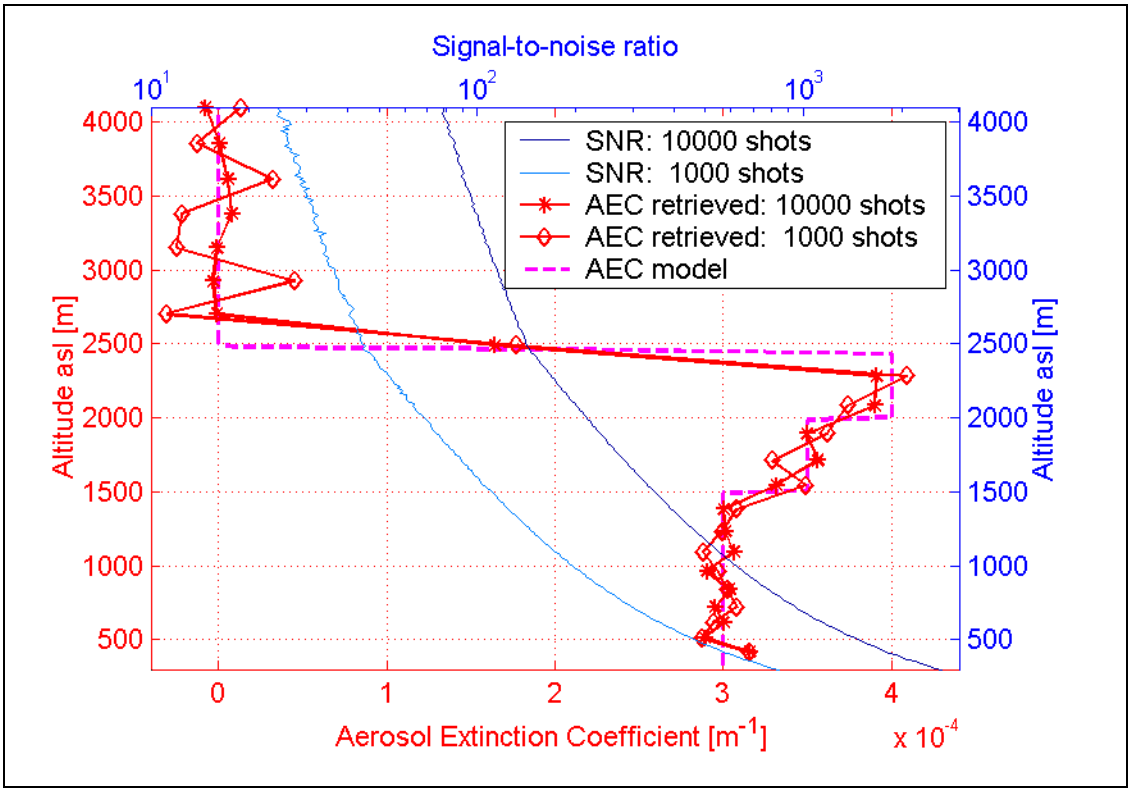


**Figure 2.30.** *EARLINET Raman simulation exercise ("case 1"). The blue lines (upper scale) reports the SNR of the unfiltered signals for two numbers of shots (accumulation times). In this case, the corresponding cumulated numbers of counts are the square of the SNR. The red lines (lower scale) report the retrieved AEC from the filtered signals (see details in text).*

Tables 2.3 and 2.4 report respectively the relative errors to the model for respectively the unfiltered and filtered signals in the three ranges with homogeneous extinction distribution. The comparison of the two last columns shows again the large sensitivity of the dispersion on the accumulation, as the average values are generally not much affected.

**Table 2.3.** *Raman simulation exercise ("case 1"): relative errors versus model (ratio of the difference between the retrieved and the model values to the model values) for the aerosol extinction retrieval, for two signal levels, without signal filtering.*

| Range domains | | 1000 shots | 10000 shots |
|---|---|---|---|
| 300 - 1500 m | Average [%] | -2.89 | -2.42 |
| | Stand. deviation [%] | 32.20 | 9.37 |
| 1500 - 2000 m | Average [%] | -0.43 | -0.31 |
| | Stand. deviation [%] | 68.56 | 14.94 |
| 2000 - 2440 m | Average [%] | 0.67 | -1.12 |
| | Stand. deviation [%] | 75.95 | 29.70 |

**Table 2.4.** *Raman simulation exercise ("case 1"): relative errors versus model (ratio of the difference between the retrieved and the model values to the model values) for the aerosol extinction retrieval, for two signal levels, with signal filtering.*

| Range domains | | 1000 shots | 10000 shots |
|---|---|---|---|
| 300 - 1500 m | Average [%] | 0.051 | 0.080 |
| | Stand. deviation [%] | 3.19 | 2.75 |
| 1500 - 2000 m | Average [%] | -0.91 | -1.17 |
| | Stand. deviation [%] | 4.69 | 3.65 |
| 2000 - 2440 m | Average [%] | -2.08 | -2.38 |
| | Stand. deviation [%] | 6.22 | 0.19 |

The comparison of the Tables 2.3 and 2.4 shows the effect of the signal filtering. The deviations are seen to be reduced of about a factor 10 for the 1000 shots case and a factor 4 for the 10000 shots case (except for the upper range, which spans over only two points of the filtered signal). On the other hand, the average error values for the two upper ranges are even larger in absolute values with than without filtering. This is a kind a bias introduced by the binning.

### 2.3.2.3 Simulation exercise with given AEC uncertainty

In the following simulation exercise, reported as "case 2" in [*Matthias et al.*, 2002], a series of 10 Raman signals have been simulated in similar conditions. The AEC profile was the same than the one of the "case 1" reported previously (§2.3.2.2). Each profile is an accumulation of 3600 shots (what corresponds to 2 min average on a Lidar with a pulse repetition rate of 30 Hz). The aim of this exercise was to determine the processing parameters such that the predicted errors in retrieved AEC did not exceed 10% below 2400 m.

Figure 2.31 presents the retrieved AEC from the filtered signals, with such a filtering that the above condition for predicted statistical error (from quantum noise only) is fulfilled. Here, the filtered data resolution varies from 30 m at 250 m to 120 m at 4000 m. On the upper scale, the profile of the predicted relative error following (Eqs 2.11-2.12) is reported.

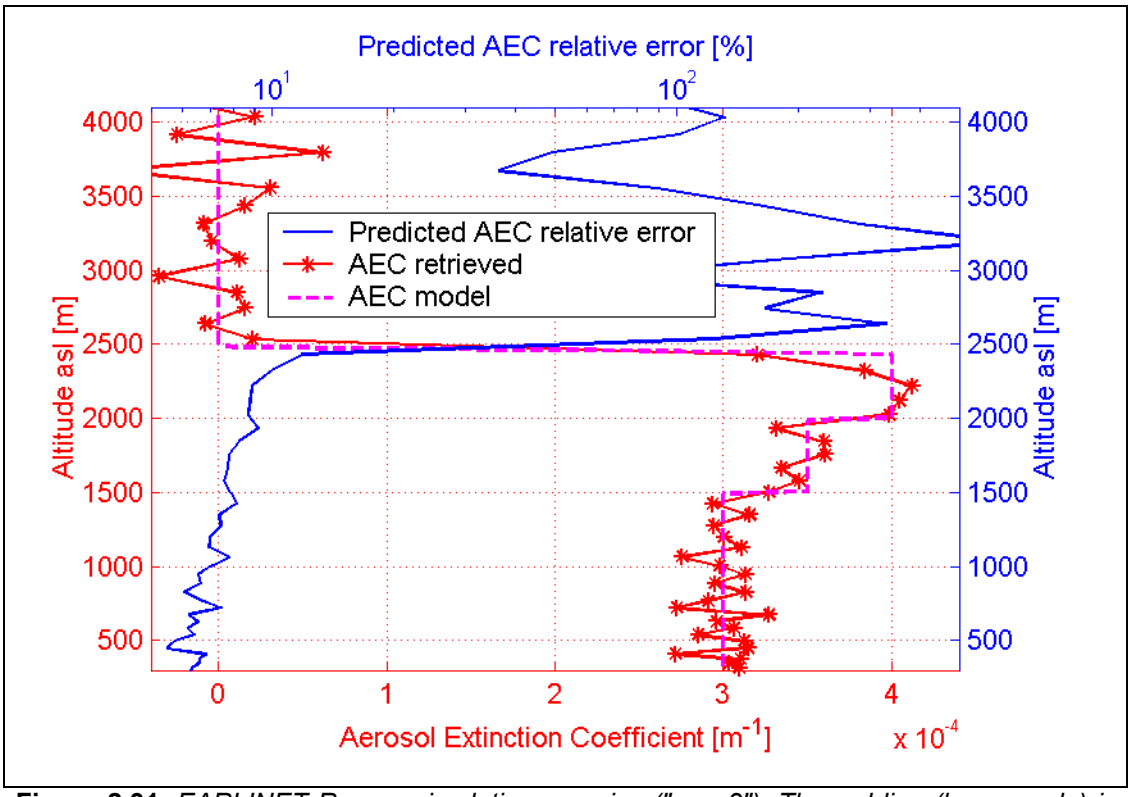


**Figure 2.31.** *EARLINET Raman simulation exercise ("case2"). The red line (lower scale) is the retrieved AEC from the filtered signal. The blue line (upper scale) reports the predicted relative error.*

### 2.3.2.4 Simulation exercise for simultaneous aerosol extinction and aerosol backscatter retrieval

One of the most interesting applications of Raman Backscatter Lidar is the possibility to measure directly the (aerosol) Lidar ratio. This is done in measuring simultaneously the elastic backscatter return and the Raman one with a single laser beam. In order to increase the signal-to-noise ratio of the relatively small Raman return, the receiving optics are different for the two channels and usually, the Raman detection mode is photon-counting.

For the following simulation exercise, reported as "case 3" in [*Matthias et al.*, 2002], a series of 20 acquisitions have been simulated, where each acquisition is an accumulation of 3600 shots. This corresponds to a measurements series with a total duration of 40 min with a Lidar with a pulse repetition rate of 30 Hz. Additionally, the used AEC models were different during the first 20 min (part I) than the twenty last ones (part II), representing a modification in atmospheric conditions. Almost vanishing values were assumed above 3300 m.

The aim of this exercise was to determine the processing parameters such that the predicted errors in retrieved AEC over the 40 min did not exceed 10% below 2500 m. Figure 2.32 presents the input signals for that exercise. The comparison of the Raman and elastic signal levels shows a typical situation (higher SNR for elastic than Raman signal). Figure 2.33 presents the extinction retrievals from the Raman signals for two cases. In the first case, the change of atmospheric conditions has been ignored (the input signal was the sum of the signals for the two parts shown in Fig. 2.32). In the second case, the two periods have been considered as distinct: for each, the AEC retrieval leads to distinct solutions, which have been averaged. The shown model represents the average values of AEC over the total measurement period. This exemplifies the non-commutatively of the AEC retrieval and the temporal averaging.

Here, one should keep in mind that in typical real conditions, the AEC profiles are changing continuously over such time period and that the accumulation time depends critically on the signal quality (minimum SNR) and effective range resolution to achieve.

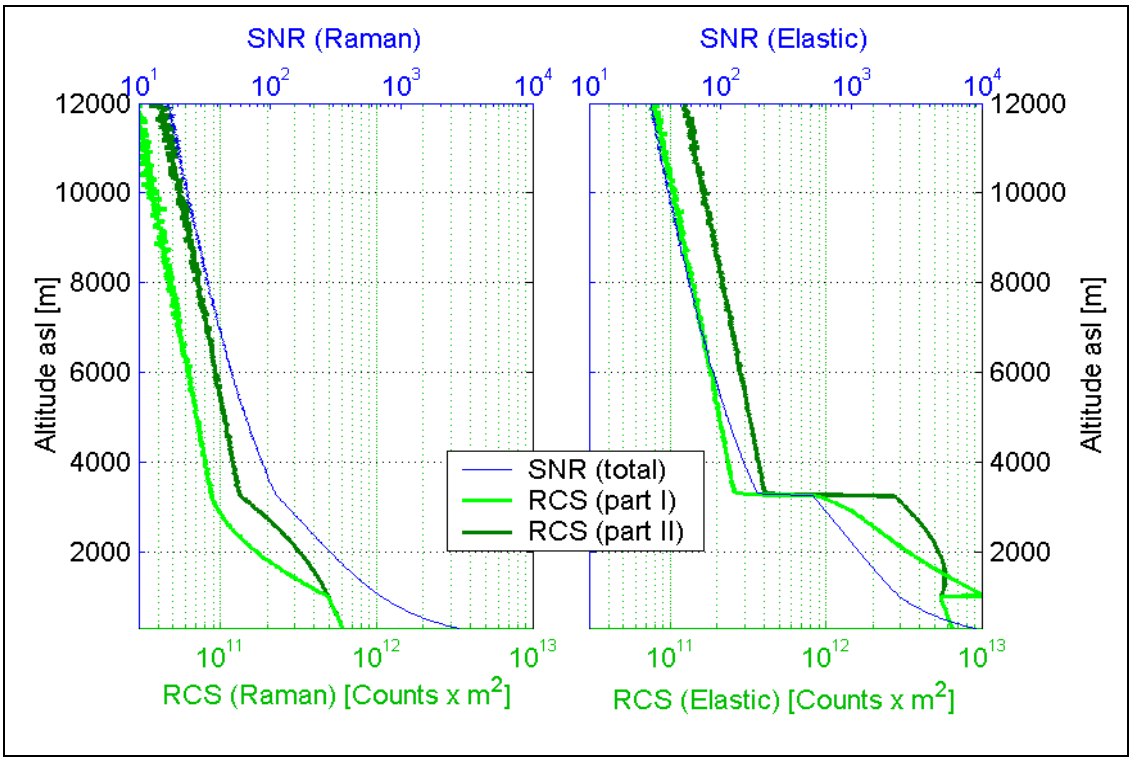


**Figure 2.32.** *EARLINET Raman simulation exercise ("case3"). The blue lines (upper scales) report the SNR of the input cumulated signal over 72000 shots (40 min). The green lines (lower scale) are the range-corrected signals for the two parts of the series of measurements (2x20 min). Left panel: Raman signals; right panel: elastic signals.*

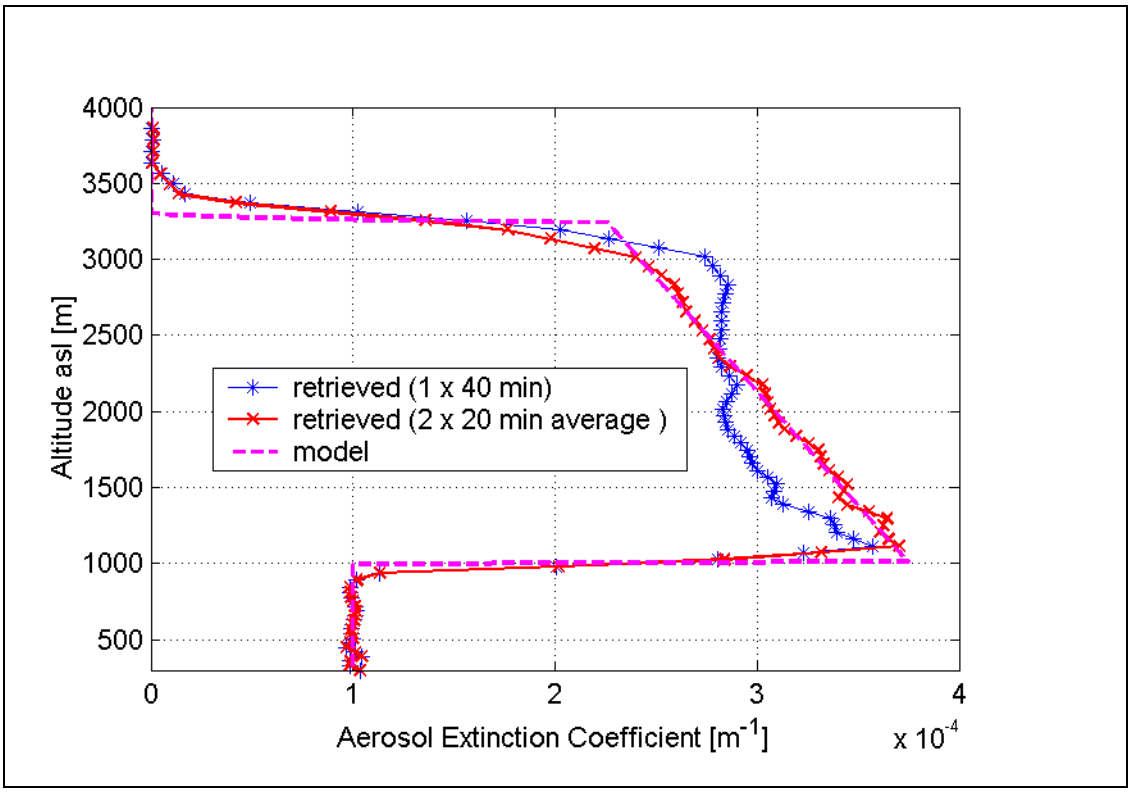


**Figure 2.33.** *EARLINET Raman simulation exercise ("case3"). Retrieved AEC profiles obtained with two procedures. The blue line (1x40 min) shows the result obtained in performing time accumulation first. The red line is obtained as the average profile from results obtained on two temporal periods with distinct atmospheric conditions (2x20 min). The model values are the average AEC value over 2x20 minutes.*

Figure 2.34 presents side by side the results of simultaneous retrievals of aerosol extinction and aerosol backscatter coefficients. Following the effect shown before, the distinct atmospheric were taken into account for both retrievals. For each sub-period of 20 min, the ABC was obtained using the elastic profile and the known AEC profile from the corresponding Raman signal. The additional following conditions were assumed:

(i) the average aerosol free conditions for ABC from 4000 to 14000 m

(ii) the retrieved AEC profiles were modified to vanish exactly above 4000 m.

These assumptions allow to determine a calibration constant for the evaluation of the total backscatter coefficient, yielding the ABC. The AEC retrieval was achieved using a variable binning with filtered signal resolution from 45 m at 300 m to 225 m at 4000 m. The ABC was retrieved using a better resolution: from 30 m at 300 m to 120 m at 10000 m (75 m at 4000 m). Since ABC and AEC were required to be defined on the same range grid, the AEC values have been interpolated.

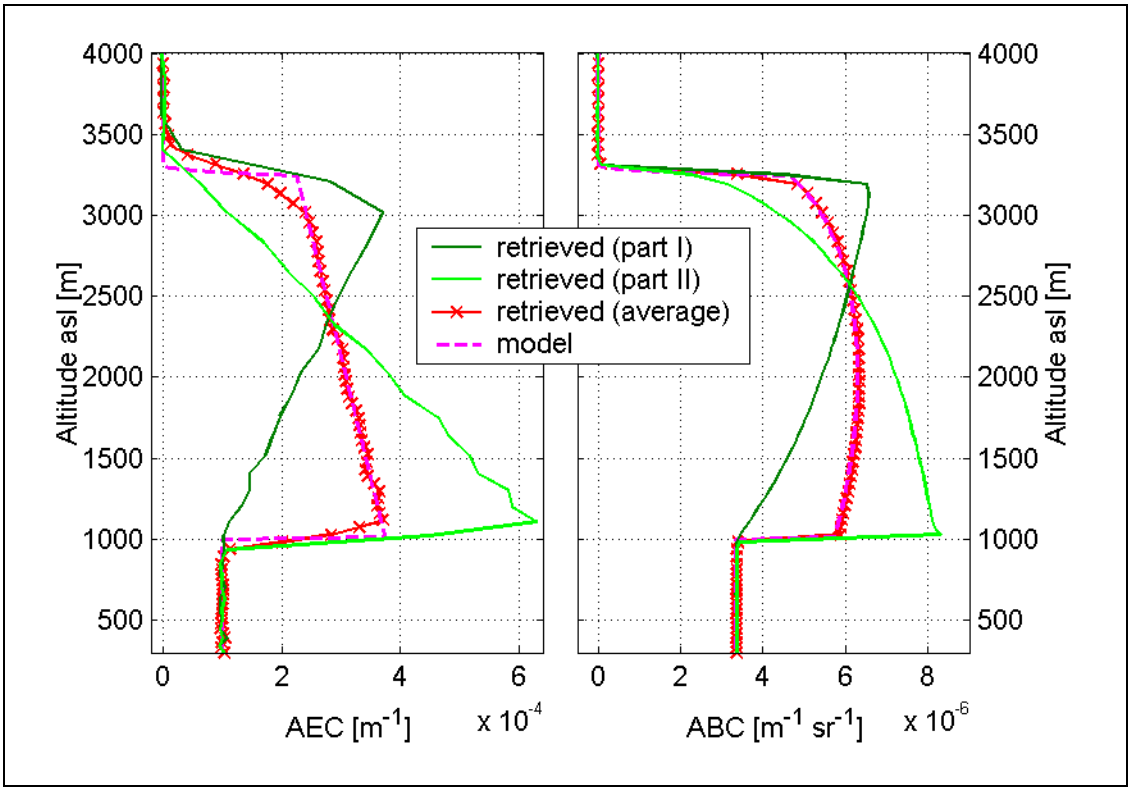


**Figure 2.34.** *EARLINET Raman simulation exercise ("case3"). Retrieved AEC and ABC profiles obtained as averaged over two periods with different atmospheric conditions (2x20 min). The model values are the average values over 2x20 minutes.*

From the above retrievals, the Lidar ratio is derived, as shown in Fig. 2.35. It reports the averaged values of Lidar ratios obtained from the distinct solutions for AEC and ABC shown in Fig. 2.34. As before, the Lidar ratio evaluation is not commutative with time averaging. As a consequence, the average Lidar ratio shown as model in Fig. 2.35 is different than the ratio of the model values of AEC to ABC from Fig. 2.34.

The results in Fig. 2.35 lead to the following conclusions:

(i) the Lidar ratio retrieval is rather good below 800 m and between 1100 to 3000 m, i.e. far from the steps areas.

(ii) at the step at 1000 m, the large errors are due to error in AEC retrieval for the second part (the filter does not reproduce such small steps).

(iii) above 3300 m, the AEC and ABC relative errors are very large. An alternative approach could be to guess the Lidar ratio a priori and improve correspondingly the AEC profile in performing an inversion. This should be done self-consistently with the calibration procedure (boundary condition for the total backscatter).

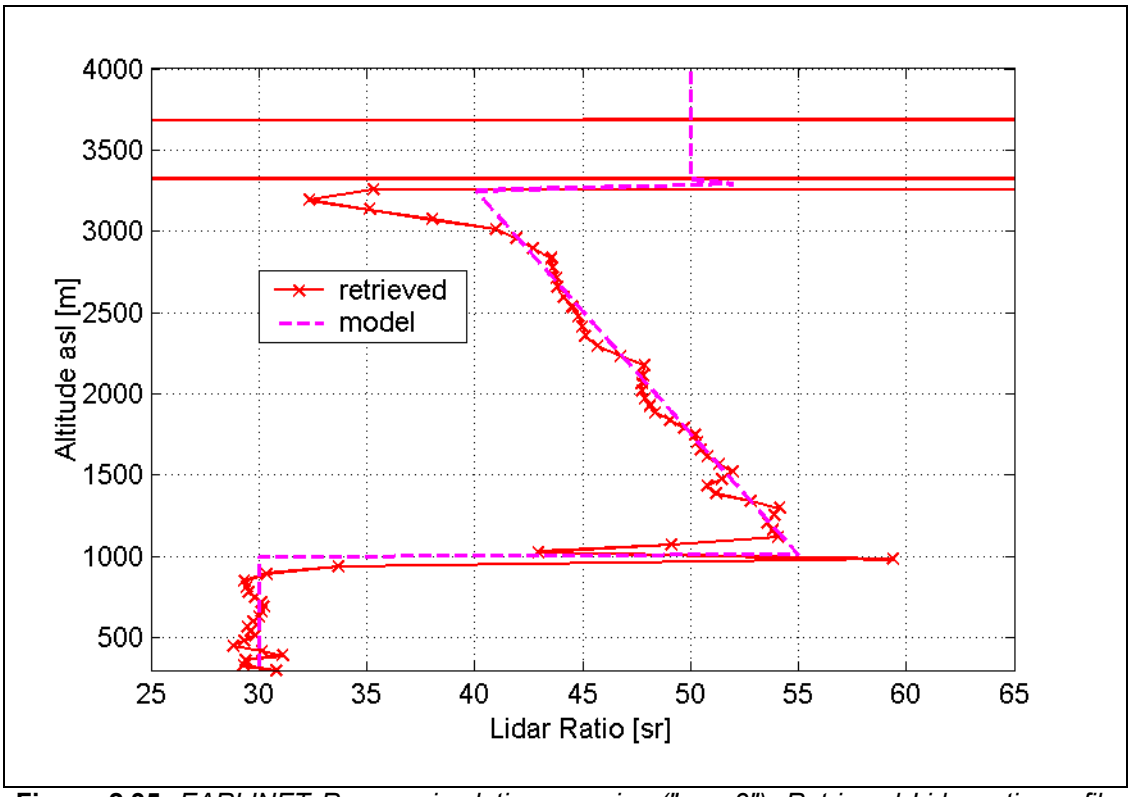


**Figure 2.35.** *EARLINET Raman simulation exercise ("case3"). Retrieved Lidar ratio profile obtained as averaged over two periods with different atmospheric conditions (2x20 min). The model value is the average value over 2x20 minutes. Values above 3300 m should be discarded.*

### 2.3.2.5 Definition of the effective resolution of the processing

The effective resolution of a process is defined on the basis of the capacity to distinguish neighboring features. In the data processing for AEC retrieval, this is achieved in applying the so-called "step method" described further.

Consider a synthetic aerosol extinction profile, defined as follow: on some range grid, the AEC vanishes everywhere except at two points where AEC values are finite and equal. The corresponding Lidar signal follows the molecular background everywhere except at the two points, where the RCS presents sharp steps.

Since we speak of processing of a noisy signal, the signal is filtered before applying (Eq 2.10). As a consequence, the retrieved AEC profile is spread over some wider range, instead of the delta-like model distribution. For some given filtering, the retrieved features from the two signal steps are more or less well distinguished depending on the distance between the steps.

The Rayleigh criterion for interference, also used in diffraction theory (see http://scienceworld .wolfram.com/physics/RayleighCriterion.html), defines a threshold for deciding whether the features (images) from two neighboring sources are resolved or not. The criterion states that the features are just resolved when the maximum of one is superimposed on the first minimum of the other. It's found that the Rayleigh criterion is fulfilled when the combined feature is such that each peak is distinguished and the minimum between the two peaks is about 75% of the average of the peaks maxima.

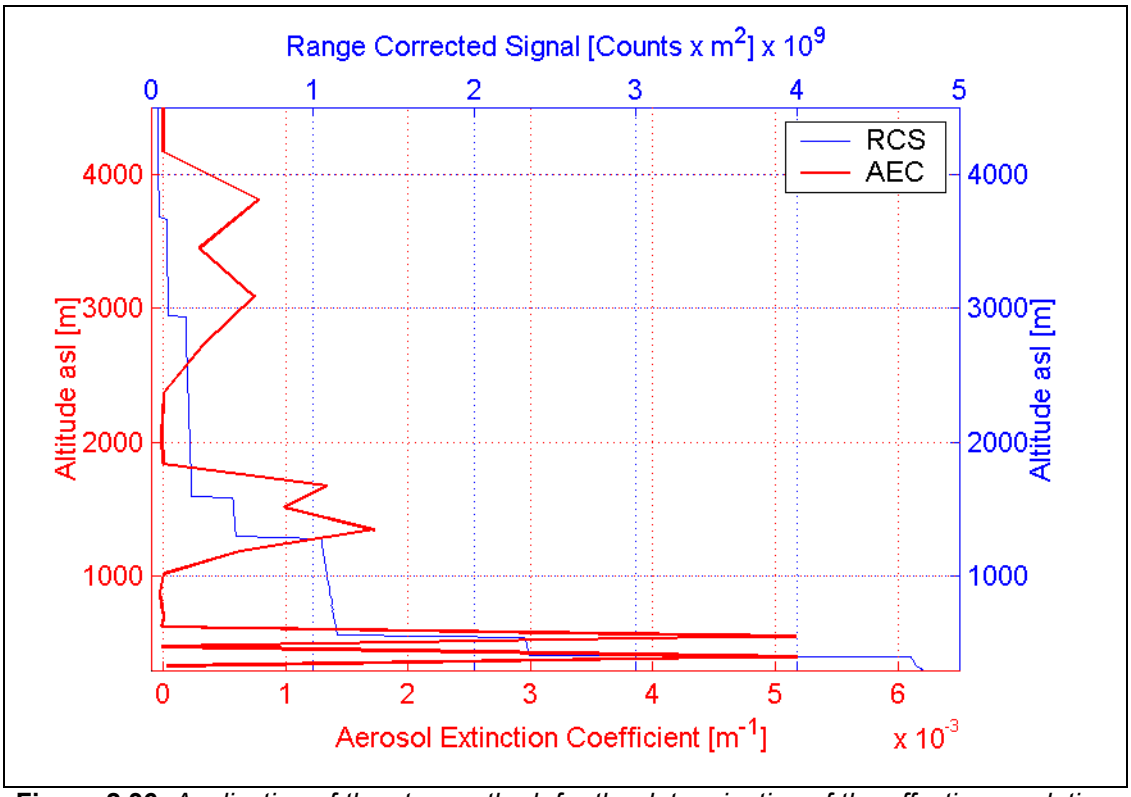


**Figure 2.36.** *Application of the step method, for the determination of the effective resolution. RCS is the range-corrected signal created with assumption of aerosol free conditions, except at the step-points. AEC is the retrieved aerosol extinction coefficient with such a filtering, that the Rayleigh criterion is fulfilled. The input signal resolution is 15 m.*

Following an agreement within EARLINET, this criterion has been retained for defining the effective resolution of any Lidar signal processing: thus, the effective resolution is that minimum distance between two steps for which the above criterion is fulfilled.

Figure 2.36 present such a simulation case, with three pairs of steps. Successive application of a signal filtering and (Eq 2.10) lead to the retrieved aerosol extinction. We applied again a binning, but with such binning numbers fulfilling the requirements on effective resolutions. Theses were respectively 150 m below 800 m, 300 m from 800 m to 2000 m and 735 m above. It was found that the resolutions of the filtered signal for reaching these above effective resolutions were respectively 75 m, 165 and 360 m. Te data resolution is seen to be about half of the effective resolution of the retrieval process. Although not a rule, this property of the binning is very useful when a given resolution is to be achieved.

# 2.4 Errors sources for ozone and water-vapor measurements in the PBL by Raman Backscatter Differential Absorption Lidar (DIAL)

## 2.4.1 Introduction

This section presents an input to a joint study with the Laboratory for Air Pollution at the Swiss Federal Institute of Technology of Lausanne (LPAS / EPFL). In this collaboration, ON is involved in the part devoted to numerical simulations of a Raman-DIAL Lidar for water-vapor and ozone measurements in the PBL.

The numerical simulations in ON reveal the influence on the measurements errors of the instrument performances and the atmospheric aerosol optical parameters, the influence of the ozone profile on the error of water vapor profile. The instrument subsystem performances were given by the group in LPAS, where the instrument was realized and operated. The results from the simulations were compared with the achieved result in a case study which is published in a joint work "Ozone and water-vapor measurements by Raman Lidar in the planetary boundary layer: error sources and field measurements", Applied Optics **40** (18), pp 2985-2997 ([*Lazzarotto et al.*, 2001]). This article is reported in Annex 1.

## 2.4.2 Determination by numerical simulation of the critical parameters for the system and for the signal processing in Raman-DIAL $O_3$ and $H_2O$ measurements

### 2.4.2.1 Raman DIAL principle

Ozone absorbs in the Hartley and Huggins bands between 220 nm and 350 nm and this affects differentially any Lidar signal in this wavelengths range [*Schoulepnikoff*, 1996]. Figure 2.37 shows a schematic of the Raman Lidar system considered here. The ozone retrieval is based only on the $N_2$ and $O_2$ Raman backscattered signals. For the water-vapor retrieval, we may use either $N_2$ and $H_2O$ or $O_2$ and $H_2O$ pairs of signals. To each of the three Raman-shifted wavelengths corresponds a Lidar equation (above full-overlap of laser beam and telescope field of view)

$$R^2 P_{SP}(R) = K_{SP} n_{SP}(R) \beta_{SP}^{Raman} \exp\left\{ -\int_o^R dr \left[ \alpha_L(r) + \alpha_{SP}(r) + n_{O_3}(r)(\sigma_L + \sigma_{SP}) \right] \right\} \quad \text{(Eq 2.14)}$$

with the following notations

Index $SP$ $N_2$, $O_2$ or $H_2O$

Index $L$ at laser wavelength $\lambda^L$

$n_{SP}$ number density of particles of species $SP$

$P_{SP}$ Raman-shifted Lidar signal power backscattered from species $SP$, at wavelength $\lambda^{SP}$

$K_{SP}$ corresponding device constant, specific at each channel ( $P_{SP} \approx K_{SP}$ )

$\beta_{SP}^{Raman}$ molecular Raman differential backscattering cross-section on species $SP$ at $\lambda^L$

$\alpha_{SP}$ atmospheric total extinction coefficient without ozone absorption at $\lambda^{SP}$

$\sigma_{SP}$ molecular ozone absorption cross-section at $\lambda^{SP}$

These three equations differ in the Raman backscattering cross-section and in the transmittance on the back travel only (ozone differential absorption). Differential absorption from other trace gases is not considered here. Then the ozone number density is deduced in combining the two Raman signals from $N_2$ and $O_2$ as follow

$$n_{O_3}(R) = \frac{\frac{d}{dR}(S_{N_2}(R) - S_{O_2}(R)) - \left[\alpha_{O_2}(R) - \alpha_{N_2}(R)\right]}{\sigma_{O_2} - \sigma_{N_2}} \qquad \text{(Eq 2.15)}$$

where $S_{SP} = \log(R^2 \cdot P_{SP})$.

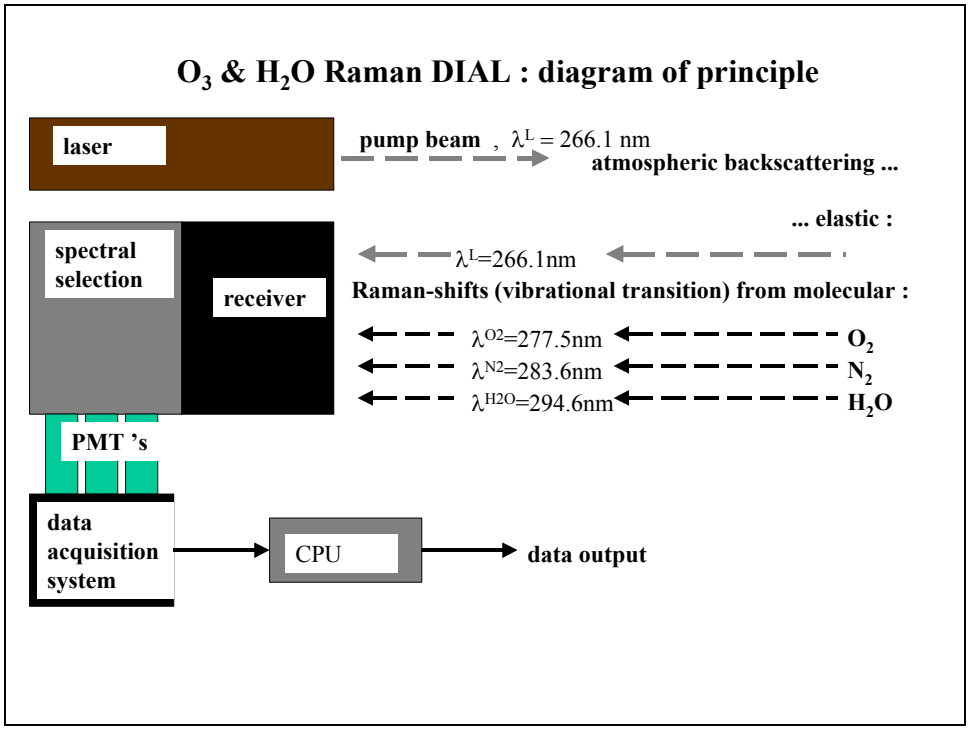


**Figure 2.37.** *Principle of Raman DIAL for simultaneous measurement of ozone and water-vapor, using a single laser wavelength.*

The water-vapor number density is obtained from the ratio of the $H_2O$ Raman shifted signal to either the Raman $N_2$ or Raman $O_2$ shifted signal. Using the $N_2$ Raman channel, this yields the following expression

$$n_{H_2O}(R) = n_{N_2}(R)\frac{K_{N_2}}{K_{H_2O}}\frac{P_{H_2O}(R)}{P_{N_2}(R)}\frac{\beta_{N_2}^{Raman}}{\beta_{H_2O}^{Raman}}\exp\left\{-\int_o^R dr\left[(\alpha_{N_2}(R) - \alpha_{H_2O}(R)) + n_{O_3}(r)(\sigma_{N_2} - \sigma_{H_2O})\right]\right\} \qquad \text{(Eq 2.16)}$$

Usually, the ozone is expressed as a (number) mixing ratio in [ppbv], i.e. it is evaluated as the ratio of $n_{O_3}$ to the (molecular) air number density $N_{air}$ (see Eq 1.48). The water-vapor content is more frequently expressed as a mass mixing ratio $r$ (as in Eq 1.37a): it is the ratio of the mass of water-vapor to the mass of dry air, and its usual unit is [[g] of water vapor/[kg] of dry air]. Considering 1 mol of mixture containing $x_{H_2O}$ mol of water-vapor, the water-vapor mixing ratio is given as $r = \frac{18}{28.966}\frac{x_{H_2O}}{(1 - x_{H_2O})}$, where we used the molecular weights. At an absolute temperature $T$ and pressure $p$, $x_{H_2O}$ is linked to the water-vapor number density $n_{H_2O}$ through $x_{H_2O} = \frac{n_{H_2O} \cdot V_A}{N_A}\frac{p_0}{T_0}\frac{T}{p}$, where $N_A$ is the Avogadro's number, $V_A$ (0.022414 $m^3$) is the volume of 1 mol of gas following Avogadro's law at the pressure $p_0$ (1013.25 hPa) and temperature $T_0$ (273.15 K).

The possibility of using either the Raman $N_2$ or the Raman $O_2$ in (Eq 2.16) gives an additional test of the consistency of the water-vapor result. Note that in (Eq 2.16) the water-vapor retrieval depends linearly upon the ratio of the Raman $H_2O$ signal to the Raman $N_2$ signal, while on the contrary in (Eq 2.15) the ozone retrieval

depends upon the first derivative of the ratio of two Raman Lidar signals ($N_2$ and $O_2$). We shall see that the different predicted error sources on ozone and respectively water-vapor will strongly depend on this point.

As the ozone retrieval does not depend on the instrument constant $K_{SP}$, the method can be regarded as self-calibrated. In contrast, for absolute water-vapor measurements the exact knowledge of $K_{SP}$ or independent parallel measurements for instrument calibration are needed. The term $n_{O_3}(r)(\sigma_{N_2} - \sigma_{H_2O})$ in the exponential part of (Eq 2.16), known as "ozone correction term", reflects the ozone influence on the $H_2O$ and $N_2$ Raman.

Table 2.5 reports some spectroscopic values of the Raman processes involved in the measurement process depicted in Fig. 2.37 and assumed in the present simulations.

**Table 2.5.** *Spectroscopic data of the Raman processes* on *$O_2$, $N_2$ and $H_20$, for a laser wavelength of 266 nm, and $O_3$ absorption cross-sections.*

| Molecule | O2 | N2 | H2O |
|---|---|---|---|
| Raman wavelength [nm] | 277.5 | 283.6 | 294.6 |
| Molecular Raman differential backscattering cross-section. [$10^{-30}$ $cm^2$/sr] | 23.3 | 10.7 | 33.3 |
| Molecular Ozone absorption cross-section at Raman wavelength [$10^{-20}$ $cm^2$] | 490.6 | 296.3 | 81.93 |

The integrated ozone content can be obtained by combining again $P_{O_2}$ and $P_{N_2}$

$$\exp\left\{\int_0^R n_{O_3}(r)dr\right\} = \left(\frac{P_{O_2}}{P_{N_2}}(R)\right)^{\frac{1}{\sigma_{N_2}-\sigma_{O_2}}} \left(\frac{K_{N_2}}{K_{O_2}}\frac{n_{N_2}}{n_{O_2}}(R)\frac{\beta_{N_2}^{Raman}}{\beta_{O_2}^{Raman}}\right)^{\frac{1}{\sigma_{N_2}-\sigma_{O_2}}} \quad \text{(Eq 2.17)}$$

Together with (Eq 2.16), this yields

$$\frac{n_{H_2O}}{n_{N_2}}(R) = \frac{P_{H_2O}}{P_{N_2}}(R)\frac{K_{N_2}}{K_{H_2O}}\frac{\beta_{N_2}^{Raman}}{\beta_{H_2O}^{Raman}}\left(\frac{K_{N_2}}{K_{O_2}}\frac{n_{N_2}}{n_{O_2}}(R)\frac{\beta_{N_2}^{Raman}}{\beta_{O_2}^{Raman}}\right)^{\frac{\sigma_{H_2O}-\sigma_{N_2}}{\sigma_{N_2}-\sigma_{O_2}}}\left(\frac{P_{O_2}}{P_{N_2}}(R)\right)^{\frac{\sigma_{H_2O}-\sigma_{N_2}}{\sigma_{N_2}-\sigma_{O_2}}} \quad \text{(Eq 2.18)}$$

Using the constant ratio of molecular $N_2$ to $O_2$ densities, this yields

$$\frac{n_{H_2O}}{n_{N_2}} = K_{cal}\frac{P_{H_2O}(R)}{P_{N_2}(R)}\left[\frac{P_{O_2}(R)}{P_{N_2}(R)}\right]^{\frac{\sigma_{H_2O}-\sigma_{N_2}}{\sigma_{N_2}-\sigma_{O_2}}} \quad \text{(Eq 2.19)}$$

where the factor $K_{cal}$ is an overall calibration constant. According to [*Renault et al.*, 1980], the molecular and aerosol differential extinction do not produce any significant error in water-vapor determination following this procedure.

## 2.4.2.2 Relation between elastic and Raman backscatter signals

Figure 2.38 presents an example of simulation of the four backscattered signals, i.e. the elastic signal (266 nm) and the three Raman signals (from $N_2$, at 283.6 nm, $O_2$ at 277.5 nm and $H_2O$ at 294.6 nm), for which the same device characteristics are used for all channels. Here, a relatively low aerosol load (constant scattering ratio of 1.1 and constant Lidar ratio 60 sr), medium ozone mixing ratio (60 ppbv) and water-vapor mass mixing ratio following the US-76 atmosphere have been assumed. The essential emerging features are

(i) the elastic signal is typically 3-4 orders of magnitude higher than the Raman signals from $N_2$ or $O_2$.
(ii) the Raman signal from $H_2O$ is typically 1 order of magnitude lower than the $O_2$ or $N_2$ return.
(iii) all RCS decrease by one order of magnitude over 1000 m range.

Point (i) is just the consequence of the low Raman scattering cross-sections. Point (ii) is mainly due to the relation among the molecular densities of $N_2$, $O_2$ and $H_2O$ and their respective Raman cross-sections. Point (iii) is characteristic of the wavelength domain: neglecting the absorption, the molecular extinction is about 16 times bigger than at 532 nm (as in section 2.2), yielding correspondingly higher signal dynamics due to the different behavior of the optical transmission.

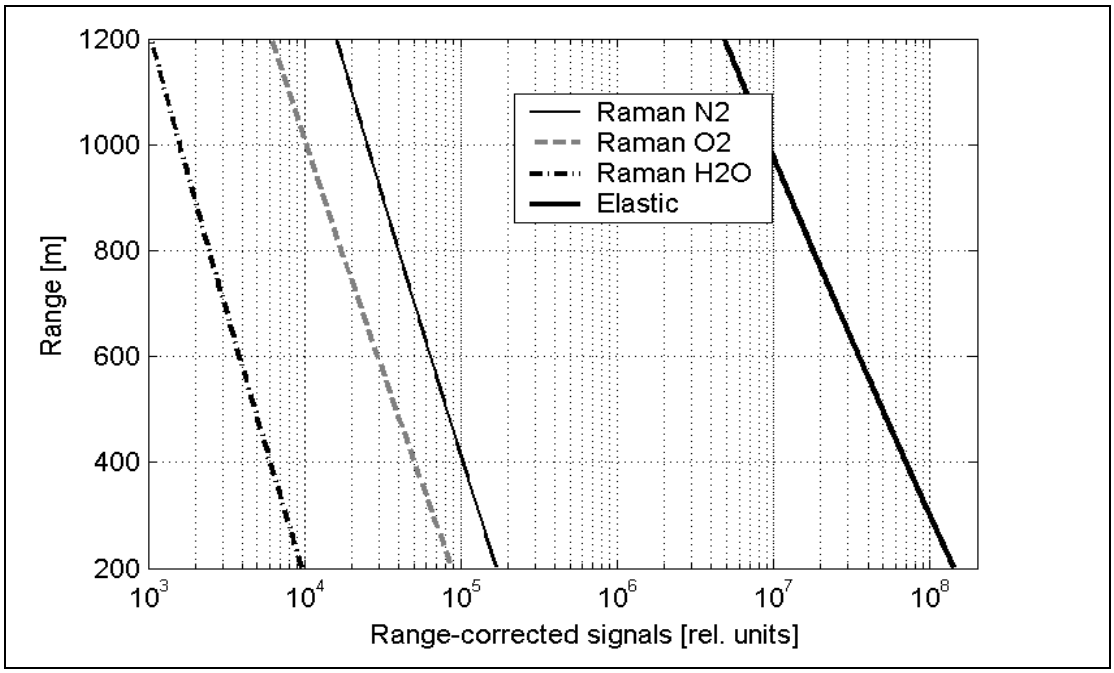


**Figure 2.38.** *Simulated elastic and Raman signals (range-corrected). Constant ozone mixing ratio (60 ppbv), aerosol scattering ratio (1.1) and Lidar ratio (60 sr) are assumed. (the range is the altitude agl (station at 400 m asl)).*

## 2.4.2.3 General conditions of the numerical simulations

Table 2.6 reports the Lidar characteristics used in all subsequent simulations. The Lidar station altitude was set to 400 m asl. A unique model of water-vapor profile, reported in Fig. 2.39, was assumed. Profiles of ozone, aerosol backscatter and Lidar ratio (at 266 nm) were adapted to different conditions. Results are presented up to a maximum range of only 1200 m agl (see timeseries in Annex 1). As in the section 2.3, we shall assume a wavelength dependency of the aerosol extinction following an Angstroem law (Eq 2.9). Following previous work ([*Sunesson et al.*, 1994]), typical exponent values $k$ in the UV are in the range 0.5-1.

The choice of additional specific device parameters as inputs of these simulations, like the optical cross-talks between the different channels, was given by the group of LPAS.

**Table 2.6.** *Device specifications for all the simulations of Raman DIAL.*

| | |
|---|---|
| Laser pulse energy | 120 mJ |
| Pulse repetition rate | 20 Hz |
| Telescope diameter | 20 cm |
| Transmitter efficiency | 90% |
| Receiver efficiency | 20% |
| Quantum efficiency | 10% |
| PMT gain | 100000 |
| PMT excess noise factor | 2 |
| Equivalent resistance output circuit | 50 Ω |
| Full overlap range | 200 m |

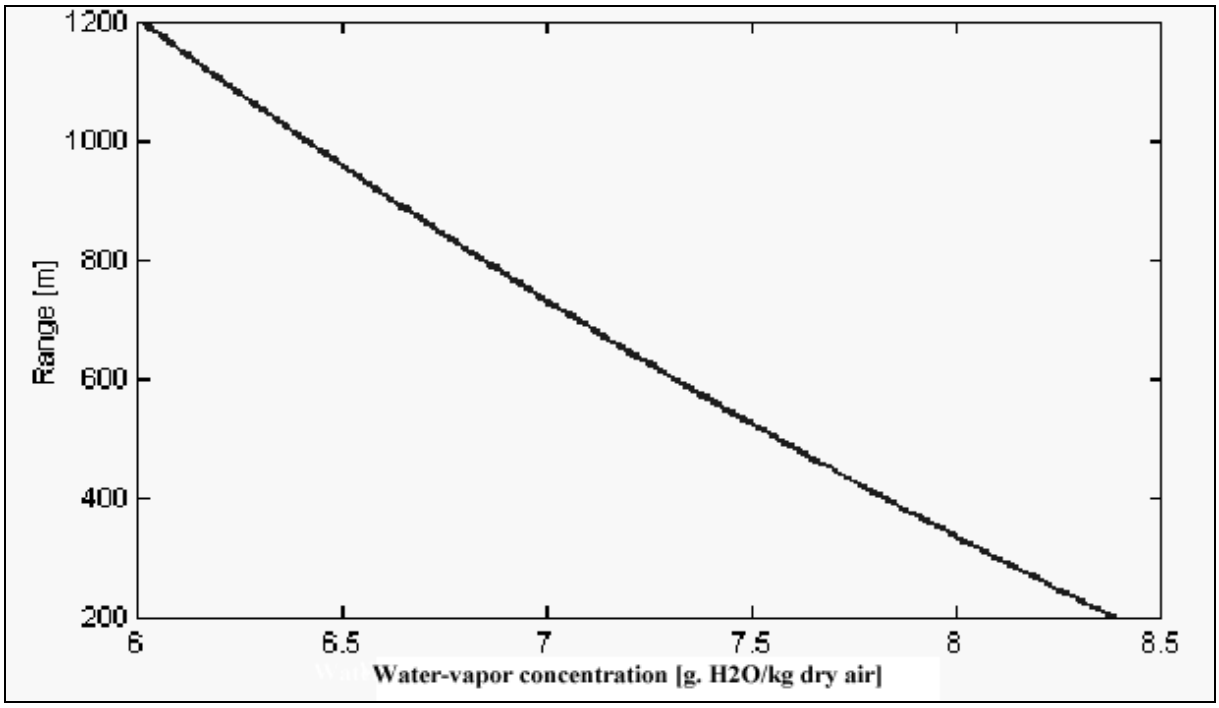


**Figure 2.39.** *Assumed water-vapor model profile in all Raman-DIAL simulations (the range is the altitude agl).*

## 2.4.2.4 Correction term for the unknown differential aerosol extinction

The term containing the difference of extinction in (Eq 2.15) depends also on the aerosol extinction profile at the two Raman shifted wavelengths. These profiles appear here as additional unknowns. Let's first evaluate the corresponding term for the molecular contribution, using the Rayleigh wavelength–dependence for the extinction. One obtains the following (negative) correction to the ozone relative content

$$\Delta^{mol} = \frac{\alpha_{O_2}^{mol} - \alpha_{N_2}^{mol}}{N_{air}(\sigma_{O_2} - \sigma_{N_2})} \qquad \text{(Eq 2.20)}$$

where $N_{air}$ is the (molecular) air number density. As the numerator in (Eq 2.17) is also directly depending upon the air density (the number densities $n_{O_2}$ and $n_{N_2}$ appearing in constant ratio), $\Delta^{mol}$ is an altitude independent value. This yields a correction of about -3 ppbv. Using the Angstroem law, the corresponding expression for the aerosol

$$\Delta^{aer} = \frac{\alpha_{O_2}^{aer} - \alpha_{N_2}^{aer}}{N_{air}(\sigma_{O_2} - \sigma_{N_2})} \qquad \text{(Eq 2.21)}$$

is evaluated as follow

$$\frac{\Delta^{aer}}{\Delta^{mol}} = \left(\lambda^{L}\right)^{-(4-k)} \frac{\left(\lambda^{O_2}\right)^{-k} - \left(\lambda^{N_2}\right)^{-k}}{\left(\lambda^{O_2}\right)^{-4} - \left(\lambda^{N_2}\right)^{-4}} \cdot \left(\frac{lr \cdot (scr - 1)}{c^{rayl}}\right) \qquad \text{(Eq 2.22)}$$

where $c^{rayl} = \frac{8\pi}{3}$ is the molecular Lidar ratio (Rayleigh), $lr$ is the aerosol Lidar ratio and $scr$ is the total scattering ratio.

Figure 2.40 reports model profiles of ozone, total extinction and backscattering: the Lidar ratio was taken as constant (80 sr) but the scattering ratio variable with height, with a maximum value of 1.8 (large value for 266 nm). The corresponding shifts of ozone mixing ratio $\Delta^{aer}$ (overestimate without correction), is reported in Fig. 2.41. A maximum relative error of approximately 8% is expected (with $k$=1). Under similar conditions, the

simulation shows that the effect of neglecting the same correction in the integrand of (Eq 2.16) yields an increasing overestimate of the retrieved water-vapor, but with a relative error of only 1.3% at 1000 m.

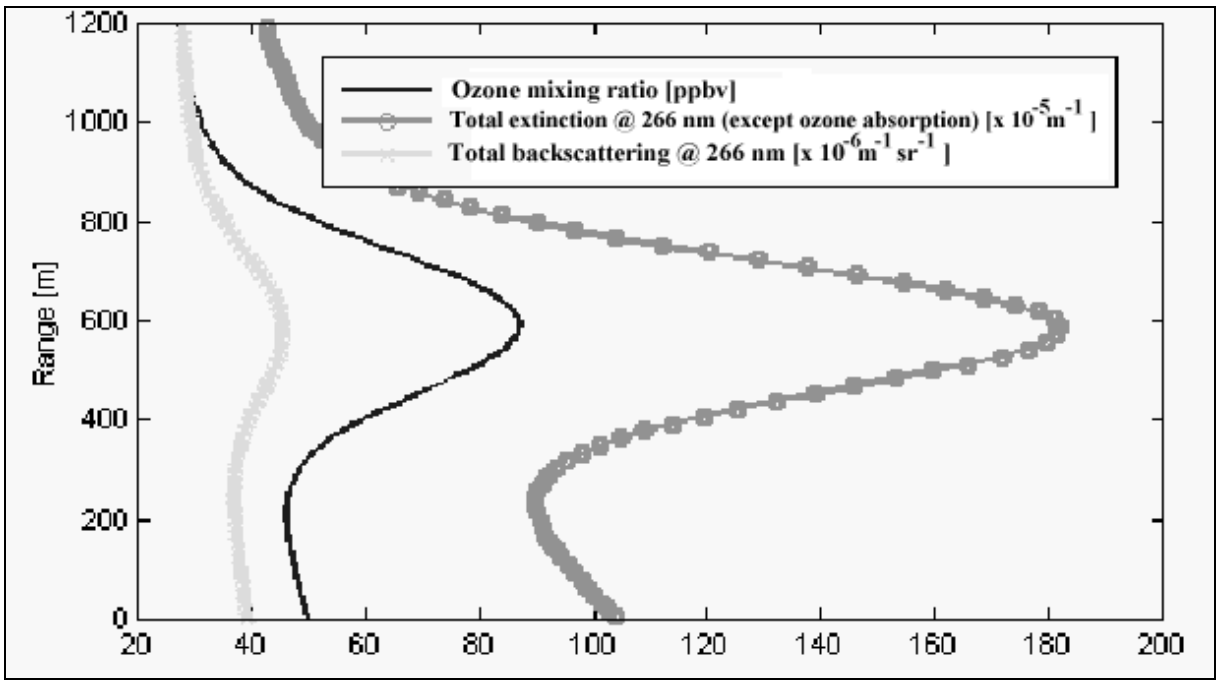


**Figure 2.40.** *Model profiles of ozone mixing ratio, total extinction (without ozone absorption) and total backscatter at 266 nm, for testing the impact of the aerosol on the ozone retrieval (the range is the altitude agl).*

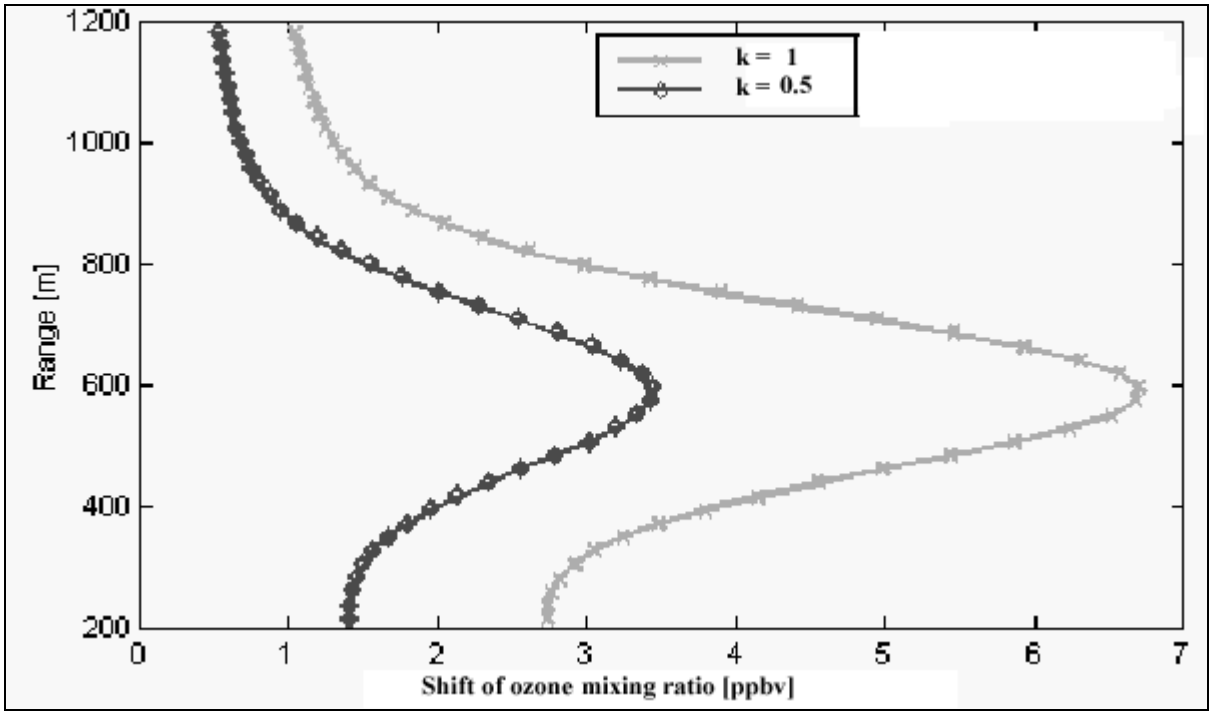


**Figure 2.41.** *Shift of ozone mixing ratio due to the aerosol differential extinction, following the model profiles in Fig. 2.40, for two values of Angstroem exponent for the aerosol extinction. The horizontal scale indicates the difference between the retrieved ozone without accounting for the differential aerosol extinction to the retrieved profile accounting for it (the range is the altitude agl).*

### 2.4.2.5 Ozone interference on water-vapor Raman Lidar retrieval

The effect of the ozone absorption on the water-vapor retrieval defined in (Eq 2.16) was simulated using a model atmosphere with different constant values of the ozone mixing ratio, and an aerosol load with constant scattering ratio ( $scr = 1.8$ ) and Lidar ratio ( $lr = 80$ ). The result of this effect is reported in Fig 2.42: the shifts in water-vapor mass mixing ratio ( $\Delta H_2 0$ ) is the difference between the water-vapor retrieval without ozone interference (i.e. neglecting the "ozone correction term") with respect to the same retrieval corrected for the ozone absorption effect. The correction values are set to 0 [(g of $H_2O$)/(kg of dry air)] at the full overlap (calibration). This simulation shows that even for moderate ozone mixing ratios of 40 ppbv the relative errors are of several tens of percents.

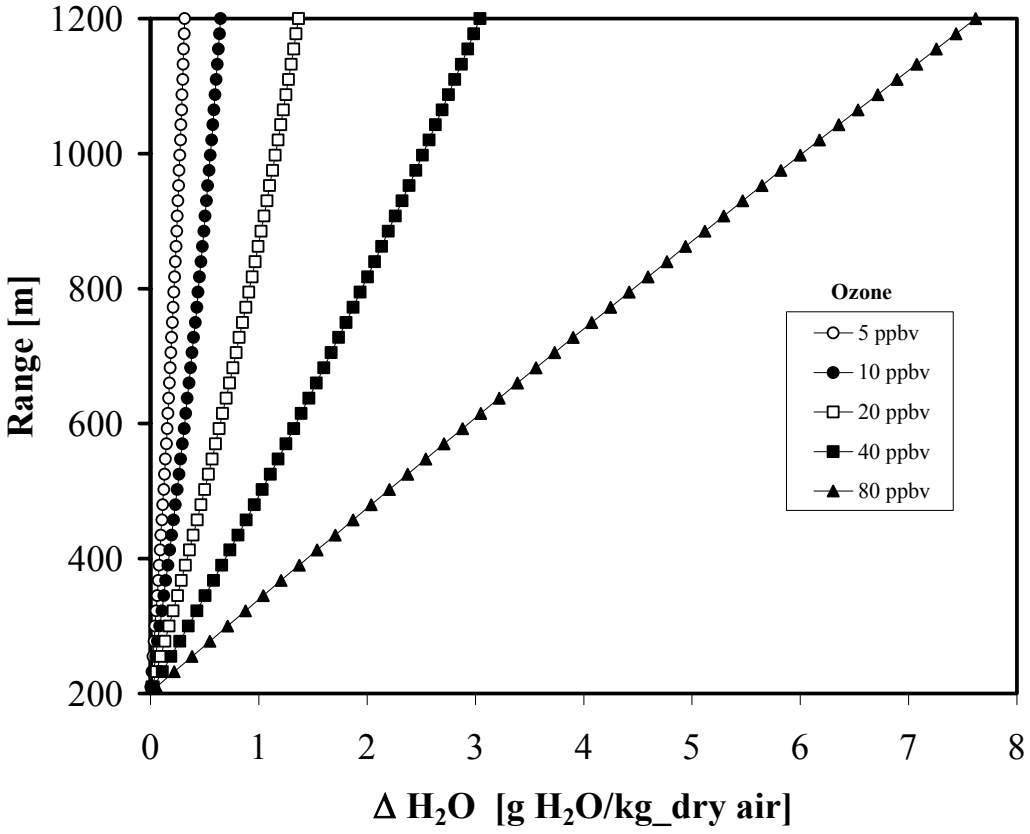


**Figure 2.42.** *Effect of ozone correction: predicted error on the water-vapor mass mixing ratio retrieved by Raman Lidar due to different ozone constant vertical profile and an homogeneous aerosol load. The horizontal scale is the difference between the water-vapor retrieval without taking into account the ozone absorption and the same retrieval with ozone absorption.*

## 2.4.2.6 Statistical (quantum) noise

The statistical noise is a major perturbation in Raman Lidar measurements due to the low level of the Raman signals. As before, the statistical noise has been modeled following the Poisson statistics (Eq 2.7) with the parameters defined in Table 2.6. In this case the model study was performed in a pure molecular atmosphere (with ozone): this yields a threshold for optimum conditions. Based on typical experimental values, we estimate a number of photo-electrons per pulse at the photo-cathode, from a distance of 200 m and for a range resolution of 7.5 m, of some hundreds for both $N_2$ and $O_2$ Raman Lidar signals and some tens for $H_2O$. This simulation was achieved in performing a series of 100 runs for each similar initial conditions. This yields the standard deviation with respect to the mean value, as reported in Figs. 2.43a-b.

Figure 2.42a shows the ozone standard deviation due to the effect of the statistical noise on the retrieved ozone mixing ratio for three profiles with constant ozone mixing ratios of respectively 0, 40 and 80 ppbv. These results are achieved averaging over 5 files of 4'000 laser shots as defined in Table 2.5, and performing a binning of 90 m.

Since the presence of ozone itself lowers significantly the Raman signals through absorption, higher ozone values directly induce greater statistical error. The results in Fig. 2.43a indicate that on one hand an average over at least 20'000 shots is needed for a suitable ozone Raman DIAL retrieval. This means that for a laser source with 20 Hz repetitions rate the averaging time will be 20 min. On the other hand above an altitude range of typically 700 m agl the error source due to the statistical noise is reaching a value higher than 5% of the measured ozone mixing ratio in the case of a constant profile with 80 ppbv. Note that even in absence of ozone the statistical noise affecting the $O_2$ and $N_2$ Raman signals already induces an ozone standard deviation. From this simulation of the statistical noise only, one may conclude that the maximum achievable range for ozone with this Raman DIAL system will be on the order of 700 m above the Lidar site with a spatial resolution of 90 meters, a time resolution of 30 min, and a precision due to the statistics of ± 5% for a typical ozone mixing ratio of 80 ppbv in the atmosphere.

A similar statistical analysis is performed for the water-vapor mass mixing ratio retrieval. Results are reported in Fig. 2.43b, where again the three constant ozone profiles are considered (0, 40, and 80 ppbv). In this case the range resolution is set at 22.5 m and reasonable water-vapor estimates are predicted for an altitude range up to 1'200 m agl. Note that the standard deviation is calculated for a water-vapor mass mixing ratio with reference value given at 200 m agl (calibration). In comparison with the results obtained for ozone, at 700 m agl the water-vapor standard deviation in an atmosphere containing 80 ppbv of ozone is less than 1% of the mean water-vapor mass mixing ratio. This better result is directly due to the linear dependence of (Eq 2.16) in the water-vapor retrieval that is less sensitive to the statistical error than in the case of the ozone Raman differential analysis. Here one may conclude that the Raman Lidar instrument will give an estimate of the water-vapor mass mixing ratio in the atmosphere with an accuracy of better than 2% (statistical noise only) for an altitude range of 1'200 m above the Lidar site, a spatial resolution of 22.5 m and a time resolution of 30 min.

## 2.4.2.7 Optical cross-talk between the various detection channels

The proportion of the mutual intrusion of signal between the Raman-shifted signals depends on the spectral selection performance (see technical details in Annex 1). Since the elastic signal is typically four orders of magnitude bigger than the Raman returns from $O_2$ or $N_2$, a very small amount of intrusion of the elastic signal into the Raman channels affects considerably the detected signals.

For these simulations, the cross-talk between any two channels is included in considering a mutual exchange of the backscattered signals $P_i$. For some given cross-talk level $ctl$, the effect is reproduced in performing following operation

$$P_i \rightarrow (1 - ctl)P_i + ctl \cdot P_j \quad \text{(i,j = 1,2 cyclically)} \qquad \text{(Eq 2.23)}$$

All results reported here were performed with a model atmosphere with constant ozone mixing ratio (80 ppbv) and an aerosol profile with constant scattering ratio ( $scr = 1.8$ ) and Lidar ratio ( $lr = 80$ ).

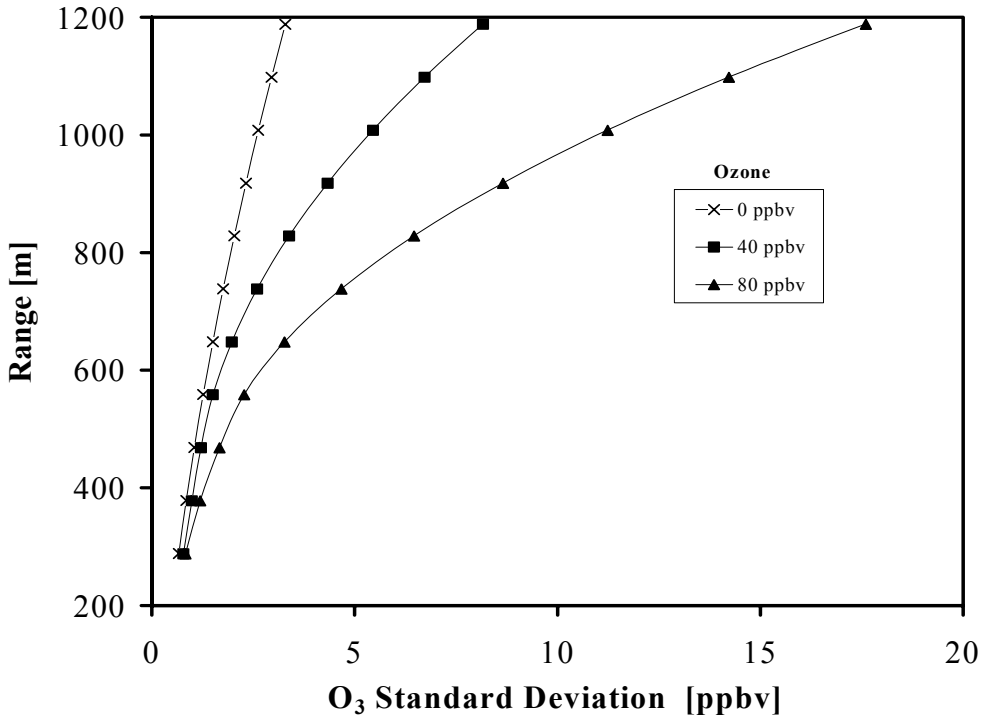


**Figure 2.43 (a)**

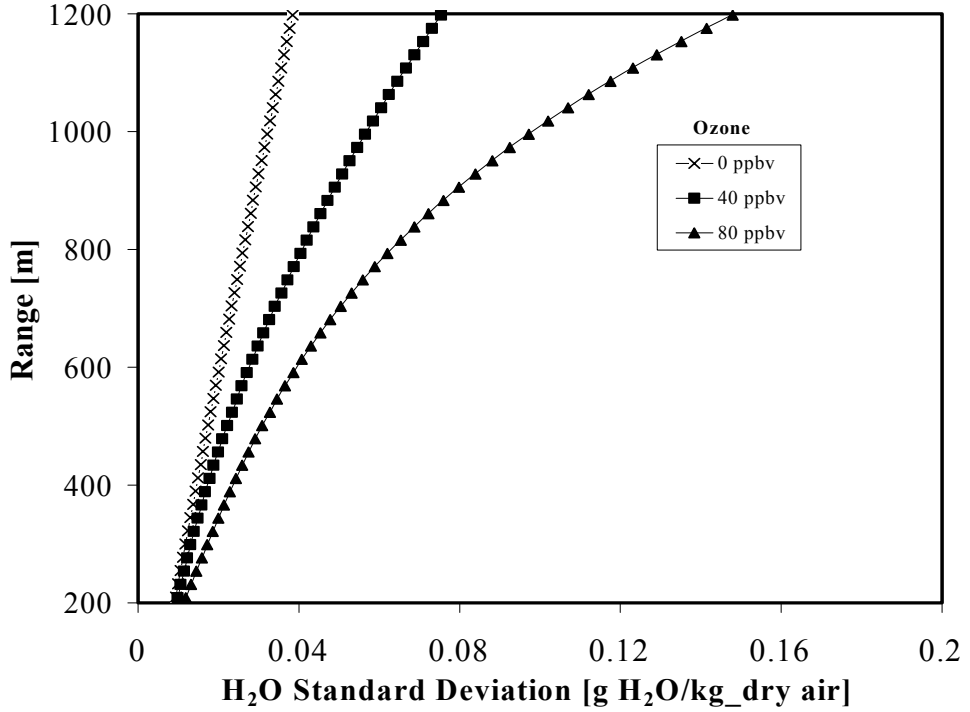


**Figure 2.43 (b)**

**Figures 2.43.** *Predicted standard deviation for ozone mixing ratio (a) and water-vapor mass mixing ratio (b) by Raman Lidar, due to the signal shot noise for 20000 shots with the experimental parameters defined in Table 2.6.*

### *(a) Effect of cross-talk between Raman channels*

Let us consider first the cross-talk between the Raman signals. The cross-talk between Raman $N_2$ and $O_2$ channels is biasing the ozone retrieval, following (Eq 2.15). Results are reported in Table 2.7, for some orders of magnitude of cross-talk levels. The relative shifts in ozone mixing ratio are seen to be very small.

Table 2.8 reports the effect of the cross-talk between all three Raman channels, for the water-vapor retrieval using (Eq 2.16) but with $O_2$ Raman signals instead of $N_2$. These simulations results are also shown in Fig. 2.44. As in §2.4.2.5, a calibration assures no shifts at 200 m. As for the previous case, the shifts are seen to be almost linear versus the cross-talk level for the chosen range of cross-talk level. The increasing values with range appear as a consequence of the relatively smaller water-vapor Raman signal (one order of magnitude lower than any of the two other Raman signals), more affected in the upper part of the altitude range.

**Table 2.7.** *Shift in ozone mixing ratio [ppbv], due to a cross-talk between the Raman $N_2$ and $O_2$ channels. Values are the difference between retrieved ozone without cross-talk effect to the one with cross-talk effect.*

| Altitude agl [m] | $ctl = 10^{-6}$ | $ctl = 10^{-5}$ | $ctl = 10^{-4}$ | $ctl = 10^{-3}$ |
|---|---|---|---|---|
| 200 | 0.000227 | 0.00227 | 0.0227 | 0.227 |
| 400 | 0.000241 | 0.00241 | 0.0241 | 0.241 |
| 600 | 0.000257 | 0.00257 | 0.0257 | 0.256 |
| 800 | 0.000274 | 0.00274 | 0.0274 | 0.274 |
| 1000 | 0.000293 | 0.00293 | 0.0293 | 0.293 |
| 1200 | 0.000314 | 0.00314 | 0.0314 | 0.313 |

**Table 2.8.** *Shift in water-vapor mass mixing ratio [(g of $H_2O$)/(kg of dry air)], due to a cross-talk between the Raman $H_2O$ and $O_2$ channels. Values are the difference between retrieved water-vapor without cross-talk effect to the one with cross-talk effect.*

| Altitude agl [m] | $ctl = 10^{-6}$ | $ctl = 10^{-5}$ | $ctl = 10^{-4}$ | $ctl = 10^{-3}$ |
|---|---|---|---|---|
| 200 | 0 | 0 | 0 | 0 |
| 400 | 0.00000677 | 0.0000677 | 0.000677 | 0.00670 |
| 600 | 0.0000114 | 0.000114 | 0.00114 | 0.0113 |
| 800 | 0.0000143 | 0.000143 | 0.00143 | 0.0141 |
| 1000 | 0.0000159 | 0.000159 | 0.00159 | 0.0157 |
| 1200 | 0.0000165 | 0.000165 | 0.00165 | 0.0163 |

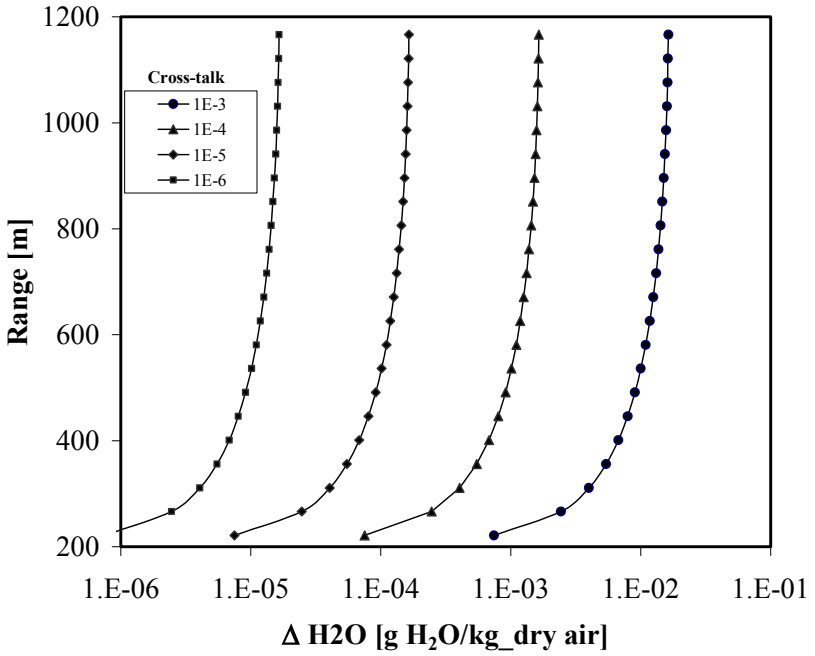


**Figure 2.44.** *Predicted error on water-vapor mass mixing ratio Raman Lidar retrieval due to the optical cross-talk between $H_2O$ and $O_2$ Raman signals. The horizontal scale is the difference between the water-vapor mass mixing ratio retrieval without cross-talk effect and the same retrieval biased by the cross-talk effect.*

***(b) Effect of cross-talk between the elastic and the Raman channels***

As seen in §2.4.2.2, the elastic signal is about 3 to 4 orders of magnitude higher than the Raman signals. Thus, a very powerful spectral rejection system is needed to avoid intrusion of the elastic signal into the Raman signals. Tables 2.9 and 2.10 report the effects of a single cross-talk level between the elastic and all Raman signals. Cross-talk values from $10^{-9}$ to $10^{-6}$ are considered. As previously, the shifts are seen to be linear function of the cross-talk level in the range considered.

**Table 2.9.** *Shift in ozone mixing ratio [ppbv], due to a cross-talk between the elastic signal and any of the Raman channels. Values are the difference between retrieved ozone without cross-talk effect to the one with cross-talk effect.*

| Altitude agl [m] | $ctl = 10^{-9}$ | $ctl = 10^{-8}$ | $ctl = 10^{-7}$ | $ctl = 10^{-6}$ |
|---|---|---|---|---|
| 200 | -0.000153 | -0.00153 | -0.0153 | -0.152 |
| 400 | -0.000153 | -0.00153 | -0.0153 | -0.152 |
| 600 | -0.000145 | -0.00145 | -0.0145 | -0.145 |
| 800 | -0.000134 | -0.00134 | -0.0134 | -0.134 |
| 1000 | -0.000121 | -0.00121 | -0.0121 | -0.121 |
| 1200 | -0.000108 | -0.00108 | -0.0108 | -0.108 |

**Table 2.10.** *Shift in water-vapor mass mixing ratio [(g of $H_2O$)/(kg of dry air)], due to a cross-talk between the elastic signal and any of the Raman channels. Values are the difference between retrieved $H_2O$ without cross-talk effect to the one with cross-talk effect.*

| Altitude agl [m] | $ctl = 10^{-9}$ | $ctl = 10^{-8}$ | $ctl = 10^{-7}$ | $ctl = 10^{-6}$ |
|---|---|---|---|---|
| 200 | 0 | 0 | 0 | 0 |
| 400 | 0.0000536 | 0.000535 | 0.00535 | 0.0523 |
| 600 | 0.0000856 | 0.000856 | 0.00852 | 0.0835 |
| 800 | 0.0001033 | 0.001033 | 0.01030 | 0.1008 |
| 1000 | 0.0001121 | 0.001121 | 0.01119 | 0.1095 |
| 1200 | 0.0001155 | 0.001155 | 0.01153 | 0.1128 |

## 2.4.2.8 Effect of PMT afterpulses

Another instrumental effect that may strongly alter the real Lidar return signal is the after pulse effect (APE) of the receiving photomultiplier ([*Sunesson et al.*, 1994]). The after-pulses caused by internal processes within the PMT appear as secondary pulses that follow the genuine pulse. The APE occurs mostly within 1-2 μs after the main pulse ([*Coates*, 1973 A]).

The time delay, the duration and the shape of the after-pulse depend on the ions involved and the PMT configuration ([*Coates*, 1973 B]). The influence of the APE on the Lidar signal can be estimated as a convolution of the after-pulse produced by a short light pulse and the Lidar signal. The result is a bias that is superimposed over the original Lidar signal. Since the after-pulse is short compared to the duration of acquisition of one profile (one shot), the influence of the APE can be presented as a delayed echo of the Lidar signal with an integrated value proportional to the Lidar signal itself. Let us define the APE relative intensity as the ratio between the APE signal and the Raman Lidar signal. In our simulation we choose a time delay for the after-pulse of 2 μs (equivalent range of 300 m) after the Lidar maximum intensity defined at 200 m agl. The model atmosphere is chosen with 80 ppbv ozone and an aerosol layer with constant scattering ratio ($scr = 1.8$) and Lidar ratio ($lr = 80$). The simulated APE error is defined as the difference between the ozone mixing ratio respectively the water-vapor mass mixing ratio profile with APE compared to their respective profile without the APE.

The APE on ozone retrieval is shown in Fig. 2.45(a) for three different values of the APE ratio. With an APE of $10^{-3}$ the maximum predicted error of ozone mixing ratio is -11 ppbv (approx. 14%) while for an APE below $10^{-4}$ this effect remains below 5%.

The same effect is studied in Fig. 2.45(b) for the water-vapor mass mixing ratio retrieval. The APE error induced on the water-vapor mass mixing ratio is less than 1% for an APE intensity of $10^{-3}$. The difference in the magnitude and shape of the errors in ozone mixing ratio and water-vapor mass mixing ratio is again explained by the fact that the ozone calculations includes a derivative, which operation reveals a characteristic perturbation in the signal.

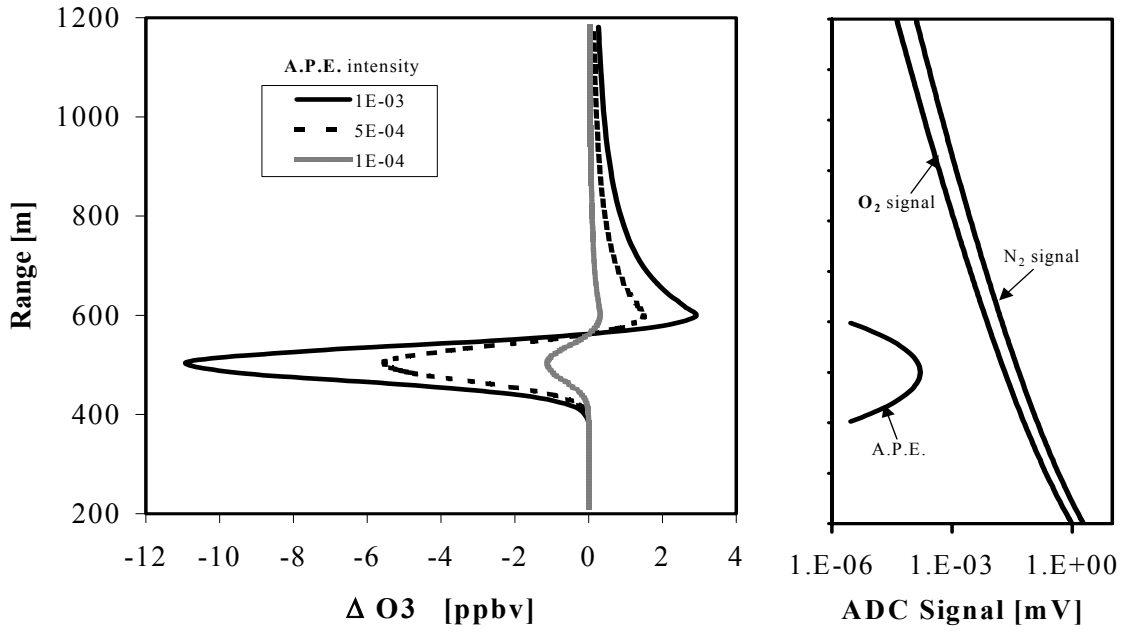


**Figure 2.45 (a)**

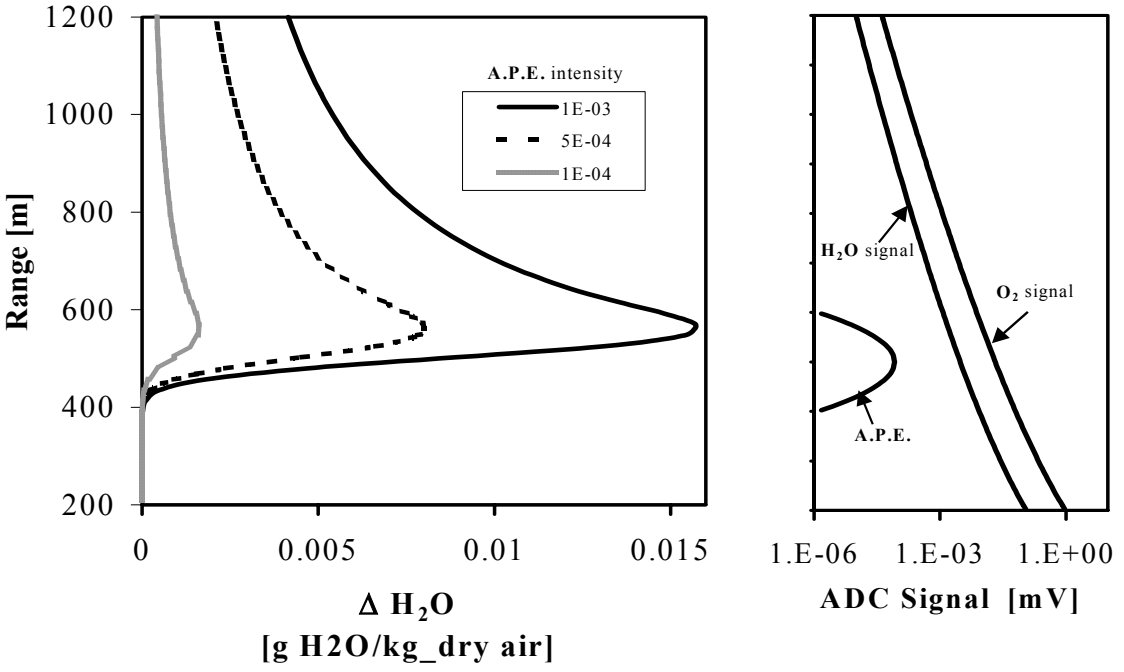


**Figure 2.45 (b)**

**Figures 2.45.** *After Pulse Effect (APE). Predicted errors on ozone mixing ratio (a) and water-vapor mass mixing ratio (b) Raman Lidar retrievals due to the APE. The horizontal scale is the difference between the ozone and the water-vapor retrieval with APE compared with their respective retrieval without the APE. The model Lidar signals are also shown versus their typical ADC voltage intensities (log scale) with the Raman $O_2$ and $N_2$ signals in the case of ozone and the Raman $H_2O$ and $O_2$ signals for the water-vapor mass mixing ratio.*

# 2.5 Conclusions

Our principle achievement in this Chapter is the development and the test of an algorithm to obtain the aerosol backscatter coefficient (ABC) by inversion of the backscatter lidar signal. The realized algorithm is stable for all feasible range of variation of the initial conditions and reference values. With this algorithm we process the atmospheric backscatter lidar signal in the study cases presented in the next Chapters. With this algorithm we also participated successfully in the validation exercises organised in the EU project EARLINET.

## 2.5.1 Elastic Backscatter Lidar simulations

Through the presented elastic backscatter simulations, we have tested several aspects of the Lidar signal processing algorithm. The effects of approximations in the atmospheric molecular model, Lidar ratio and reference value have been shown. For applications in future Chapters, we find that the following points are particularly relevant:

1. For monitoring of the relative temporal and spatial variation of the aerosol backscatter coefficient (ABC) vertical profile in the PBL, the range-corrected signal (RCS) can be also used instead of ABC. This increases the number of the study cases of aerosol dynamics, since the RCS is readily available and does not depend on the conditions for inversion (cloud–free troposphere, sufficient signal-to-noise ratio). This approximation is valid when the variations of the transmission can be neglected.
2. In the inversion procedure for ABC determination, the error associated to the algorithm, with known reference value and Lidar ratio profile, is negligible.
3. In the inversion procedure for ABC determination, the error is negligible when using a model molecular atmosphere for the reference value determination instead of the actual one.
4. The substantial contributions to the error in the inversion procedure are the uncertainties of the ABC reference value and the Lidar ratio.
5. The corrected-signal-gradient (CSG) is a good approximation to the gradient of ABC. The locations of their extrema are very close. Also, the CSG is very poorly affected by the use of an atmospheric molecular model. Thus, it is well suited for the detection of transition zone between layers with nearly homogeneous aerosol distribution.

## 2.5.2 Raman Backscatter Lidar simulations

1. We exposed the principle of aerosol extinction coefficient (AEC) retrieval through Raman Backscatter Lidar. We have investigated the effect of quantum noise with various effective resolutions. We have shown the non-commutability of the AEC retrieval with time averaging.
2. The results demonstrate the possibility to measure aerosol Lidar ratios in performing simultaneous measurements of the elastic and Raman backscattered signals.

## 2.5.3 Raman Backscatter DIAL simulations

We have shown that the determination of the water-vapor mixing ratio by a solar-blind UV Raman Lidar (i.e., operating below 300 nm) requires a simultaneous determination of ozone concentration vertical profile, i.e., three Raman signals shall be measured simultaneously (corresponding to the Raman shifts for $O_2$, $N_2$, and $H_2O$).

The error analysis of the Raman-DIAL Lidar measurement of the ozone and water-vapor profiles demonstrates the following:

1 The systematical error of the ozone concentration due to the influence of the aerosol profile.

2 The systematical error of the water-vapor concentration due to the ozone concentration profile.

3. The error in determination of the ozone and water vapor profiles due to the of the signal shot-noise.

4. The effect of detector after pulses, the spectral cross-talk between Raman channels and the influence of the residual elastically scattered light in the spectrometer.

5. A perspective solar-blind Raman DIAL system for water-vapor measurement shall include also channels for simultaneous measurement of ozone concentration and for aerosol determination.

# Chapter 3

# Elevated aerosol stratification above Rhine Valley in strong anticyclonic conditions

## 3.1 Introduction

Lidar studies of episodes of elevated aerosol mixed layers over mountainous terrain have been reported in a number of recent studies ([*Nyeki et al.*, 2000], [*Carnuth and Trickl*, 2000], [*Kreipl et al.*, 2000]). Such studies are motivated by the connection of elevated aerosol layers with the PBL-troposphere exchange above complex terrain and its potential for long-range pollution transport (see also [*Baltensperger et al.*, 1997], [*Seibert et al.*, 1998], [*Lugauer et al.*, 1998], [*Kossmann et al.*, 1999], [*Furger et al.*, 2000], [*Henning et al.*, 2002]). The Backscatter Lidar observations and the in-situ measurements lead to a conclusion that, in convective conditions, the aerosol-rich (and trace gases-rich) air masses may elevate from the PBL in the mountain valleys to the altitudes of the highest surrounding mountain peaks. For the Alpine region this is approximately to 4000-4500 m (highest is 4810 m) above sea level (asl)*. A likely reason for this effect, as suggested in the above studies, is the enhanced vertical transport on the steep slopes. In this way, the development of the convective PBL over mountainous terrain leads to an elevation of the PBL features with a potential for an enhanced mixing with the free troposphere.

In this chapter, we describe a Backscatter Lidar study of the aerosol stratification above the Rhine Valley in the Alps (RV). The study, performed during a stable anticyclone weather system over Central Europe including the Alpine region, presents a development of the valley Planetary Boundary Layer (PBL) consistent with a thermally established wind system in the Valley, as well as the presence of a stratified aerosol layer above the valley reaching up to altitudes of 4500-5000 m. The study is performed by a ground-based Backscatter Lidar, together with wind temperature Radar (WTR), radiosondes and a number of surface stations. The ground-based Backscatter Lidar gives the possibility to monitor, with a convenient temporal and spatial resolution, the diurnal dynamics of the aerosol layers above the fixed Lidar site. At the same time, its fixed position allows to increase the integration time and in this way to make possible observations of weak aerosol layers at higher altitudes. The measurements are performed during the Special Observation Period (SOP) in the campaign FORM "Foehn in the Rhine Valley in the Mesoscale Alpine Program** ([*Bougeault et al.*, 2001]).

* Here and further in this Chapter, all altitudes are asl, unless stated otherwise
** www.map.ethz.ch/map-doc/form/form.html

# 3.2 Target area and measurement technique

## 3.2.1 The site

A bird's eye view of the RV is shown in Fig. 3.1 with the instrumentation sites. The list of the sites is presented in Table 3.1. RV is a few km broad and approximately 70 km long valley, extending from Chur to Bodensee (lake Constance). Its axis is oriented very close to North-South. The altitude of the surrounding mountain peaks (further referred as "valley-top") is approximately 2200-2400 m, i.e. 1700-1900 m above the valley floor. The Lidar site was in the village of Trübbach, Switzerland (47°04' N, 9°28' E, 490 m). The RV is a populated area, having dense traffic, agriculture, as well as a number of small and medium size industries.

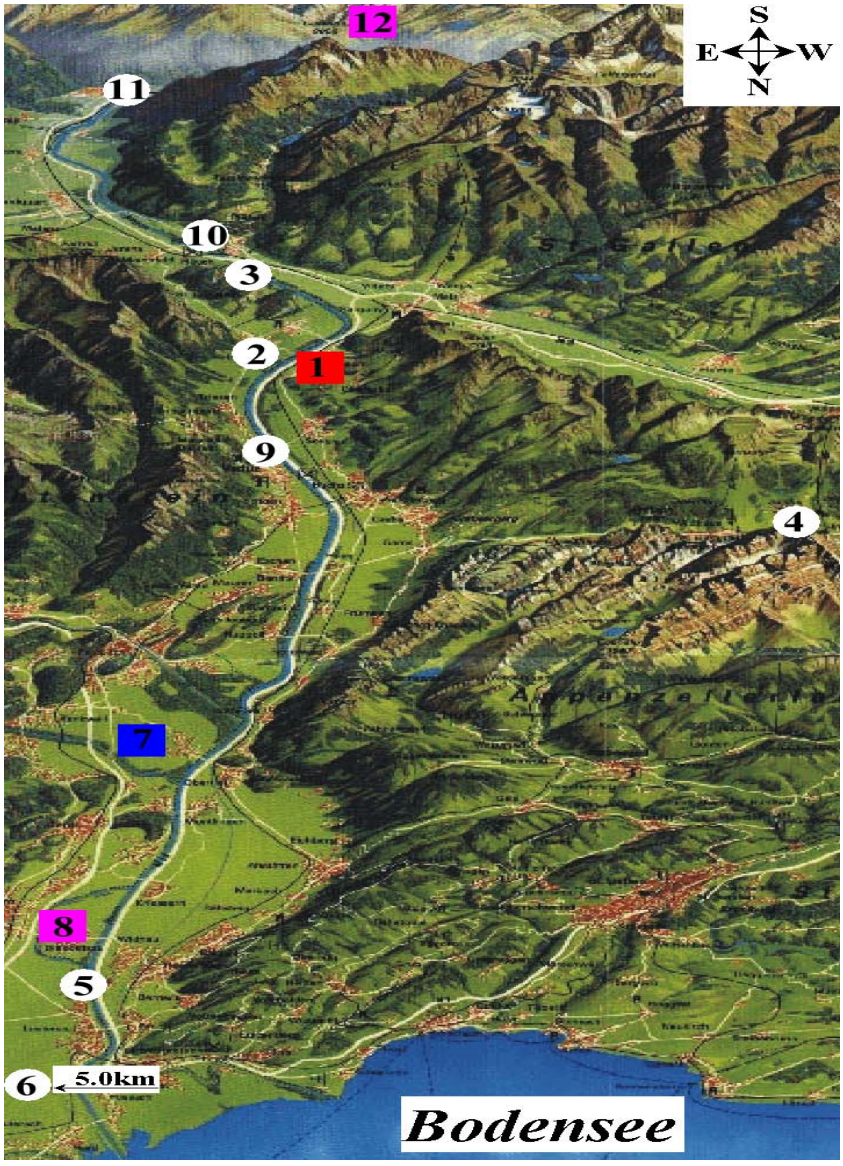


**Figure 3.1.** *Bird-eye view from north of the Rhine Valley (courtesy of Tourismusverband Ostschweiz). The list of the stations providing measurements for the present study is given in Table 3.1. Stations indicated with arrows are located outside the field of bird-eye view, eastward, at the specified distance from the image border.*

**Table 3.1.** *Observation stations in the Rhine Valley during the Special Observation Period of MAP-FORM, presented in Fig. 3.1.*

| No in Fig. 3.1 | Name | Altitude asl [m] | Instruments |
|---|---|---|---|
| 1 | Truebbach | 490 | Elastic Backscatter Lidar |
| 2 | Flaesherberg | 918 | Surface Meteo |
| 3 | Balzers | 522 | Surface Meteo |
| 4 | Saentis | 2490 | Surface Meteo |
| 5 | Lustenau | 400 | Surface Meteo |
| 6 | Dornbirn | 410 | Surface Meteo |
| 7 | Rankweil | 435 | WTR-RASS |
| 8 | Diepoldsau | 411 | Radiosondes: pressure, temperature, wind |
| 9 | Vaduz | 460 | Surface Meteo |
| 10 | Bad-Ragaz | 510 | Surface Meteo |
| 11 | Chur | 555 | Surface Meteo |
| 12 | Masein | 865 | Radiosondes: pressure, temperature, wind |

## 3.2.2 Backscatter Lidar technique

The Backscatter Lidar used during the MAP-SOP operated at the second harmonic of a Nd:YAG laser (532 nm) used with reduced output pulse energy of 10-15 mJ at pulse repetition rate of 20 pulses per second. The receiver had diameter of 15 cm. The detection and data acquisition were performed by PMT EMI 9829QB and two digital oscilloscopes LeCroy 9310 and LeCroy 9314. The altitude resolution in detection of a single Lidar signal profile was 3 m and the temporal resolution was 200 s. In the signal processing, the resolution was degraded in order to decrease the influence of the raw signal statistical error on the obtained values. The full overlap altitude of the Lidar began from about 400 m above ground level (agl) or approximately from 900 m asl. Part of the transmitted laser power was deviated to a power monitor and used for a normalization of the detected atmospheric backscatter signal.

In the PBL-troposphere aerosol stratification we may distinguish basically two types of aerosol layers, following the altitude distribution of their aerosol backscatter coefficient (ABC). One type is a layer staying separately or detached from the ambient aerosol load or molecular atmosphere. It is seen with "bump-like" altitude distribution of the ABC. Such layer may be connected to a transport or accumulation, the latter occurring frequently below a temperature inversion. Another type is an aerosol layer with homogeneous (or very shallow-drop) altitude distribution of the ABC. Example for such is the PBL as convective mixed layer ([*Melfi et al.*, 1985], [*Endlich et al.*, 1979]).

To assess the aerosol distribution from the Lidar measurements, we show series of range-corrected signal, normalized on the transmitter laser power (RCS). As has been pointed out in Chapter 2, the relative temporal evolution of RCS is similar to the relative evolution of ABC. This will be shown together with the evolution of the altitude of the tops of aerosol layers with nearly homogeneous altitude ABC distribution, following the processing exposed in Chapter 1 (routine for detection of local minima of the corrected-signal-gradient (CSG)).

In addition, the CSG is used for the recognition of ABC peaks (detached or accumulation aerosol layers): this process has been done "manually", by visual inspection of the RCS and CSG. Since such layers are distinguished by altitude distribution of their ABC as having a “bump-like” shape with a maximum value at an altitude referred here as “layer's altitude”. At this altitude the CSG changes from a positive value to a negative, i.e., above a local maximum and below a local minimum. A threshold has been considered for the maximum distance between these two local extrema.

A number of selected Lidar profiles have also been inverted following the inversion procedure presented in Chapter 1 and tested in Chapter 2. The justification for the choice of the guessed Lidar ratio is given in Annex 3.1. The inversion results will be combined to show the statistical vertical distribution of the ABC.

### 3.2.3 Other instruments

Wind profiles are provided by a (WTR) described in [*Vogt et al.*, 1998] and [*Bauer-Pfundstein*, 1999]. The radio frequency of the WTR used in this study was 1.29 GHz corresponding to a wavelength of 23.5 cm. From the Doppler-effect-induced frequency shift between emitted and received radiations, the wind velocity is derived. The WTR has been extended to a radio acoustic sounding system by a sound source. It yields the vertical profiles of the horizontal and vertical wind components up to approximately 2000 m, and temperature profiles up to about 1300 m with spatial and temporal resolutions of 60 m and 30 min respectively. In this study, we used only the wind profile measurements.

To assess temperature (T) and relative humidity (RH) profiles, we also used the data from radiosondes launched from stations in the Rhine Valley (Diepoldsau and Masein), from the Inn Valley (Innsbruck) and the Swiss Plateau (Payerne). The data for surface T and RH are also used from a number of surface stations (Table 3.1).

## 3.3 Weather conditions

The Lidar measurements reported here were done in the period from September 6 to 14, 1999 (further referred as "studied period")***. The weather system during this period was strong anti-cyclonic and due to its extremity, it is further referred in this study as “heat-wave” (see Fig. 3.2). The heat-wave with a small horizontal pressure gradient prevailed over a large area in Central Europe, including most of the Alpine region around RV. Table 3.2 shows that for a very long period of observations (more than 50 years), the days from September 6 to 14 are ranking among the warmest. Every day in these heat-wave conditions the relative sunshine duration was more than 95% at Chur and Vaduz, with a trend of increasing the mean daily temperature of 0.57 °C/day in Balzers and 0.23 °C/day for Dornbirn and Lustenau.

**Table 3.2.** *The place of the respective day during the heat-wave in September 1999, in the statistics of the warmest days in various Alpine stations. The years with observations for this statistics are indicated in the brackets.*

| Day of September 1999 | Chur (1931-2000) | Bad-Ragaz (1940-2000) | Vaduz (1979 – 2000) |
|---|---|---|---|
| 8 | 14 | 6 | 2 |
| 9 | 12 | 8 | 3 |
| 10 | 9 | 7 | 3 |
| 11 | 8 | 3 | 1 |
| 12 | 9 | 4 | 3 |
| 13 | 4 | 5 | 2 |
| 14 | 4 | 3 | 2 |

The wind system in the RV cross-section, below the valley-top was monitored with the WTR. The results are statistically averaged for the days of the studied period and are presented in Figs. 3.3a and 3.3b for the horizontal and vertical wind components respectively. Figures 3.3a and 3.3b show that the wind components below the valley-top follow the diurnal cycle of a thermally developed valley wind system, as presented in Figs. 1.6-1.7 (see also [*Blumen*, 1990], [*Whiteman*, 2000]). The periods with down-valley (i.e., South) wind and up-valley (i.e., North) wind are seen in Fig. 3.3a. The vertical wind component presented in Fig. 3.3b shows the return circulation above the valley floor corresponding to the katabatic (down-slope) and the anabatic (up-slope) winds. This return circulation is seen as upward wind component in early night and respectively as downward wind component during day-time. Such thermally developed wind system is typical for fair weather conditions in the RV in absence of Foehn ([*Häberli et al.*, 2001]).

*** Further in this Chapter, all dates refer to 1999.

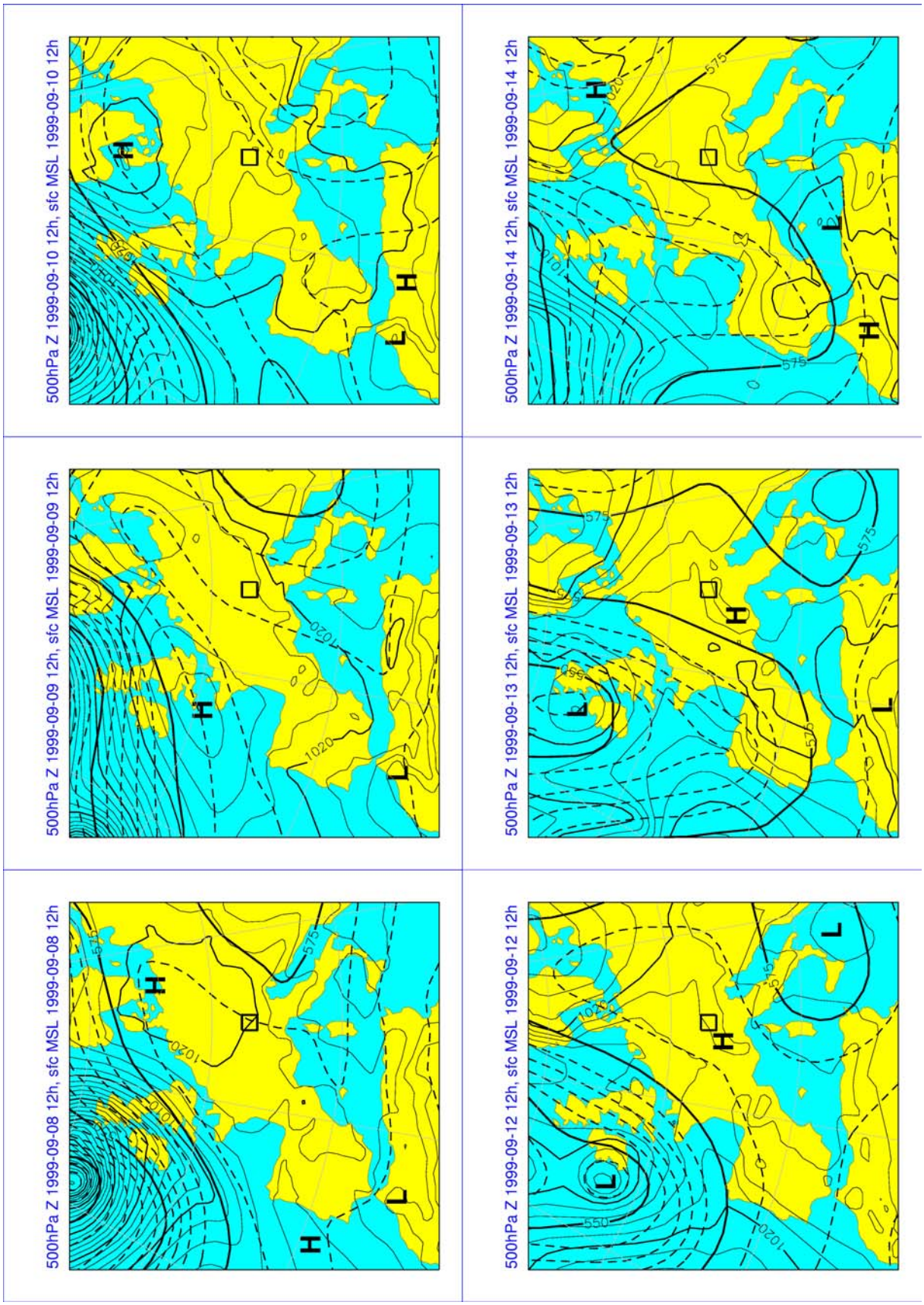


**Figure 3.2.** *Weather maps for the days 8, 9, 10, 12, 13 and 14 September 1999. The square mark shows the position of the Rhine Valley.*

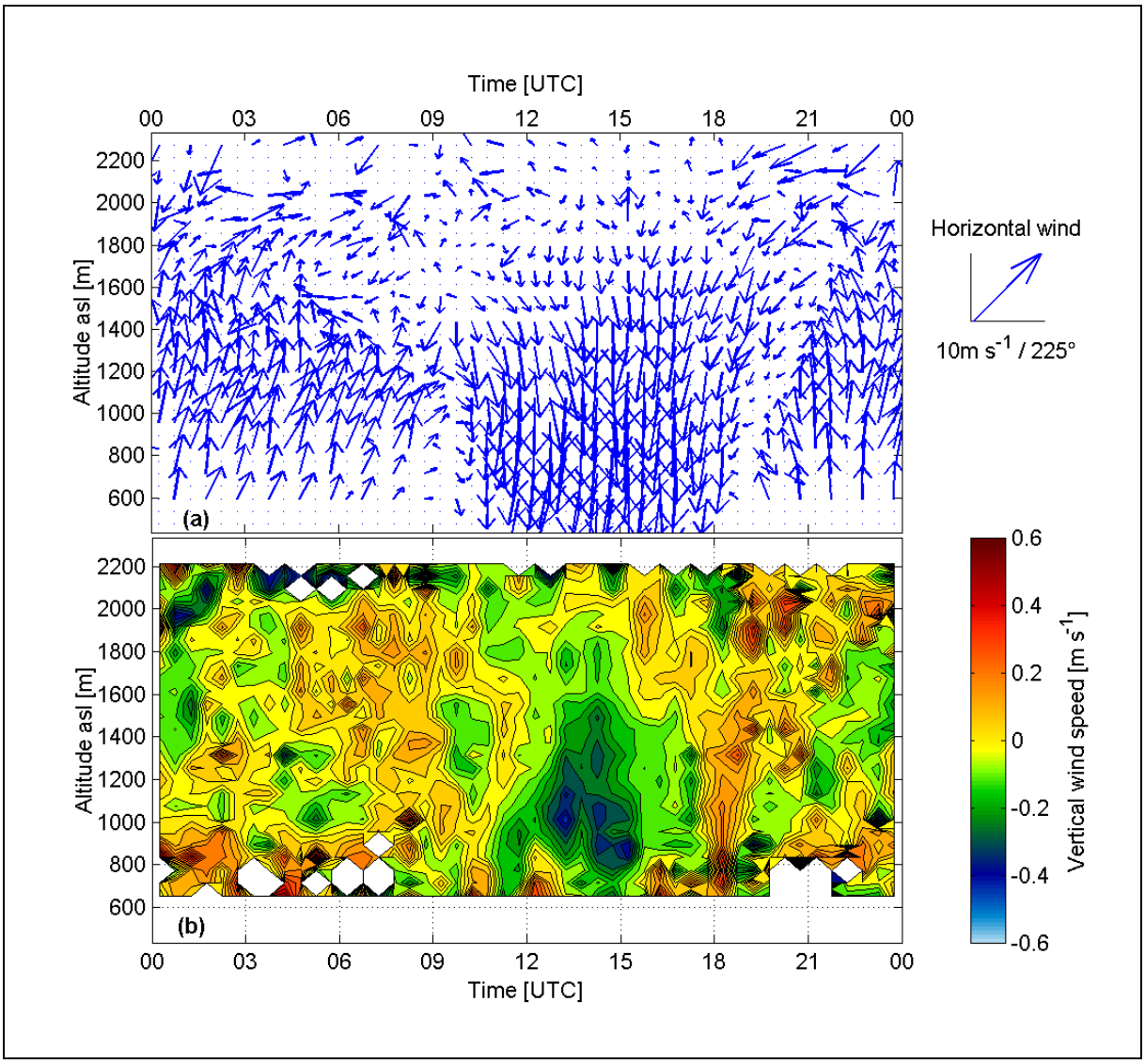


**Figure 3.3.** *Wind measured by WTR above Rankweil. Averaged diurnal variation of the wind field components for the period 8-14/09/1999: (a) horizontal component; (b) vertical component.*

Figure 3.4 shows the diurnal development of the temperature difference normalized on the stations altitude difference (TDN) for the pairs of stations Balzers-Flaescherberg (lower layer) and Flaescherberg-Saentis (upper layer), for the period September 9 to 10. The TDN for both stations pairs, with respect to the temperature gradient of the standard US-76 atmosphere (see Fig. 1.2) suggests a rough estimate of stability or instability of these layers ([*Werner*, 1998]). It suggests that during early morning, both layers are likely stable; during late morning, the lower layer is likely unstable and the upper one is likely neutral or stable; during early afternoon, both layers are likely unstable and finally, during the night, both layers are stable or neutral. In Fig. 3.4, we also see the evolution of the nocturnal temperature inversion between approximately 21h00 and 01h00, typical for such valleys ([*Stull*, 1988], [*Whiteman*, 2000], [*Hindman*, 1973], [*Stewart et al.*, 2001]).

During the studied period, radiosonde measurements were performed from the stations Masein and Diepolsdau in the RV, as well as from other places in the alpine region, e.g. Innsbruck (Inn Valley, 200 km eastward) and Payerne (Swiss Plateau, 170 km westward). The profiles are presented in Fig. 3.5a to 3.5d. In the left panels in these figures, we show the virtual potential temperature (VPT) and its gradient (VPTG), while in the right panels the water-vapor mass mixing ratio (MR) and the relative humidity (RH) are presented. The VPTG demonstrates separate altitude intervals with small gradient, typical for unstable (mixed) layers. The water-vapor mass mixing ratio is high and suggesting a mixed layer to 3500-4500 m. These profiles in the above radiosonde measurements and their similarity above various stations in the Alpine region, suggest the presence of a deep mixed layer during the studied period, as well as its spatial homogeneity over a large area around RV.

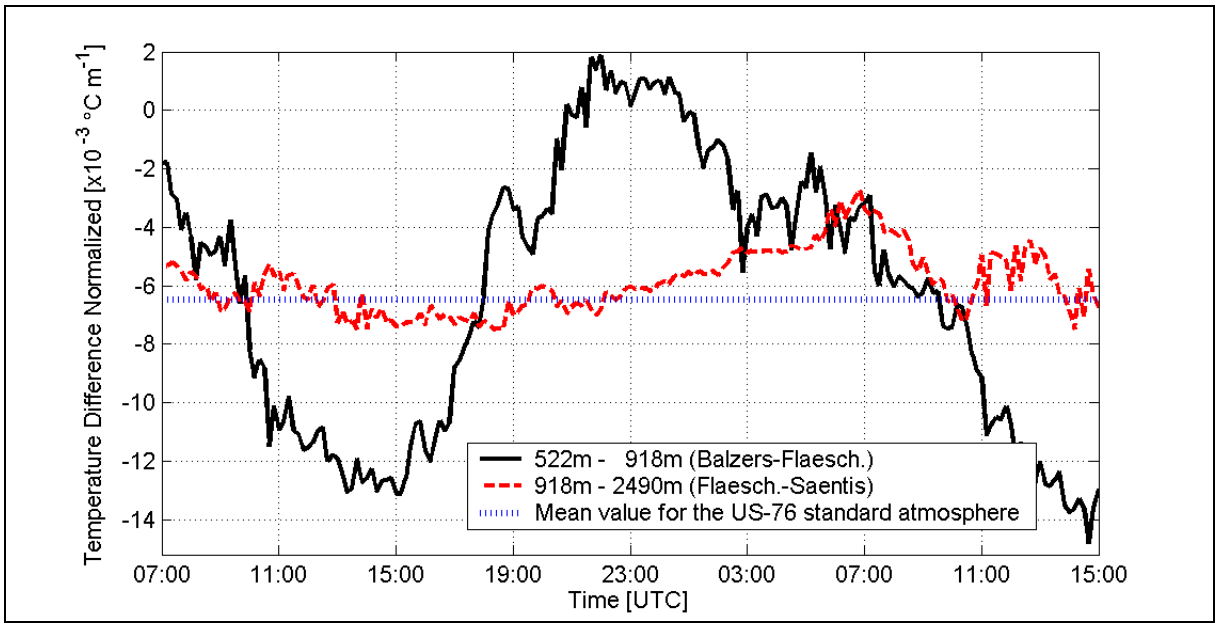


**Figure 3.4.** *Temperature difference for the surface station pairs Balzers-Flaescherberg and Flaescherberg-Saentis, normalized on the stations altitude difference (TDN). Variation for 9-10/09/1999. The horizontal dash line is the standard atmosphere mean temperature gradient.*

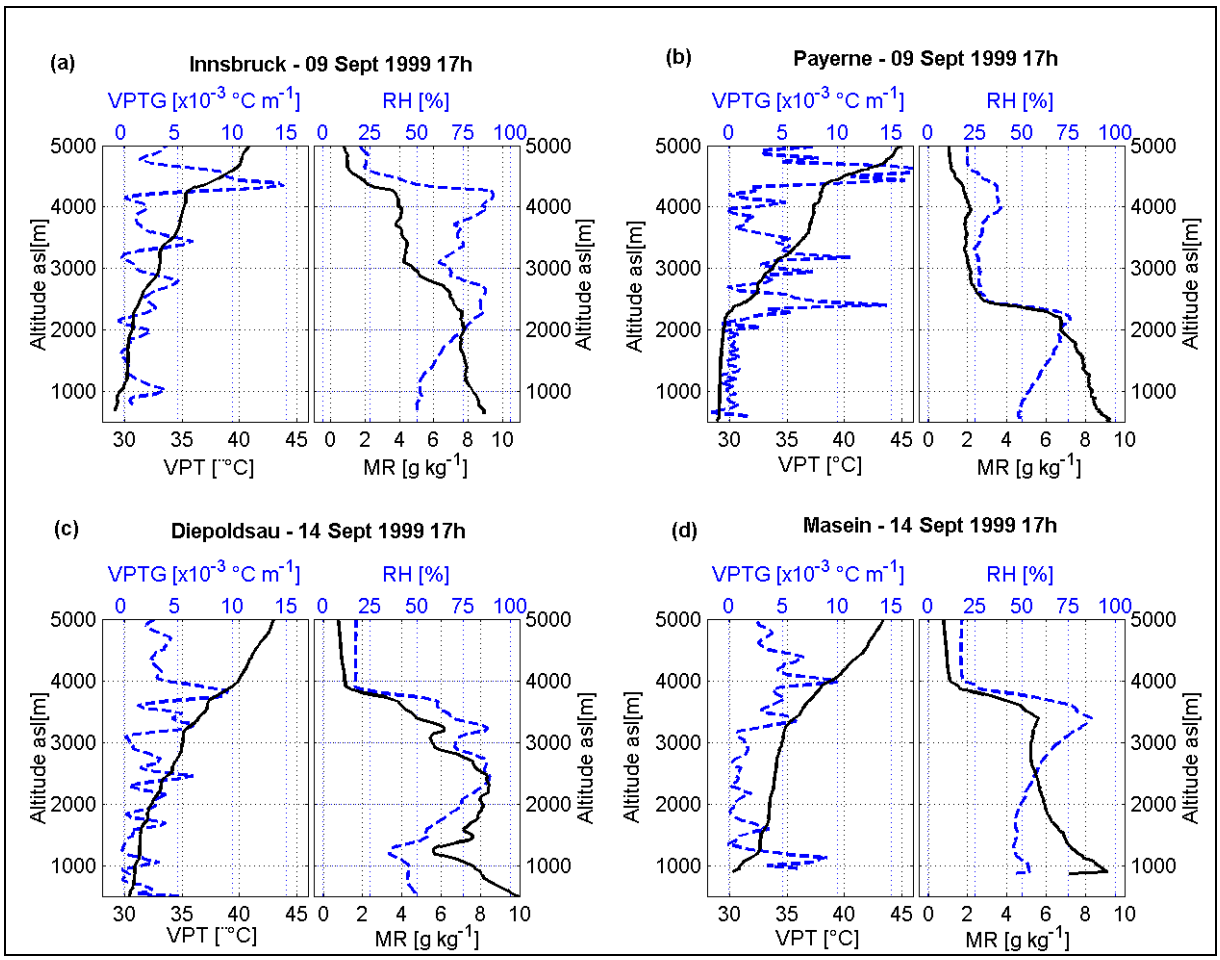


**Figure 3.5.** *Radiosondes data from different stations on September 9 and 14, 1999. Virtual potential temperature VPT (continuous lines, left panels, bottom scale) and virtual potential temperature gradient VPTG (dashed lines, left panels, top scale); water-vapor mass mixing ratio MR (continuous lines, right panels, bottom scale) and relative humidity RH (dashed lines, right panels, top scale).*

# 3.4 Timeseries of the aerosol stratification in the PBL and the lower troposphere over Rhine Valley

Figure 3.6a presents time-altitude variation of the RCS above Trübbach from 08h00 UTC on September 9 till 14h00 UTC on September 10. The white areas in the figure show time and altitudes with no sufficient signal quality. Figure 3.6b shows only the negative values of the CSG. The altitudes for positive CSG values are given as blank. The lines with the symbol "x" in Fig. 3.6b are altitudes of local maxina of the RCS, i.e., local maxima the ABC, showing a detached aerosol layers. This may be a local maximum of the aerosol number density, or relative humidity, or both ([*Dupont et al.*, 1994]). To present the altitudes of these two types of aerosol layers in Fig. 3.6b, we apply a temporal continuity condition and a threshold to discriminate the local minima and maxima from the noise. The altitude resolution for presentation of the values in Figs. 3.6a and 3.6b varies from 27 m at altitude 800 m till 140 m at altitude 5500 m, with an integration time of approximately 10 min.

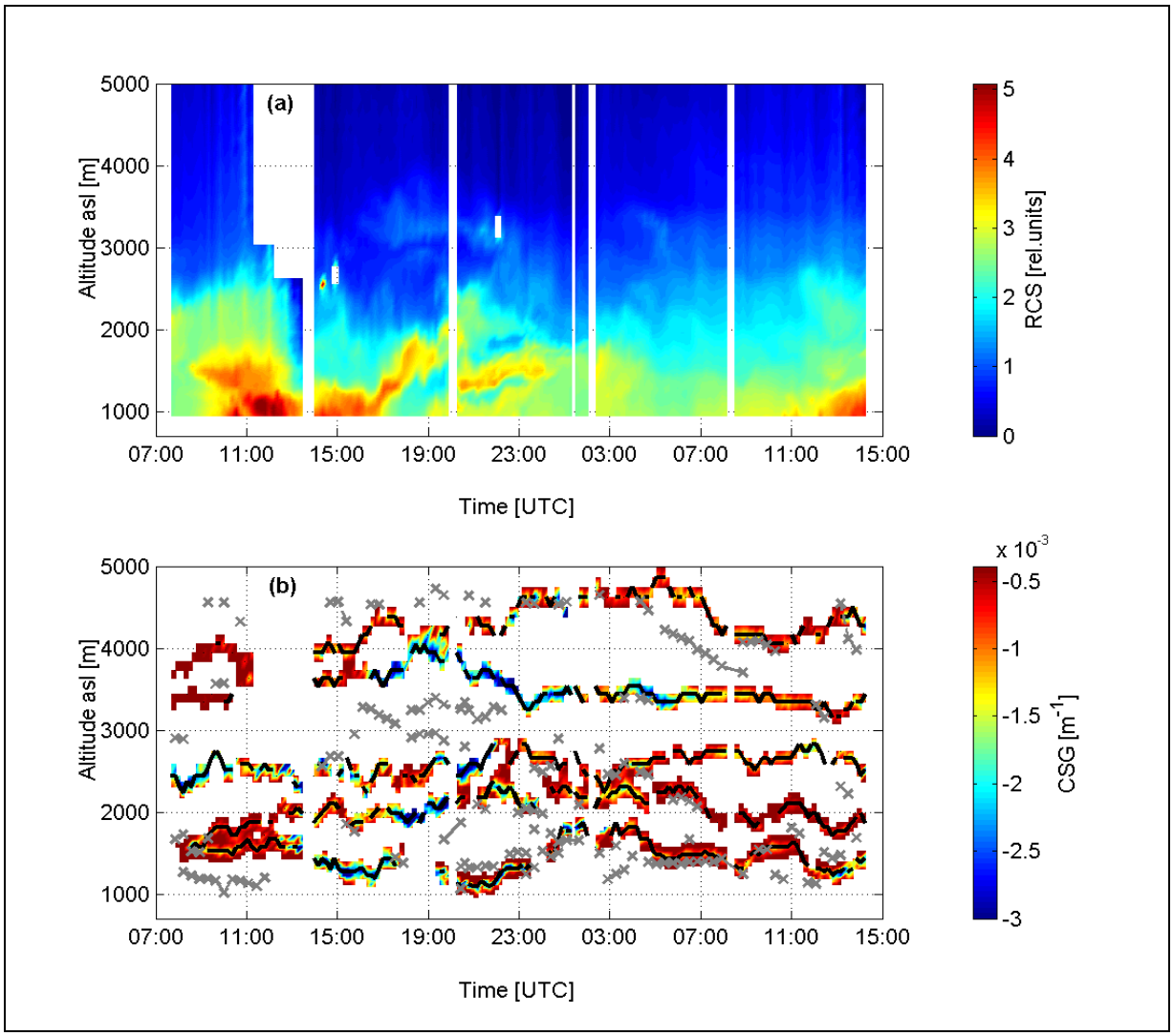


**Figure 3.6.** *Range-Corrected Signal (RCS, panel (a)) and Corrected Signal Gradient (CSG, panel (b)) in the PBL and low troposphere over Trübbach for the period 9-10/09/1999. (RCS): white band between 11h00 and 14h00 at high altitude and between 1330 and 1350 – low signal quality; white spots at 2600 m-2800 m around 1430 and at 3200-3400 m around 2140 – 2200 show spots of aerosol with high value RCS (above the color bar scale). (CSG): top of mixed layers (dark lines) deduced with the gradient method with a threshold of $-3.5 \times 10^{-4} m^{-1}$, the colored strips showing the gradient intensity (CSG); strips without lines are the most likely continuous extensions below the threshold; ABC peak value for accumulation or separate layers (gray crosses).*

The aerosol layers recognized from Figs. 3.6a and 3.6b, belongs to two groups following their altitudes: One group is associated to the diurnal development of the PBL in the Valley itself, i.e. below the valley-top. The second group, situated above the valley-top, is an evidence for an elevated aerosol stratification from altitudes around the valley-top to 4500-5000 m

The dynamics of the observed layers below the valley-top follows the wind and temperature cycle in the Valley. Figure 3.6a shows an increase of the RCS during the morning-noon hours till approximately 1000 m. This increase may be associated to an increase of the aerosol and humidity emission from the RV floor and to aerosol and humidity advected by the up-valley wind (Fig. 3.3a). At the same time, a layer is seen, centered at around 1500 m, which dissipates in time and is likely related to the vanishing signature of the morning inversion core ([*Stull*, 1988]). The RCS and CSG dynamics between 14h00 UTC and 16h00 UTC may be interpreted as a combination of an unstable 'lower layer' and a stable 'upper layer' (see Fig. 3.4). The uplifting of the lowermost aerosol layer to approximately 2000 m asl between 16h00 UTC and 19h00 UTC shows the instability of the 'upper layer' and the increasing stability of the 'lower layer', as well as the katabatic flow bringing cleaner air with less aerosol content to lower altitudes. There is no exact coincidence between the temperature inversion shown in Fig. 3.4 and the aerosol layer dynamics shown in Fig. 3.6. This may be caused by the following reasons: the katabatic flow is neither horizontally homogeneous nor stably stratified due to the mechanically generated mixing (see the short-time temperature differences in Fig. 3.4). From approximately 04h00 UTC till 09h00 UTC, air with low aerosol concentration fills the whole Valley, which means that the katabatic flow is strong enough to remove the residual layer from the valley ([*Stull*, 1988]).

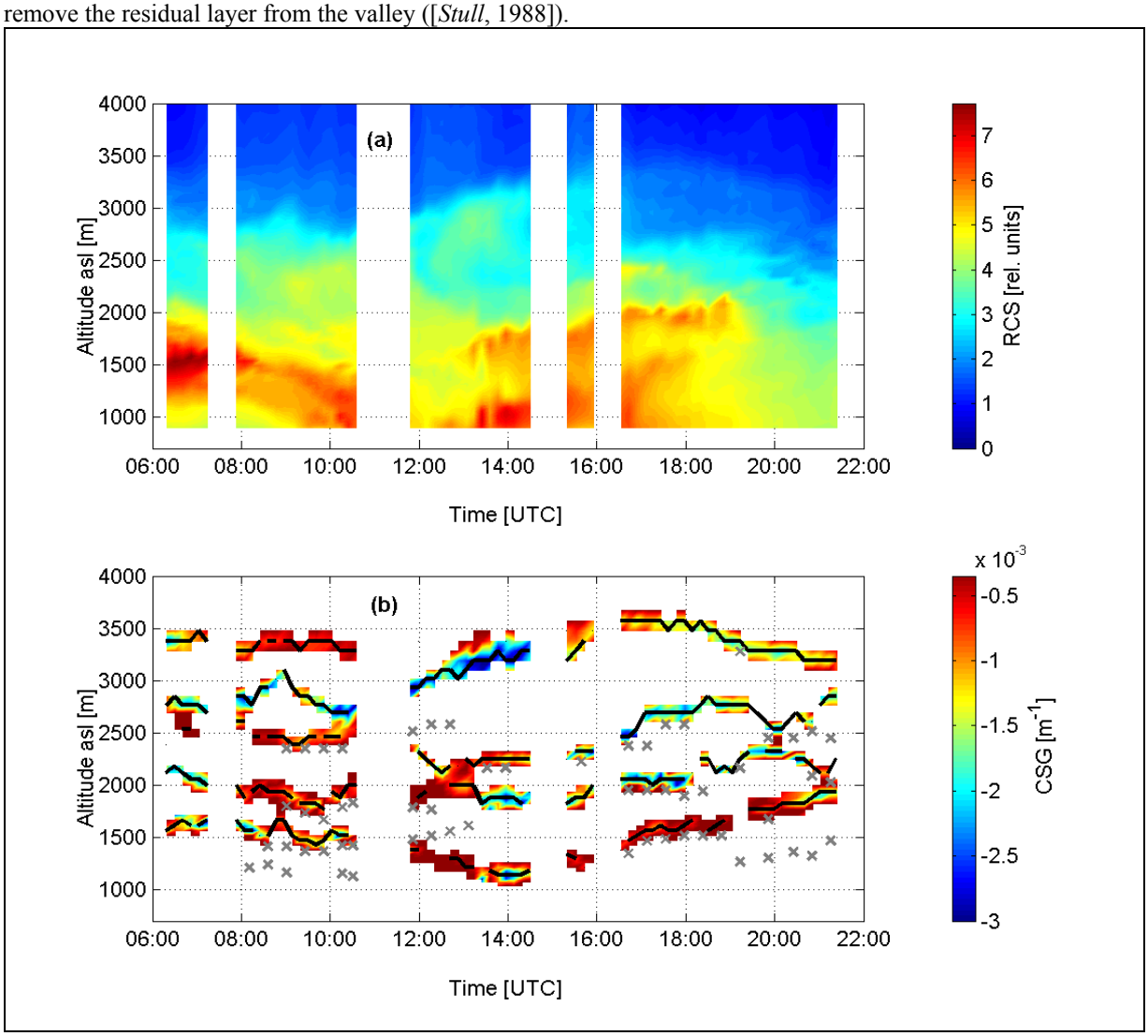


**Figure 3.7.** *Range-Corrected Signal (RCS, panel (a)) and Corrected Signal Gradient (CSG, panel (b)) in the PBL and low troposphere over Trübbach on 8/09/1999. (CSG): top of mixed layers (dark lines) deduced with the gradient method with a threshold of -3.5x10$^{-4}$m$^{-1}$, the colored strips showing the gradient intensity (CSG); strips without lines are the most likely continuous extensions below the threshold; ABC peak value for accumulation or separate layers (gray crosses).*

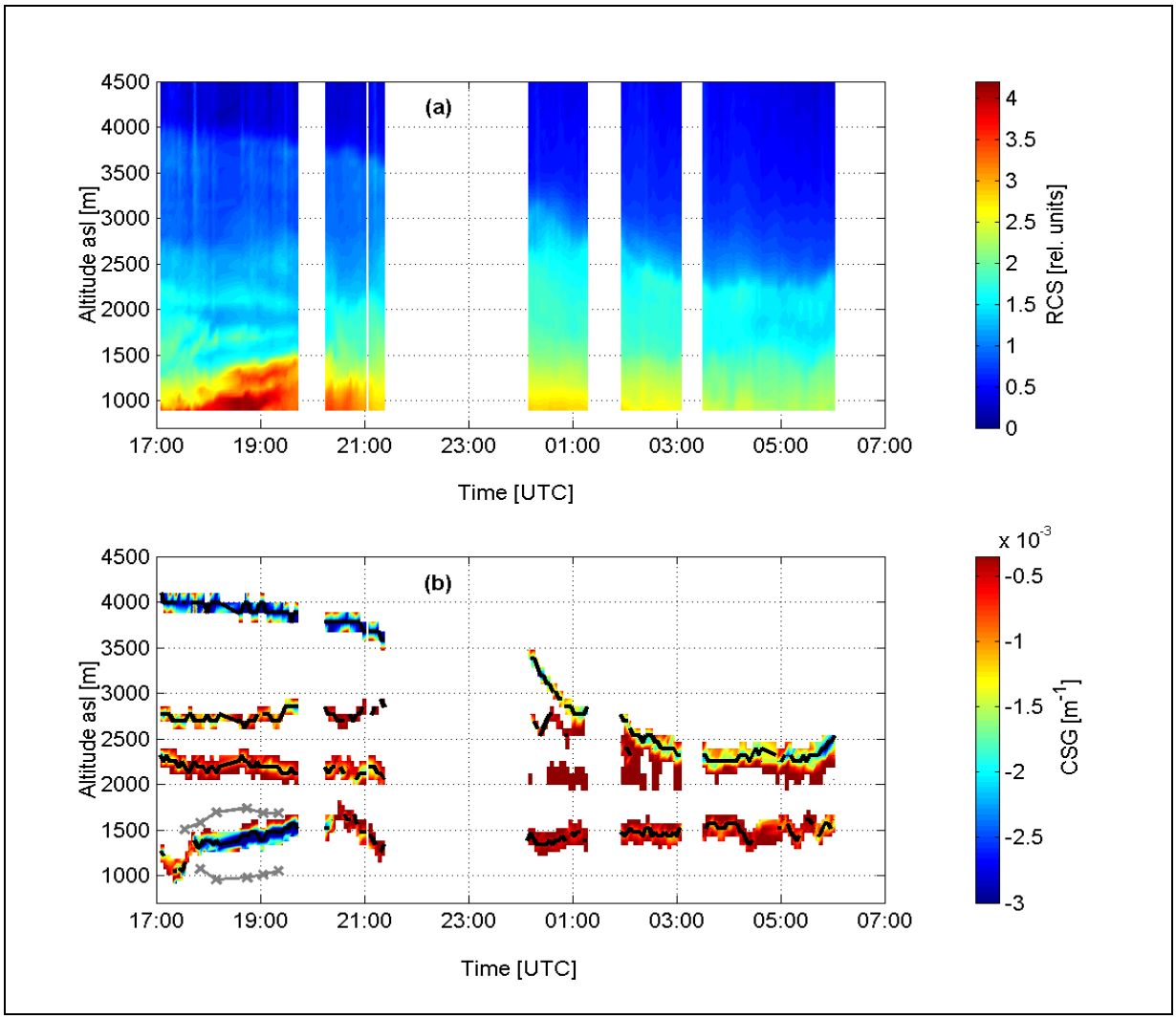


**Figure 3.8.** *Range-Corrected Signal (RCS, panel (a)) and Corrected Signal Gradient (CSG, panel (b)) in the PBL and low troposphere over Trübbach for the overnight period 13-14/09/1999. (CSG): top of mixed layers (dark lines) deduced with the gradient method with a threshold of –3.5x10$^{-4}$m$^{-1}$, the colored strips showing the gradient intensity (CSG); strips without lines are the most likely continuous extensions below the threshold; ABC peak value for accumulation or separate layers (gray crosses).*

The dynamics of the altitude of the first layer above the surface with vertically homogeneous ABC distribution in Fig. 3.6b may be explained by the evolution of the lower-most mixed layer over the RV floor during day-time and the cold-pool evolution during night-time and early morning. The altitude of the second layer from the surface with vertical homogeneous ABC distribution appears at approximately 2000 m. Several hundred meters above this level, a third similar layer appears. I.e., both layers appear close to the valley-top. Figures 3.6a and 3.6b also show aerosol detached (accumulation) layers close to the top of the lowermost layer with homogeneous altitude distribution of ABC. The presence of accumulation layers in valley PBL is also noticed by [*Wakimoto and McElroy*, 1986], [*McKendry et al.*, 1997], [*Hoff et al.*, 1997].

Figures 3.6a and 3.6b present a complex elevated aerosol stratification above the valley-top. Fig. 3.6b shows two altitude levels with local minima of CSG seen with continuity during substantially long intervals. One of these levels appears at altitudes 3200-3900 m, with a slight elevation observed during noon-afternoon hours. The second altitude level is at 4000-4800 m reaching the higher altitude during late night-morning hours. As it is commented in Annex 1, such behavior of CSG may be associated to a drop of ABC, i.e., the top of a layer with homogeneous altitude distribution of ABC. A detached aerosol layer appears at around of 3000-3400 m during late afternoon until mid-night, descending to 2000 m during early morning. Another detached layer is observed at around 4500 m during late-afternoon early morning hours, descending during morning hours.

The comparison of the results in Figs. 3.6a and 3.6b with Fig. 3.5 shows that the elevated aerosol stratification coexists with an elevated mixed layer. Figure 3.5a shows a high value of water-vapor mass mixing ratio with a top altitude elevated to 4500 m over Inn Valley. Similar T and RH profiles as in Fig. 3.5a we see in

Figs. 3.5c and 3.5d, where the radiosondes are launched from other sites in the RV under similar meteorological conditions (in the heat-wave), although not on the same day. Since the horizontal pressure gradient on the synoptic scale is very small, the synoptic conditions were stable and since the RV and the Inn Valley have similar topography, we may expect similar RH and VPT profiles above the RV top during the days of measurements. From these radiosonde results, we may expect existence of elevated mixed and residual layers as discussed in [*Arrit and Young*, 1990], and in [*Stensrud*, 1993].

Figure 3.7 and respectively Fig. 3.8 show in a similar form the Lidar observations on September 8 (day-time) respectively on September 13 to 14 (night-time). The comparison with the previous diurnal cycle shows that in both cases, the top of the upper detected layer is seen to appear approximately 1000 m below. This fact is likely related to the position of the measurement periods in the heat-wave. Below the valley-top, we notice a similar stratification, with typically three detected layer tops with defined continuity. On Fig. 3.7, the descending feature from 1500 m at 06h00 to 1000 m at 14h00 UTC is very likely the signature of the progressive vanishing of the morning inversion core. This is followed by elevating features during the hottest afternoon hours, in accord with a marked convective PBL development. On Fig. 3.8, the sharp night-time descent of the upper feature (from 4000 m to approximately the valley-top) appears in excellent accordance with the synoptic evolution (see two last charts in Fig. 3.2).

# 3.5 Average Values of Aerosol Backscatter Coefficient (ABC) and Corrected Signal Gradient (CSG)

Figure 3.9 presents the statistically averaged profiles of ABC and CSG values for the period from September 6 to 14. Figures 3.9a and 3.9c present the average altitude distribution of the CSG values respectively for day-time (from 10h00 until 17h00 UTC) and for night-time (from 00h00 until 07h00 UTC). Figures 3.9b and 3.9d present the average altitude distribution of the ABC, respectively for day-time and night-time hours as for CSG. Above 3000 m, a zoomed scale (top scale in Figs. 3.9b and 3.9d) allows a better visualization of the low ABC values. The altitude resolution is as in Figs. 3.6a and 3.6b, with an integration time for a single profile approximately 50 min for all altitudes. The dashed lines for both CSG and ABC show the standard deviation of the statistical average, weighted according to the relative frequency of occurrence. The relative frequency distribution (color bars) shows that the distribution of the individual values for ABC and the CSG is not gaussian. In Figs. 3.9b and 3.9d, on both scales, the error bars present the range of ABC variations due to the uncertainty of the reference values from the Lidar signal inversion procedure. The number of the individual profiles included in the averaged profiles of CSG and ABC, as well as the combined total integration time for these average profiles, are presented in Table 3.3.

**Table 3.3.** *Number of individual measurements and the total integration time to obtain the average values for the Lidar Corrected Signal Gradient (CSG) and the Aerosol Backscatter Coefficient (ABC), presented in Fig. 3.9.*

| Day-time<br>(Figs. 3.9a and 3.9b)<br>10h00 – 17h00 UTC | Night-time<br>(Figs. 3.9c and 3.9d)<br>00h00 – 07h00 UTC |
|---|---|
| CSG<br>28 measurements<br>total of 1234 min | CSG<br>14 measurements<br>total of 603 min |
| ABC<br>22 measurements<br>total of 937 min | ABC<br>14 measurements<br>total of 603 min |

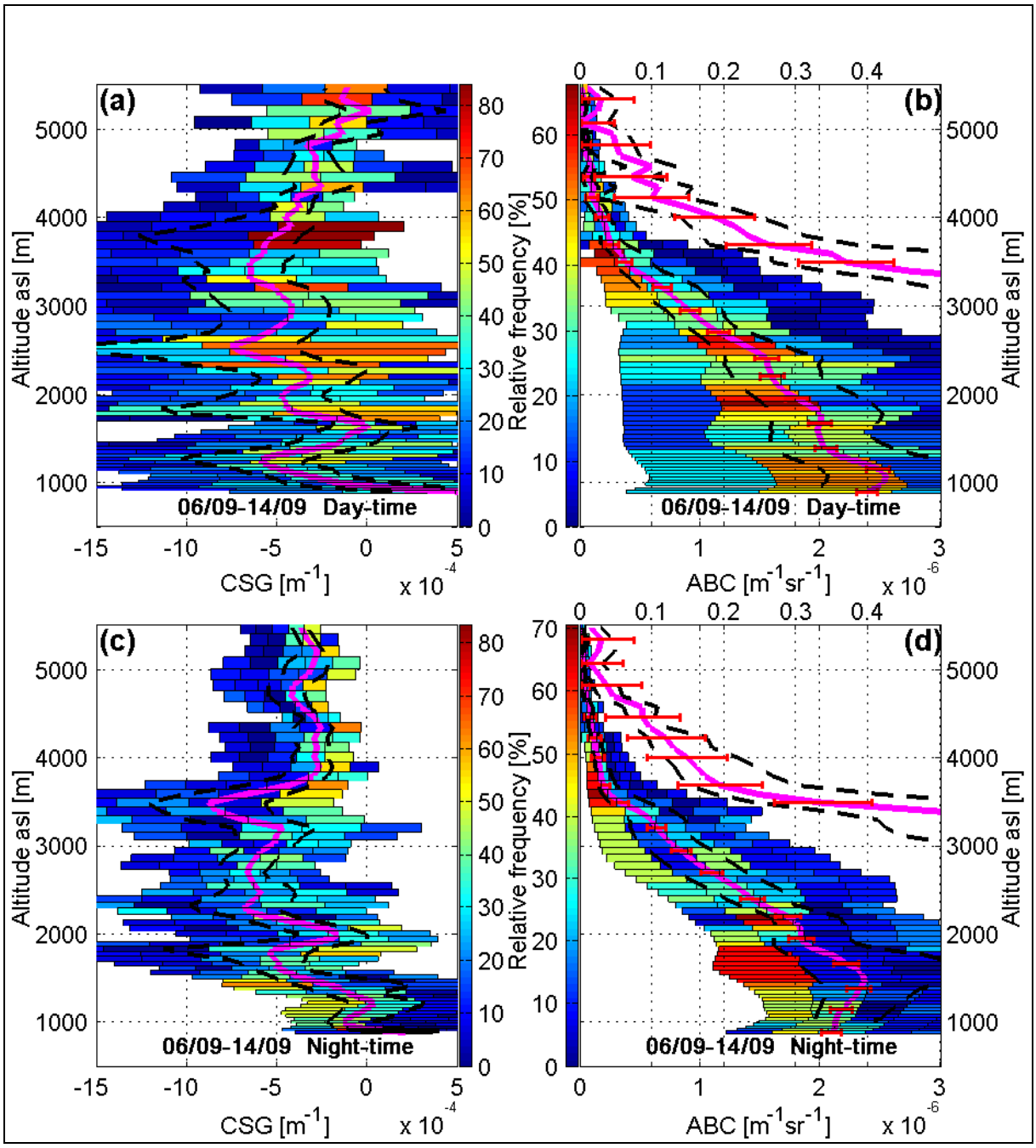


**Figure 3.9.** *Average values for Corrected Signal Gradient (CSG, panels (a) and (c)) and Aerosol Backscatter Coefficient (ABC, panels (b) and (d)) during the period 6-14/09/1999; panels (a) and (b) are for daytime 10h00–17h00; panels (c) and (d) are for night-time, 00h00-07h00. The upper horizontal axes of panels (b) and (d) presents ABC panels ((b)-(d)) show the ABC value above 3000 m zoomed; the grayscale bars show the relative frequency of occurrence; the continuous black lines presents the average value while the dashed black lines show the standard deviation of the distributions, the error bars presented in white for the normal scale and in black for the zoomed scale in panels (b) and (d) show the uncertainty in ABC value due to the uncertainty of the reference values for the inversion procedure. In the day-time averaged CSG altitude profile local minima appear at altitudes approximately 1250 m, 1950 m, 2550 m, 3400-3700 m, 4000-4200 m and the highest is at 4800 m. The night-time average CSG profile shows local minima at 1000 m, 1800 m, 2300-2800 m, 3500 m and 4700-4800 m. At both, for the day-time and for the night-time cases, the altitudes of local minima of the CSG coincide with altitudes of drops of the ABC average values.*

The ABC altitude profiles in Fig. 3.9 indicate to a stratification with a number of successive drops. Up to the altitudes of the valley-top the drops are steeper and above the valley-top the drops are shallow. The uppermost drop, being rather shallow, occurs at altitudes of 4500-4700 m. The altitudes of the local CSG minima and the drops of the ABC values are coinciding. The ABC value at the highest altitudes (4000-4700 m) corresponds to a total scattering ratio in the range of 1.05 to 1.10. This indicates an uplifting of aerosol particles to the altitudes of the highest Alpine peaks. Such observation is consistent with in-situ aerosol measurements in high altitude alpine sites (see [*Baltensperger et al.*, 1997], [*Seibert et al.*, 1998], [*Lugauer et al.*, 1998]).

The comparison between Figs. 3.7a and 3.7b shows a difference between the night-time and day-time values for ABC below approximately 2500 m, i.e., below the valley-top. The day-time average ABC value is higher, as may be expected from the diurnal cycle of the valley PBL. On the other hand, no substantial differences between the night-time and day-time average ABC values and their altitude distribution are observed above the valley-top. In both cases, the uppermost aerosol layer extends till approximately 4500 m.

It is interesting to compare again the results in Figs. 3.7 with the radiosonde sounding presented in Fig. 3.5 in view of possible elevated mixed and elevated residual layers as suggested in [*Arrit and Young*, 1990] and [*Stensrud*, 1993]. We have already discussed the features observed in Figs. 3.5 a, c and d above RV and Inn Valley. Figure 3.5b presents the profiles of VPT and its gradient, as well as the water-vapor mass mixing ratio and the RH profiles measured by a profile from Payerne. This station is away from the Alpine sites, but still close to this mountain system. These profiles show a mixed layer with a top at 2400 m and a detached water-vapor layer at 4000-4500 m. This is an evidence that the elevated mixed and residual layers are over the Alpine region only (seen in Figs. 3.5 a, c and d) while the observed detached layer may be connected to an advection from this elevated residual layer. This coincidence suggests that the observed elevated aerosol stratification above RV may be a result of the existence of elevated mixed and residual layers over a larger Alpine region.

The retrieved value of the ABC depends on the chosen Lidar ratio (see Chapters 1-2). This parameter depends on the type of aerosol and the RH. In the present study, we use typical Lidar ratio values following [*Ackermann*, 1998], where the Lidar ratio for aerosols of continental type at 532 nm range is found to vary from 45 sr for RH = 0% to 80 sr for RH = 100% (Mie-scattering calculations). To determine the respective value for the Lidar ratio at altitudes around the valley-top, we use the RH values from the station at Saentis. As seen in Annex 3.1, the temperature and RH measured by radiosonde, i.e. probing air parcels far from the terrain surface as the Lidar probes, correlate well with the surface data at this station.

Another critical issue in the Backscatter Lidar inversion procedure is the reference value for the backscatter coefficient. As has been seen in Chapter 2, uncertainty in this reference value, as well as in the value of the Lidar ratio does not lead to change of the shape in the obtained ABC altitude profile. It may lead to an uncertainty in the absolute value of ABC but not in its relative altitude distribution. Since no assumptions are used to calculate the CSG profile, no uncertainty shall be expected in it, apart from that coming from the noise contributions.

# 3.6 Conclusions

The identification of elevated aerosol layers above high mountain is our original contribution in this Chapter.

To study the aerosol distribution above the Rhine Valley we operated a Backscatter Lidar during the FORM-SOP. We combined the Lidar observation of the aerosol profile with the wind measurements from Wind-Temperature Radar, temperature measurements from surface stations and radiosonde temperature and humidity measurements.

1. The results show that the diurnal cycle of the aerosol stratification in the Rhine valley PBL during the measurement period follows the wind and temperature patterns determined from the radiation dominated weather situation. The PBL development below the valley-top shows the formation of aerosol accumulation layers and layers with homogeneous altitude distribution of ABC (aerosol mixed layers) with the aerosol likely to originate basically from valley emissions and transport.

2. The Lidar observations identify elevated aerosol stratification above the valley-top. This elevated stratification is reaching altitudes of 4500-5000 m with evidences for step-wise drops of ABC value and for presence of detached (accumulation) layers. The ABC and the altitude of the layers in this elevated stratification show much less diurnal variation compared to the diurnal dynamics in the valley PBL. In this way we cannot associate directly the elevated aerosol stratification above the valley-top with the development of the PBL in the Valley and we interpret them as elevated residual layers.

3. The radiosondes profiles of T and RH over a large Alpine area in stable and horizontally homogeneous synoptic conditions also suggest the existence of elevated mixed and residual layers. Although there is no direct collocation of the Lidar measurements and the radiosonde measurements, the similarity of the conditions suggests that the observed aerosol stratification above the valley-top may be a demonstration of this elevated residual layer, being an accumulative product of the aerosol emission, mesoscale advection and convective mixing from a large mountain area around the Valley.
4. In order to know how representative are the observed elevated layers, next studies shall show if they also appear in not so extreme meteorological conditions.
5. Another question to be answered in a future study is to determine to which extent the appearance of stable accumulation layers correlates with the dynamics of the temperature inversions in the valley.

# Annex 3.1 Reference humidity data for the choice of Lidar ratio

During the studied period (6/09/1999–14/09/1999) and the SOP of FORM-MAP (15/09/1999-7/11/1999), we benefited from the measurements by a large set of surface stations in the Rhine Valley, located at different altitudes above the valley floor, as well as a high frequency of radiosonde measurements during SOP. This provides an opportunity to examine the correlation between the temperature and the relative humidity at the same altitude determined by radiosonde and surface measurements.

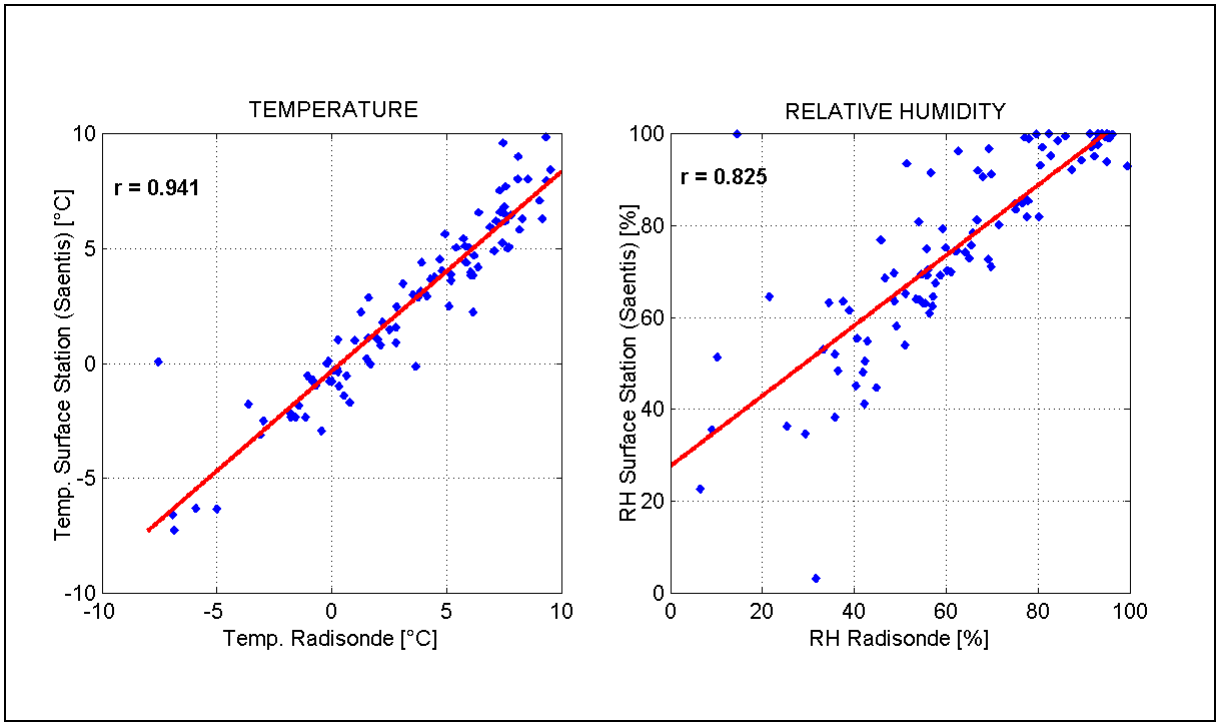


**Figure 3.10.** *Scatter plots of the values for the temperature (left panel) and the relative humidity (right panel) measured by radiosondes at 2490 m and at surface station Saentis 2490 ml). The lines are the least square linear fit, the indicated "r" values are the linear correlation coefficients. The number of the radiosondes is 98, all launched from the station Diepoldsau during the period 15/09/1999-31/10/1999.*

Figure 3.10 shows a scatter plot of 98 occurrences of simultaneous measurements of radiosonde and surface measurements at an elevated station (Saentis, 2490 m asl) for temperature and and respectively relative humidity. Correlations coefficients of 0.941 and respectively 0.825 are found for temperature and RH. It is seen that for both variables, the measured values at the surface station are well representative for air parcels far from the terrain surface. This high correlation justifies the use of the RH values from the surface station Saentis (in absence of regular soundings during the studied period) for the choice of Lidar ratio in the Backscatter Lidar inversion procedure.

# Chapter 4

# Aerosol stratification above Rhine Valley in Foehnic conditions

## 4.1 Introduction

Foehn is a warm, dry, strong and frequently gusty wind in the lee-side of a mountain range ([*McIlveen,* 1992], [*Hoinka,* 1985], [*Brinkmann* 1971]). A generally accepted explanation for the Foehn winds is that they are caused by forced ascent and descent of airflow over a high mountain range.

A typical scenario for Foehn appearance North of the Alpine range is connected with a pressure gradient across the Alpine ridge ([*Egger and Hoinka*, 1992], [*Seibert*, 1990]). When the pressure gradient becomes sufficiently strong, a flow of humid air mass is directed North across the Alpine range (see the artistic presentation in Fig. 4.1). The upslope winds on the windward side of the mountains force the air mass to ascent with subsequent adiabatic expansion and cooling. At a certain temperature the water-vapor starts to condense and a precipitation follows, sometime as heavy showers. The condensation induces the release of latent heat and results in drying and warming of the air mass at the level of the mountain ridge. Foehn wind may also occur in cases when the flow on the windward side is confined above the mountain range, while the lower level airflow largely stays restricted (blocking effect [*Baines*, 1987] below the mountain barrier. In such cases there is no precipitation on the windward slope of the mountain.

When the already dry and warm air flows downhill from a higher elevation, its temperature is raised even more by the adiabatic compression. In this sense, the Foehn down-slope at the lee-side of the mountains, are strong winds carrying air mass with high temperature and low relative humidity. In addition, due to precipitation, the air mass is relatively cleaned from aerosol particles typical for PBL air mass. As the Foehn wind enters the valleys, its flow may be sharply restricted by the channeling effect of the mountainsides. Depending on the topography this may cause local increases of the wind speed pressure drops, gusts and turbulent action. Under these conditions an oscillating quasi-stationary warm front is maintained dynamically in the lee of the mountains at a sharp boundary between the warm Foehn air invading the valley from above and the pool of cold air (cold pool) in the valley. Across this boundary a strong inversion takes place, where the temperature may change by as much as 15 °C, being very effective in trapping aerosol rich air [*Hoinka and Rösler*, 1987].

The objective of the Backscatter Lidar measurements in the experiment FORM (Foehn in the Rhine Valley during the Mesoscale Alpine Program) was the observation of the variation (modification) of the aerosol profile in the PBL during the development of Foehn events. The Lidar backscatter signal profile, its gradient and the aerosol backscatter profile provide the following information: (i) What is the dynamics of the Foehn wind penetration in the valley, i.e., what is the dynamic of the cold pool top; (ii) How Foehn modifies the aerosol content in the valley air and above it, at altitudes typical for the valley PBL and lower troposphere.

The synoptic of the Foehn development during FORM Special Observation Period (SOP) was provided by a number of surface meteorological stations and balloon launching stations (see Fig. 4.2 and Table 4.1). A continuous monitoring of the wind velocity at level of 500 m above the Lidar was provided by a scintillation measurement (crosswind Scintillometer or Scidar) ([*Furger*, 2000], [*Furger et al.*, 2001]). This provides the opportunity to compare the dynamics of the Lidar signal profile and values determined from it, with the

meteorological parameters characterizing the Foehn development. The task in this chapter is to characterize the aerosol stratification above the Rhine Valley by the Lidar range corrected signal (RCS), corrected signal gradient (CSG) and the aerosol backscattering coefficient (ABC) during the development of Foehn. To verify the Foehn state we use the meteorological parameters determined in the surface stations around the Lidar site, radiosondes and the wind determined by the Scintillometer.

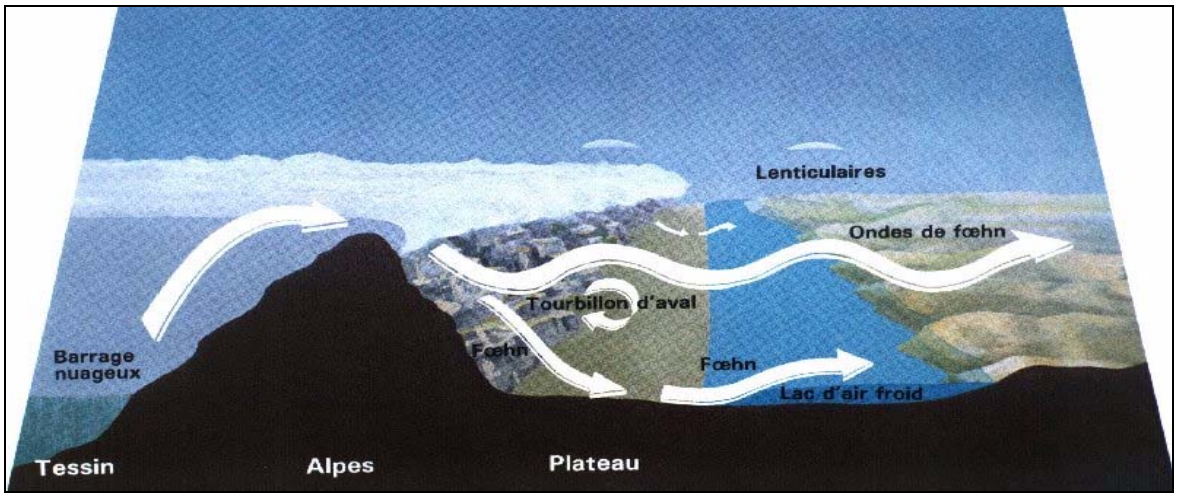


**Figure 4.1.** *A simplified artistic presentation of Foehn flow over the Alps (from [*Hack*, 1994]). The presentation helps to « visualize » the objectives for determination of the dynamics of the PBL structure, waves, interaction with the cold air pool, possible transport of aerosol in the troposphere.*

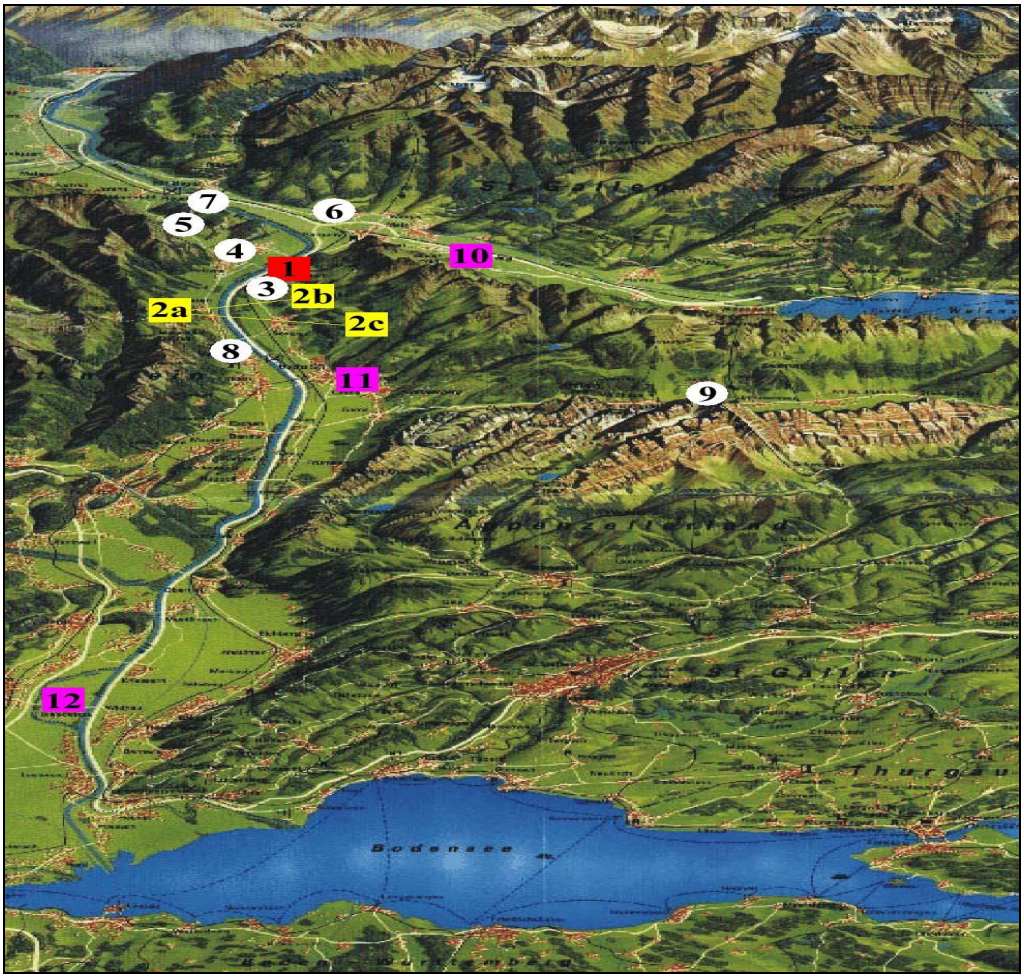


**Figure 4.2.** *Stations involved in the Foehn study in the Rhine Valley (see Table 4.1).*

**Table 4.1.** *Observation stations in the Rhine Valley during the Special Observation Period of MAP-FORM, presented in Fig. 4.2.*

| No in Fig.1 | Name | Altitude asl [m] | Instruments |
|---|---|---|---|
| 1 | Truebbach | 490 | Elastic Backscatter Lidar |
| 2a | Triesenberg | 1070 | Scintillometer transmitters |
| 2b | Oberschan | 840 | Scintillometer receiver ("South" channel) |
| 2c | Sevelen | 920 | Scintillometer receiver ("North" channel) |
| 3 | Weite | 530 | Surface Meteo |
| 4 | Balzers | 522 | Surface Meteo |
| 5 | Luzisteig | 550 | Surface Meteo |
| 6 | Vilters | 485 | Surface Meteo |
| 7 | Flaesherberg | 918 | Surface Meteo |
| 8 | Vaduz | 460 | Surface Meteo |
| 9 | Saentis | 2490 | Surface Meteo |
| 10 | Heiligkreuz | 475 | Radiosondes: pressure, temperature, wind |
| 11 | Buchs-Grabs | 445 | Radiosondes: pressure, temperature, wind |
| 12 | Diepoldsau | 411 | Radiosondes: pressure, temperature, wind |

In the Rhine Valley (RV), a large set of surface meteorological stations was operating during the SOP. In addition to the stations presented in Fig. 4.2, we will use the data from the surface station Guetsch [outside the field of view of Fig. 4.2, altitude 2287 m, approximately 90 km at SW from our area, on the alpine ridge], as indicator for pass-Foehn in the RV.

In the FORM group activity, Foehn criteria [see in http://www.lapeth.ethz.ch/ ~stefan/research/ Foehn%20criteria/] have been elaborated at the different surface stations. Table 4.2 summarizes the adopted criteria at stations near the Lidar site.

**Table 4.2.** *Foehn criteria used at surface stations in the RV. ΔT is the temperature variation at Foehn onset and end, FF is the minimum wind speed, and PF is the gust speed, RH the maximum relative humidity during the Foehn flow at the station.*

| Station | Foehn onset | Foehn | | Foehn end |
|---|---|---|---|---|
| | ΔT [K/h] | FF—PF [m/s] | RH [%] | ΔT [K/10'] |
| Luzisteig | 3 | 3.0 – x | 45 | -1 |
| Vilters | 3 | 3.0 – x | 45 | -1 |
| Flaescherberg | 3 | 5.0 – x | 54 | -1 |
| Balzers | 3 | 5.0 – x | 45 | -1 |
| Weite | 3 | 4.6 – x | 45 | -1 |
| Vaduz | 3 | 3.0 – 10.0 | 45 | -1 |
| Buchs-Grabs | 3 | x – x - | 45 | -1 |
| Saentis | 3 | 3.0 – x | 45 | -1 |

In addition to these criteria we use Foehn definition based on scintillation measurements, following [http://www.lapeth.ethz.ch/~stefan/research/definitions_glossary/Foehn%20defini-tions%20(members).htm]:
"The scintillometric Foehn definition is based on the behavior of two measured quantities, the crosswind speed and the scintillation strength (represented by the standard deviation of the scintillometer light signal strength). A threshold value can be defined that separates Foehn flow from non-Foehn, southerly flow. This threshold value lies between 10 and 15 m/s, but an exact value (if there exists one) has to be determined from more data than is presently available. The second parameter, the scintillation strength, and shows a remarkable decreases once the Foehn has started. The reason for this decrease is presumably the reduced humidity in the Foehn air, which reduces refractive index variations. However, this explanation has not yet been verified. The scintillation strength has not been calibrated absolutely in our instruments, hence only relative variations might yield a criterion useful for Foehn determination."

In [*Drobinski* et *al.*, 2002], it is further demonstrated that Scintillometer's data analysis allows for a separation between Foehn and southerly flow.

Within FORM community, *following* terminology has been adopted: [http://www.iac.ethz.ch/ ~stefan/research/definitions_glossary/pass%20Foehn.htm]: a Foehn event is considered as 'valley Foehn'

[*Steinacker et al.*, 2001] for a specific Foehn-prone alpine valley when the Foehn criteria are fulfilled at least at one mountaintop and at least at one station within the valley flow regime. A case is classified as 'pass Foehn' if the Foehn criteria are fulfilled at least at one pass or mountaintop station. Pass Foehn events might often *not* be recorded at the valley floor. A Foehn flow is considered as 'deep', when the Foehn flow crosses the Alps from south throughout the troposphere ([*Häberli*, http://www.lapeth.ethz.ch/~stefan/research/definitions_glossary/deep%20Foehn.htm)]. A Foehn flow is considered as 'shallow' in following conditions [*Seibert*, 1990]: this is a Foehn with all typical properties in the valleys, but without pronounced southerly wind component at upper level (above crest height). It can be understood as a compensation flow due to cross-ridge pressure gradients which are a result of different air masses on both sides, and therefore occurs in the lee of major alpine passes (acting as "holes" in the mountain barrier). Since such temperature and pressure gradients are present also during high-reaching Foehn (even stronger in these cases), a kind of shallow Foehn is always superimposed to the high-reaching type, being visible by relatively low Foehn temperatures in the affected regions. Shallow Foehn often is a temporary stage in the evolution of a Foehn situation.

# 4.2 Examples for Backscatter Lidar profiles in and out of the Foehn events: RCS, CSG and ABC

Since the Foehn wind brings a clean air (lower humidity and aerosol content), it modifies the aerosol profile in the valley, by removing the valley PBL. Examples of such modification during successive steps of Foehn development are presented in Figs 4.3–4.11. The studied cases are during IOP 04-05 [October 1-2, 1999*], IOP 01 [September 15, 1999], IOP 02 [September 19, 1999] and IOP 04 [September 30, 1999].

## 4.2.1 IOP's 04-05 (1-2/10/1999)

IOP 05 Foehn event was a shallow and valley Foehn case, slowly descending and ascending. Figure 4.3 presents the PBL status before the start of the Foehn event on October 1 between 16h05** and 17h00 (end of IOP 04). The figure presents a typical state of valley PBL, in non-Foehnic conditions. We may see the vertical profile of ABC as nearly uniform below the temperature inversion at about 2000 m. An accumulated aerosol layer is formed below the inversion, i.e. at the top of the PBL. The synoptic westerly flow is limited above the surrounding mountain peaks level (SMPL).

Figure 4.4 presents measurements on October 1 (23h15-23h55) and radiosonde data (23h15). The right panel shows that the Foehn layer starts to form above around 1500 m (a case probably of wind channeling. Above the SMPL, the synoptic wind direction has changed from W to SW. The Foehn flow is marked also by a strong temperature inversion at about 1900 m (central panel). The PBL aerosol layer top altitude has decreased by about 200 m compared to the measurement around 17h00 (see Fig. 4.3). CSG and PTG show a good anti-correlation, i.e., the altitude of the local minima of the CSG is close to the altitude of the local maxima of PTG. A light aerosol layer with top at 2800 m has formed, marked also by successive maximum and minimum of the CSG.

* Further in this Chapter, all indicated dates refer to the year 1999
** All time indications are UTC

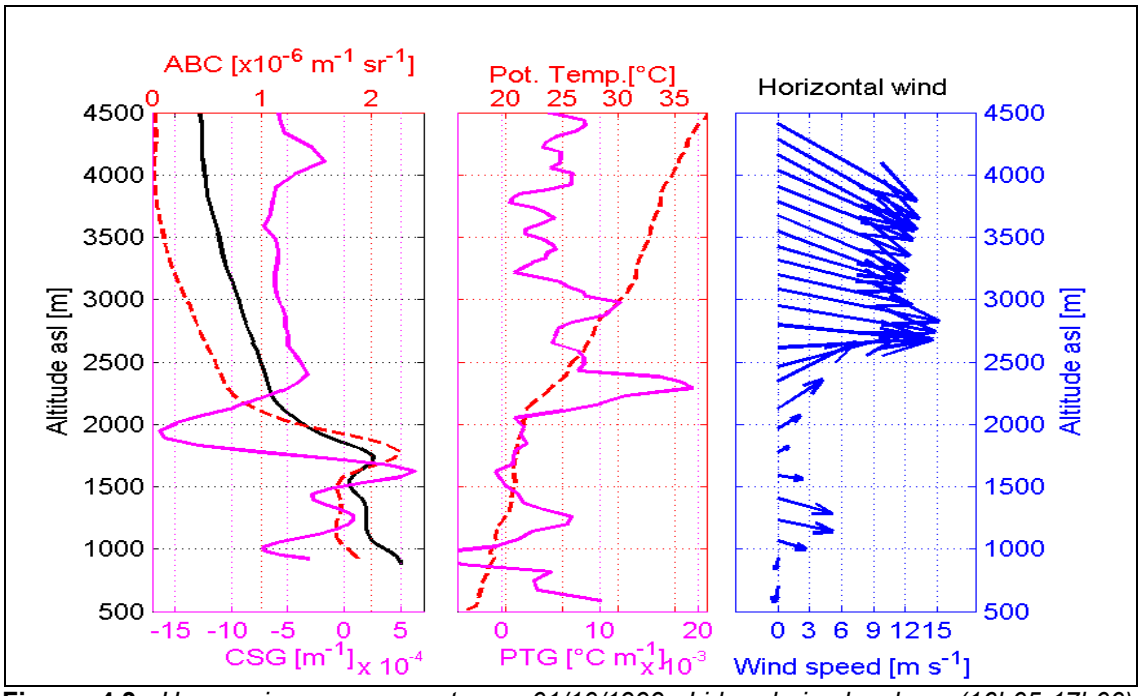


**Figure 4.3.** *Upper air measurements on 01/10/1999. Lidar derived values (16h05-17h00), radiosonde data (17h00). Left panel: RCS (black line, no scale, zero value indicated as a tick on upper axis); CSG (magenta line, lower axis, aerosol backscatter coefficient ABC (red dash line, top axis); central and right panels: radiosonde data from the station Buchs-Grabs; central panel: potential temperature (red dash line, upper axis), potential temperature gradient (magenta line, bottom axis); right panel: horizontal wind speed (wind speed scale bottom, north upward). Range resolutions are: (i) Lidar: from 25 m at 900 m to 125 m at 4500 m; (ii): radiosonde temperatures: 60 m; (iii): radiosonde wind: 180 m.*

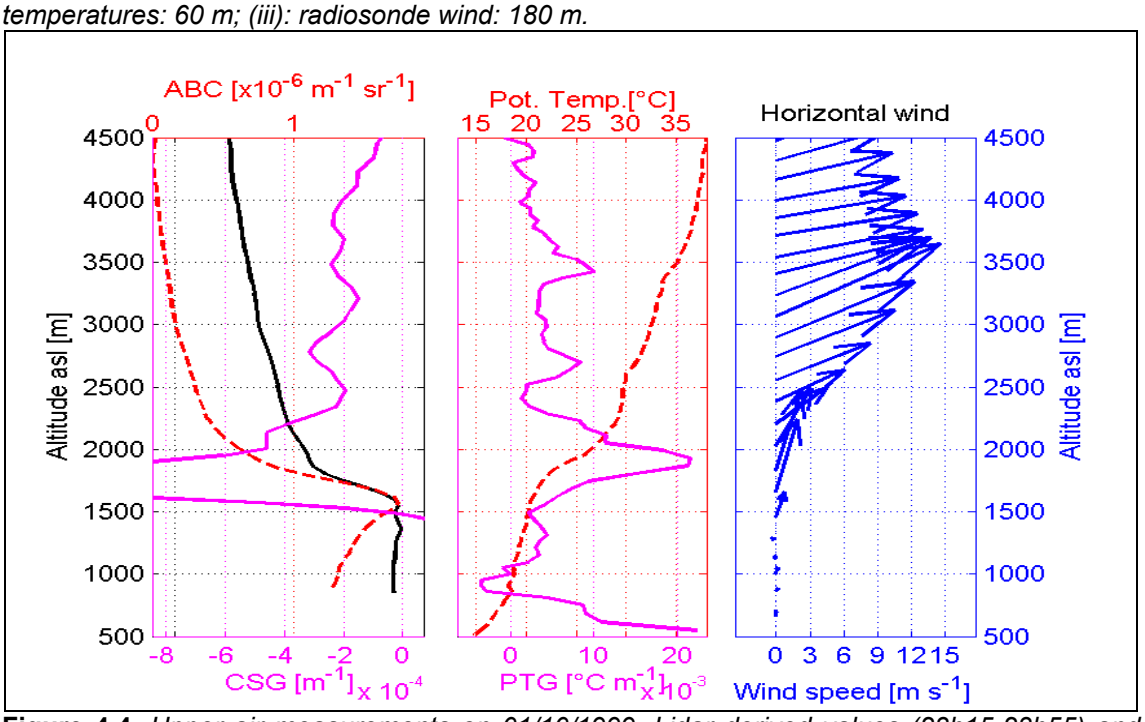


**Figure 4.4.** *Upper air measurements on 01/10/1999. Lidar derived values (23h15-23h55) and radiosonde data (23h15). Left panel: RCS (black line, no scale, zero value indicated as a tick on upper axis); CSG (magenta line, lower axis, aerosol backscatter coefficient ABC (red dash line, top axis); central and right panels: radiosonde data from the station Buchs-Grabs; central panel: potential temperature (red dash line, upper axis), potential temperature gradient (magenta line, bottom axis); right panel: horizontal wind speed (wind speed scale bottom, north upward). Range resolutions are: (i) Lidar: from 25 m at 900 m to 125 m at 4500 m; (ii): radiosonde temperatures: 60 m; (iii): radiosonde wind: 180 m.*

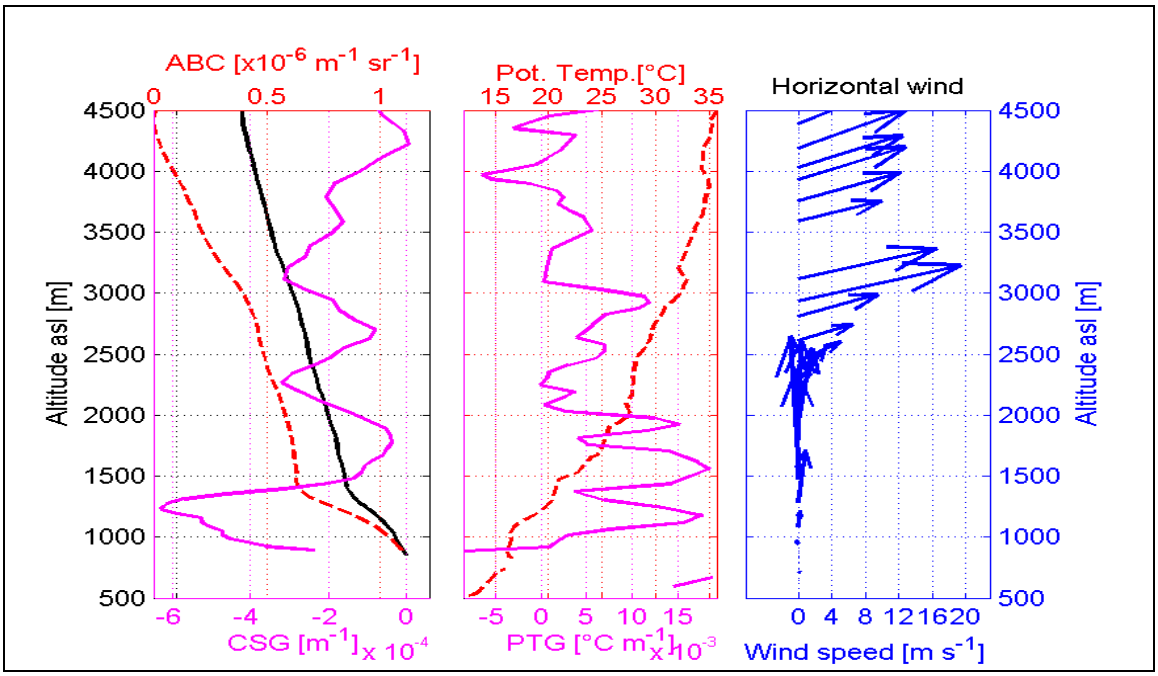


**Figure 4.5.** *Upper air measurements on 02/10/1999. Lidar derived values (04h40-05h20) and radiosonde data (05h00). Left panel: RCS (black line, no scale, zero value indicated as a tick on upper axis); CSG (magenta line, lower axis, aerosol backscatter coefficient ABC (red dash line, top axis); central and right panels: radiosonde data from the station Buchs-Grabs; central panel: potential temperature (red dash line, upper axis), potential temperature gradient (magenta line, bottom axis); right panel: horizontal wind speed (wind speed scale bottom, north upward). Range resolutions are: (i) Lidar: from 25 m at 900 m to 125 m at 4500 m; (ii): radiosonde temperatures: 60 m; (iii): radiosonde wind: 180 m.*

Figure 4.5 presents the Lidar measurement from 04h40 till 05h20 on October 2, together with the radiosonde measurement at 05h00. As the right panel shows, the Foehn layer has extended down to around 1300 m and is well channeled to the altitude of SMPL. The flow is marked also by a strong temperature inversion at about 1200 m (central panel). The left panel shows that the aerosol layer top altitude has decreased by about 600 m since the previous measurement around 23h30 (Fig. 4.4). Two nearly uniform aerosol layers with weak changes of the ABC, with tops at 2300 m and 3200 m respectively have developed. The comparison between CSG and the PTG shows again a good coincidence between the altitude of the first CSG minimum (from the surface) and the first maximum of the PTG (also from the surface). A decrease of the ABC value in the lowermost part of the profile is seen, compared to the same value in Fig. 4.3 and Fig. 4.4.

Figure 4.6 presents Lidar measurements from 08h00 till 09h00 on October 2, together with radiosonde data at 08h00. As seen in the right panel, the Foehn extends down to approximately 1000 m. The surface station Balzers indicated the Foehn penetration to the surface at around 08h50. The ABC value at the lowermost part of the profile has dropped down to $0.75 \times 10^{-6}$ $m^{-1}sr^{-1}$. Compared to the same value shown in Figs. 4.3, 4.4 and 4.5, this value is the smallest in a row of a gradual decrease. The altitude of the lowermost minimum of CSG and the lowermost maximum of the PTG are very close to each other. The difference may be explained by the local differences in the Foehn flow, which may be significant at lower altitudes.

Figure 4.7 presents again established Foehn, with a lower limit down to approx 1000 m. Weite surface station data indicates the Foehn arrival at 11h40. We notice an excellent coincidence between the altitudes of the PTG first maximum and the CSG first minimum, coinciding also with the altitude of the lower boundary of the Foehn layer.

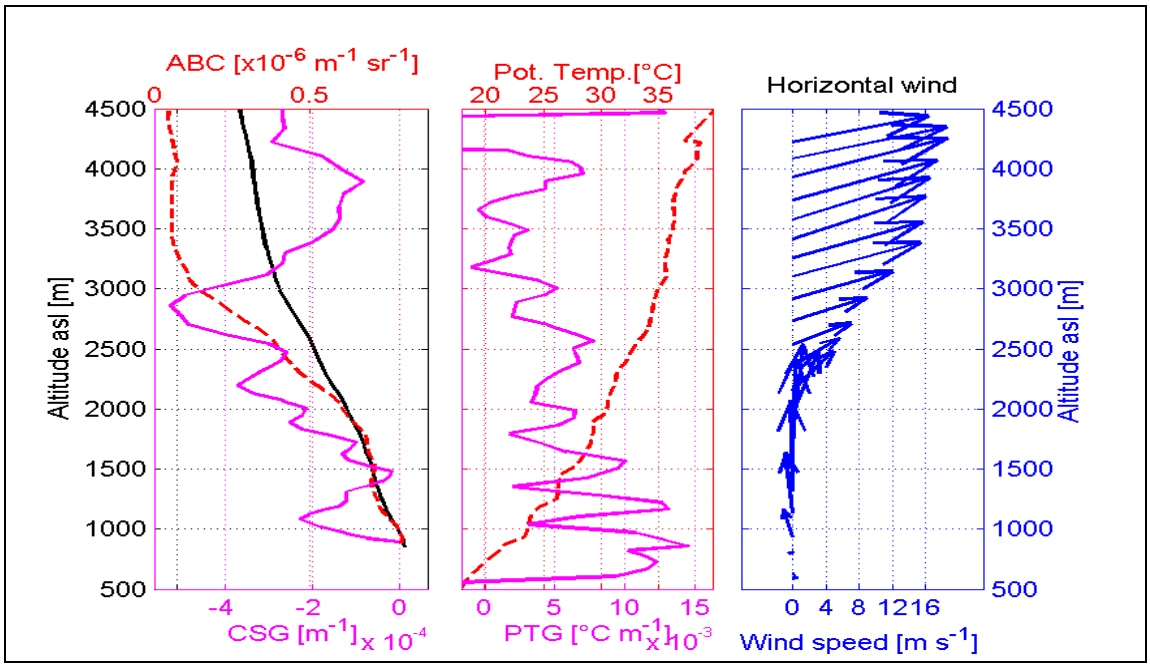


**Figure 4.6.** *Upper air measurements on 02/10/1999. Lidar derived values (08h00-09h00) and radiosonde data (08h00). Left panel: RCS (black line, no scale, zero value indicated as a tick on upper axis); CSG (magenta line, lower axis, aerosol backscatter coefficient ABC (red dash line, top axis); central and right panels: radiosonde data from the station Buchs-Grabs; central panel: potential temperature (red dash line, upper axis), potential temperature gradient (magenta line, bottom axis); right panel: horizontal wind speed (wind speed scale bottom, north upward). Range resolutions are: (i) Lidar: from 25 m at 900 m to 125 m at 4500 m; (ii): radiosonde temperatures: 60 m; (iii): radiosonde wind: 180 m.*

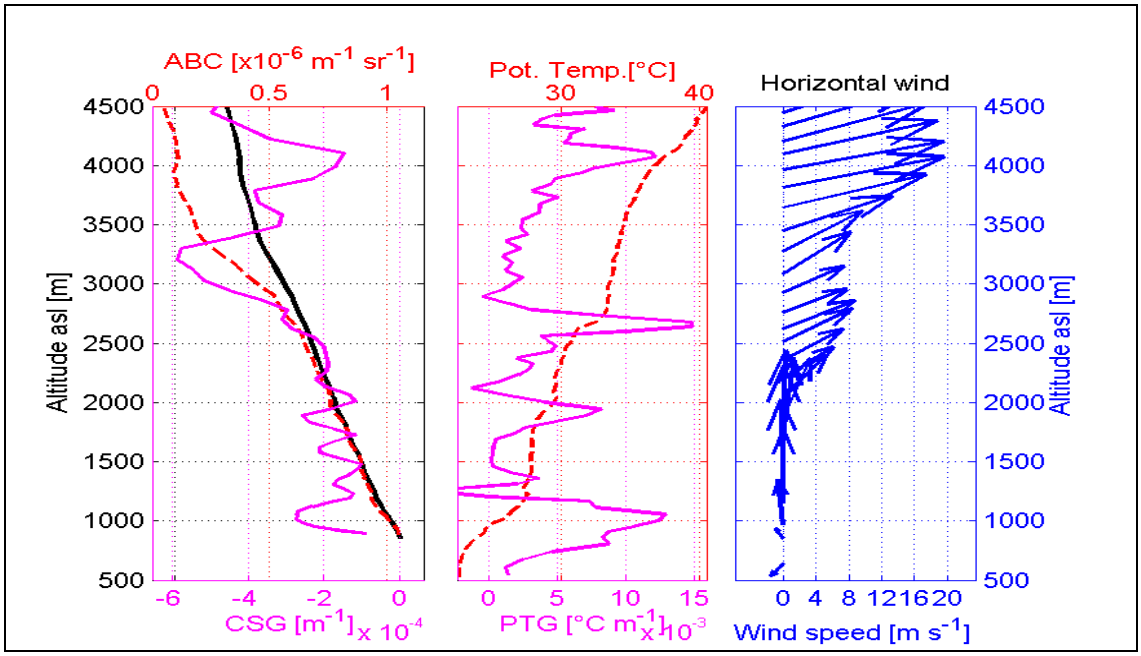


**Figure 4.7.** *Upper air measurements on 02/10/1999. Lidar derived values (11h30-12h30) and radiosonde data (11h45). Left panel: RCS (black line, no scale, zero value indicated as a tick on upper axis); CSG (magenta line, lower axis, aerosol backscatter coefficient ABC (red dash line, top axis); central and right panels: radiosonde data from the station Buchs-Grabs; central panel: potential temperature (red dash line, upper axis), potential temperature gradient (magenta line, bottom axis); right panel: horizontal wind speed (wind speed scale bottom, north upward). Range resolutions are: (i) Lidar: from 25 m at 900 m to 125 m at 4500 m; (ii): radiosonde temperatures: 60 m; (iii): radiosonde wind: 180 m.*

## 4.2.2 IOP 01 (15/09/1999)

IOP 01 took place after the "heat-wave" described in Chapter 3. The measurements presented in Fig. 4.8 shows Foehn to the surface with a first maximum of the PTG evidently so close to the surface, that the respective CSG minima is below the Lidar overlap altitude and in this way, cannot be detected. The ABC has a twice-higher value than during Foehn in IOP 05. It is interesting to see that there is three successive drops of the ABC stratification, shown also by the CSG (left panel), similar to the case of "heat-wave" which expired the day before.

During this measurement the Foehn was register at all surface stations listed in Table 4.1 (Foehn onset was registered during this period at Vilters (11h00) and Vaduz (11h20)).

The measurements during the same IOP but later (16h30-17h30 on the same day) are presented in Fig. 4.9. The Foehn layer is higher, with lower limit at 1000-1200 m. The CSG indicates likely a cold pool recovery (see the CSG first minimum altitude at 1200 m in the left panel). ABC values are approximately twice smaller than values around 11h00 between 2000-3000 m. On the other side, below the altitudes of 1000-1200 m, there is a rapid increase of ABC, indication also a fast cold pool re-forming. Possible mechanisms for this re-forming are:

(i) advection of cold air, made possible by a local weakening of the Foehn (that forced cold air northwards)
(ii) advection of cold air by an enforced advance of the cold air pool up the valley, which lifts the Foehn air
(iii) local cold air production

At around 3000 m, a PTG minimum corresponds to a CSG maximum, below a temperature inversion around 3500 m, corresponding approximately to the altitude of an accumulation layer.

During this IOP, the expiration of the Foehn at surface stations was recorded at 14h40 in Weite and at 16h20 in Flaescherberg. It is interesting to notice that, at the station Luenersee (altitude: 1980 m; location: outside of the field of view in Fig. 4.2, 20 km eastward from Truebbach, nearby a ridge above a tributary of the RV), the Foehn left only at 18h00. In Guetsch, pass Foehn ended at 18h50.

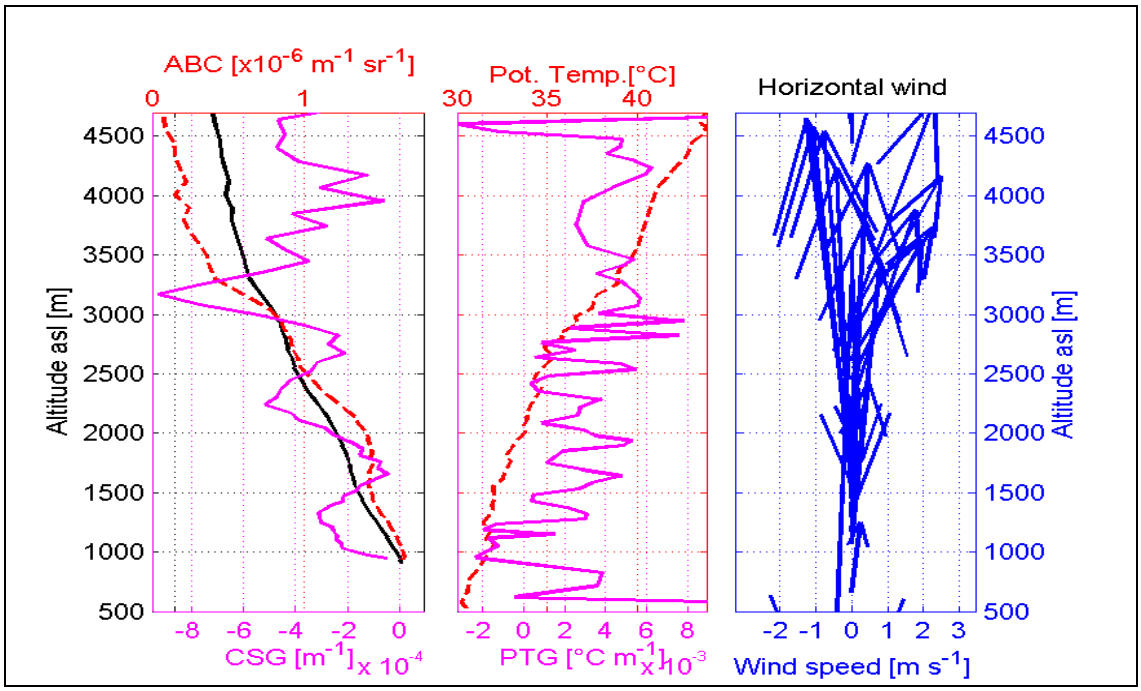


**Figure 4.8.** *Upper air measurements on 15/09/1999 (IOP 01). Lidar derived values (10h45-11h30) and radiosonde data (11h00). Left panel: RCS (black line, no scale, zero value indicated as a tick on upper axis); CSG (magenta line, lower axis, aerosol backscatter coefficient ABC (red dash line, top axis); central and right panels: radiosonde data from the station Buchs-Grabs; central panel: potential temperature (red dash line, upper axis), potential temperature gradient (magenta line, bottom axis); right panel: horizontal wind speed (wind speed scale bottom, north upward). Range resolutions are: (i) Lidar: from 25 m at 900 m to 125 m at 4500 m; (ii): radiosonde temperatures: 60 m; (iii): radiosonde wind: 180 m.*

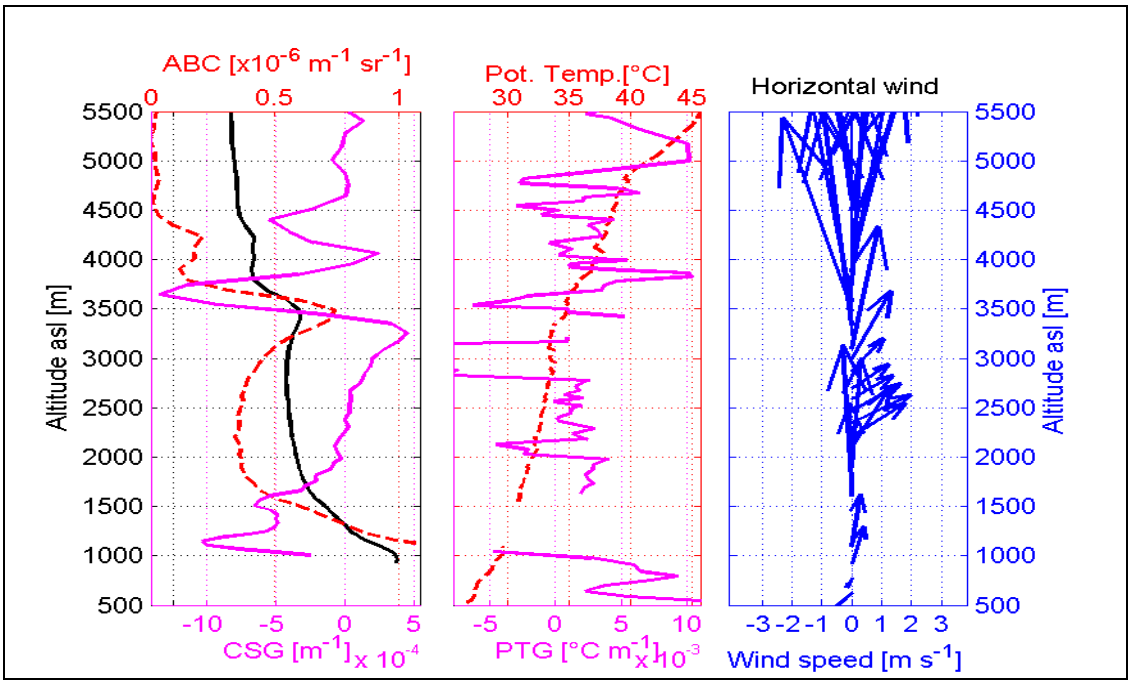


**Figure 4.9.** *Upper air measurements on 15/09/1999 (IOP 01). Lidar derived values (16h30-17h30) and radiosonde data (17h00). Left panel: RCS (black line, no scale, zero value indicated as a tick on upper axis); CSG (magenta line, lower axis, aerosol backscatter coefficient ABC (red dash line, top axis); central and right panels: radiosonde data from the station Buchs-Grabs; central panel: potential temperature (red dash line, upper axis), potential temperature gradient (magenta line, bottom axis); right panel: horizontal wind speed (wind speed scale bottom, north upward). Range resolutions are: (i) Lidar: from 25 m at 900 m to 125 m at 4500 m; (ii): radiosonde temperatures: 60 m; (iii): radiosonde wind: 180 m.*

## 4.2.3 IOP 02 (19/09/1999) and IOP 04 (30/09/1999)

During IOP 02 (September 19, 1999), the Foehn was indicated at surface by the stations as follows: in Weite at 07h00 on September 19, in Balzers at 22h30 on September 18, in Flaesherberg at 07h10 on September 19, in Luenersee (1980 m) at 20h00 on September 18. Figure 4.10 presents Lidar measurements from 04h30 till 05h15 and radiosonde data on 05h00, on September 19. The Foehn is down to the surface (see right panel, next page) and this is seen also in the PTG as a sharp increase close to the surface. The Foehn flow is well channeled below SMPL and the first minimum of the CSG ((if it exists) lies obviously below the Lidar overlap altitude. It is interesting to see that the upper boundary of the Foehn is also "marked" by a drop in the ABC value, i.e., by a strong CSG minimum at approx 3500 m, corresponding also to a PTG maximum. Also, a slight CSG minimum corresponds to PTG maximum at 1500 m.

Another measurement example, taken during IOP 04 (September 30) is presented in Fig. 4.11. Foehn onset was indicated at the surface stations as follows: in Flaescherberg at 03h10, in Balzers at 7h50. In Weite, Foehn was not detected. The radiosonde was launched from Buchs-Grabs at 05h00 and the Lidar measurements were taken between 03h45 and 04h50. Foehn flow was detected above approximately 1000 m (see right panel, next page). ABC and CSG showed aerosol stratification with several steps of similar magnitude till altitudes slightly above the Foehn upper boundary. Similar set of successive local maxima is seen in the PTG profile. The altitudes of the first minimum in CSG and the first maximum in PTG coincide well, as well as they coincide with the lower boundary of the Foehn flow.

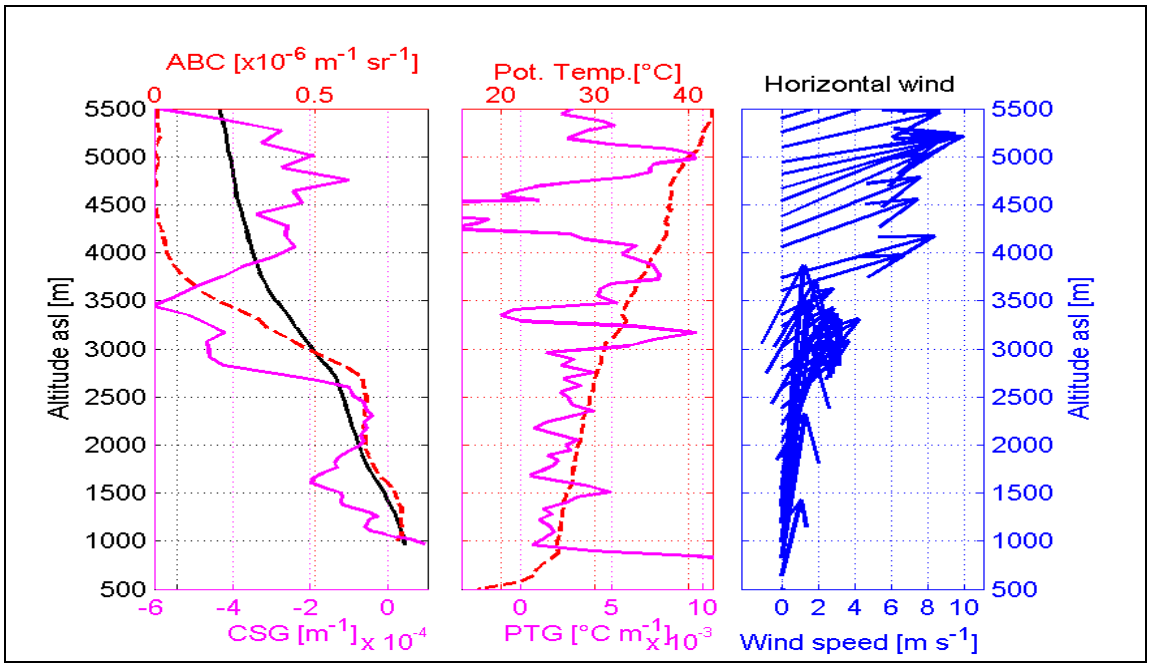


**Figure 4.10.** *Upper air measurements on 19/09/1999 (IOP 02). Lidar derived values (04h30-05h15) and radiosonde data (05h). Left panel: RCS (black line, no scale, zero value indicated as a tick on upper axis); CSG (magenta line, lower axis, aerosol backscatter coefficient ABC (red dash line, top axis); central and right panels: radiosonde data from the station Buchs-Grabs; central panel: potential temperature (red dash line, upper axis), potential temperature gradient (magenta line, bottom axis); right panel: horizontal wind speed (wind speed scale bottom, north upward). Range resolutions are: (i) Lidar: from 25 m at 900 m to 125 m at 4500 m; (ii): radiosonde temperatures: 60 m; (iii): radiosonde wind: 180 m.*

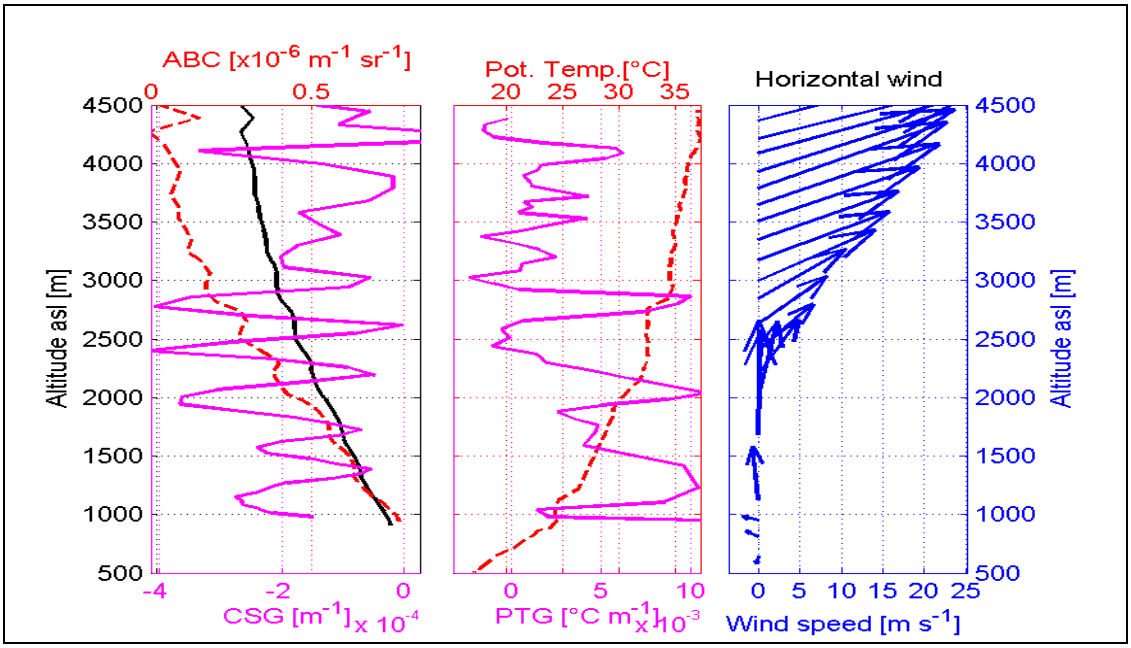


**Figure 4.11.** *Upper air measurements on 30/09/1999 (IOP 04). Lidar derived values (03h45-04h50) and radiosonde data (05h00). Left panel: RCS (black line, no scale, zero value indicated as a tick on upper axis); CSG (magenta line, lower axis, aerosol backscatter coefficient ABC (red dash line, top axis); central and right panels: radiosonde data from the station Buchs-Grabs; central panel: potential temperature (red dash line, upper axis), potential temperature gradient (magenta line, bottom axis); right panel: horizontal wind speed (wind speed scale bottom, north upward). Range resolutions are: (i) Lidar: from 25 m at 900 m to 125 m at 4500 m; (ii): radiosonde temperatures: 60 m; (iii): radiosonde wind: 180 m.*

# 4.3 Temporal variation of the aerosol profiles during Foehn, shown by RCS, surface meteorological parameters and Scintillometer wind measurements

One of the conclusions from the Chapter 2 is that we may use the Lidar RCS to present the relative evolution of the aerosol vertical profile (aerosol stratification). We will use this in the present sub-chapter to present the correlation between the observed variation in the aerosol stratification during Foehn with the meteorological observations from a number of surface stations and with the Scintillometer wind measurements. The surface meteorological parameters of importance for Foehn definition are: temperature, relative humidity, wind velocity and direction. The Scintillometer gives the horizontal and the vertical wind velocity. This instrument is positioned above the Lidar site at altitude just above the Lidar overlap altitude. Because of this it is critical for observation of the correlation between the Lidar CSG and the wind.

## 4.3.1 Case study 1: IOP's 04-05 (1-3/10/1999)

***Short description of the Foehn event in the RV:***

On October 1 (end of IOP 04), valley Foehn was not detected anywhere in the RV. Pass Foehn begins at 21h20 (Guetsch). The Foehn descent lasted for about 10 hours till valley Foehn was detected in Balzers at 08h50 on October 2. Around our area, the valley Foehn lasted for about 18 hours: A short precipitation occurs around 07h00 on October 3, and a continuous one begins at approximately 12h00. Pass Foehn ended at 11h20 (Guetsch). This event was considered as a short, but slowly descending and slowly ascending Foehn event.

Figure 4.12 presents the evolution of the RCS and the altitude of the first minimum of CSG, together with the surface meteorological data and Scintillometer wind values for IOP's 04-05, October 1-3.

Figure 4.13 presents the evolution of the RCS up to 4500 m. Clouds are detected having base altitude above 4500 m at noon on October 2, with a gradually falling base altitude to 3000 m at morning on October 3 and then a sudden cloud appearance with base altitude at approximately 1000 m and even below (see the saturated colors for high values of RCS in Fig. 4.13).

As we have mentioned in Chapter 1, two methods to define the top of mixed layers are presented in [*Menut*, 1999]: (i) the gradient method and (ii) the variance (centroid) method. The gradient minimum method is based on the more or less constant altitude distribution of the aerosol in the mixed layer below altitudes with much less aerosol concentration. In this way, at the altitude of mixing with the free troposphere, there is a minimum of the CSG. The centroid method makes use of the fact that at the top of convective mixed layer there is an intensive mixing of aerosol rich air from the PBL with the aerosol poor air from the free troposphere. This mixing takes place via up-drafts containing aerosol rich air from the convectively mixed PBL to the free troposphere and down-drafts containing aerosol-poor air from the free troposphere to the PBL. Due to this, the Lidar backscatter signal at altitude of convective PBL top takes place successively from air parcels with higher and lower aerosol content. In this way, the variance of the RCS at such altitude presents a maximum.

Physically, the situation of the cold pool erosion by the Foehn is different from the situation of convective PBL mixing with the free troposphere. Nevertheless, we decided to apply the two methods on the Lidar measurements during IOP's 04-05, the phase from 12h00 on October 1 till 06h00 on October 2 (as seen on Fig. 4.12, the end of this period corresponds approximately to the passage of the first CSG minimum below the Lidar field of view). Figures 4.14a and 4.14b present with the same time scale respectively the CSG and the centroid. As we see, the altitude of the variance maximum during the phase of the cold pool erosion coincides exactly with the altitude of the first minimum of the CSG. As we have seen it in the previous section, the altitude of the lowermost CSG minimum is consistently coinciding with the cold pool top. The fact that the altitude of maximum variance of the RCS coincides with the cold pool top suggests to the turbulent partial mixing between the Foehn air and the air in the cold pool, taking place at the interface between them, i.e., at the cold pool top.

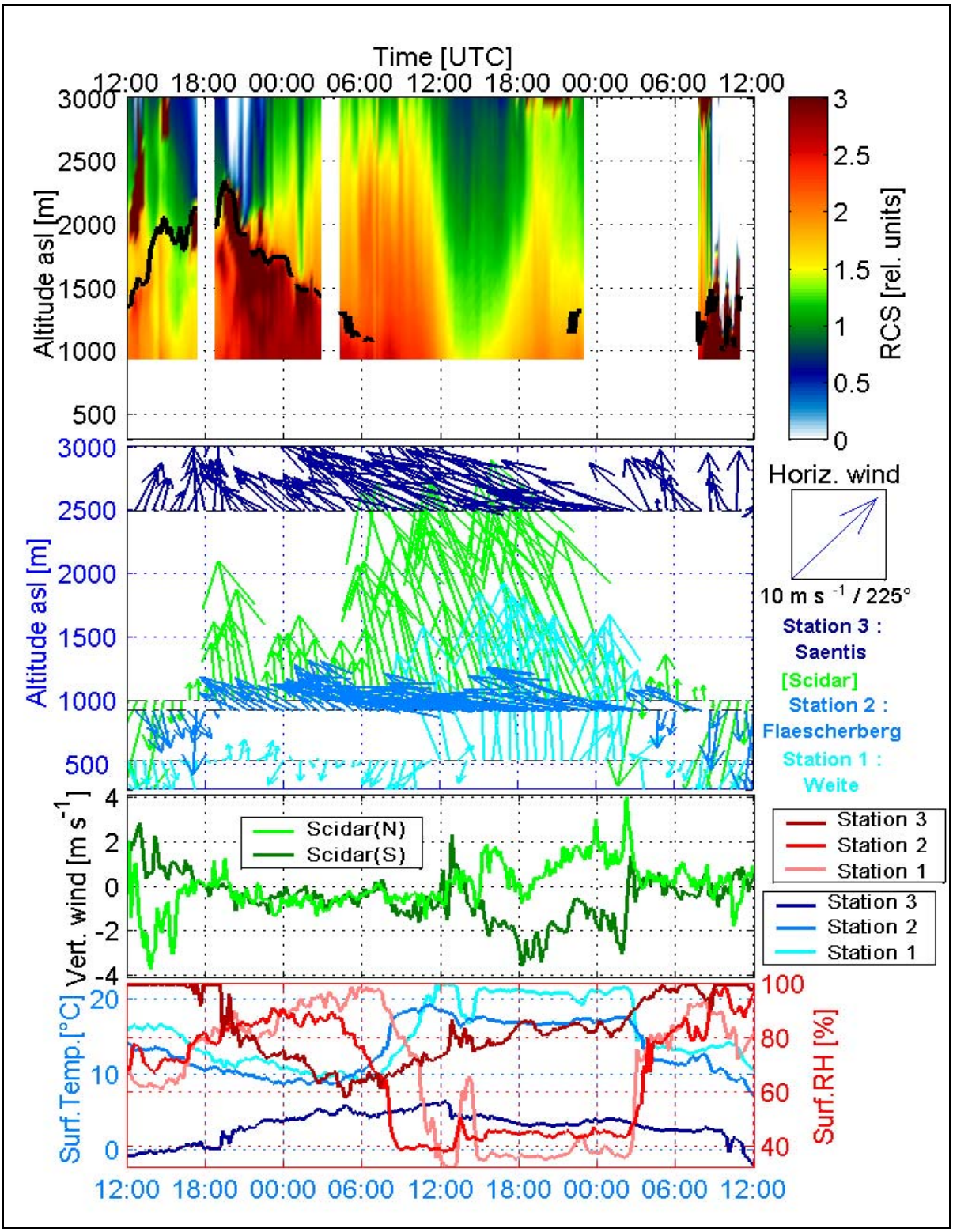


**Figure 4.12.** *Evolution of aerosol profile in relative units and meteorological parameters in the RV during IOP's 04-05 (1-3/10/1999). Top panel: Lidar RCS with 12 min resolution; clouds are shown in saturated colors. The black line indicates the evolution of the first altitude above the Lidar field of view of the CSG minimum as detected by the gradient method. Second panel from top: horizontal wind measurements at three surface stations and the Scintillometer, with 40 min resolution. Third panel from top: vertical wind measurements measured by the Scintillometer. Bottom panel: temperature (red lines, right scale) and relative humidity (blue lines, left scale) measured at the surface stations.*

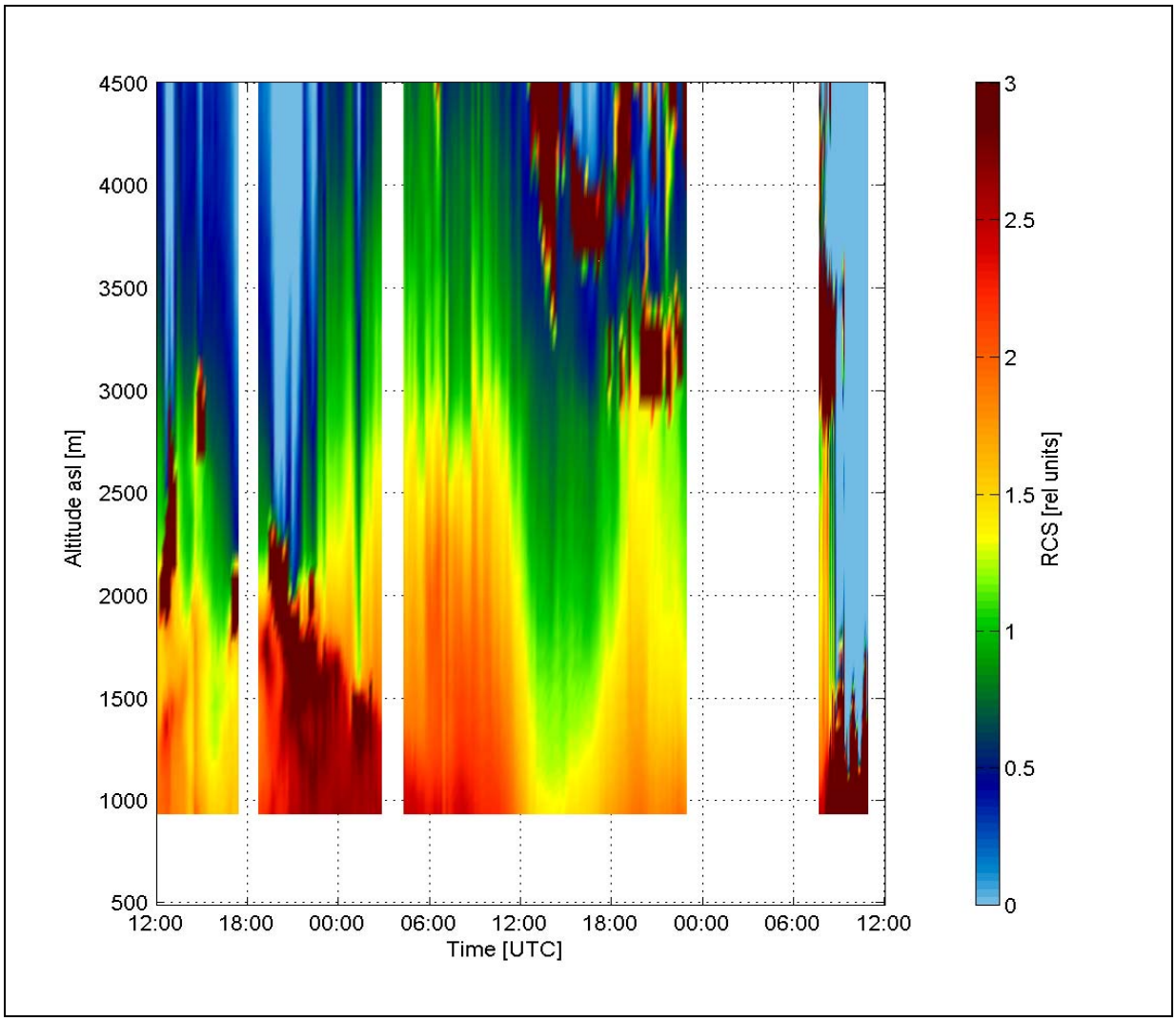


**Figure 4.13.** *IOP's 04-05 (1-3/10/1999): evolution of the RCS signal up to 4500 m, with saturated colors for clouds. Cyan colored areas correspond to very low signal.*

**Table 4.3.** *Radiosonde measurements from Buchs-Grabs: wind direction and speed at altitude of cloud base detected by the Lidar on IOP's 04-05 (1-3/10/1999).*

| Day | Hour | Altitude asl [m] | Wind direction [deg] | Wind speed [m/s] |
|---|---|---|---|---|
| 1 October | 11h00 | 2000 | 250 | 15 |
| 1 October | 17h00 | 2000 | 230 | 04 |
| 1 October | 23h00 | 1700 | 190 | 07 |
| 2 October | 02h00 | 1300 | 200 | 07 |
| 2 October | 12h00 | 4200 | 250 | 17 |
| 2 October | 14h00 | 3900 | - | - |
| 2 October | 17h00 | 3800 | 260 | 19 |
| 2 October | 20h00 | 3200 | 235 | 11 |
| 2 October | 23h00 | 4200 | 250 | 20 |
| 3 October | 08h00 | 3200 | 215 | 12 |
| 3 October | 08h00 | 1000 | 190 | 03 |
| 3 October | 11h00 | 1000 | 315 | 03 |

Figure 4.14c presents the altitude of the lowermost CSG minimum (as in Fig. 4.14a) together with the meteorological parameters. At the beginning of the measurements, the Lidar profile shows a typical valley PBL and PBL top up to the altitude of the surrounding mountains, with a top reaching around 2300 m on the afternoon of October 1. During early night of October 2, the Scintillometer indicated a sudden change of the wind from North to predominant direction South and high wind speed (up to approximately 15 m/s). Station Saentis also show a high velocity of SE wind. Station Flaesherberg show high SE wind starting from 00h00 on October 2. The strong decrease of the RCS during October 2 (see Fig. 4.13) is combined with a drop of the altitude of the first minimum of the CSG to values close to and below the altitude of the Lidar full overlap, i.e., below 500 m agl: see the period from approximately 06h00 till 23h00. During this period, the Scintillometer shows a strong South wind (up to 20-25 m/s), that is, well channeled along the valley axis. Station Weite shows that this wind penetrates to the surface around noon on October 2. During first half of October 2, the Scintillometer shows also a consistent downward vertical wind velocity in the two channels ("North" and "South"). This coincides with the period when the Foehn is still not indicated at the surface in Weite. During the second half of the day the "North" and "South" channels reading for the vertical wind start to differ. A probable explanation is that there is a standing mountain wave in that area with a downward branch near Ergellen and its upward branch near Flusa*. Indication for such wave at that location is also reported in [*Beffrey et al.*, 2002], but for IOP 08.

The time for the decrease of the surface relative humidity (RH) and the increase of the temperature, as indicated in Weite and Flaesherberg correlate well with the appearance of strong wind from South in Weite and by the Scintillometer. Respectively the time for the increase of RH and temperature decrease correlates with the disappearing of the South wind in Weite and by the Scintillometer. Such behavior of the meteorological parameters correlates with the Lidar RCS (aerosol backscatter) and CSG (cold pool top). The period when the Lidar determined cold pool top is below the Lidar overlap altitude (i.e. close to the surface), coincides with the sharp increase of the Scintillometer horizontal South wind and also with the increase of downward vertical velocity measured on the Scintillometer South sensor. During this phase the Foehn is channeled in the valley. The upper air radiosonde measurements presented in Figs. 4.3-4.7 show that the Foehn flow upper boundary is around altitudes of 2000-2400 m. This is seen also on Saentis data, as the wind changes from South to SE, combined with a slight temperature increase during the Foehn period.

During late night of October 2-3 and early morning on October 3, the Lidar measurements were blocked by a technical problem. The continuation of the measurements after the morning of October 3 shows a recovered cold pool (PBL). This is consistent with the patterns of the wind, temperature and RH, showing the expiration of the Foehn.

As we see from Figs. 4.3-4.7, during the IOP's 04-05, the radiosonde measurements at Buchs-Grabs show westerly synoptic flow, turning to W-SW during the Foehn phase. At 17h00 on October 1, an up-valley wind (i.e. northerly) is blowing below 1000 m. At 23h15, as a southerly flow begins to channel between 1500-2000 m, the wind in the cold pool below 1500 m is very weak. During the cold pool erosion, a northerly wind is detected at the surface. During the valley Foehn, all wind measurements till altitudes of about 2000 m indicate southerly flow with typical wind speed of 10 m/s. At the end of valley Foehn period, a northerly wind is triggered, bringing aerosol rich air masses. Table 4.3 presents the wind direction and speed determined from Buchs-Grabs radiosondes, at altitudes of cloud base and for the time of clouds appearance, detected by the Lidar (Fig. 4.13). As we see, in all cases the clouds are brought by wind from West, with exception for the clouds at the end of the Foehn, when the wind at the altitude of the cloud base is from North.

* In the Scintillometer's dataset, persistent differences in vertical wind component between the two paths have been noticed several times. The reasons may be: (i) meteorological (dynamical) (ii) local environment at the devices (like eg. dew formation on the glasses)

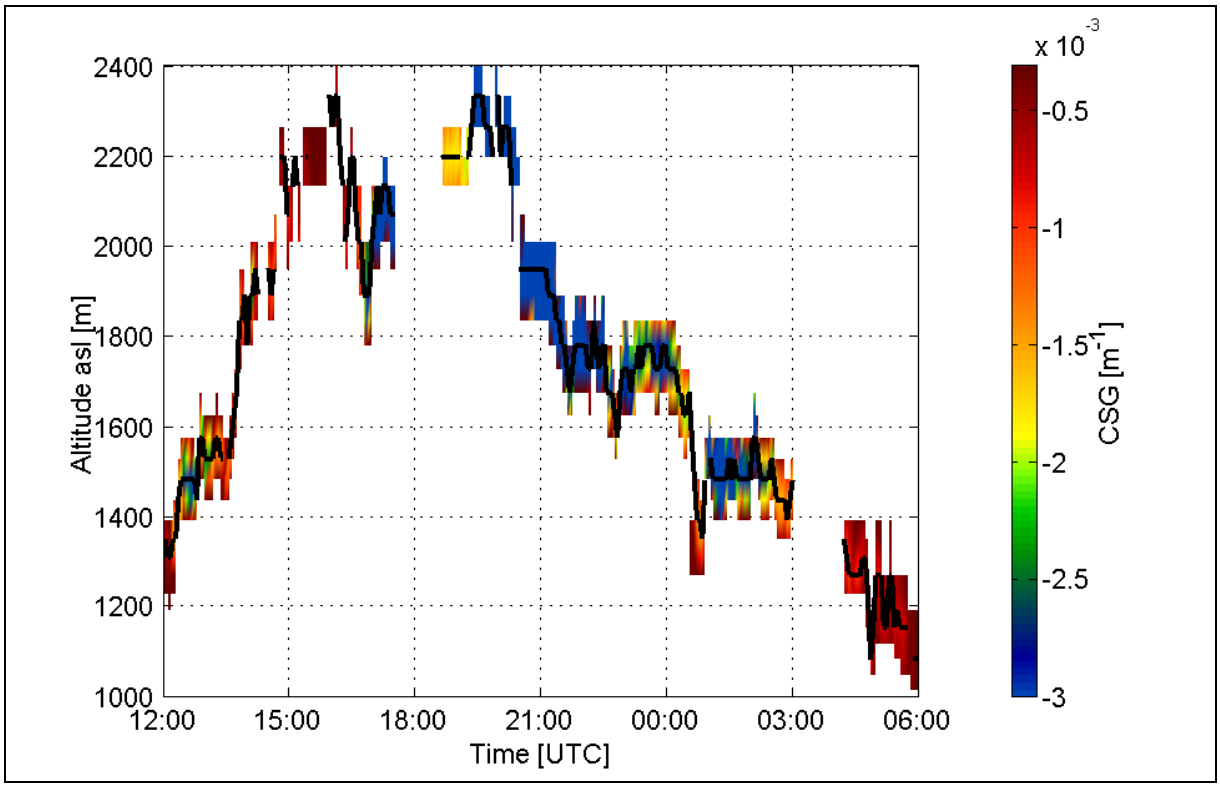


**Figure 4.14a.** *Evolution of the first altitude above the Lidar field of view of the CSG minimum during IOP 05 (1-2/10/1999) Foehn onset, with 5 min resolution. The black line marks the altitude of the detected minima; the colors trips show in saturated colors the CSG values.*

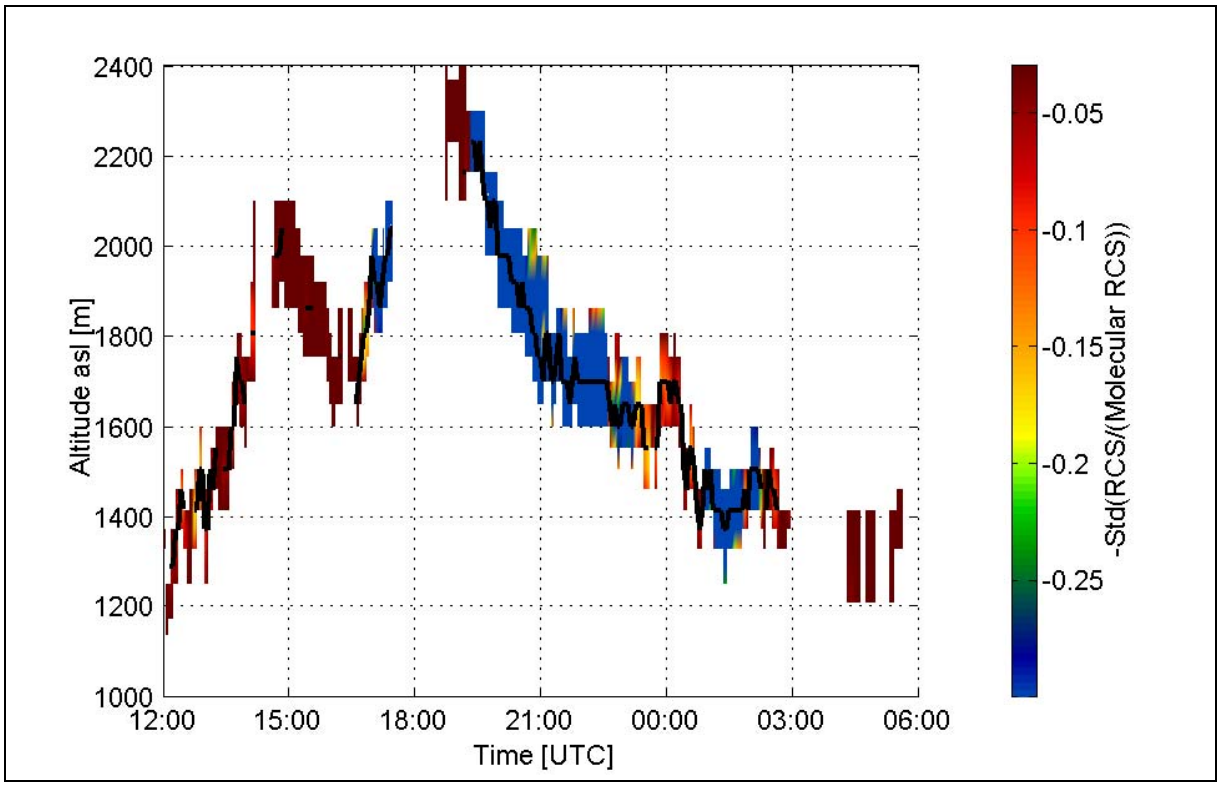


**Figure 4.14b.** *Evolution of the first altitude above the Lidar field of view of the centroid values maximum during IOP 05 (1-2/10/1999) Foehn onset, with 5 min resolution. The black line marks the altitude of the detected maxima, the colors strips show in saturated colors the variance values, with a minus sign for presentation similarity with Fig. 4.14a.*

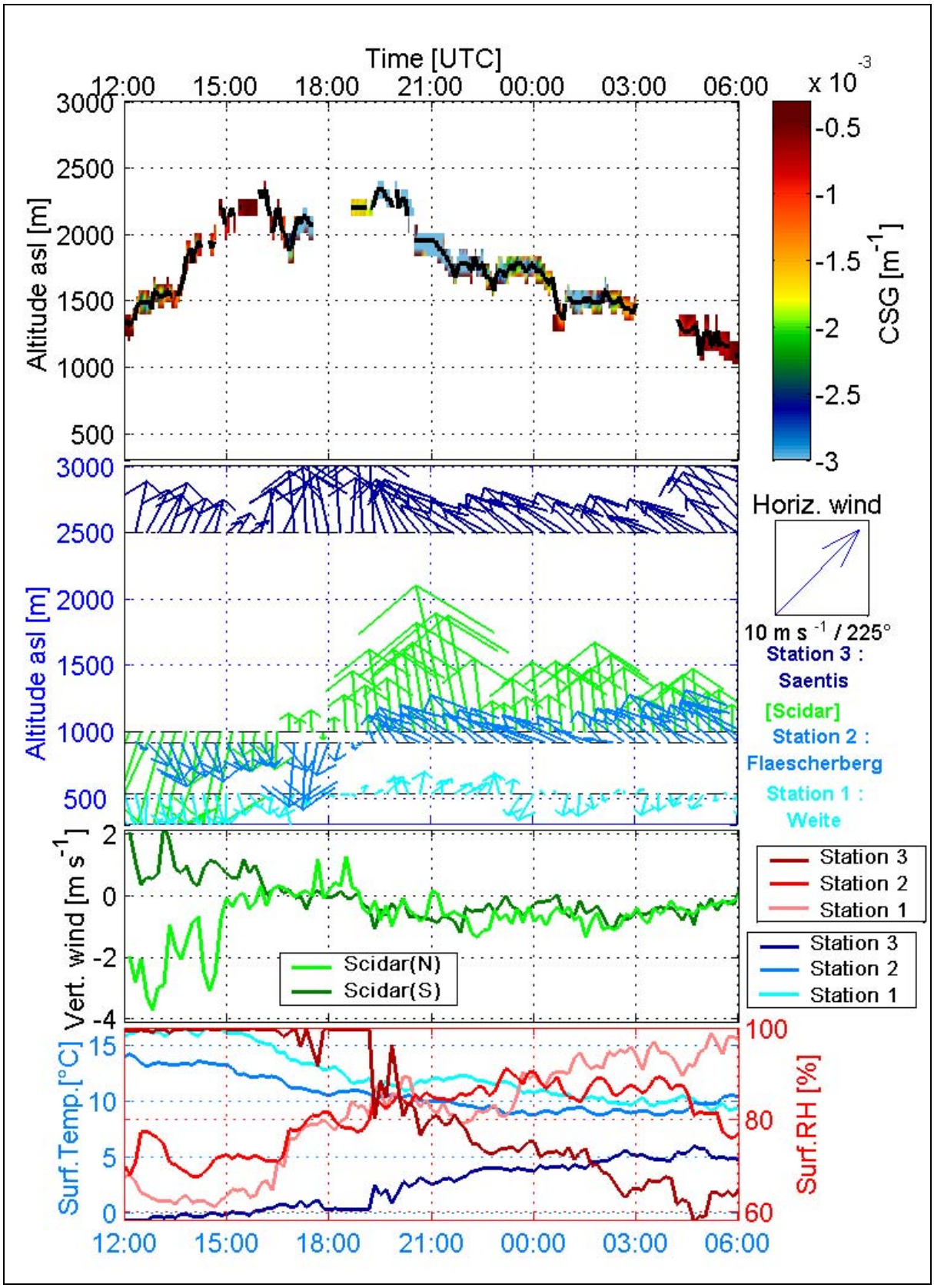


**Figure 4.14c.** *IOP 05 Foehn onset (1-2/10/1999): evolution of the first altitude above the Lidar field of view of the CSG minimum and meteorological parameters in the RV. Top panel: CSG first minimum as in Fig. 4.14a. Other panels: meteorological parameters as in Fig. 4.12 (horizontal winds with 20 min resolution).*

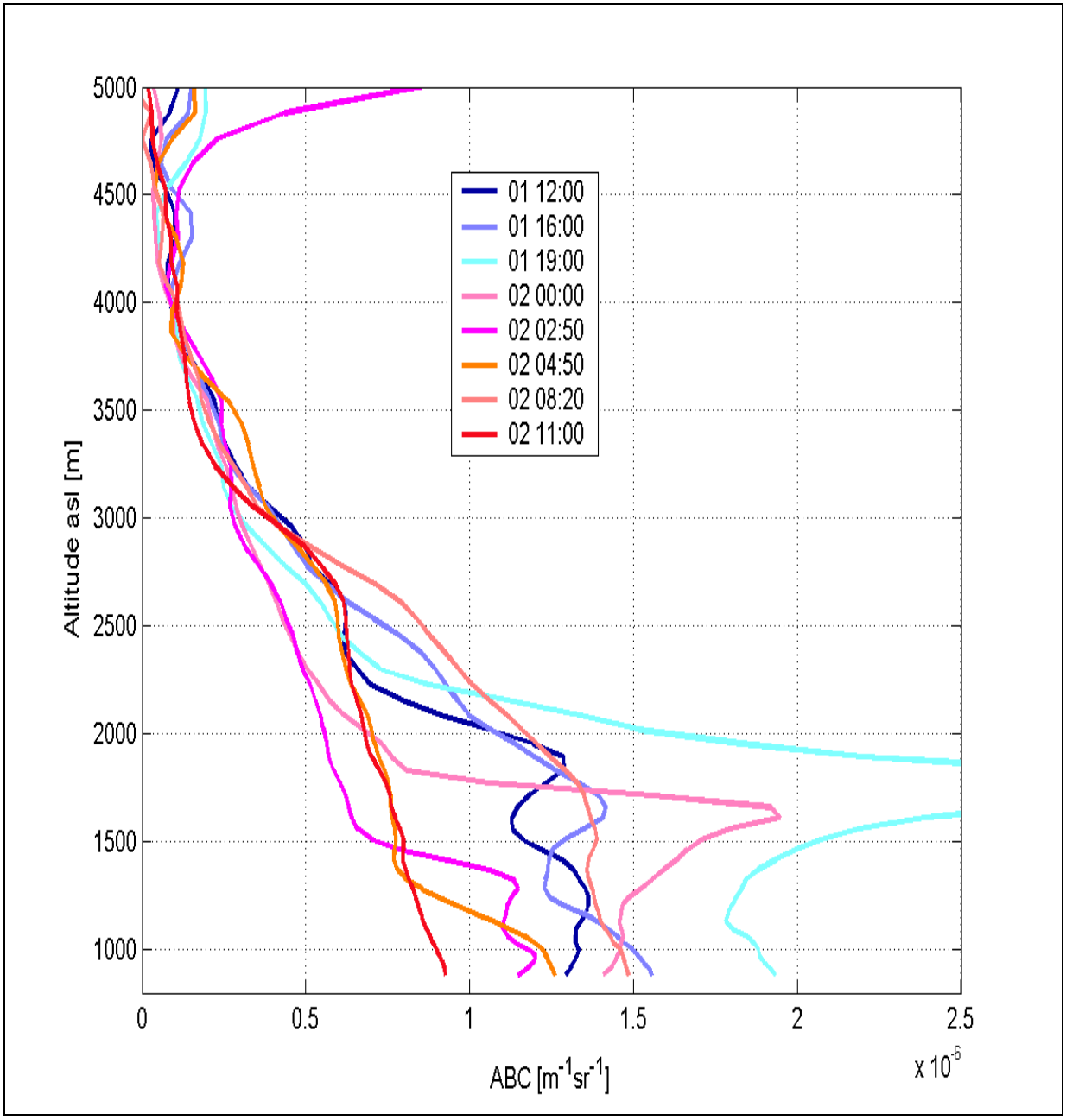


**Figure 4.15.** *Evolution of the ABC during IOP 04-05 (1-2/10/1999), with approximately 30 min resolution. The legend indicates the center of the measurement periods, in format "dd hh:mm".*

Figure 4.15 present the ABC profiles during successive steps of cold pool erosion. As we see, the Foehn development and the erosion of the cold pool lead to an increase of the ABC above it, i.e., above the cold pool top (compare the profile at 04h50 with the profile at 08h20). There are two possible explanations. One is that the aerosol content of the Foehn air is higher than the same for the free troposphere above the Valley PBL. The second may be an advection of precontaminated air masses with the Foehn flow. The figure shows the sinking of the top of the aerosol-contaminated layer over night. After valley Foehn onset, the ABC tends to be uniformly decreasing with the altitude increase, i.e. with a very poor stratification (see the value at 11h00). Below altitudes corresponding to approximately SMPL, ABC decreases by about 50% during the Foehn development.

## 4.3.2 Case study 2: IOP's 08-09 (19-23/10/1999)

***Short description of the Foehn events in the RV:***

IOP 08: On October 19, pass Foehn begins at 15h40 (Guetsch). The Foehn reaches 1000 m level in our area at 23h10 (Flaescherberg). It reaches valley floor intermittently in Balzers on October 20 around 07h00 and 08h30, and continuously after approximately 10h00. All surrounding surface stations indicate that the valley Foehn lasted till approximately 13h00 on October 21, and 13h30 at 1000 m level (Flaesherberg).

IOP 09: On October 22, Foehn was again detected at 08h10 (Flaescherberg), 08h30 (Balzers), 09h40 (Weite). Valley Foehn lasted till about 03h00 on October 23. Pass Foehn did not stop over both IOP's, i.e. till 04h40 on October 23 (Guetsch). Precipitation occurs around 07h00 in our area.

Figure 4.16 presents the evolution of the RCS and the altitude of the first minimum of CSG (cold pool top), together with the surface meteorological data and Scintillometer wind values for IOP's 08-09, from October 20 to 23. Figure 4.17 shows only the RCS till altitudes of 4500 m, so the appearance of the clouds may be visualized.

There are two periods of strong South wind detected by the Scintillometer and in the station Weite. During both periods Flaesherberg station detected strong wind from SE. There is also sharp increase of the surface temperature and sharp decrease of the RH during these periods, so we may define these Foehn periods. The Foehn period for the Scintillometer starts from 06h00 on October 20 till approx 15h00 on October 21 and from 00h00 on October 22 till 03h00 on October 23. The first Foehn period for Weite is from 18h00 on October 20 till 12h00 on October 21 and the second is from 10h00 on October 22 till 01h00 on October 23. Flaescherberg also detected Foehn during these periods. Saentis recorded stronger wind from SE with a slight temperature increase during the second period. During both Foehn periods the "South sensor" of the Scintillometer shows very high downward vertical wind velocity – up to –3 and –5 m/s, while slightly upward motion is observed at the "North sensor".

During these periods of Foehn the Lidar RCS has substantially decreased, what is consistent with the decrease of the aerosol content or the RH, or both. With the start of the measurements, the altitude of the cold pool top (the first from the surface minimum of the CSG) started to decrease and during the first Foehn period frequently it was likely below the overlap altitude of the Lidar. Between the two Foehn periods, i.e., between 18h00 on October 21 and 10h00 on October 22, the cold pool recovers, what is seen by the RCS increase and by the increase of the cold pool top altitude. During the second Foehn event the cold pool top was alternatively indicated by the Lidar above and below the Lidar overlap altitude.

The observed behavior of the Lidar signal is consistent with the Foehn development as monitored by the meteorological and Scintillometer measurements. A noticeable difference with IOP 05 is the behavior of the cold pool top, i.e., the first minimum of the CSG. This behavior is shown on Fig. 4.18. Despite of the continuous Foehnic conditions as measured at Flaescherberg, the descending feature on October 20, 06h00-09h00 between approximately 1200-1000 m is likely the cold pool top above our site. It becomes discontinuous after 09h00, in accordance to Foehn arrival times on the valley floor around 10h00. Further, no continuous feature appears till approximately 14h00 on October 21, after Foehn end at surface stations around in our area (13h00 in Balzers, 13h30 in Flaescherberg).

Despite of the continuous Foehnic conditions as measured at Flaescherberg, the descending feature on October 20 06h00-09h00 between approximately 1200-1000 m is likely the cold pool top above our site. It becomes discontinuous after 09h00, in accordance to Foehn arrival times on the valley floor around 10h00. Further, no continuous feature appears till 14h00 on October 21, after Foehn end at surface stations (13h00 in Balzers, 13h30 in Flaescherberg). The cold pool elevates above our field of view at 1350 m till about 02h00 on October 22. It elevates again to 1250 m till 04h00. Lidar stops to operate from 04h00 till about 09h00, as Foehn again starts to blow in Flaescherberg and Balzers. No more continuous feature appears till approximately 04h00 on October 23, almost 1 hour after the valley Foehn stops at Weite (02h40) and northerly wind onset at 03h00. After 04h00, the cold pool ascends of about 500 m in two hours.

The cold pool top during the two Foehn periods oscillates about the Lidar overlap altitude. One reason for this may be the occasional blowing of dust lifted from the surface through the Lidar field of view: this would lead to the discontinuous detection of CSG minimum above the overlap altitude. Notice also that during these periods, the Scintillometer shows high downward vertical velocity.

A zoom of the cold pool top dynamics is presented in Fig. 4.18. It is also interesting to see that the cases of the sudden increase of the altitude of the cold pool top are during the day-time in both Foehn periods.

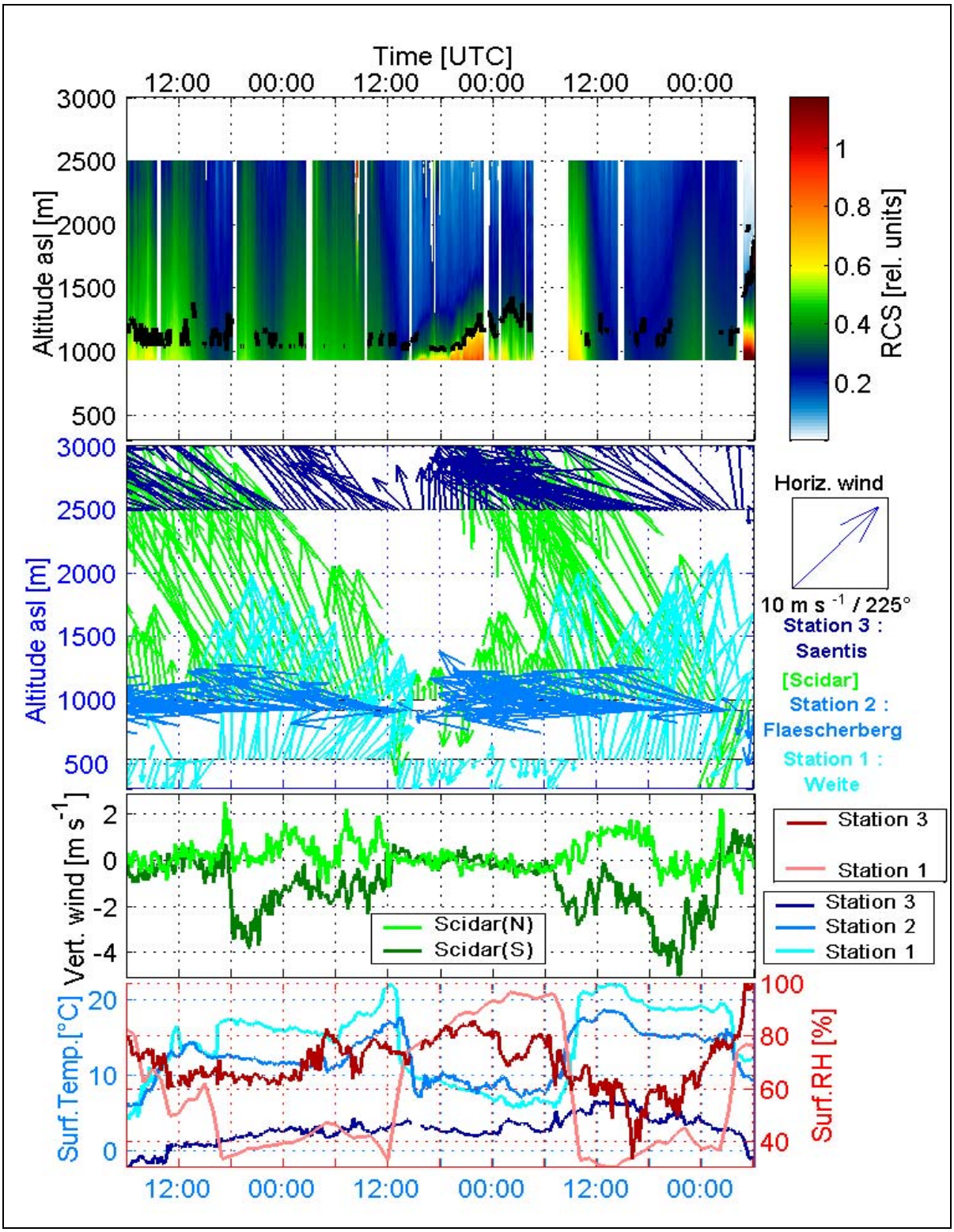


**Figure 4.16.** *Evolution of aerosol distribution and meteorological parameters in the RV during IOP's 08-09 (20-23/10/1999). Top panel: Lidar RCS with 5 min resolution, with saturated colors for clouds. The black line indicates the evolution of the first altitude above the Lidar field of view of the CSG minimum as detected by the gradient method. Other panels: meteorological parameters as in Fig. 4.12 (horizontal winds with 40 min resolution).*

During IOP 08 on October 20, surface stations indicate northerly flow during "cold pool erosion" state, till valley Foehn onset in Balzers at 10h00 and in Weite at 16h30. On October 21 at approximately 13h00 when the valley Foehn expired, a northerly flow started to bring high aerosol load, seen in Fig. 4.16 as increases of the

RCS and of the altitude of the cold pool top. A similar scenario occurs on IOP 09, i.e. a surface northerly flow during larger part of the cold pool erosion.

During IOP's 08-09 clouds were also detected with descending base altitude (see Fig. 4.17). Table 4.4 presents the wind direction and velocity at altitudes of the clouds during the Foehn periods.

**Table 4.4.** *Radiosonde measurements: wind direction and speed at altitude of cloud base detected by the Lidar on IOP's 08-09 (20-23/10/1999). Stations are Buchs-Grabs (BUG) and Heiligkreuz (HEI).*

| Station / Day | Hour | Altitude asl [m] | Wind direction [deg] | Wind speed [m/s] |
|---|---|---|---|---|
| BUG / 20 October | 05h00 | 4200 | 240 | 06 |
| BUG / 20 October | 0900h | 4000 | 240 | 08 |
| BUG / 20 October | 14h00 | 3800 | 240 | 10 |
| BUG / 20 October | 18h00 | 4200 | 240 | 08 |
| BUG / 21 October | 03h00 | 3500 | 210 | 15 |
| BUG / 21 October | 06h00 | 3600 | 215 | 12 |
| BUG / 21 October | 08h30 | 3200 | 355 | 06 |
| BUG / 21 October | 11h00 | 3000 | 165 | 22 |
| BUG / 21 October | 15h00 | 3500 | 170 | 13 |
| BUG / 21 October | 18h00 | 3300 | 190 | 03 |
| HEI / 21 October | 23h30 | 4500 | 190 | 03 |
| BUG / 22 October | 20h00 | 3500 | 236 | 05 |
| BUG / 23 October | 00h00 | 3500 | 225 | 22 |
| BUG / 23 October | 05h00 | <800 | NW | <10 |
| BUG / 23 October | 07h00 | 3500 | 205 | 22 |

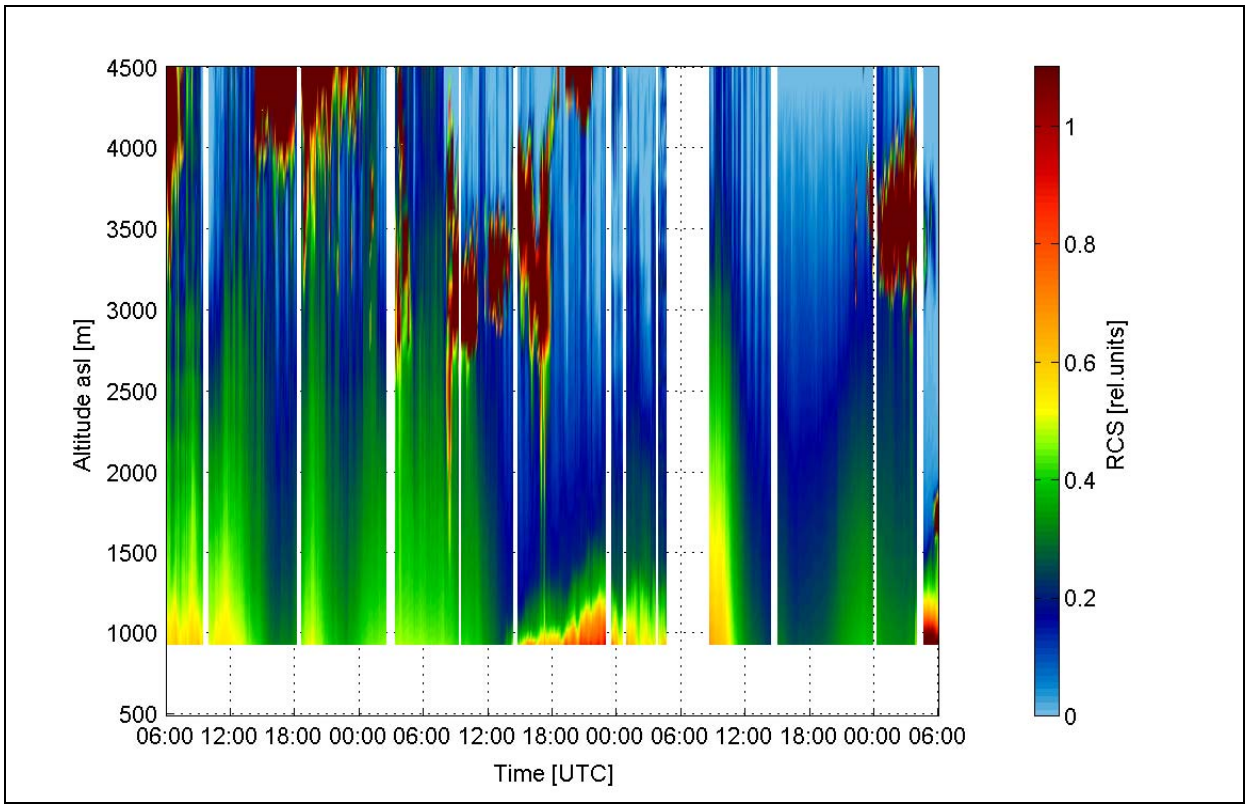


**Figure 4.17.** *IOP's 08-09 (20-23/10/1999): evolution of the RCS signal up to 4500 m, with saturated colors for clouds. Cyan areas correspond to very low signal.*

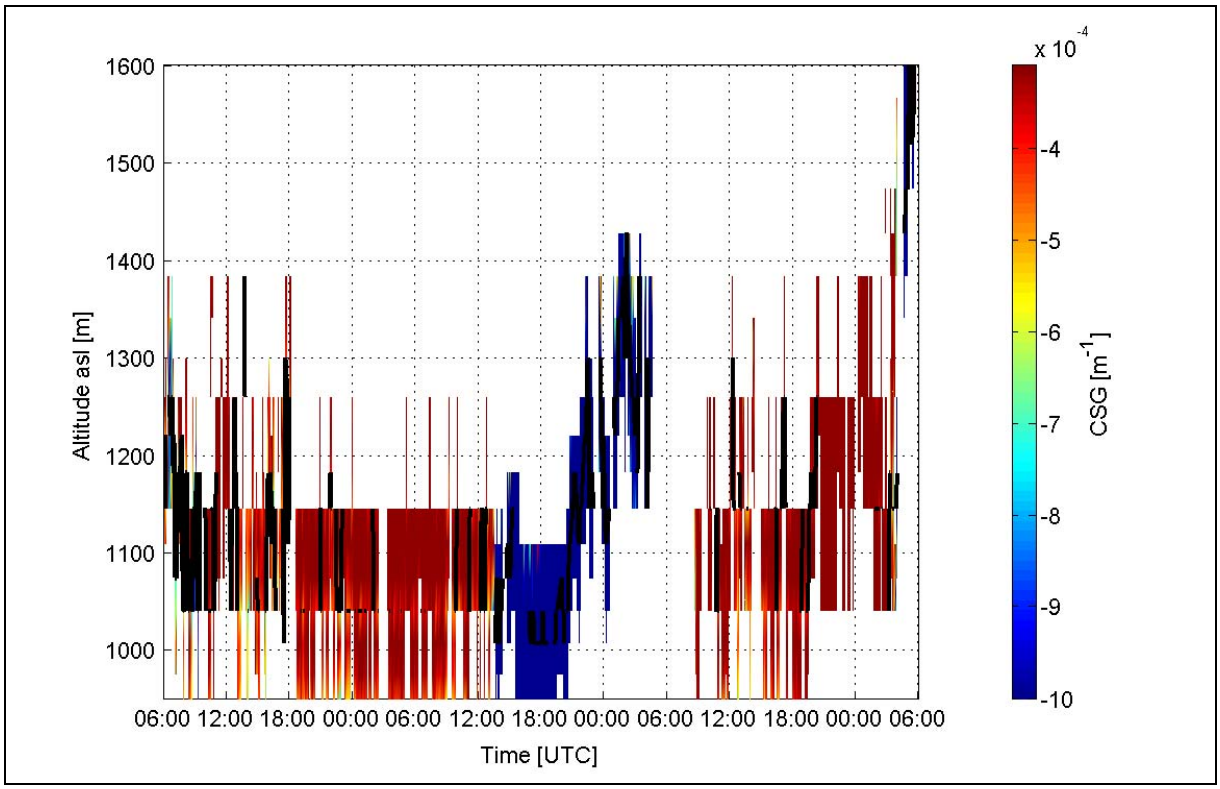


**Figure 4.18.** *Evolution of the first altitude above the Lidar field of view of the CSG minimum during IOP's 08-09 (20-23/10/1999) Foehn events, with 5 min resolution. The black line marks the altitude of the detected minima; the colors trips show in saturated colors the CSG values. Trips with line indicate the most likely extension of the gradient above the threshold value.*

## 4.3.3 Case study 3: IOP's 09-10 (23-25/10/1999)

***Short description of the Foehn events in the RV:***

On October 23, pass Foehn begins 22h20 (Guetsch). Foehn onset was detected at 05h00 on October 24 (Flaescherberg) and 03h20 in Balzers, 05h30 in Weite. Surrounding surface stations indicate that the valley. On October 24, Foehn lasted till approximately 17h00 at the valley floor, and 17h10 at 1000 m level (Flaescherberg). A short precipitation period occurs at 07h00 on October 25, and a continuous one from approximately 13h00-18h00 (Vaduz). Pass Foehn was continuous till 12h40 on October 26, but with a weaker flow from 19h10 on October 25 to 02h30 on October 26 (Guetsch).

At 23h10 on October 23, Buchs-Grabs's radiosonde indicates a W-SW synoptic flow. Figure 4.19 presents the evolution of the RCS and first minimum of the corrected signal gradient for IOP's 09-10 from October 23 to 25. The Scintillometer started to detect an increase of the southerly wind around midnight (October 23 to 24). After the Foehn indication by the Scintillometer and before the arrival of the Foehn in Weite, the Lidar RCS started to decrease, as well as the first minimum of the CSG (the cold pool top).

It is interesting to see that during Foehn there are two periods with a local increase of the aerosol backscatter, as well as a number of "jumps" of the altitude of the first minimum of the CSG. As in the case during IOP's 08-09, this coincides with high value of the downward vertical Foehn velocity. This period ended at approximately 16h00 on October 24, when the expiration of the Foehn was noticed practically simultaneously in Weite, Flaescherberg and by the Scintillometer. The wind turned from N (Flaescherberg, Scintillometer) and from SW (low speed) in Weite. During this period the cold pool recovered fast, its top rising of about 700 m in 3 hours interval. At 20h15, radiosonde from Buchs-Grabs indicates northerly flow below approx 900 m, coinciding with high aerosol load appearance (cold pool recovering). This flow leads to a low cloud with top at 1700 m at 05h00 on October 25.

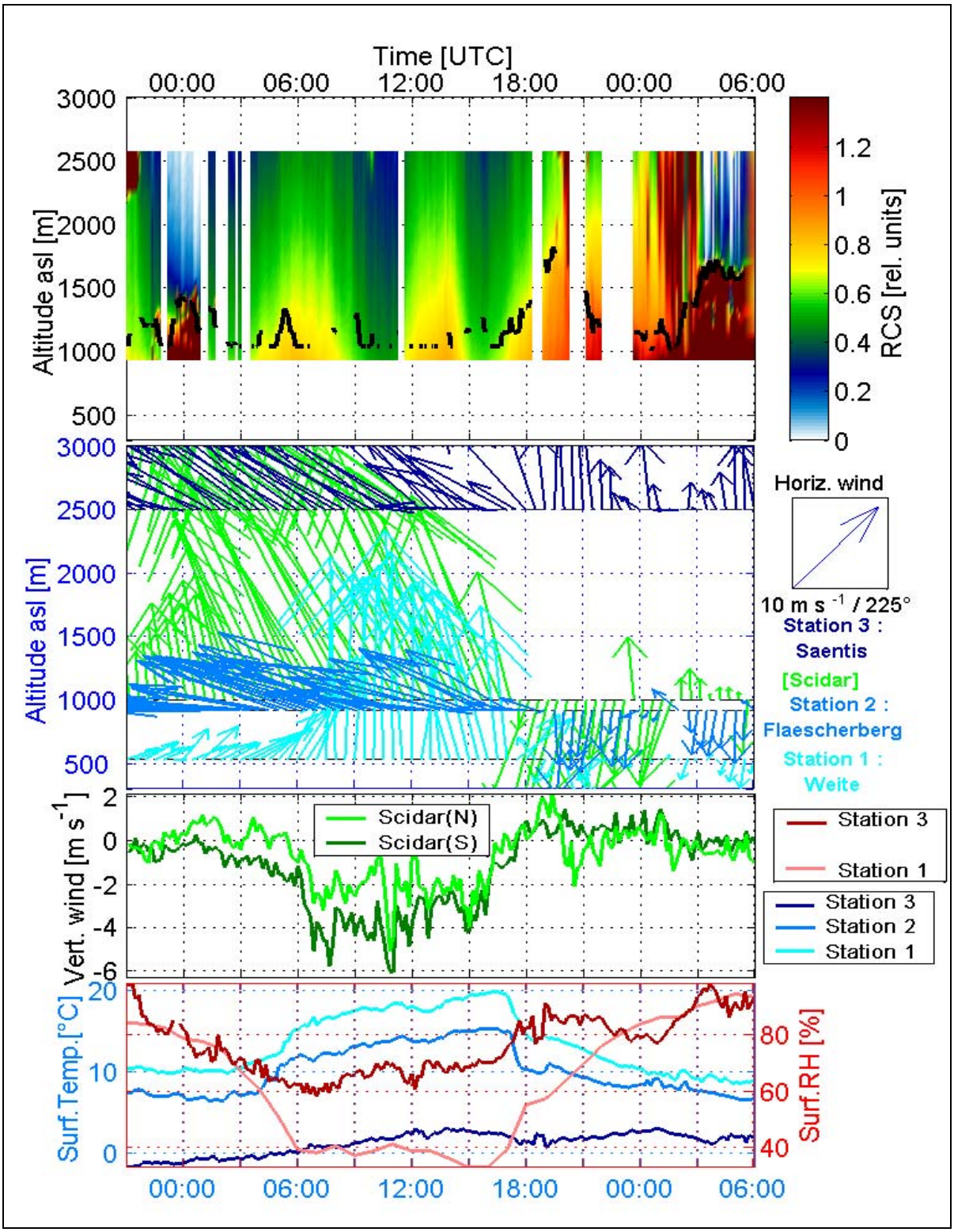


**Figure 4.19.** *Evolution of aerosol distribution and meteorological parameters in the RV during IOP's 09-10 (23-25/10/1999). Top panel: Lidar RCS with 5 min resolution, with saturated colors for clouds. The black line indicates the evolution of the first altitude above the Lidar field of view of the CSG minimum as detected by the gradient method. Other panels: meteorological parameters as in Fig. 4.12 (horizontal winds with 30 min resolution).*

**Table 4.5.** *Radiosonde measurements: wind direction and speed at altitude of cloud base detected by the Lidar on IOP's 09-10 (23-25/10/1999). Stations are Buchs-Grabs (BUG), Heiligkreuz (HEI) and Diepoldsau (DIE).*

| Station / Day | Hour | Altitude asl [m] | Wind direction [deg] | Wind speed [m/s] |
|---|---|---|---|---|
| BUG / 23 October | 17h00 | 2500 | 260 | 08 |
| BUG / 24 October | 00h00 | 1200 | 170 | 09 |
| BUG / 24 October | 08h30 | 4500 | 220 | 18 |
| BUG / 24 October | 10h30 | 3200 | 245 | 11 |
| BUG / 24 October | 14h00 | 3500 | 235 | 20 |
| BUG / 24 October | 17h00 | 3500 | 215 | 28 |
| BUG / 24 October | 20h15 | 2500 | 180 | 16 |
| HEI / 24 October | 23h00 | 3100 | 205 | 25 |
| DIE / 24 October | 23h40 | <1500 | S | <5 |
| BUG / 25 October | 04h00 | 1100 | 015 | 18 |
| BUG / 25 October | 04h00 | 1500 | 170 | 06 |
| BUG / 25 October | 04h00 | 3000 | 205 | 23 |
| HEI / 25 October | 05h00 | 3000 | 200 | 22 |

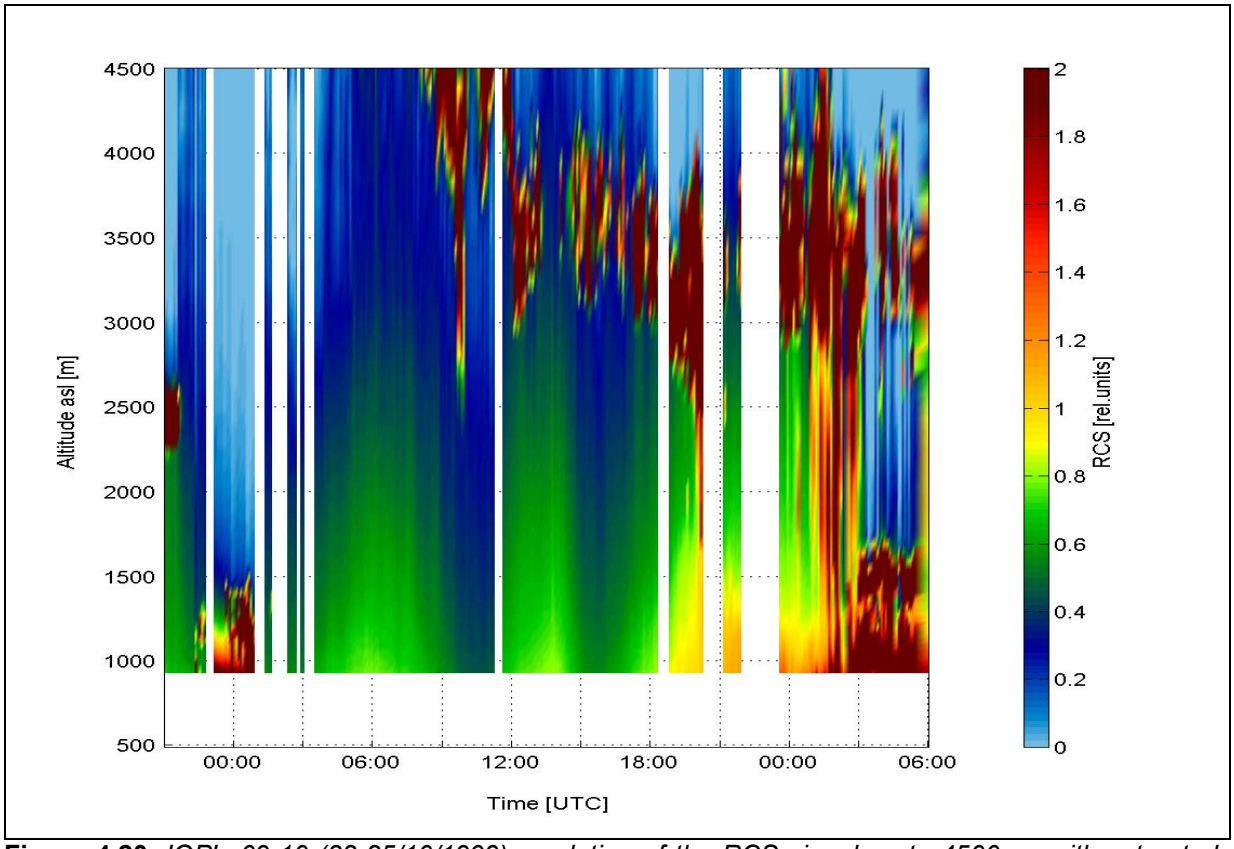


**Figure 4.20.** *IOP's 09-10 (23-25/10/1999): evolution of the RCS signal up to 4500 m, with saturated colors for clouds. Cyan areas correspond to very low signal.*

Figure 4.20 presents the cloud evolution above RV during IOP's 09-10. Table 4.5 gives the wind direction and the wind speed at altitude of the Lidar detected cloud base.

# 4.4 Average values of the ABC and the CSG above Rhine Valley in absence of Foehn and during Foehn

Figures 4.21 and 4.22 present the statistically averaged profiles of ABC and CSG above the RV in absence of Foehn and in presence of Foehn (at least pass-Foehn) for respectively nigh-time and day-time. Panels (a) in the figures present the Foehnic CSG values, panels (b) present the Foehnic ABC, panels (c) present the non-Foehnic CSG and panels (d) present the non-Foehnic ABC. The upper horizontal axis in panels (b) and (d) present the ABC values in zoomed scale, what is applicable for the upper altitudes for better visualization of the ABC values. The altitude resolution varies from 27 m at altitude 800 m till 140 m at altitude 5500 m. The integration time is in the order of 30-50 min for a single profile. The dashed lines for both CSG and ABC show the standard deviation of the statistical average, weighted according to the relative frequency of occurrence. The relative frequency distribution is presented in colors bars. It shows that the distribution of the individual values for ABC and the CSG is not gaussian. The error bars for the ABC determination are not presented here but they are in the same order of magnitude as in Fig. 3.9 and as there, they present the range of ABC variations due to the uncertainty of the reference values from the Lidar signal inversion procedure. The number of the individual profiles included in the averaged profiles of CSG and ABC, as well as the combined total integration time for these average profiles, are presented in Table 4.6.

In the presented statistics in Figs 4.21 and 4.22 there participate only measurements done in cloud-free conditions, or conditions with high and scattered clouds. This comes from the conditions for the application of the inversion procedure (see section 1.3).

**Table 4.6.** *Number of individual measurements and the total integration time to obtain the average values for the Lidar Corrected Signal Gradient (CSG) and the Aerosol Backscatter Coefficient (ABC), presented in Figs 4.21-4.22, related Optical Depths (OD) and number of soundings from the station Buchs-Grabs presented in Fig. 4.27.*

| | Foehnic Day-time | Non-Foehnic Day-time | Foehnic Night-time | Non-Foehnic Night-time |
|---|---|---|---|---|
| CSG : | | | | |
| # measurements | 43 | 62 | 44 | 66 |
| total time [min] | 2172 | 3047 | 2212 | 3101 |
| ABC : | | | | |
| # measurements | 16 | 28 | 13 | 26 |
| total time [min] | 768 | 1280 | 684 | 1160 |
| OD 0900-2000 m | 0.051 | 0.086 | 0.044 | 0.084 |
| OD 2000-3000 m | 0.030 | 0.054 | 0.018 | 0.046 |
| OD 3000-5500 m | 0.015 | 0.033 | 0.011 | 0.022 |
| OD 0900-5500 m | 0.10 | 0.18 | 0.075 | 0.159 |
| # radiosoundings | 31 | 62 | 19 | 48 |

The non-Foehnic day-time ABC shows an increase at lower altitude down to altitudes of the Lidar overlap (Fig. 4.21d). A drop is seen at around 1400 m, also well marked by the CSG minimum. The ABC distribution at these altitudes for the non-Foehnic night-time case looks different (Fig. 4.22d): An accumulation layer developed below 1500 m, also confirmed by the CSG. The ABC value at the lowest altitudes of measurements is higher in day-time than in night-time, although slightly, with a tendency to increase even further below the Lidar overlap altitude. This gives a reason to associated the observed ABC distribution below 1500-1800 m with the diurnal cycle of valley PBL in conditions of thermally developed wind system [*Stull*, 1988]. Above these altitudes the ABC distributions show a succession of shallow drops till altitudes, first to 3200-3500 m and then to approximately 4000-4200 m. The shape of the altitude distribution for day-time and night-time at these altitudes is similar, with slightly higher values for day-time.

The ABC distribution during Foehn demonstrates a quite similar stratification for both day-time and night-time: a shallow drop, marked by ABC and CSG around 3200-4000 m. The value for the day-time is higher. The ABC values both for day-time and night-time are substantially lower in Foehnic conditions for all altitudes till

3000-3500 m. Table 4.6 presents also the optical depth for different layers calculated from the ABC profile, with the same extinction-to-backscatter ratio value used for the inversion procedure. As we see, the optical depth in case of Foehn is substantially lower than in non-Foehnic conditions, what may be an additional explanation for the effect of "Foehn clearance" (see [*Hoinka K. P.*, 1985]).

Figure 4.23 presents the average values of the PTG from Buchs-Grabs's radiosoundings as follows: Fig. 4.23a for Foehnic cases in day-time, Fig. 4.23b for Foehnic cases in night-time, Fig. 4.23c for non-foenic cases in day-time, Fig. 4.23d for non-Foehnic cases in night-time. The color bars show the relative frequency of distribution. The number of measurements participating in each case is given as the last line of Table 4.6.

It is interesting to compare the observed averaged aerosol stratification in and out of the Foehn period with the observed average temperature stratification, i.e. to compare the altitudes where there is a local minimum of the GSG for the four cases presented in Figs. 4.21 and 4.22, close to the altitudes where there is a local maximum of the PTG for the same respective cases.

Figures 4.24a, 4.24b, 4.24c and 4.24d present together the CSG and the PTG. In these Figures, the PTG is shown with a reversed (minus) sign, in order to better visualize possible coincidences. Evaluating possible coincidences and discrepancies, we shall have in mind the altitude resolution, which is approx 140 m for the CSG and 60 m for PTG. In this way, the error bar of such comparison is in the order of 200 m. Also, the Lidar and radiosonde measurements do not occur at the same place, i.e., there is a difference due to possible horizontal inhomogeneity, larger for the higher altitudes. Such coincidences are seen as follows:

In Fig. 4.24a (Foehnic day-time): a common general trend may be followed. There is a well-defined minimum in (–1)PTG well below 1000 m. With the limitation of the overlap altitude for the Lidar, we see such tendency to minimum in CSG too. There is also a group of coinciding minima between 3000 and 4000 m. No coincidences may be traced above those altitudes.

In Fig. 4.24b (Foehnic night-time): a similar trend is seen with coincidences at 1000-1500 m, approximately 2000 m and a group at 3000-3500 m. The strong minimum in (-1)PTG at 4250 m is an artefact. The coinciding patterns in Fig. 4.24a and 4.24b are likely due to the fact that at these altitudes both average PTG and average CSG are determined by the Foehn flow

In Fig. 4.24c (non-Foehnic day-time): coinciding general trend till 3500 m where coinciding minima for (-1x)PTG and CSG are seen at altitudes of 1300-1400 m, 2100 m, 2900-3000 m. In Fig. 4.24d (non-Foehnic night-time) we also see a common general trend with coinciding minima at 1500 m, around 2500-2800 m and 3000-3500 m. As we already see in Figs. 4.21d and 4.22d, there is an aerosol layer with a shallow dropping ABC from the altitudes of the mountains surrounding the valley to altitudes of approximately 3500 m. The potential temperature local maximum is a characteristic for a layer with lower stability (convective or mixed). From this point of view, such elevated aerosol layer and the similarity of the CSG and the (-1)PTG altitude profiles, may be connected to a possible existence of elevated residual layer (see [*Stenstrud*, 1993]) above the valley likely similar in nature to the layers observed during the "heat-wave" (Chapter 3). This figure provides an evidence that the presence of such layers is statistically significant in conditions favorable for convective development.

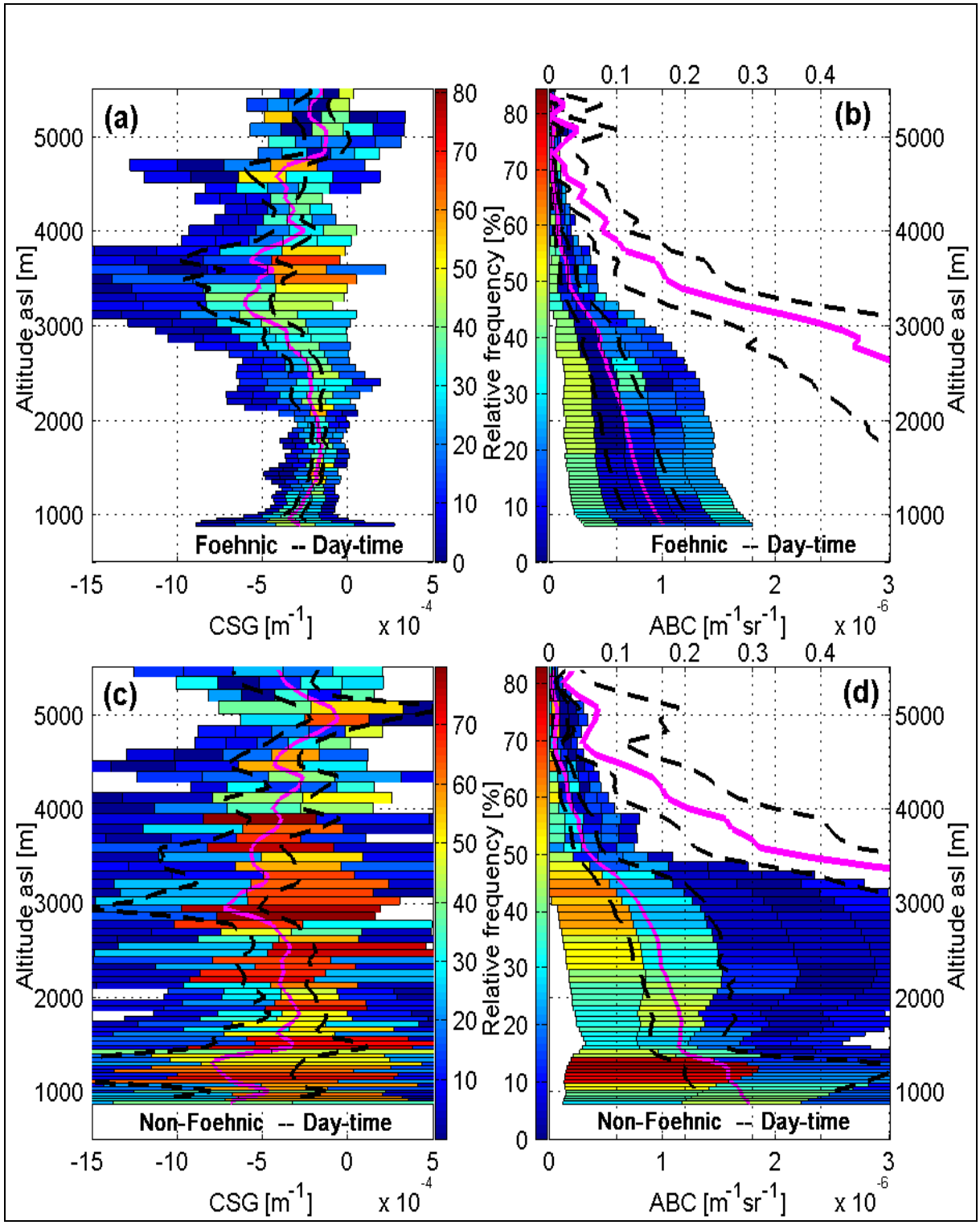


**Figure 4.21.** *Distributions of CSG and ABC during the period 15/09/1999-7/11/1999, for day-time (10h00-17h00). The upper horizontal axes of panels (b) and (d) presents ABC panels ((b)-(d)) show the ABC value above 2500-3000 m zoomed; the colorscale bars show the relative frequency of occurrence; the continuous magenta lines present the average values while the dashed black lines show the standard deviations of the distributions.*

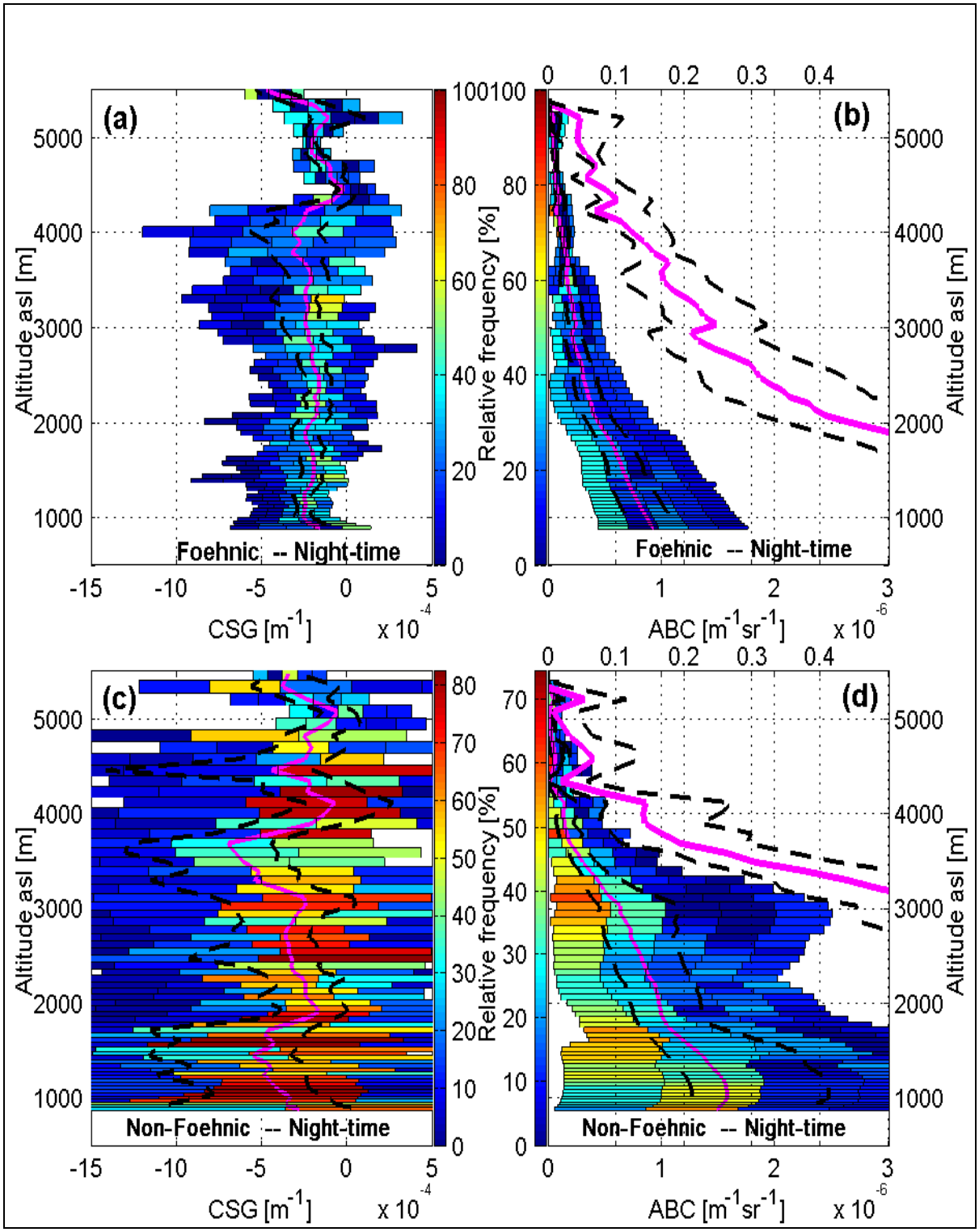


**Figure 4.22.** *Distributions of CSG and ABC during the period 15/09/1999-7/11/1999, for night-time (00h00-07h00). The upper horizontal axes of panels (b) and (d) presents ABC panels ((b)-(d)) show the ABC value above 2500-3000 m zoomed; the colorscale bars show the relative frequency of occurrence; the continuous magenta lines present the average values while the dashed black lines show the standard deviations of the distributions.*

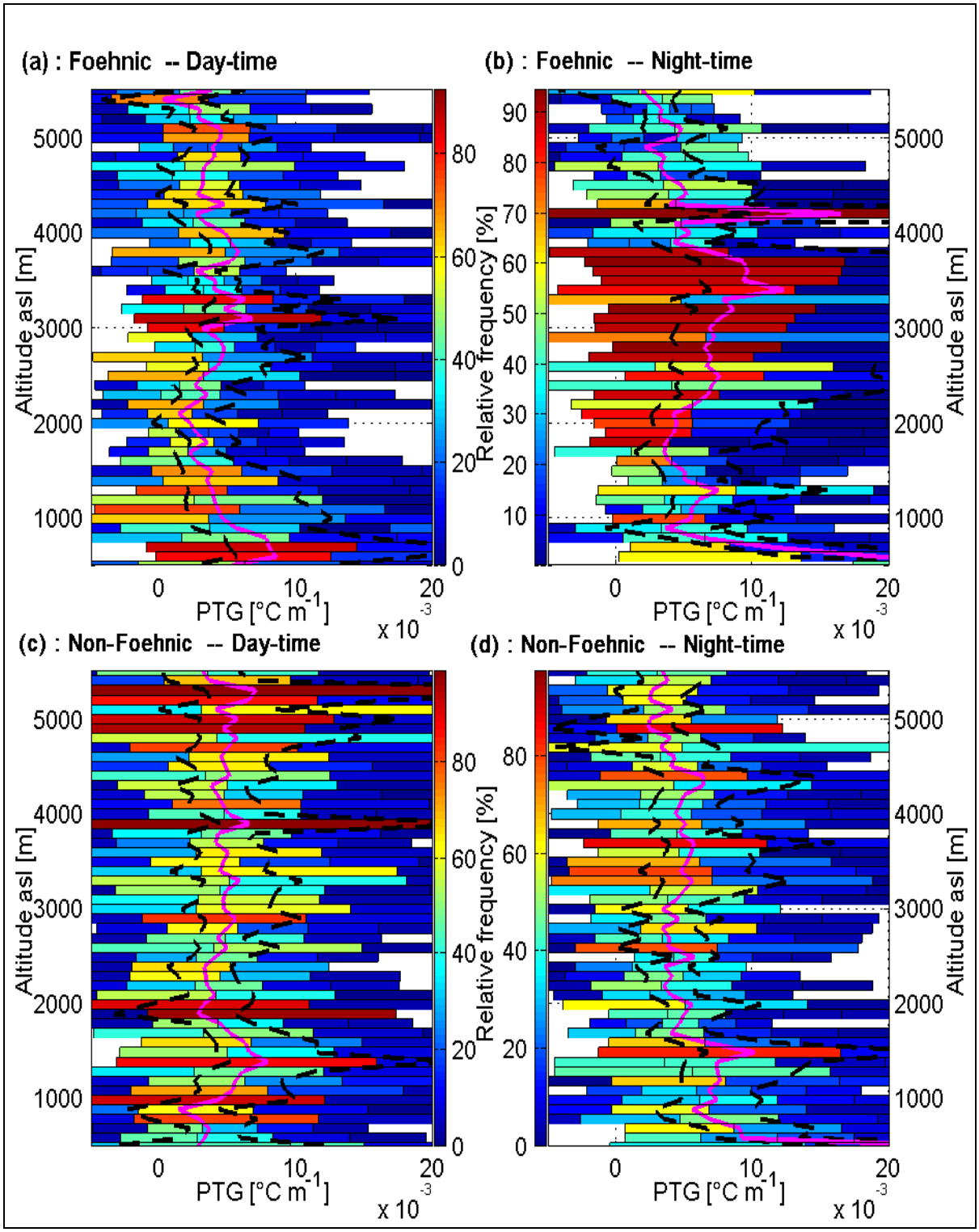


**Figure 4.23.** *Distributions of PTG based on radiosonde data from Buchs-Grabs during the period 15/09/1999-7/11/1999, for the 4 indicated cases. Day-time includes soundings from 10h00-17h00, night-time from 00h00-07h00. The colorscale bars show the relative frequency of occurrence; the continuous magenta lines present the average values while the dashed black lines show the standard deviations of the distributions. On panel (b), the peak of PTG at 4200 m is an artefact.*

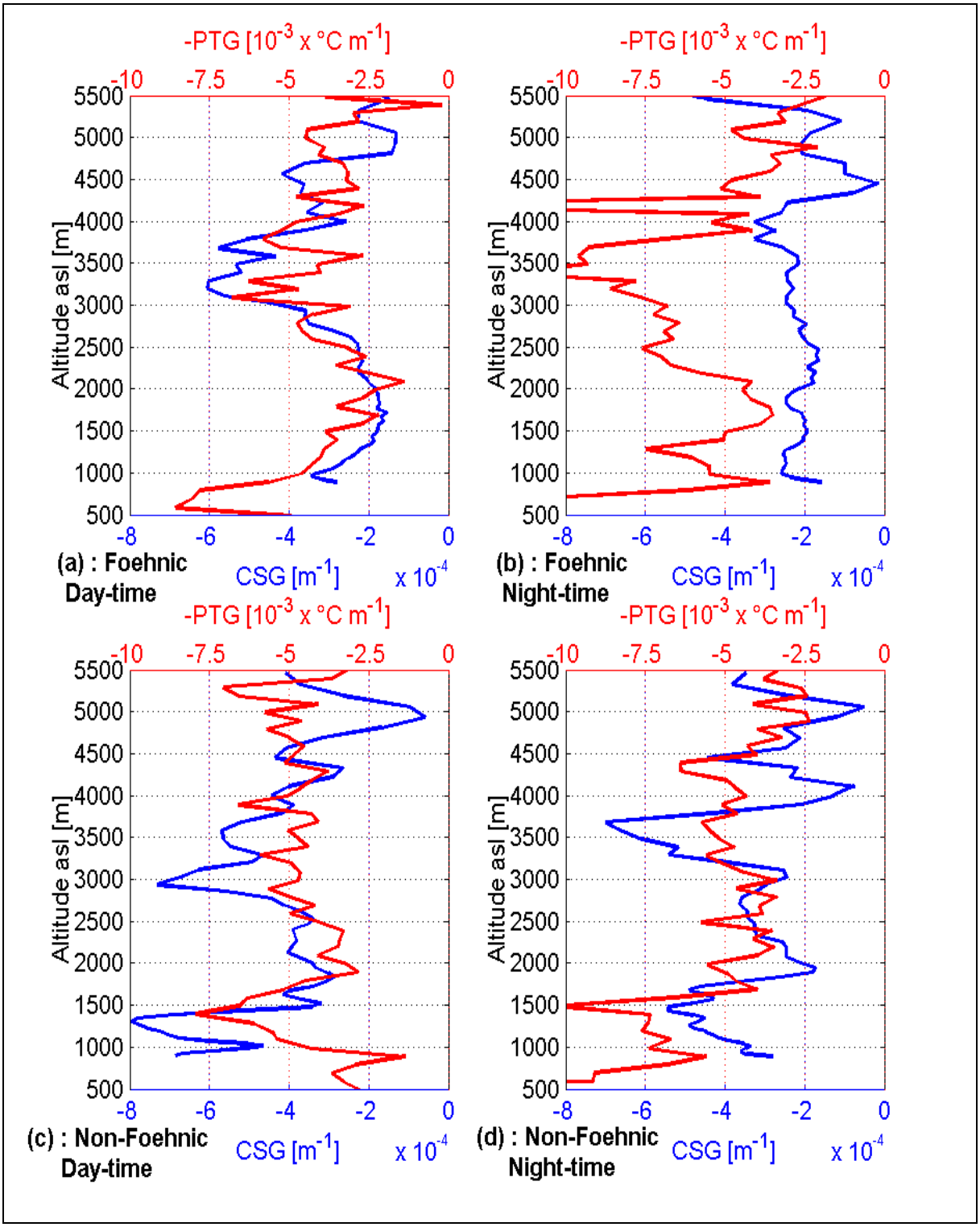


**Figure 4.24.** *Mean values of the distributions of CSG (see Figs 4.21 and 4.22) and PTG (see Fig. 4.23) during the period 15/09/1999-7/11/1999, for the 4 indicated cases. PTG is shown with a minus sign, in order to better visualize the (anti-)correlation. On panel (b), the peak of PTG at 4200 m is an artefact.*

# 4.5 Conclusions

Our main contributions in this Chapter are:

(i) to identify the cold-pool top during Foehn as an aerosol mixed layer

(ii) to demonstrate that the cold pool top is the region of turbulent mixing with the air carried by the Foehn

To study the development of aerosol stratification above the Rhine Valley under Foehnic conditions, we installed a Backscatter Lidar on the Valley floor during the FORM-SOP. We combined Backscatter Lidar observation of the aerosol profiles above the Rhine Valley with the wind measurements from Wind-Temperature Radar, temperature measurements from surface stations and radiosonde temperature and humidity measurements. In non-Foehnic conditions the aerosol stratification in the valley PBL is similar to the one reported in Chapter 3. There are similarities in the ABC, CSG and PTG showing also a likely existence of elevated residual layer above the valley as in the case described in Chapter 3.

The comparison between the PBL in absence and presence of Foehn shows the following:

1. During the development of the Foehn events, the aerosol layer formed in the PBL above the valley is progressively eroded. A decrease of ABC by 50% is typically observed. Within the Foehn layer, the aerosol distribution tends to be poorly stratified, what may be explained by the strong mixing induced by a turbulent flow. In presence of Foehn, there is no sharp drop of the ABC profile at the altitude of the surrounding mountains, as observed in the absence of Foehn.

2. When the lower boundary of the Foehn flow is above the overlap altitude of the Lidar, we notice a good coincidence between the altitudes of the first from the surface PTG maximum and the CSG minimum. Also, these altitudes coincide well with the altitude of the lower Foehn boundary from radiosonde wind measurement. Below this altitude it is observed an increase of the ABC what is an increase of either the aerosol content or the relative humidity, or both. This double coincidence gives the reason to associate the lowermost minimum of the CSG with the "cold pool" top.

3. The erosion of the cold pool is a process of "washing" of the aerosol rich air in the valley PBL by the Foehn. The cold pool erosion observed by the Lidar starts approximately at the time when the Scintillometer started to detect high wind speed from South, as well as when the surface stations start also to detect the Foehn pattern (high speed of South or South East wind, temperature increase and RH decrease). The time of start of cold pool re-forming is at the time of Foehn expiration, as detected by the Scintillometer and the surface stations surrounding the Lidar site. During Foehn development, a cloud layer appears at altitudes of 3500-4500 m: this coincides with the altitudes of the synoptic wind. The re-forming of the cold pool is connected with wind from North and with the appearance of low clouds (1000-1500 m). This cold pool erosion is characterized by a high variance of the Lidar RCS at an altitude associated to the cold pool top.

4. The statistical average of the ABC values in Foehnic conditions shows that approximately to 3200-3500 m the aerosol backscatter is considerably lower than in non-Foehnic conditions. The aerosol stratification above the cold pool top is characterized by a single shallow drop, where the altitude of this drop is also close to the altitude of a PTG local maximum. There is a substantial decrease of the aerosol optical depth, contributing to the so-called "Foehn clearance".

5. A future investigation with a Lidar having lower full overlap altitude will help to better study the dynamics of the cold pool top, in conditions of high vertical Foehn wind component.

6. As the local topography is a relevant factor for the Foehn development, therefore for a future study, we recommend to collocate closely the Lidar, WTR and radiosonde launch sites.

# Chapter 5

# Aerosols statistics in the PBL and lower troposphere above Neuchâtel: two years of routine observations

## 5.1 Introduction

The increasing aerosol content in the atmosphere has various direct and indirect effects on the air quality and radiation balance. Its potential influence on the atmospheric radiation balance and, in this way, in possible climate change is documented in a number of studies (see [*IPCC*, 2001]). As example, recently Travis et al. [*Travis et al.*, 2002] assessed the importance of such aerosol-enforced changes on the basis of temperature records after 3-days ban on airplane flights in America, following the September 11, 2001 terrorist attack. They concluded that the atmospheric temperature has significantly changed in the absence of the airplane exhaust (contrails) and postulated that the contrails change the intensity of incoming solar radiation and outgoing long-wave radiation. However, optical, physical and chemical properties of aerosols and various other effects are still under research following various types of aerosols, their atmospheric lifetime and various meteorological conditions ([*Ackermann*, 1998], [*Kaufman et al.*, 2002]).

Global and regional variations of aerosol distribution, as well as the local affects make it difficult to select only one observational method for aerosol assessment. Local affects change from one region to another, depending upon meteorological factors, topography, surface cover etc. The study of the aerosol optical characteristics for different regions, in this respect, requires observations by complementary methods, which includes satellite based photometers ([*Herman et al.*, 1997], [*Kaufman et al.*, 1997]), sun photometer ([*Holben et al.*, 1998]), airborne *in situ* probes ([*Bates et al.*, 1998], [*Russell et al.*, 1999], [*Ansmann*, 2001]) etc. Among the aerosol measurement techniques, the backscatter lidar is instrumental in regional studies. Lidar is found useful due to its independence of the time of measurement in the diurnal cycle, convenient temporal and spatial resolution and for possibilities of vertical profiling of aerosols. Regional aerosol study by lidar for a longer period has appeared recently in [*Matthias and Bösenberg*, 2002], [*Schneider and Eixmann*, 2002], [*Mattis et al.*, 2000]. Case studies for particular regions and for limited period have been presented in Chapters 3 and 4.

This Chapter presents a study of aerosol backscatter coefficient (ABC) over Neuchâtel, Switzerland (Fig. 5.1; $47.0^0$ N; $6.95^0$ E, 485 m asl). The study is performed by a ground based elastic backscatter lidar system operating at 532 nm wavelength. Atmospheric layering for this study is based on a broader classification of lower atmosphere from 1 km to 2 km above sea level (asl) and from 2 km to 5 km asl, respectively. The effect of weather parameters on ABC values at these altitudes is studied using upper-air weather data from Payerne station ($46.82^0$ N, $6.95^0$ E, 491 m asl). Payerne station is situated at about 20 km south of the lidar site. Analytical back

trajectories for 850 hPa and 700 hPa levels are used to evaluate the possible air mass history and its relationship with ABC values obtained at Neuchâtel.

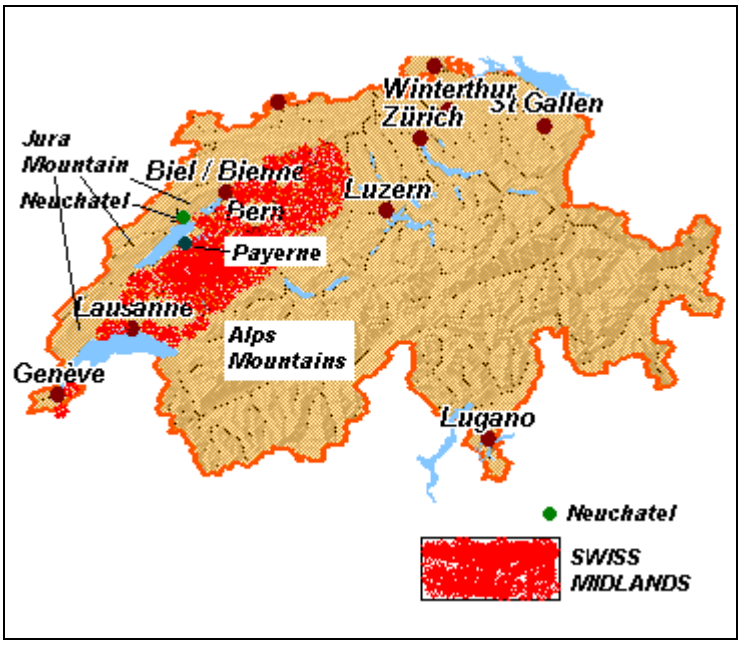


**Figure 5.1.** *Location of Neuchâtel site of Lidar measurement in Switzerland.*

# 5.2 Backscatter Lidar and ABC data

The Backscatter Lidar used in this study is similar to the one described in the subsection 3.2.2. The receiver optics has been modified to better focus on the upper troposphere: the telescope diameter is of 25 cm and the full overlap altitude for the Lidar starts at about 600 m above ground level (~1 km asl). The altitude and temporal resolution in detection of a single Lidar signal profile are respectively 6 m and 50 s. These resolutions are degraded substantially in the signal processing in order to decrease the contribution of the statistical noise in data retrieved from the Lidar backscatter signal.

Since May 2000, this set-up is running with a number of other stations as part of EU project 'European Aerosol Research Lidar Network (EARLINET)' to establish aerosol climatology over Europe (see [*Bösenberg et al.*, 2000], [*Schneider et al.*, 2000] and http://lidarb.dkrz.de/earlinet). To obtain the ABC profiles, the measured lidar backscatter data are processed by Fernald inversion procedure presented in Chapter 1 and tested in Chapter 2. As it is reported in sub-section 2.2.2, a set of successful inter-comparison exercises in determination of ABC profiles have been performed in the frame of EARLINET, contributing substantially to the quality control of the data in EARLINET lidar network and as well as to the data used in the present study.

As it has been shown in section 2.2, the inversion procedure for ABC value retrieval from the elastic backscatter lidar signal has the setback of uncertainties in reference parameters: extinction to backscatter ratio (lidar ratio) and ABC reference values at reference altitude. This is a limitation for the elastic backscatter lidar compared to the combined elastic-Raman backscatter lidars (see §2.3.2.4 and [*Matthias and Bösenberg*, 2002], [*Schneider and Eixmann*, 2002]). On the other hand, the ABC values retrieval by inversion procedure from the elastic backscatter lidar gives possibilities to evaluate the day and night ABC profiles by the same procedure, i.e. not to be restricted to nighttime observations only, as in the case of Raman lidar systems (see §2.2.1.10 and §2.4.2.2). A constant lidar ratio profile is considered for this study. The value is based on the studies of [*Franke et al.*, 2003]) and [*Ackermann*, 1998]. A typical value of lidar ratio for aerosols over Europe is found to vary between 20 - 80 steradian (see [*Franke et al.*, 2003]). Among these, high occurrence is seen for 30-40 sr and 40-50 sr. Considering these references ([*Franke et al.*, 2003]) and [*Ackermann*, 1998]), a constant lidar-ratio of 50 sr is taken for the present study. Following results from sub-section 2.2.1, the uncertainty in ABC retrieval due to inadequate lidar ratio is found to be approximately 3% in the lower troposphere and 10% in planetary boundary layer (PBL) altitudes. The uncertainty in determining ABC value due to the uncertainties of the ABC reference value is also in the same order of magnitude.

The set of lidar data included in this study corresponds to regular measurements for Monday noon (–1H to +3H of noon), Monday evening (–1H to +3H of sunset) and Thursday evening for each opportunity between May 2000 and June 2002, when low and mid-altitude opaque clouds is not present. The absence of such cloud is necessary in defining the reference value at a reference altitude for inversion procedure, and in this sense, the present study is biased to fair-weather conditions. Few non-regular measurements (i.e. other days than Mondays or Thursdays) are also included in the statistics. These additional days comprise observation of outburst of specific large-scale aerosol sources e.g. Saharan dust (Papayannis et al, 2002), Bise wind event from northeast azimuth crossing the industrialized parts of the European continent (Wanner and Furger, 1990). Subsequently, total number comprise to 147 cases for 2-5 km layer asl (i.e. upper layer). Data number for 1-2 km layer asl (i.e. lower layer) comprises to 142 cases. Figure 5.2 presents example of individual profiles of ABC value. The thick line in Fig. 5.2 presents a forecasted transport of Saharan dust to the lidar site.

As it is seen from Fig. 5.2, the considered atmospheric layering follows the overlap restriction of the lidar and the altitude of aerosol mixed layer (AML) top. AML is the layer in PBL (or the residual layer during evening and night) with homogeneous distribution of aerosols. The convective and mixing processes in PBL lead to the development of aerosol mixed layers. As has been described in the sub-sections 1.2.3 and and 1.3.3, a sharp drop of ABC values is expected in the zone of the transition from PBL to free troposphere (see also [*Schneider and Eixmann*, 2002]). In this way, a drop in ABC value with respect to altitude in each profile determines AML top. Full overlap starts at altitudes of approximately 600 m above ground level (~1 km asl), limiting the possibility of measurements below this level. The AML top is found typically between 1 km and 2 km asl (Figure 5.2). Following these criteria, the considered lower layer represents the AML as assessed by the lidar above its overlap altitudes, while the upper layer represents the lower part of free troposphere. For analyzing the effect of weather parameters on ABC variability for considered two layers, upper-air weather data from Payerne station and data in ABC profiles are averaged for lower and upper layers.

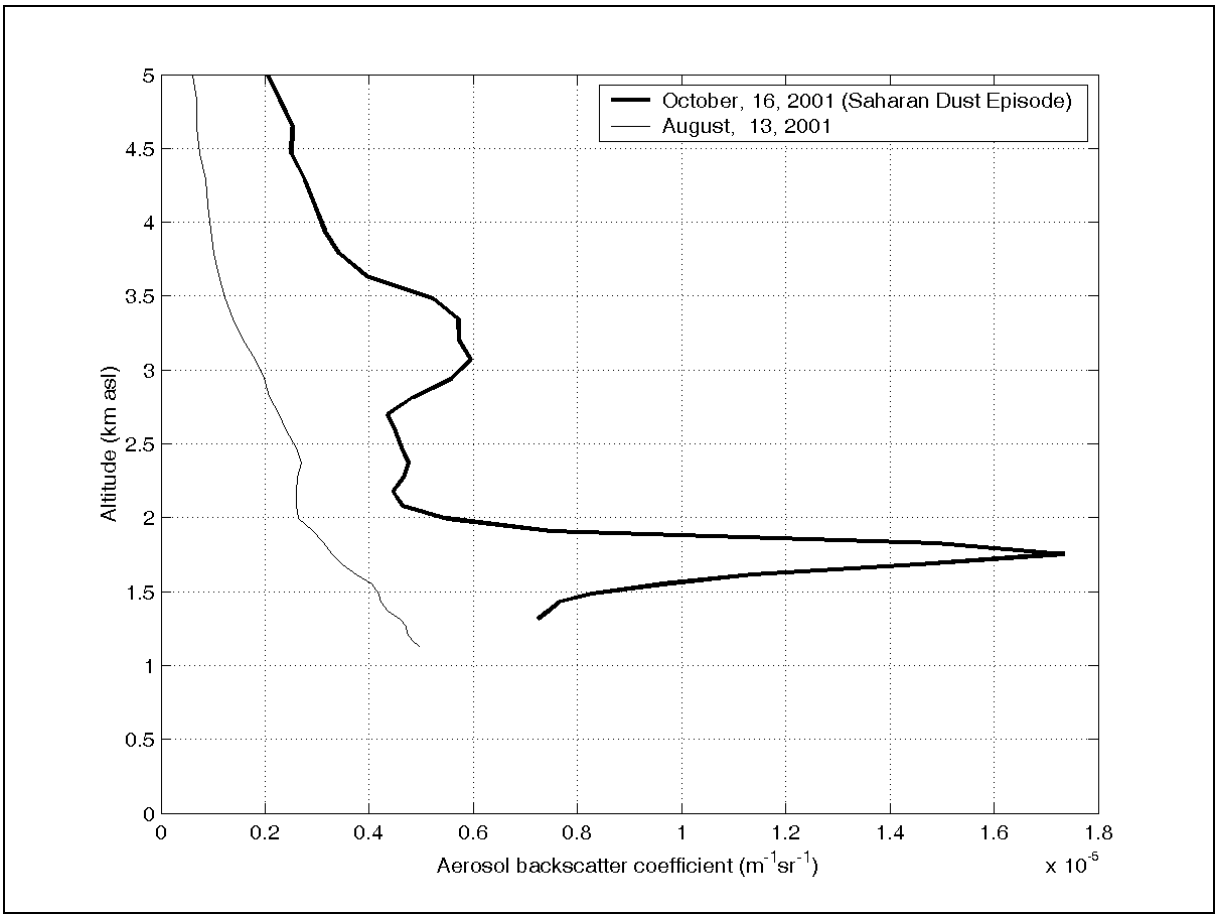


**Figure 5.2.** *Profiles of aerosol backscatter coefficient (ABC) at Neuchâtel. Thick line is showing a Saharan dust outburst of October 16, 2001. This figure helps in classifying different considered layers (viz. 1-2 km and 2-5 km asl) for the study.*

# 5.3 Results and discussion

## 5.3.1 Annual variability of ABC and AML height

Figures 5.3 (a and b) presents the annual variation of ABC values for considered two layers. Continuous line in Fig. 5.3 a and 5.3 b show monthly-averaged ABC values. It is showing higher ABC value during summer in comparison to other seasons for both layers. The range of variations in monthly-averaged ABC values for both layers is different. It varies between $0.89*10^{-6}$ $m^{-1}sr^{-1}$ to $5.35*10^{-6}$ $m^{-1}sr^{-1}$ for lower layer and $0.39*10^{-6}$ $m^{-1}sr^{-1}$ to $2.23*10^{-6}$ $m^{-1}sr^{-1}$ for upper layer. For both layers, the lowest ABC value is found during winter. ABC values for lower layer is approximately 2.5 times higher than that of ABC values for upper layer.

Figure 5.4 depicts the annual variation of AML top altitude. Continuous line in Fig. 5.4 is showing the monthly average of the AML top altitude. AML top is found the highest during fall, followed by summer, spring and winter.

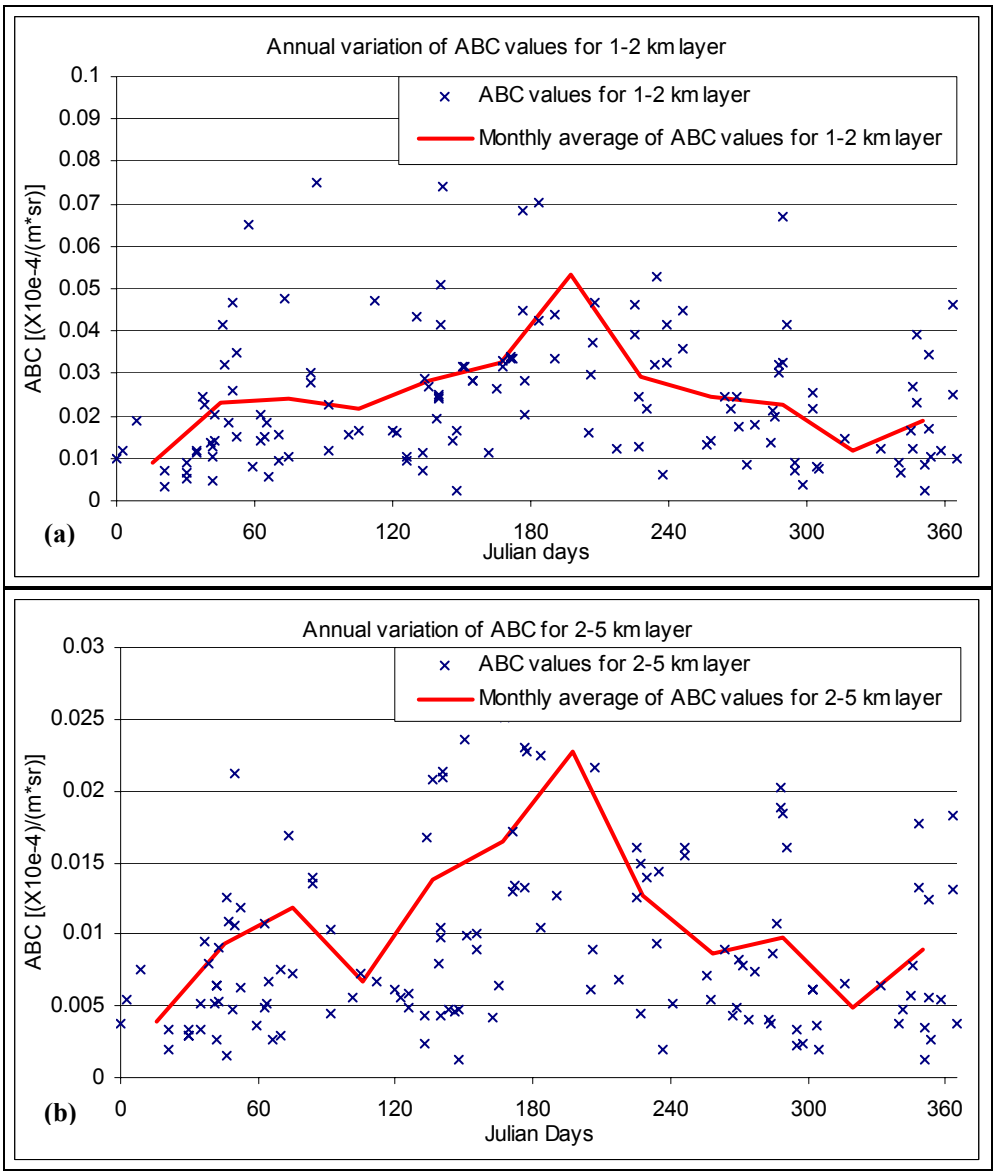


**Figure 5.3 (a and b).** *Annual variation of aerosol backscatter coefficient (ABC) for 1-2 km layer (a) and 2-5 km layer (b). 'x' are ABC values for different Julian days during May 2000- June 2002; thin line represents monthly-mean of ABC values.*

Table 5.1 presents the seasonal variation of ABC for noon time respectively evening time measurements, for the two considered layers.

**Table 5.1.** *Mean, Standard Deviation (St.Dev.) and Median of aerosol backscatter coefficient (ABC) and scattering ratio for 1-2 km and 2-5 km layers for different seasons and for noon and evening, from Lidar measurements above Neuchâtel. The observation period is May 2000-June 2002.*

| Data set selection | | Aerosol Backscatter Coefficient ($x10^{-5}m^{-1}sr^{-1}$) | | Total Scattering Ratio | |
|---|---|---|---|---|---|
| | | 1-2 km | 2-5 km | 1-2 km | 2-5 km |
| ***All seasons*** | | | | | |
| ***All data (147 samples)*** | ***Mean*** | **0.0259** | **0.0115** | **2.9283** | **1.9991** |
| | ***St.Dev.*** | 0.0192 | 0.0104 | 1.4596 | 0.9183 |
| | ***Median*** | **0.0217** | **0.0078** | **2.5907** | **1.6616** |
| ***Noon data (64 samples)*** | ***Mean*** | **0.0240** | **0.0104** | **2.8426** | **1.9165** |
| | ***St.Dev.*** | 0.0241 | 0.0123 | 1.6235 | 1.0952 |
| | ***Median*** | **0.0217** | **0.0078** | **2.5907** | **1.6616** |
| ***Evening data (83 samples)*** | ***Mean*** | **0.0235** | **0.0099** | **2.7540** | **1.8589** |
| | ***St.Dev.*** | 0.0168 | 0.0082 | 1.2736 | 0.7146 |
| | ***Median*** | **0.0195** | **0.0065** | **2.4823** | **1.5427** |
| ***Spring (16 March-30 April)*** | | | | | |
| ***Noon data (9 samples)*** | ***Mean*** | **0.0284** | **0.0133** | **3.0587** | **2.1594** |
| | ***St.Dev.*** | 0.0209 | 0.0145 | 1.4667 | 1.3116 |
| | ***Median*** | **0.0225** | **0.0072** | **2.5972** | **1.6005** |
| ***Evening data (8 samples)*** | ***Mean*** | **0.0203** | **0.0109** | **2.5159** | **1.9503** |
| | ***St.Dev.*** | 0.0124 | 0.0091 | 0.9549 | 0.7931 |
| | ***Median*** | **0.0164** | **0.0060** | **2.1962** | **1.5285** |
| ***Summer (1 May – 15 Sept)*** | | | | | |
| ***Noon data (18 samples)*** | ***Mean*** | **0.0457** | **0.0231** | **3.9038** | **2.6622** |
| | ***St.Dev.*** | 0.0271 | 0.0160 | 0.1294 | 0.0816 |
| | ***Median*** | **0.0365** | **0.0219** | **3.2726** | **2.0106** |
| ***Evening data (24 samples)*** | ***Mean*** | **0.0310** | **0.0123** | **3.3744** | **2.0820** |
| | ***St.Dev.*** | 0.0196 | 0.0081 | 1.4964 | 0.7240 |
| | ***Median*** | **0.0282** | **0.0102** | **3.1641** | **1.9027** |
| ***Fall (15 Sept – 31 Oct )*** | | | | | |
| ***Noon data (10 samples)*** | ***Mean*** | **0.0263** | **0.0125** | **2.9565** | **2.0619** |
| | ***St.Dev.*** | 0.0122 | 0.0075 | 0.9422 | 0.6460 |
| | ***Median*** | **0.0247** | **0.0099** | **2.8960** | **1.8446** |
| ***Evening data (16 samples)*** | ***Mean*** | **0.0278** | **0.0109** | **3.0974** | **1.9406** |
| | ***St.Dev.*** | 0.0163 | 0.0079 | 1.2006 | 0.6612 |
| | ***Median*** | **0.0232** | **0.0080** | **2.8121** | **1.7128** |
| ***Winter (1 Nov – 15 March)*** | | | | | |
| ***Noon data (27 samples)*** | ***Mean*** | **0.0189** | **0.0077** | **2.3442** | **1.6564** |
| | ***St.Dev.*** | 0.0124 | 0.0049 | 0.8759 | 0.4200 |
| | ***Median*** | **0.0126** | **0.0064** | **1.9111** | **1.5301** |
| ***Evening data (35 samples)*** | ***Mean*** | **0.0174** | **0.0077** | **2.2490** | **1.6477** |
| | ***St.Dev.*** | 0.0138 | 0.0080 | 0.9926 | 0.6845 |
| | ***Median*** | **0.0143** | **0.0052** | **2.0063** | **1.4472** |

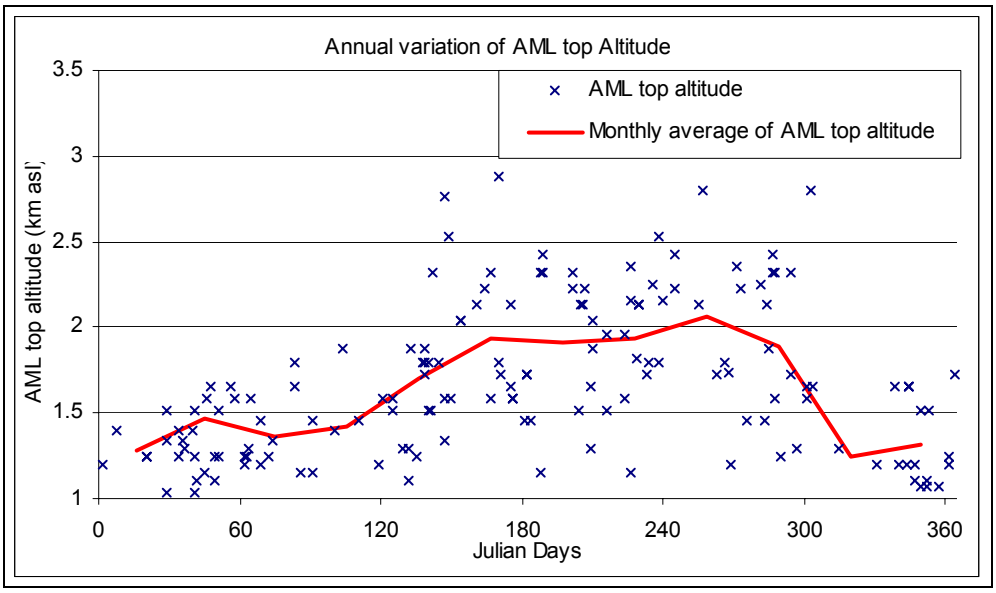


**Figure 5.4.** *Annual variation of the altitude of the aerosol mixed layer. 'x' are AML top altitude for different Julian days during May 2000- June 2002; thin line represents monthly-mean of altitude of AML top.*

## 5.3.2 Relationship with weather parameters

For determining the affect of meteorological parameters on ABC, a relation between layer-averaged ABC values and layer-averaged weather parameters for lower and upper layer has been made. Upper air weather parameters are taken from radiosonde observations at Payerne station for 00UTC and 12UTC. As most of the evening lidar observations are for sunset hours or later, the upper air weather data for 00UTC are used in this study representing evening.

Figure 5.5 is showing the relationship between ABC values and weather parameters. ABC value relationship with temperature shows that the aerosol in the lower layer is more affected, as expected due to its vicinity to the surface. With a low temperature in the lower layer, the aerosols-rich air parcels close to the surface are likely not to be uplifted, as the thermal energy is not available. High temperature causes vertical development of AML top. In such case, larger part of AML falls within the limits of considered lower layer and respectively higher average of ABC values are expected. The relationship between the wind speed and the ABC values clarifies that for both layers, the ABC value is higher for low-medium wind speed. For high wind speed for both layers, the cluster of ABC value is scanty. Relationship with wind direction is showing that the number of occurrence is higher for NE-SW sector in comparison to other sectors, particularly for lower layer. This may be connected to the NE-SW orientation of Jura mountain range (Figure 5.1). Due to this orientation of the Jura Mountains, the wind gets topographically oriented from either of two directions. Relationship between the relative humidity (RH) and ABC values shows that the highest ABC values correspond to the middle range of RH and decreases with lower or higher RH. It may be understood that low RH do not create critical conditions for aerosol growth. This is in agreement with tendency reported in [*Ackermann*, 1998] and [*Dupont et al.*, 1994]. High RH is likely connected to conditions for aerosol deposition. The ABC values are higher for high pressure for both layers. This is in agreement with finding of [*Matthias and Bösenberg*, 2002].

## 5.3.3 Backtrajectory analysis and relation to ABC data

Analytical back trajectories for Neuchâtel (developed by German Weather Service in the frame of EARLINET) are used to assess the history of air masses, reaching Neuchâtel and their likely origin and modifications. The 'prior location at *N*-hours', in this regard, is considered as the geographic location, at which the particular pressure level air mass was present at *N*-hours before the arrival time at Neuchâtel. This analysis is performed for three prior locations, i.e., before 12H, 24H and 48H. These back trajectories are collected in accordance with considered lidar measurements for 850 hPa pressure level and 700 hPa pressure level representing approximately 1-2 km (i.e. lower) and 2-5 km (i.e. upper) layers, respectively. The distribution of

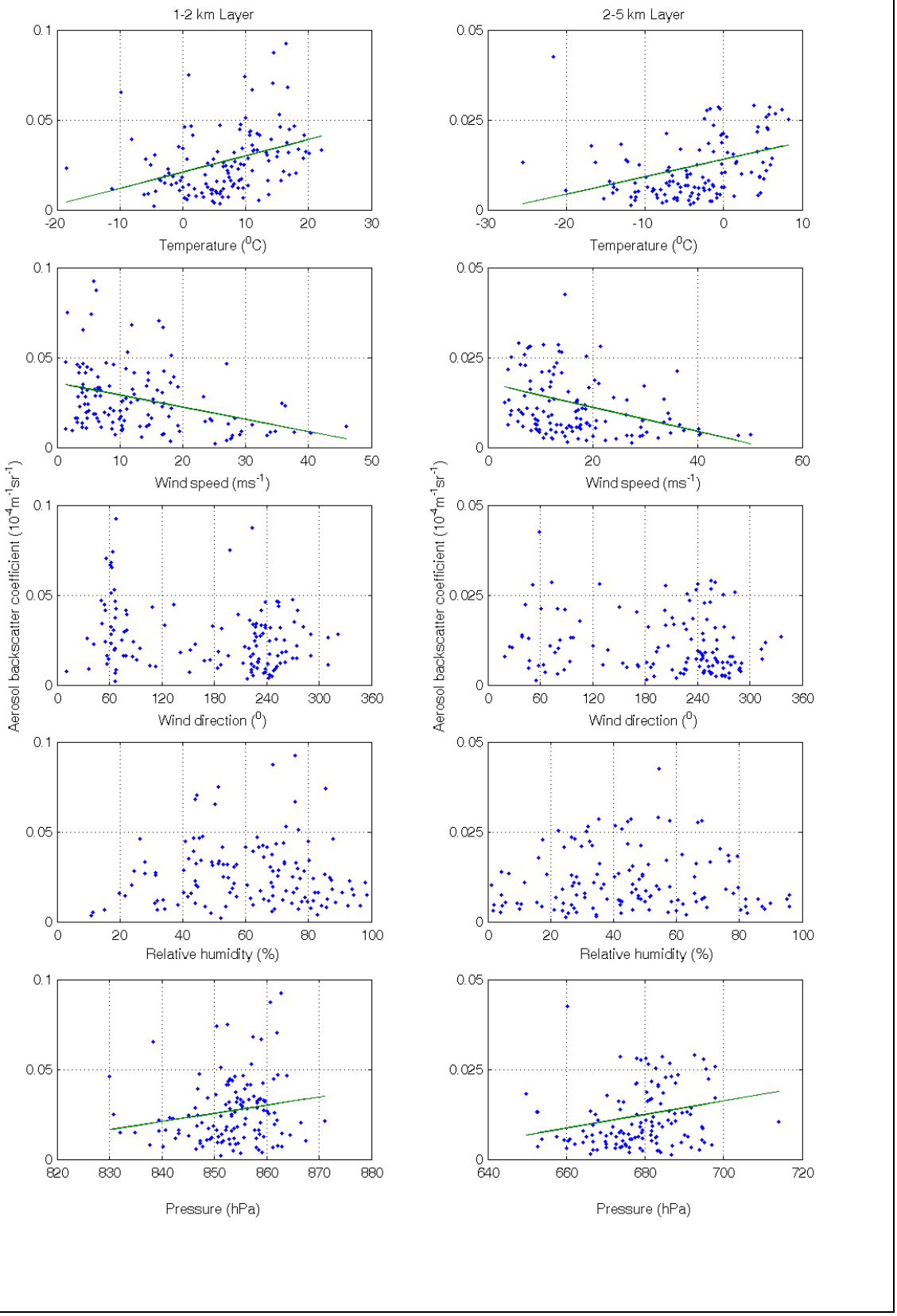


**Figure 5.5.** *Relation between ABC and various weather parameters for 1-2 km and 2-5 km layers. Wind direction is showing high ABC cluster for 60° and 240° and relative humidity is showing high clustering for middle range of RH.*

the origin of air masses is categorized versus two parameters: the distance and the azimuth of the prior location before various considered times with respect to Neuchâtel.

### 5.3.3.1 Classification of air masses with respect to Neuchâtel

Figure 5.6 presents an insight towards dominant regions surrounding the lidar site on the basis of distance of prior locations at 12H, 24H and 48H for 850 hPa pressure level. These distances may be in any direction encircling Neuchâtel. The number of occurrence and respective distances for different considered prior locations are shown. It is seen in Fig. 5.6 that 12H prior locations show a clear maximum in their distance distribution at approximately 150 km with a sharp drop beyond it. The same is seen for 24H prior locations, but at approximately 250 km. This shows that the 12H and 24H back trajectories carry air masses that either originate above European landmass or predominantly stay above it. The case for 48H prior location is different. For this case, more than one maximum are seen in the distance distribution, where the closest is at approximately 250 km from Neuchâtel. This shows that even in the case of these long back trajectories, a considerable part of them are located in their origin or modification above the European landmass. Any way there is a considerable part of 48H prior location, which is further from Neuchâtel. See the maxima at approximately 750 km and beyond in Fig. 5.6. As both 12H and 24H prior locations are likely in European landmass around Neuchâtel, for further study only 12H and 48H prior locations are considered.

Table 5.2 shows percentages of occurrence of air masses for 8 azimuths for 12H and 48H prior locations with respect to Neuchâtel. Table 5.2 informs that, for lower layer, for 12H prior locations, the air masses were mainly at NE, SW and S azimuths with 26.76%, 17.61% and 17.61% occurrences, respectively. For upper layer and for 12H prior locations with respect to Neuchâtel, the locations were mainly at N, W, SW and NW azimuths with 19.73%, 19.73%, 17.01% and 16.33% occurrences, respectively. For 48H prior locations with respect to Neuchâtel for lower layer, air masses were mainly at N, W, NW and SW azimuths with 22.54%, 22.54%, 16.90% and 15.49% occurrences and for upper layer, they were at W, N, NW and SW azimuths with 32.65%, 17.69%, 16.33% and 14.97% occurrences, respectively. For 12H prior locations, the orientation effect of Jura mountain range plays an important role in defining lower layer winds. It is indicated in table 5.2 for percentage occurrence for this layer, where high occurrence is seen from NE and SW/S azimuths. E-SE azimuths are showing low occurrence for both layers, except for SE azimuth for 12H prior locations for lower layer. Individual inspections of trajectories for low occurrence cases of E-SE azimuth show that air masses are from short distances and show a longer residence time over European landmass.

### 5.3.3.2 Effect of air masses history on ABC values

The region of Neuchâtel is almost equally distant from the possible source of cleaner oceanic air masses. In all directions, large water-bodies are far and air masses, which are reaching Neuchâtel, are modified during their pathway over the continental landmass. The modification in this way may be different, depending on its pathway and accordingly the sources of aerosols, residence time, meteorological conditions etc ([*Wandinger et al.*, 2002]). From this point, Neuchâtel is different from the sites investigated in [*Matthias and Bösenberg*, 2002] and [*Schneider and Eixmann*, 2002], where, in some cases, the air masses from oceanic origin reach to their measurement sites. In other words, before reaching to Neuchâtel, air masses from any origin travels over the European continent for considerably longer period and gets substantially modified. The example presented in Fig 5.7 shows that the 850hPa air mass originated in the North Sea and reaches Neuchâtel from NE after staying over the landmass for more than 48H.

Figure 5.8 presents ABC values in the lower layer for different azimuths for 12H and 48H prior locations. Figure 5.9 presents the same for the upper layer. In Figs. 5.8 and 5.9, continuous line is the median of all considered ABC values. Median of lower and upper layer is $2.2*10^{-6}$ $m^{-1}sr^{-1}$ and $0.79*10^{-6}$ $m^{-1}sr^{-1}$, respectively.

Figure 5.8 shows that ABC values, for 12H prior locations with respect to Neuchâtel, for S, SE and NW azimuths are about 1.5 times higher than ABC values from other azimuths. Possible explanation for these higher ABC values is the presence of industrialized areas of northern Italy (for S/SE azimuths) and northern France (for NW azimuth). In Fig. 5.8, for 48H prior locations with respect to Neuchâtel, NE and S azimuths are showing comparatively higher ABC values. Air masses from NE azimuth typically stay on the European continent for longer time, crossing the continental Europe landmass and are expected to bring aerosol-rich air to the lidar site. The example presented in Fig. 5.7 shows residence time of more than 48H over European continent for 850 hPa level air mass. Higher ABC values for S azimuth possibly owe their origin from Saharan dust. For 48H prior locations with respect to Neuchâtel, for lower layer, the ratio between maximum/minimum values of ABC varies by approximately a factor of 1.2. Such low variation in ABC values for various azimuths for 12H and 48H prior locations at Neuchâtel, compared to the results of [*Matthias and Bösenberg*, 2002] and [*Schneider and Eixmann*,

2002], indicates that the quality of air masses, that affect the lower layer at Neuchâtel, is always substantially modified.

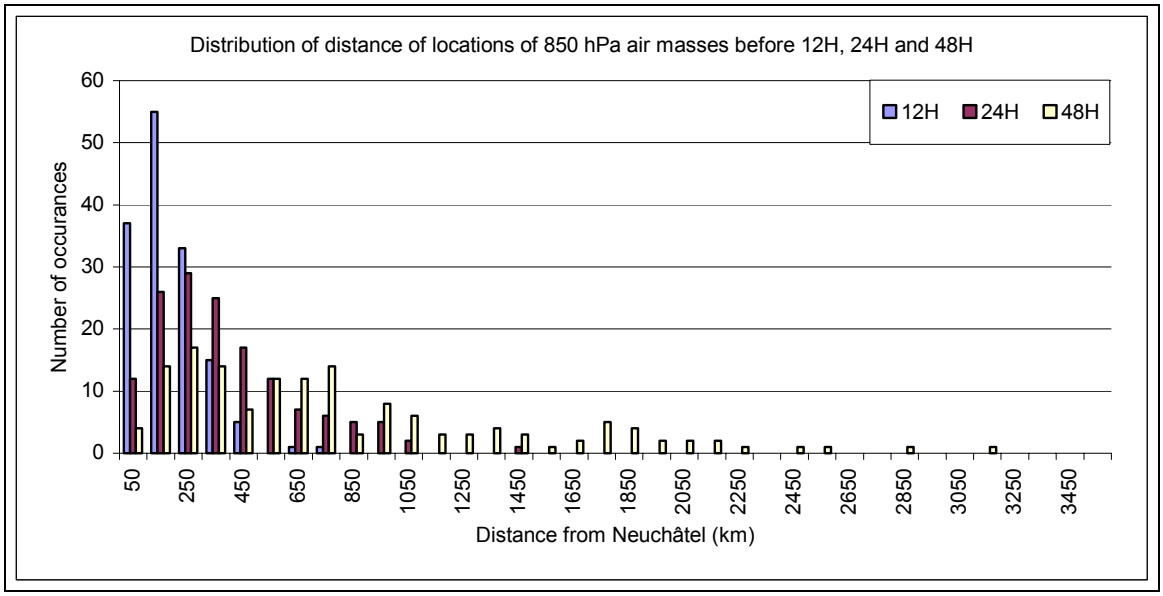


**Figure 5.6** *Distribution of distance of locations from Neuchâtel of 850 hPa air masses reaching before 12H, 24H and 48H with respect to the time of arrival of air masses at Neuchâtel.*

**Table 5.2.** *Percentage of occurrences of incoming airmasses from different directions for Neuchâtel station. Column 1 is the position of airmass before mentioned time with respect to Neuchâtel station.*

| Direction | N | NE | E | SE | S | SW | W | NW |
|---|---|---|---|---|---|---|---|---|
| **Occurrences (12 H before) at 850hPa** | 11.27 | 26.76 | 2.11 | 7.04 | 17.61 | 17.61 | 9.15 | 8.45 |
| **Occurrences (48 H before) at 850hPa** | 22.54 | 9.86 | 2.11 | 4.23 | 6.34 | 15.49 | 22.54 | 16.90 |
| **Occurrences (12 H before) at 700 hPa** | 19.73 | 9.52 | 4.08 | 4.76 | 8.84 | 17.01 | 19.73 | 16.33 |
| **Occurrences (48 H before) at 700 hPa** | 17.69 | 4.76 | 2.72 | 2.72 | 8.16 | 14.97 | 32.65 | 16.33 |

Figure 5.9 presents ABC values for the upper layer for 12H and 48H prior locations. In Fig. 5.9, for 12H prior locations, the ratio between maximum and minimum ABC varies by approximately a factor of 2.5. The highest ABC value in this case corresponds to SE azimuth. In Fig. 5.9, for 48H prior locations, higher ABC is seen from the various eastern azimuths (NE, E and SE). These azimuths are also showing low percentage of occurrence (Table 5.2). From individual inspection of back trajectories in each case for these azimuths, it is seen that, for most of the cases, the air masses stayed over European landmass for longer residence time, which increases the possibility for aerosol accumulation in air masses and increases the mixing possibilities of aerosols between PBL and lower troposphere. A case example presented in Fig. 5.7 show that the 700 hPa air mass has stayed over European continent for more than 48H and it was at SE azimuth before 48H to the time of arrival at Neuchâtel. Inspection of 4 cases from E azimuth shows that three cases were over European landmass for more than 48H and one case has crossed the industrialized northern Italy during its pathway i.e. in all of these cases, these air masses are likely to be aerosol-rich. The same can be concluded for SE azimuth, for which, individual inspection of each back trajectories informs that the air masses were over European landmass for longer period. For 48H prior locations for upper layer, the maximum/minimum ratio of ABC value from various azimuths is approximately 4.

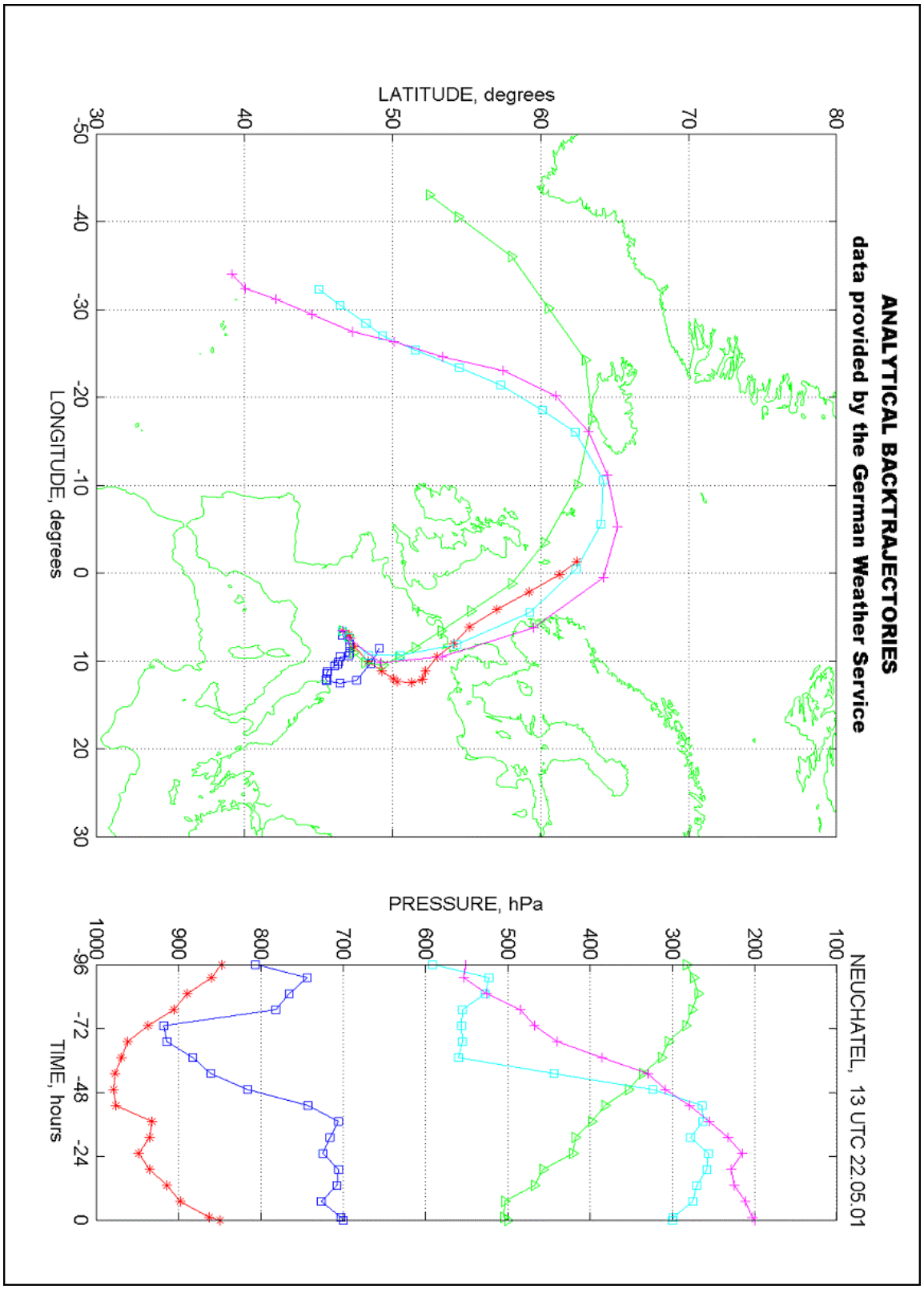


**Figure 5.7.** *An example of back trajectory (May 22, 2001, 1300H) for air mass location with respect to Neuchâtel. Two consecutive markers, after the first one, are showing 6H travel for air masses at different pressure levels. The air masses reaching at 850hPa (marked as '*') show that before 48H to the time of arrival of air masses at Neuchâtel, they were at N azimuth with respect to Neuchâtel and at NE azimuth before 24H and 12H. For 700 hPa level (marked as 'square'), air mass is seen at SE azimuth before 48H and 24H and at NE azimuth before 12H with respect to the time of arrival of air mass at Neuchâtel.*

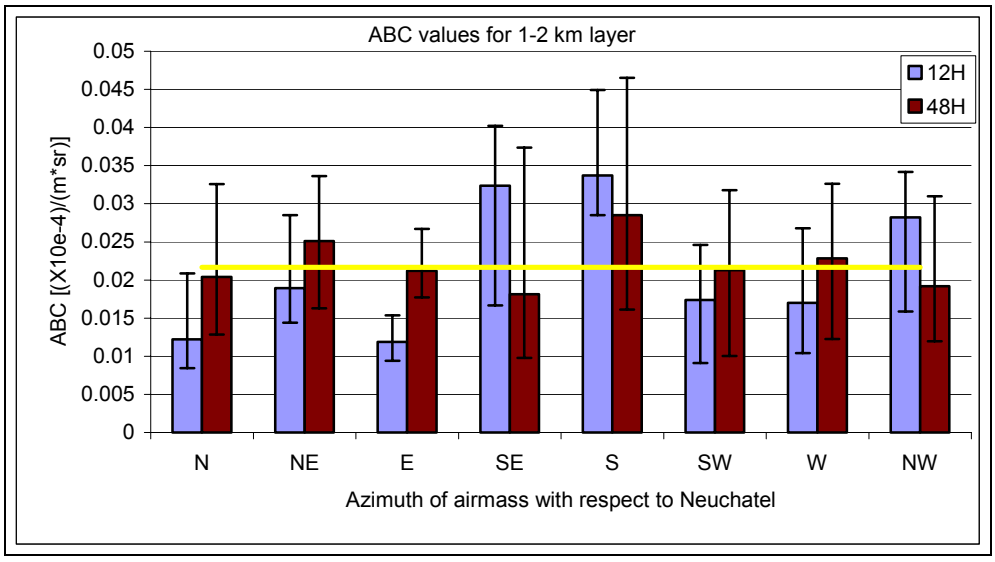


**Figure 5.8.** *Relationship between ABC values and air mass location at different azimuths with respect to Neuchâtel for 1-2km layer. Air masses are classified for their geographical location at 12H prior and 48H prior to the arrival time of these air masses at Neuchâtel. Error-bars show first and third quartile of ABC values. Continuous line in figure is showing median of all ABC values.*

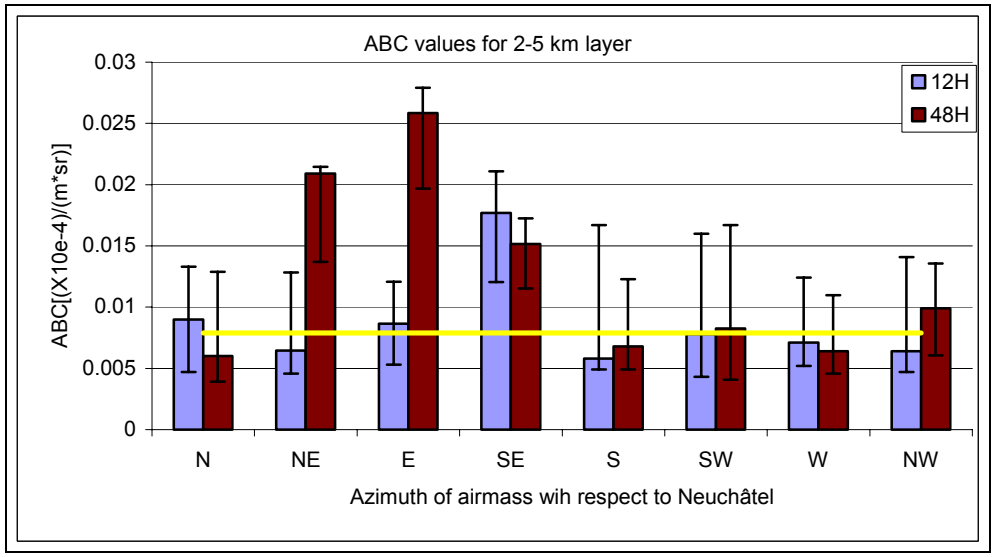


**Figure 5.9.** *Relationship between ABC values and air mass location at different azimuths with respect to Neuchâtel for 1-2km layer. Air masses are classified for their geographical location at 12H prior and 48H prior to the arrival time of these air masses at Neuchâtel. Error-bars show first and third quartile of ABC values. Continuous line in figure is showing median of all ABC values.*

**Table 5.3.** *Correlation coefficients between ABC values above Neuchâtel and average airmass speed for two layers and two airmass prior locations with respect to Neuchâtel.*

| | 1–2 km layer | 2–5 km layer |
|---|---|---|
| **12H prior location** | -0.31 | -0.23 |
| **24H prior location** | -0.35 | -0.25 |

Air mass speed is an important factor for its modification. It affects its residence time over continent and hence the probability of air mass modifications. To get information for such modifications, average air mass speed is calculated using back trajectory data. Air mass speed along the back trajectory is calculated by distance and time traveled by air masses. The air mass speed data are statistically correlated with ABC values for 12H and 48H prior locations for both layers. The results for correlation coefficient for both considered layers and for 12H and 48H prior locations are shown in Table 5.3. As seen by anti-correlation, low air mass speed is prone for more mixing and hence more effective air mass modification.

# 5.4 Conclusions

Our basic contribution in this Chapter is the data-base containing the two years of regular lidar measurements of the aerosol vertical distribution above Neuchâtel.

In the frame of the European project EARLINET, we applied Backscatter Lidar to investigate the aerosol backscatter coefficient (ABC) over Neuchâtel in different meteorological conditions and following the airmass history. The results are discussed for two vertical layers i.e. from 1-2 km asl (lower layer) and 2-5 km asl (upper layer), representing approximately the aerosol mixed layer (PBL) above Neuchâtel and the lower free troposphere, respectively. Our Lidar observations over two years (set of about 150 periods of measurements) lead to the following conclusions:

1. Relationship between layer-averaged weather parameters and layer-averaged ABC values show influence of temperature, wind speed, relative humidity and pressure on ABC values. Relationship with wind direction is showing a locally derived wind distribution i.e. NE-SW, or the orientation of nearby Jura mountain range. The annual cycle of the ABC values shows maxima in summer and minima in winter. Altitude of the aerosol mixed layer (AML) top is highest during fall, followed by summer, spring and winter.

2. From the air mass history analyses, it is found that the affecting regions with respect to Neuchâtel can be classified on the basis of distances and azimuths. The east-southeast azimuths are showing the lowest percentage occurrence of air masses and high ABC values for upper layer. The relatively high ABC values from eastern sector for upper layer in comparison to ABC values from other azimuths is due to the longer residence time of the air mass over the European continent. The ABC values in the lower layer are approximately 2.5 times higher than the ABC values in the upper layer. ABC values are affected by continental sources and are showing anti-correlation with air masses speeds reaching Neuchâtel.

3. The perspective for this study is the inclusions of results from signal inversion for other wavelengths and also those from the depolarization properties of the particles. This will help to distinguish aerosol layers having different origin.

4. The present approach to air mass history shall be extended to a study of the clusters of the backtrajectories reaching Neuchâtel.

# Conclusion and perspective

After years of developing of the Atmospheric Backscatter Lidar as hardware and data processing algorithms, the task of the Lidar research community is to demonstrate how this instrument may contribute a new knowledge. The best way to do this is when the Lidar is applied in practical case studies in atmospheric research and in the ecological monitoring. The work performed in this PhD thesis contains the results of the Lidar application in such case studies. All reported case studies are performed in the Planetary Boundary Layer (PBL) and in the lower troposphere above complex terrain.

In the first case we applied the Lidar to study the existence of elevated aerosol layers above the Rhine Valley – an example of a deep mountain valley. The study is carried during weather conditions when the convection is expected to be the predominant factor in the formation of the PBL and in this way, to the aerosol stratification. In this study the Lidar measurements show that the formation of the aerosol layers in the Valley PBL may be understood following the generally accepted description for the thermally established wind system in the Valley. In addition to this, the Lidar results show aerosol layers elevated for a considerably long period till altitudes of 4000 m-5000 m asl, i.e., well above the Valley PBL. This observation of elevated aerosol layers complements to previous studies showing the possibility for elevated residual layers, as well as to the studies pointing the role of mountains in the mixing and transport of polluted airmass with the air in the free troposphere.

In the second case our Lidar study shows how the Foehn wind development correlates with the modifications of the aerosol stratification, as determined from the Backscatter Lidar. The study is done also above the Rhine Valley. The results from the Lidar measurement demonstrate the dynamics of "taking away" of the aerosol rich air by the Foehn airmass during the development of the Foehn. The Lidar determination of the general decrease of the aerosol backscatter coefficient along all measured profile contributes to the interpretation of the known "Foehn clearance". That is, the increase of the radiation on the surface during Foehn is caused not only by the absence of clouds during Foehn, but also by the fact that less aerosol is present in the atmosphere. This is the first application of Backscatter Lidar to study the dynamics of such wind. This study, as well as the above one, show the benefits of adding the Lidar measurements of the aerosol vertical profile to the measurements of the surface values and profile values of the meteorological parameters.

In the third case our Lidar study provides information about the aerosol backscatter coefficient above the town of Neuchâtel. The atmosphere above Neuchâtel also presents an interesting case study: Neuchâtel is in a central part of European landmass, surrounded by urbanized and industrialized regions. It is also a good example of a "complex terrain" with a mountain slope and a lake. Combining this information with the surface meteorological data and with the analysis of the airmass backtrajectory, it is possible to demonstrate how the atmospheric aerosol values varies with the seasons, how it depends on the surface meteorological parameters, as well as to show the role of the airmass transport from the different regions. The study in the presented PhD thesis is based on the results obtained in 2-years of systematic Lidar measurements and is only the start of such statistical study. Anyway, this case study demonstrates the important contribution that the Backscatter Lidar may have in the aerosol pollution monitoring.

To apply the Backscatter Lidar in these practical cases, we performed first a study of the sensitivity of the obtained results on applied algorithms for Lidar data processing and the assumed initial and reference values. This study is based on numerically simulated Lidar signals and answered the important question: what are the statistical and systematic errors we make when we solve the Lidar equation with different degrees of deficiencies in our "a priory" information and assumptions. The answer of this question made possible to obtain quantitative results about the aerosol optical parameters from the single wavelength Backscatter Lidar signal.

The results obtained by the lidar application in the cases presented in the thesis are contributions to the knowledge about the atmospheric dynamics and atmospheric environment. In all these cases we operated reliably the Lidar in long series of measurements. Our processing algorithm made it possible to characterize the aerosol content and its vertical distribution. In all these cases the Lidar measurements were interpreted and correlated

together with the measurements of both traditional and advanced atmospheric research instruments and methods. Those were surface and radiosonde meteorological measurements, wind Radar, Scintillometer, and backtrajectory analysis. Such application of the Lidar in combination with the other instruments helps to identify the factors determining the aerosol vertical distribution.

In each of the reported case studies there are possibilities for further improvement of the results by revealing with better resolution the aerosol temporal and vertical distribution. This may be done by improving the technical performance of the used Lidar hardware, combining it with detection of the backscatter signal at additional wavelengths and polarizations. Also, it is necessary to develop faster algorithms for noise reduction and to automatize the application of the signal inversion method.

Following our study, we see the newly opened questions requiring further application of atmospheric Backscatter Lidar above complex terrain:

(i) What is the depth of layers of mixing in convective PBL above valley and above mountain-lake system ? Under Foehnic conditions, what is the depth of the layer of mixing between the cold pool and the Foehn layer ?
(ii) How the local minima of the Lidar signal gradient correlate with the local maxima of the potenial temperature gradient both in convective PBL and above the valley during Foehn event ?
(iii) How frequently the elevated aerosol layers appear and how we may distinguish from the Lidar signal the aerosol layers having different origin ?

Another important contribution in the thesis is the demonstration that the atmospheric Backscatter Lidar is a mature instrument for practical applications. This maturity is demonstrated by the possibility to have systematic and routine measurements during campaign and in a fixed site. The information from the Lidar helps to study the dynamic processes in the lower atmosphere. It is also important in the understanding of the atmospheric ecological status. The conclusion is that the Backscatter Lidar has its place in the inventory of the instruments and methods used in the atmospheric research.

# Annex 1

# "Ozone and water-vapor measurements by Raman Lidar in the planetary boundary layer: error sources and field measurements": a paper in Applied Optics*

* Lazzarotto B., M. Frioud, G. Larchevêque, V. Mitev, P. Quaglia, V. Simeonov, A. Thompson, H. van den Bergh and B. Calpini, "Ozone and water-vapor measurements by Raman Lidar in the planetary boundary layer: error sources and field measurements", Applied Optics 40 (18), 2985-2997 (2001).

# Ozone and water-vapor measurements by Raman lidar in the planetary boundary layer: error sources and field measurements

Benoît Lazzarotto, Max Frioud, Gilles Larchevêque, Valentin Mitev, Philippe Quaglia, Valentin Simeonov, Anne Thompson, Hubert van den Bergh, and Bertrand Calpini

A new lidar instrument has been developed to measure tropospheric ozone and water vapor at low altitude. The lidar uses Raman scattering of an UV beam from atmospheric nitrogen, oxygen, and water vapor to retrieve ozone and water-vapor vertical profiles. By numerical simulation we investigate the sensitivity of the method to both atmospheric and device perturbations. The aerosol optical effect in the planetary boundary layer, ozone interference in water-vapor retrieval, statistical error, optical cross talk between Raman-shifted channels, and optical cross talk between an elastically backscattered signal in Raman-shifted signals and an afterpulse effect are studied in detail. In support of the main conclusions of this model study, time series of ozone and water vapor obtained at the Swiss Federal Institute of Technology in Lausanne and during a field campaign in Crete are presented. They are compared with point monitor and balloon sounding measurements for daytime and nighttime conditions. © 2001 Optical Society of America

*OCIS codes:* 280.0280, 280.1910, 010.1120, 010.3640, 010.7030.

## 1. Introduction

The degradation of air quality is a serious environmental problem that affects urban and industrial areas worldwide. Air pollution injures human health and ecosystems, diminishes crop yield, and spoils patrimony and materials. The phenomena involved in air pollution are complex. Once they are emitted into the atmosphere, (primary) pollutants are transported, dispersed, transformed by gas–solid phase change and chemical reaction, and finally removed by dry and wet deposition.

Most challenging is the fact that the health and environmental effects of secondary pollutants (formed in the atmosphere) are frequently more severe than those of their precursors (primary pollutants). This is so for ozone and other photochemical pollutants, such as peroxyacetyl-nitrate, and for secondary particles produced in the atmosphere by the photooxidation of volatile organic compounds catalyzed by nitrogen oxides ($NO_x$). Photochemical air pollution is a complex science because of the nonlinearity of its response to changes in primary emission (see, for example, Ref. 1).

Three-dimensional air quality models are used as the most powerful tools for identifying effective strategies to improve air quality. With the mesoscale Eulerian chemical transport model developed at the Ecole Polytechnique Federal Lausanne (EPFL) we can simulate pollutant dynamics over cities such as Athens and Milan and over regions with high traffic loads in Switzerland and provide technical guidance to air quality management agencies.[2–4] The model resolution is of the order of 1 km on the horizontal scale, with a vertical resolution of some tens of meters for the lowest layer of the model, as much as 500 m for the top layer, and a total height of 5 km above ground level. The domain size is typically 100 km × 100 km. Before the model results can be used with confidence, they must be validated against field measurements with similar spatial and time resolutions.

Most of the time, an air quality network in a densely urbanized region is built upon a set of ground-

B. Lazzarotto, G. Larchevêque, P. Quaglia, V. Simeonov, H. van den Bergh, and B. Calpini (bertrand.calpini@epfl.ch) are with the Lidar Group, Laboratory for Air Pollution, Swiss Federal Institute of Technology, CH-1015 Lausanne, Switzerland. M. Frioud and V. Mitev are with the Observatory of Neuchatel, CH-2000 Neuchatel, Switzerland. A. Thompson is with the NASA Goddard Space Flight Center, Code 916, Greenbelt, Maryland 20771.

Received 14 June 2000; revised manuscript received 23 January 2001.

0003-6935/01/182985-13$15.00/0

based stations equipped with point detectors. Trace-gas measurements are often influenced by local sources and thus are not representative of the average concentrations over the typical grid size of the model. Tropospheric lidar measurements, however, are based on an integrated optical path of typically 50–500 m, depending on the trace-gas species. This spatial resolution is in ideal agreement with the model resolution. Therefore the lidar measurements can supply essential information, including ozone and water-vapor vertical profiles, for validation of the model.

Ozone as a secondary pollutant is an ideal species for comparison with its predicted values obtained from the model. Because ozone is produced in the model by photochemical reactions and transport effects, good agreement between field measurements and model values is an indicator of the model performance.

The water-vapor content of the atmosphere plays a major role in the dynamics and climatology of the atmosphere and is also a clear tracer of the daily evolution of the top of the planetary boundary layer (PBL). Thus its continuous remote detection over a period of time of some days, the typical duration of an air pollution event, may also contribute significantly to improvement of the model predictions.

In this paper we present the design and development of a Raman lidar system with optimized resolution in comparison with model results. This ozone–water-vapor Raman lidar development is a follow-up of our recent research on an elastic ozone differential absorption lidar (DIAL) technique.[5–7] This technique is a method with higher sensitivity than Raman lidar, and with well-established ozone measurements in atmospheric conditions in which the aerosol density is low enough, or homogeneous, as such in the free troposphere. In the PBL, where highly variable aerosol concentrations are frequently observed, elastic DIAL may fail or even no longer be used because of strong and unpredictable aerosol optical interference on the ozone retrieval.[8,9] In particular, the aerosol backscatter and its high but poorly known wavelength dependence were pointed out by Völger *et al.*[10]

The PBL is also the atmospheric layer with the highest vertical resolution in the model. This fact brought us to the idea of developing an alternative instrument to the elastic DIAL, an instrument much less perturbed by the nonhomogeneous aerosol load condition in the PBL and able to perform simultaneous ozone and water-vapor measurements with high resolution at low altitudes. This instrument is based on measurement of the Raman-shifted backscattered light induced by the most abundant molecular species in the atmosphere, i.e., nitrogen, oxygen, and water vapor, from an UV laser pulse emitted in the atmosphere. The water-vapor content is obtained by the classic Raman analysis.[11,12] Ozone is calculated by a differential absorption method that uses oxygen and nitrogen Raman backscatter as ON and OFF signals. The various Raman return signals are generated simultaneously from a single laser source, thus probing the same volume of air at a given time and essentially avoiding the problems related to pulse-to-pulse laser stability or to atmospheric turbulence that usually occur for most elastic DIAL instruments in which two successive pulses are emitted.[13] The disadvantage caused by the weaker Raman signals compared with the elastic signals is compensated for by the high molecular densities and the well-known values of the Raman cross sections. This idea refers to the pioneering studies of Melfi *et al.*[11] and by Renault *et al.*[12]; those authors published a first measurement of the vertical water-vapor distribution in the PBL and later proposed to correct the water-vapor Raman return for tropospheric ozone attenuation.[14] The same principle was successfully applied for the stratosphere.[15]

Here we apply these earlier concepts to the development of an operational lidar instrument for daytime and nighttime measurements and for time series of some days to follow the vertical dynamics and time evolution of an air-pollution episode. In Section 2 of this paper we present a model estimate for determinating the critical system parameters. In Section 3 we define the experimental setup, and in Section 4 we give some typical results obtained for various time series of ozone and water-vapor concentrations and comparisons with other instruments.

## 2. Raman Lidar: Principle and Predicted Sources of Error

Figure 1 is a schematic of the Raman lidar system. The ozone retrieval is based only on the nitrogen and oxygen Raman backscattered signals. For the water-vapor retrieval we can use either nitrogen and water-vapor or oxygen and water-vapor pairs of signals. Each of the three Raman-shifted wavelengths corresponds to a lidar equation:

$$P_X(\lambda_X^{\text{Raman}}, R) = P_L(\lambda_L) K_X \frac{O(R)}{R^2} n_X(R) \beta_X^{\text{Raman}} \Delta R \times \exp\left\{ -\int_0^R [\alpha_L(r) + \alpha_X(r) + n_{O_3}(r)(\sigma_L + \sigma_X)] dr \right\}, \quad (1)$$

where the subscript $X$ stands for ozone, nitrogen, or water vapor; $P_X(\lambda_X^{\text{Raman}}, R)$ is the Raman lidar power backscattered from species $X$ at Raman-shifted wavelength $\lambda_X^{\text{Raman}}$ and distance $R$; $P_L(\lambda_L)$ is the laser emitted power at wavelength $\lambda_L$; $K_X$ is the instrument constant at Raman-shifted wavelength $\lambda_X^{\text{Raman}}$; $O(R)$ is the telescope active surface area; $n_X(R)$ is the molecular density of species $X$ at distance $R$; $\beta_X^{\text{Raman}}$ is the Raman differential backscattering cross section for species $X$; $\alpha_X(r)$ and $\alpha_L(r)$ are the atmospheric extinction coefficients, without the ozone absorption coefficient, at Raman-shifted wavelength $\lambda_X^{\text{Raman}}$ and at pump laser wavelength $\lambda_L$, respectively; and $\sigma_X$ and $\sigma_L$ are the ozone absorption cross sections at Raman-shifted wavelength $\lambda_X^{\text{Raman}}$ and the pump la-

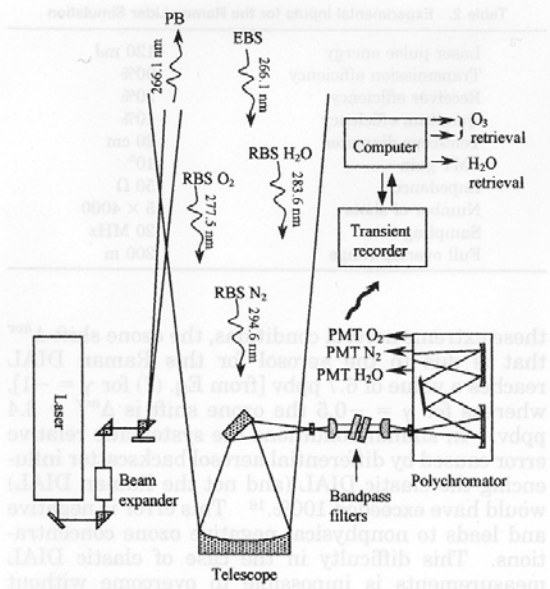


Fig. 1. Schematic of Raman lidar. A pulsed laser beam (PB) is emitted into the atmosphere via a beam expander (3×) and a set of right-angle prisms. The elastically backscattered signal (EBS) and the Raman-shifted backscattered signals (RBSs) are collected by a 200-mm Newtonian telescope, filtered at the entrance of a polychromator where they are spectrally resolved, and detected by three photomultiplier tubes (PMTs). The PMT signals are stored in a transient recorder (20-MHz/12-bit and photon counting) and a PC-based computer unit allows for real-time ozone and water-vapor retrieval (raw data).

ser wavelength $\lambda_L$, respectively. The ozone concentration $n_{O_3}(R)$ can be calculated from the nitrogen and oxygen Raman signals by use of a modified DIAL equation in the following form:

$$n_{O_3}(R) = \frac{1}{\sigma_{O_2} - \sigma_{N_2}} \frac{d}{dR}\left[\ln \frac{P_{N_2}(R)}{P_{O_2}(R)}\right] - \frac{[\alpha_{O_2}(R) - \alpha_{N_2}(R)]}{\sigma_{O_2} - \sigma_{N_2}}. \quad (2)$$

The water-vapor mixing ratio in g of $H_2O$/kg of dry air is obtained from the ratio of the water-vapor Raman-shifted signal to either the Raman nitrogen- or the Raman oxygen-shifted signal. Using the nitrogen channel yields the following expression:

$$\frac{n_{H_2O}}{n_{N_2}}(R) = \frac{P_{H_2O}}{P_{N_2}}(R) \frac{K_{N_2}}{K_{H_2O}} \frac{\beta_{N_2}^{Raman}}{\beta_{H_2O}^{Raman}} \times \exp\left(\int_0^R \left\{ \underbrace{(\sigma_{H_2O} - \sigma_{N_2}) n_{O_3}(r)}_{\text{ozone correction}} + [\alpha_{H_2O}(r) - \alpha_{N_2}(r)] \right\} dr\right). \quad (3)$$

As the oxygen signal is approximately three times weaker than the nitrogen signal, the water-vapor mixing ratio calculated by use of an oxygen Raman-shifted signal will be less accurate, and we use it only as an additional test of the consistency of the water-vapor result. Note that in Eq. (3) the water-vapor concentration retrieval depends linearly on the ratio of the Raman water-vapor signal to the Raman nitrogen signal, whereas in Eq. (2) the ozone concentration depends on the first derivative of the two Raman lidar signals (nitrogen versus oxygen). We shall see below that the various predicted error sources for ozone and water vapor will have a strong relation to this dependence and that in any case the ozone differential retrieval will be much more affected than the water-vapor linear retrieval.

As the ozone retrieval does not depend on the instrument constant $K_X$, the method can be regarded as self-calibrated. In contrast, for absolute water-vapor measurements, exact knowledge of $K_X$ or independent parallel measurements for instrument calibration are needed. The term $(\sigma_{H_2O} - \sigma_{N_2}) n_{O_3}(r)$, denoted ozone correction in the exponential part of Eq. (3), reflects the ozone influence on the water-vapor and nitrogen Raman signals and can significantly affect the final results,[12] as is emphasized below.

### A. Molecular and Aerosol Dependence of the Raman Lidar

From Eq. (2), the ozone retrieval does not depend on the backscattering properties of the atmosphere. This is the major advantage of the Raman–DIAL method compared with the conventional (elastic) DIAL and may be of crucial importance, particularly in the case of a strong and inhomogeneous aerosol load.[10] The influence of atmospheric extinction on ozone retrieval is expressed by the second term of Eq. (2). This term also appears in the elastic DIAL formalism and can be split into its molecular and its aerosol contributions.

First, the molecular atmosphere contribution to ozone retrieval is estimated by use of the Rayleigh wavelength dependence for the extinction. One obtains the following (negative) correction to the ozone relative content:

$$\Delta^{mol} = \frac{\alpha_{O_2}^{mol} - \alpha_{N_2}^{mol}}{n_{air}^{mol}(\sigma_{O_2} - \sigma_{N_2})}, \quad (4)$$

where $n_{air}^{mol}$ is the air's molecular density. As the numerator in Eq. (4) also directly depends on the air density, the result $\Delta^{mol}$ is given as an altitude-independent value in this formalism. It corresponds to a correction of $\sim -3$ parts in $10^9$ by volume (ppbv).

Let us now add a homogeneous aerosol layer characterized by two variables to the model, namely, the total lidar ratio $e$, defined as the total extinction $\alpha_{total}$ divided by the total backscattering $\beta_{total}$, and the backscattering ratio $b$, defined as the total backscattering $\beta_{total}$ divided by the molecular backscattering $\beta_g$. With the assumption of atmospheric molecular

Table 1. Spectroscopic Data Used for a 266-nm Pump Laser Source

| Property | Molecule $O_2$ | $N_2$ | $H_2O$ |
|---|---|---|---|
| Vibrational Raman shift ($cm^{-1}$) | 1555 | 2331 | 3651 |
| Corresponding Raman wavelength (nm) | 277.5 | 283.6 | 294.6 |
| Raman differential scattering cross section ($10^{-30}$ $cm^2/sr$)[a] | 23.3 | 10.7 | 33.3 |
| Ozone absorption cross section at $\lambda_X^{Raman}$ ($10^{-20}$ $cm^2$/molecule)[b] | 490.6 | 296.3 | 81.93 |
| $SO_2$ absorption cross section at $\lambda_X^{Raman}$ ($10^{-20}$ $cm^2$/molecule)[c] | 64.4 | 84.5 | 90.8 |
| $NO_2$ absorption cross section at $\lambda_X^{Raman}$ ($10^{-20}$ $cm^2$/molecule)[d] | 4.82 | 6.30 | 9.98 |

[a]Ref. 18.
[b]Ref. 19.
[c]Ref. 20.
[d]Ref. 21.

species with a mean diameter much smaller than the laser wavelength, molecular backscattering $\beta_g$ is defined according to Collis and Russell[16] by

$$\beta_g = n_{air}^{mol} \frac{d\sigma^{Rayleigh}(\pi)}{d\Omega} = n_{air}^{mol}\left(\frac{550}{\lambda_L}\right)^4 5.45 \times 10^{-32}, \quad (5)$$

where the molecular backscattering $\beta_g$ is given in units of inverse meters per steradian, the laser wavelength $\lambda_L$ is in nanometers, and the air density $n_{air}^{mol}$ is in inverse cubic meters. One may also assume a power law for the wavelength dependency of the extinction that is caused by Mie particles ($\alpha^{aer} \sim \lambda^{\gamma}$), following previous research[17] in which $\gamma$ was shown to have a range of $\gamma \in [-1, -0.5]$. With $\gamma = -1$, the following estimation of the aerosol correction $\Delta^{aer}$ to the ozone concentration is obtained:

$$\frac{\Delta^{aer}}{\Delta^{mol}} = (\lambda_L)^{-3} \frac{(\lambda_{O_2}^{Raman})^{-1} - (\lambda_{N_2}^{Raman})^{-1}}{(\lambda_{O_2}^{Raman})^{-4} - (\lambda_{N_2}^{Raman})^{-4}} \left(\frac{eb}{c^{Rayl}} - 1\right), \quad (6)$$

where $c^{Rayl} = 8\pi/3$ is the molecular lidar ratio (Rayleigh contribution). With the parameters listed in Table 1, this notation yields the following aerosol contribution to the ozone correction:

$$\Delta^{aer} \cong (0.035 \times eb - 0.3)\Delta^{mol}. \quad (7)$$

Here we have used for the molecular density and the water-vapor content a model atmosphere defined in Ref. 22 (Model 3), with "mid-latitude winter" conditions. The water-vapor vertical profile was taken directly from this model atmosphere but was multiplied by a factor of 3 for comparison with experimental results presented below. The total extinction and backscattering coefficients were defined for the fourth harmonic of a Nd:YAG laser source at 266 nm, with the effect of a constant aerosol vertical profile taken into account. To simulate the most severe aerosol conditions, we tuned the aerosol's optical properties to their maximum acceptable (or worse) values for $e$ and $b$, 40 and 1.8, respectively. With

Table 2. Experimental Inputs for the Raman Lidar Simulation

| | |
|---|---|
| Laser pulse energy | 120 mJ |
| Transmission efficiency | 90% |
| Receiver efficiency | 20% |
| Quantum efficiency | 10% |
| Telescope diameter | 20 cm |
| PMT gain | $10^5$ |
| Impedance | 50 Ω |
| Number of shots | $5 \times 4000$ |
| Sampling rate | 20 MHz |
| Full overlap range | 200 m |

these extreme aerosol conditions, the ozone shift $\Delta^{aer}$ that is due to the aerosol for this Raman DIAL reaches a value of 6.7 ppbv [from Eq. (7) for $\gamma = -1$], whereas for $\gamma = -0.5$ the ozone shift is $\Delta^{aer} = 3.4$ ppbv. In similar conditions the systematic relative error caused by differential aerosol backscatter influencing the elastic DIAL (and not the Raman DIAL) would have exceeded 100%.[16] This error is negative and leads to nonphysical negative ozone concentrations. This difficulty in the case of elastic DIAL measurements is impossible to overcome without their being additional information about the backscatter properties of the aerosol or without additional assumptions about the aerosol properties.[8]

### B. Ozone Interference in Water-Vapor Raman Lidar Retrieval

Ozone absorbs in the Hartley and Huggins bands at 220–350 nm and thus affects the signal at each of the Raman oxygen, nitrogen, and water-vapor wavelengths. The effect of the ozone absorption on the water-vapor retrieval defined in Eq. (3) was simulated with a model atmosphere with various constant values of ozone concentration, a homogeneous aerosol load ($e = 40$, $b = 1.8$), and the lidar parameters listed in Table 2. The ozone corrections $\Delta H_2O$ for the water-vapor retrieval are shown in Fig. 2 as the difference between the water-vapor retrieval profile

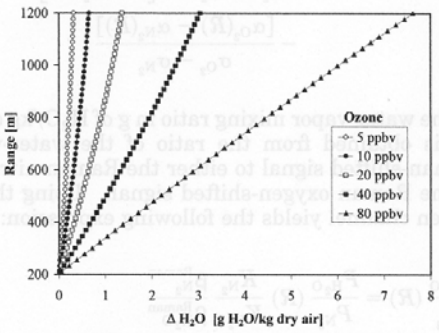


Fig. 2. Ozone effect on water-vapor retrieval. Predicted error in the water-vapor mixing ratio retrieved by Raman lidar as a result of various ozone constant vertical profiles and a homogeneous aerosol load. The horizontal scale is the difference between the water-vapor retrieval without the ozone absorption taken into account and the same retrieval with ozone absorption.

without ozone interference and the same retrieval corrected for the ozone absorption effect. The correction values are set to 0 g of $H_2O$/kg of dry air at 200 m, at which a full overlap between the laser beam and the telescope's field of view is assumed. The model shows that, even for moderate ozone concentrations of 40 ppbv, the correction can exceed 1 g of $H_2O$/kg of dry air at 600 m and more than 2.5 g of $H_2O$/kg of dry air at 1200 m, that is, ~20% of the water-vapor content in the standard atmosphere.

The integrated ozone content that one needs to be able to take the ozone correction into account can be obtained either by independent ozone (e.g., balloon) measurements or by additional use of the ratio of the oxygen and nitrogen Raman signals. The first method requires additional absolute ozone concentrations but is not convenient for practical purposes and therefore is more suitable for calibration and verification of the lidar system. The second method has the advantage of a self-corrected water-vapor measurement with the risk of additional uncertainty owing to the contribution of each of the three Raman backscattered lidar signals. Both methods were applied in our experiments.

In the second method, the integrated ozone content to distance $R$ can be calculated from oxygen and nitrogen Raman signals as

$$\exp\left[\int_0^R n_{O_3}(r)\mathrm{d}r\right] = \left[\frac{P_{O_2}}{P_{N_2}}(R)\right]^{1/(\sigma_{N_2}-\sigma_{O_2})} \times \left[\frac{K_{N_2}}{K_{O_2}}\frac{n_{N_2}}{n_{O_2}}(R)\frac{\beta_{N_2}^{\mathrm{Raman}}}{\beta_{O_2}^{\mathrm{Raman}}}\right]^{1/(\sigma_{N_2}-\sigma_{O_2})}. \quad (8)$$

Further, by replacing the integrated ozone content in Eq. (3) by Eq. (8) and neglecting the differential extinction that is due to Rayleigh and Mie scattering processes in accordance with Ref. 12, we can determine the water-vapor mixing ratio as

$$\frac{n_{H_2O}}{n_{N_2}}(R) = \frac{P_{H_2O}}{P_{N_2}}(R)\frac{K_{N_2}}{K_{H_2O}}\frac{\beta_{N_2}^{\mathrm{Raman}}}{\beta_{H_2O}^{\mathrm{Raman}}} \times \left[\frac{K_{N_2}}{K_{O_2}}\frac{n_{N_2}}{n_{O_2}}(R)\frac{\beta_{N_2}^{\mathrm{Raman}}}{\beta_{O_2}^{\mathrm{Raman}}}\right]^{\sigma_{H_2O}-\sigma_{N_2}/\sigma_{N_2}-\sigma_{O_2}} \times \left[\frac{P_{O_2}}{P_{N_2}}(R)\right]^{\sigma_{H_2O}-\sigma_{N_2}/\sigma_{N_2}-\sigma_{O_2}} \quad (9)$$

or as

$$\frac{n_{H_2O}}{n_{N_2}} = K_{\mathrm{cal}}\frac{P_{H_2O}(R)}{P_{N_2(R)}}\left[\frac{P_{O_2}(R)}{P_{N_2}(R)}\right]^{\sigma_{H_2O}-\sigma_{N_2}/\sigma_{N_2}-\sigma_{O_2}}, \quad (10)$$

where the factor $K_{\mathrm{cal}}$ is the overall instrument constant value and must be established by calibration of the lidar.

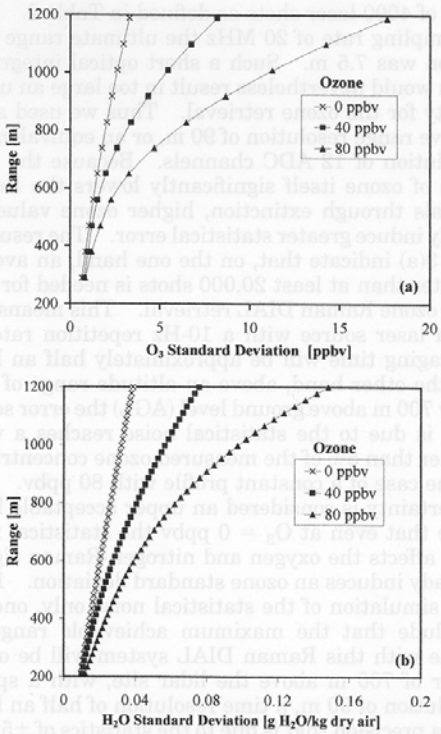


Fig. 3. Statistical noise. Predicted standard deviations for (a) ozone and (b) water-vapor Raman lidar retrieval as a result of statistical noise (Poisson statistics) with the experimental parameters defined in Table 2.

### C. Statistical (Quantum) Noise

The statistical noise is a major perturbation in Raman lidar measurements[17] because of the low Raman cross section, typically 4 orders of magnitude lower than the elastic cross section, and therefore because of the low Raman signal level. The statistical noise has been modeled following the Poisson statistics with the parameters defined in Table 2. In this case the model study was performed in a purely molecular atmosphere (no aerosol load). Based on typical experimental values, we estimate a number of photoelectrons per pulse at the photocathode, from a distance of 200 m and for one analog-to-digital converter (ADC) channel of 7.5-m resolution, of some hundreds for both nitrogen and oxygen Raman lidar signals and some counts for water vapor. This model simulation of the statistical noise is based on series of 100 runs for each similar initial condition. From these series of runs the standard deviation with respect to the mean value is obtained, and it is shown in Fig. 3 relative to the range.

Figure 3(a) shows the ozone standard deviation that is due to the effect of statistical noise on the retrieved ozone concentration for three profiles with constant ozone concentrations of 0, 40, and 80 ppbv. These results were achieved by averaging over five

files of 4000 laser shots as defined in Table 2. With a sampling rate of 20 MHz the ultimate range resolution was 7.5 m. Such a short optical integration path would nevertheless result in too large an uncertainty for the ozone retrieval. Thus we used an effective range resolution of 90 m, or an equivalent bin resolution of 12 ADC channels. Because the presence of ozone itself significantly lowers the Raman signals through extinction, higher ozone values directly induce greater statistical error. The results in Fig. 3(a) indicate that, on the one hand, an average greater than at least 20,000 shots is needed for suitable ozone Raman DIAL retrieval. This means that for a laser source with a 10-Hz repetition rate the averaging time will be approximately half an hour. On the other hand, above an altitude range of typically 700 m above ground level (AGL) the error source that is due to the statistical noise reaches a value higher than 5% of the measured ozone concentration in the case of a constant profile with 80 ppbv. This uncertainty is considered an upper acceptable limit. Note that even at $O_3 = 0$ ppbv the statistical noise that affects the oxygen and nitrogen Raman signals already induces an ozone standard deviation. From this simulation of the statistical noise only, one can conclude that the maximum achievable range for ozone with this Raman DIAL system will be of the order of 700 m above the lidar site, with a spatial resolution of 90 m, a time resolution of half an hour, and a precision that is due to the statistics of $\pm 5\%$ for a typical ozone concentration of 80 ppbv in the atmosphere.

A similar statistical analysis was performed for retrieval of the Raman water-mixing ratio [Fig. 3(b)], where again the three constant ozone profiles (0, 40, and 80 ppbv) were considered. In this case the range resolution was set at 22.5 m (three ADC channels), and reasonable water-vapor estimates were predicted for an altitude range of as much as 1200 m AGL. Note that the standard deviation is calculated for a water-vapor mixing ratio with a referenced value given at 200 m AGL (full overlap condition) by the water-content model atmosphere. In comparison with the results obtained for ozone, at 700 m AGL the water-vapor standard deviation in an atmosphere that contains 80 ppbv of ozone is less than 1% of the mean water-vapor mixing ratio. This better result is due directly to the linear dependence of Eq. (3) on a water-vapor retrieval that is less sensitive to statistical error than in the case of the ozone Raman differential analysis. Here one can conclude that the Raman lidar instrument will yield an estimate of the water-vapor content in the atmosphere with an accuracy of better than 2% (statistical noise only) for an altitude range of 1200 m above the lidar site, a spatial resolution of 22.5 m, and a time resolution of half an hour.

### D. Optical Cross Talk in the Detection Box

Spectral separation of the three Raman signals and rejection of the elastic wavelength are performed by a grating polychromator. For such a device we could consider mutual optical cross talk among the Raman channels and a leak of an elastic signal that has not been totally suppressed into the Raman channels. These two types of optical cross talk are simulated: One is due to the elastically backscattered light added to each of the different Raman channels and the other is due to the cross talk between adjacent Raman-shifted channels.

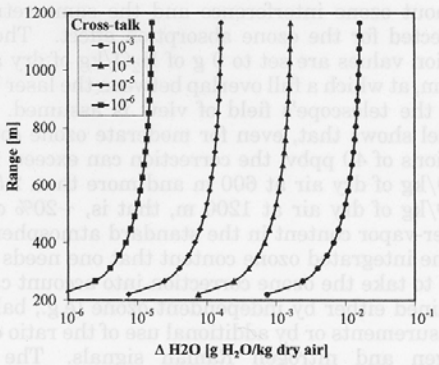


Fig. 4. Optical cross talk. Predicted error in water-vapor Raman lidar retrieval owing to optical cross talk between water-vapor and oxygen Raman signals. The horizontal scale is the difference between the water-vapor mixing-ratio retrieval without the cross-talk effect and the same retrieval biased by the cross-talk effect.

Let us consider first the cross talk between nitrogen and oxygen Raman signals that bias the ozone retrieval and the cross talk between water-vapor and oxygen Raman signals that bias the water-vapor retrieval. Several model runs were performed for cross talk that ranged from $10^{-6}$ to $10^{-3}$ with a model atmosphere with a constant ozone vertical profile (80 ppbv) and an aerosol layer with $b = 1.8$ and $e = 40$. The model results show that this cross talk has only an extremely small effect. The associated errors for ozone were always less than 0.3 ppbv, whereas they remained below 0.01 g of $H_2O$/kg of dry air for the water vapor in the worst case. As an example of these simulation runs, Fig. 4 shows the cross-talk effect that is due to the Raman-shifted oxygen signal on water vapor relative to the altitude range. Because the water-vapor Raman signal has by far the weakest signal intensity compared with the two other Raman signals, mainly because of its comparatively much lower concentration, one could expect the strongest (or worst) effect of the cross talk in this case. The predicted shift $\Delta H_2O$ in the water-vapor mixing-ratio retrieval presented in Fig. 4 is the difference between water-vapor retrieval with no cross-talk effect and the same retrieval biased by the cross talk of the oxygen signal on water vapor. As these runs are performed in an atmosphere with a high aerosol load and a constant 80 ppbv of ozone, the simulation shows that the largest cross-talk effect is expected over long range, where the signal-to-noise ratio is the weakest. For a cross talk of $10^{-3}$ at a range of 200 m the expected shift is $\sim -10^{-3}$ g of $H_2O$/kg of dry air

(negative correction), and it reaches a value of $-10^{-2}$ at 1200 m, or an effect that is higher by typically 1 order of magnitude. This simulation is performed with a constant detection efficiency relative to the range. In this sense the effect of incomplete detection of the Raman signal at a short distance where the probed air volume image in the grating polychromator is the largest is not taken into account.

For the cross talk between the elastic backscattered light and the Raman channels, one can expect a stronger effect because the elastic backscatter cross section is as much as 4 orders of magnitude higher than the Raman cross section. This result is addressed in detail in the experimental layout presented in Section 3 below. To prevent such strong optical interference, additional filters were set at the entrance of the polychromator with a rejection ratio between the 266-nm light and the other Raman channels of more than 5 orders of magnitude. Model runs were performed with cross-talk values that ranged from $10^{-9}$ to $10^{-6}$ between the elastic backscattered light and any of the Raman channels. The associated errors that are due to the elastic cross talk for ozone always remained below $-0.15$ ppbv, and those for water vapor below $-0.1$ g of $H_2O$/kg of dry air in the worst case.

In summary, the two types of optical cross talk have negligible effects if the wavelength separation unit permits a cross-talk level lower than $10^{-3}$ to be achieved for two adjacent Raman channels, and a level lower than $10^{-6}$ between the elastic backscattered signal at 266 nm and the closest Raman backscattered signal, namely, oxygen at 277.5 nm.

### E. Afterpulse Effect

Another instrumental effect that could strongly alter the real lidar return signal is the afterpulse effect (APE) of the receiving photomultiplier.[17] The afterpulses caused by internal processes within the PMT appear as secondary pulses that follow the genuine pulse. In modern PMTs, most afterpulses are assumed to be due primarily to positive ions (either residual ions from manufacture or atoms of helium, which diffuse through the glass envelope) that strike the photocathode to release secondary electrons. The APE occurs mostly within 1–2 μs after the main pulse.[23,24]

The time delay and the duration and the shape of the afterpulse depend on the ions involved and on the PMT configuration.[25] The influence of the APE on the lidar signal can be estimated as a convolution of the afterpulse produced by a short light pulse and the lidar signal. The result is a bias that is superimposed upon the original lidar signal. Because the afterpulse is shorter than the duration of the lidar signal, the influence of the APE can be presented as a delayed echo of the lidar signal with an integrated value that is proportional to the lidar signal itself. Let us define the APE's relative intensity as the ratio between the APE signal and the Raman lidar signal. In our simulation we chose a time delay for the afterpulse of 2 μs, or an equivalent range of 300 m after the lidar maximum intensity, defined at 200 m far from the lidar experiment. The model atmosphere was chosen with 80 ppbv of ozone and the homogeneous aerosol layer ($e = 40$, $b = 1.8$). The simulated APE error is defined as the difference between the ozone concentration profile [Fig. 5(a)] and the water-vapor mixing ratio profile [Fig. 5(b)] with the APE and the profile without the APE.

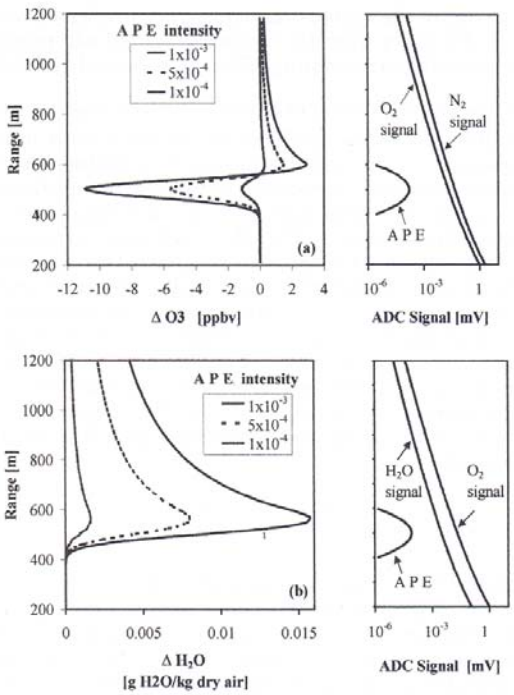


Fig. 5. APE. Predicted error in (a) ozone and (b) water-vapor Raman lidar retrieval owing to the APE. The horizontal scale is the difference between the ozone and the water-vapor mixing-ratio retrievals with and without the APE. The model lidar signals are also shown relative to their typical ADC voltage intensities (log scale) with the Raman oxygen and nitrogen signals for ozone and with the Raman water-vapor and oxygen signals for the water-vapor mixing ratio.

The APE on ozone retrieval is shown in Fig. 5(a) for three values of the APE ratio. With an APE of $10^{-3}$ the maximum predicted ozone error is $-11$ ppbv ($\sim$14%), whereas for an APE below $10^{-4}$ this effect remains within the acceptable limit of precision of the method.

The same effect is studied in Fig. 5(b) for the water-vapor mixing-ratio retrieval. The APE error induced in the water-vapor mixing ratio is less than 1% for an APE intensity of $10^{-3}$. The difference in the magnitude and the shape of the errors in ozone concentration and water-vapor mixing ratio is again explained by the fact that the ozone calculations in Eq. (2) include taking a derivative, which operation reveals a characteristic perturbation in the signal. In conclusion, if the photomultiplier units that one uses

to acquire the various Raman signals are tested with an APE lower than $10^{-4}$, this simulation will predict essentially no remaining effect on the signal analysis.

### F. Additional Sources of Systematic Error in Raman Lidar

Systematic errors such as interference with other trace-gas species in the atmosphere or in the spectral stability of the laser source must also be considered.

In Eq. (2) ozone was the only absorbing species taken into account. The DIAL technique is sensitive to the influence of any other absorbing trace-gas species in the wavelength region used. The main interference in the UV for tropospheric measurements comes from $SO_2$ and $NO_2$. Table 1 lists their respective absorption cross sections compared with that of ozone for the three Raman wavelengths considered in this study. The systematic error $\Delta O_3$ induced in the ozone retrieval by any interfering gas (IG) can be presented as

$$\Delta O_3 = -\frac{[\sigma_{IG}(\lambda_{N_2}) - \sigma_{IG}(\lambda_{O_2})]N_{IG}}{[\sigma_{O_3}(\lambda_{N_2}) - \sigma_{O_3}(\lambda_{O_2})]}, \qquad (11)$$

where $N_{IG}$ is the concentration of IG. The ratio of the differential absorption cross section for IG = $NO_2$ to ozone is $-7.61 \times 10^{-3}$, whereas it reaches a value of $-10^{-1}$ for $SO_2$. In other words, the systematic error $\Delta O_3$ in the ozone concentration caused by 100 ppbv of $NO_2$ is less than $-1$ ppbv, whereas 100 ppbv of $SO_2$ will induce a systematic error of $-10$ ppbv. One should point out that such error sources affect not only the Raman DIAL but also any elastic DIAL measurements, but remain relatively small in most case studies.

The systematic error induced by IG in water-vapor measurements can be calculated by use of the same formalism as the one used for ozone correction. The magnitude of this error will be proportional to the differential cross section of the IG at nitrogen and water-vapor Raman wavelengths (see Table 1). The differential cross sections of $NO_2$ and $SO_2$ are, correspondingly, $-2.9 \times 10^{-2}$ and $-1.17 \times 10^{-2}$ of the ozone differential cross section. Inasmuch as the expected $NO_2$ and $SO_2$ systematic errors represent a proportionally small part of the ozone correction, the latter can be neglected. One should nevertheless point out that this correction term appears in the integral term in Eq. (3) and will play a more significant role in the calculation for a longer range of measurements.

The spectral stability of the laser source could as well be a source of systematic error because a shift in the emitted wavelength will induce a displacement of the lidar signal image at the output of the polychromator. Hence the spectral stability of the laser source specified by the manufacturer is 1 $cm^{-1}$, or a wavelength shift of less than 0.015 nm at 266 nm. With a grating spectral resolution of 0.51 nm/mm the wavelength shift that is due to the spectral stability of the laser source will be 30 $\mu$m. This effect can be neglected.

In summary, interference with other trace-gas species can also be ruled out in most atmospheric conditions. The remaining (and by far the largest) uncertainty in this experiment will be the signal statistics. An accuracy of 5% for an altitude range of as much as 700 m, a spatial resolution of 90 m, and a temporal resolution of 30 min is expected for ozone retrieval in typical atmospheric conditions with 80 ppbv of ozone, whereas 2% accuracy is expected for an altitude range of as much as 1200 m and a spatial resolution of 22.5 m for the water-vapor retrieval.

## 3. Raman Lidar Experimental Setup

The Raman lidar system shown in Fig. 1 is based on a frequency-quadrupled Nd:YAG laser (Continuum, Inc. Powerlite-8000) used in the transmitter.[26] The laser output energy at 266 nm is 120 mJ at a 10-Hz repetition rate with a 7-ns FWHM pulse duration. The initial laser beam divergence of 0.5 mrad is reduced to 0.17 mrad by a three-time beam expander. The beam is emitted into the atmosphere by a right-angle prism mounted upon a piezoelectric controlled stage that simplifies the final alignment. The large field of view and the relatively small separation (30 cm) between the transmitting and the receiving axes of the lidar make possible the full overlap between the laser beam and the telescope's field of view at a typical altitude of 150 m AGL.

The backscattered light is collected by a 20-cm-diameter, 60-cm focal-length Newtonian telescope ($f/3$). A diaphragm is used to adapt the telescope's field of view set at 5 mrad. Two custom-designed bandpass filters (Omega Optical Company) at the entrance of the polychromator achieve an initial suppression of the strong elastic backscattered signal at 266 nm. The filters are tilted at 18° for an optimum transmission of the three Raman backscattered signals and a maximum rejection of the elastic backscattered light. At this angle each filter has as much as 80% transmission for the three Raman wavelengths and an optical density of 2.6 at 266 nm. These specifications were measured directly after the filters were delivered. One year later the filters showed a loss of ~10% in transmission. The filters were placed in the parallel beam between two lenses that fit the $f$-numbers of the telescope and the polychromator. A 500-mm Czerny–Turner polychromator ($f/4$) was used for wavelength separation of the Raman signals as well to reject the daylight background and the elastically backscattered light. The polychromator resolution with a 3600-groove/mm UV-enhanced holographic grating was 0.51 nm/mm. For additional suppression of the daylight background a solar-blind filter (Corion 300F-430T) was placed at the polychromator entrance. The filter rejects light throughout the visible ($\lambda > 360$ nm) of better than $10^{-4}$ and a 70% transmission in the 250–320-nm band.

The Raman signals from oxygen, nitrogen, and water vapor were detected simultaneously by three Hamamatsu H-5780-06 photosensor modules. Each module is equipped with an optical diffuser and a short-focal-length lens to improve the spatial unifor-

mity of the photosensor module.[27] Because a pulse duration of less than 0.65 ns is achieved by such photodetectors, both analog and photon-counting detection modes are possible. The signals were acquired by a Licel transient recorder that combines photon counting with a 12-bit 20-MHz ADC. Raw data were averaged over 4000 shots and stored with an ultimate range resolution of 7.5 m.

### A. Experimental Determination of the Optical Cross Talk

A careful analysis of the cross talk measured in our experimental setup was made. Even though the three signals could affect one another, the influence of the nitrogen channel on the two others is stronger because the nitrogen channel is the central wavelength and has the highest intensity level. Therefore we measured the optical cross talk caused by the nitrogen signal in the oxygen and water-vapor channels. For the measurements we used light produced by stimulated Raman scattering of a 266-nm laser beam in 35 atm of nitrogen. A small fraction of the beam's first Stokes at 283.6 nm was injected by an optical fiber into the lidar-receiving telescope, and the resultant cross-talk intensities in the oxygen and water-vapor channels were measured by the respective PMT. The intensity of the injected 283.6-nm light was chosen such that the resultant cross-talk intensities were well above the photodetector's noise level. The light intensity in the nitrogen channel was measured with neutral-density filters that attenuate the signal below the saturation level of the photodetector. The cross talk in the oxygen and water-vapor channels was calculated as a ratio between the cross-talk intensity in the respective channel and the intensity in the nitrogen channel, with the relative photodetector sensitivity and the neutral-density filter attenuation in the nitrogen channel taken into account. The measured cross-talk levels were $2.2 \times 10^{-5}$ for $O_2/N_2$ and $5.2 \times 10^{-5}$ for $H_2O/N_2$. The simulation study presented in Section 2 showed that it is only with cross talk greater than $10^{-3}$ that a detectable bias in ozone or water-vapor retrieval was expected. Our experimental cross-talk values were much lower, low enough that we could neglect their influence. These values are also in good agreement with the stray-light level specified by the polychromator's manufacturer.

Furthermore, care was taken to suppress the residual elastic signal and to measure the degree of this suppression in the Raman channels. As this degree is quite high, its direct measurement was impossible. Instead, suppression of the elastic signal by the bandpass filters and that by the polychromator were measured separately. For the polychromator, the suppression of elastic backscatter light was measured in a way similar to that described above for the cross talk among the Raman channels, this time with a fraction of the 266-nm light injected directly into the receiving telescope. The degrees of suppression for the various Raman channels were calculated as a ratio of the intensity of the 266-nm light entering the polychromator presented in Section 2 to the light intensities detected in these channels. The measured values were as follows: for the nitrogen channel, $1.5 \times 10^5$; for the oxygen channel, $5.9 \times 10^4$; and for the water-vapor channel, $3.5 \times 10^4$. The bandpass filters were measured separately, with a total attenuation ratio of the elastic signal (ratio before versus ratio after the addition of filters) of $1.58 \times 10^5$ times. Thus the total suppression of the elastic backscatter signal at the receiver was always greater than $5 \times 10^9$. This value ensured that the residual pump beam in the three Raman channels was not the source of systematic error, as was confirmed by the model results. This high rate of rejection of the elastic signal was further confirmed by the fact that no detectable echo from low-altitude dense clouds was observed in the three Raman channels.

### B. Experimental Determination of the Afterpulse Effect

During the initial tests of the Raman lidar setup, classic-type glass-bulb/head-on PMTs were used that showed APEs. An upgrade of the system was made with a new type of metal package photomultiplier.[27,28] With these new PMTs, no APE was detectable, even when the photocathode was illuminated directly with 7-ns laser pulses with high intensity. Such laser pulses induced PMT output pulse amplitudes of as much as 1 V on a 50Ω load without an APE. A possible explanation for this fact is the short time delay of the afterpulses, which is due to the very small (less than 1-mm) distance between the cathode and the first dynode and makes it difficult to distinguish the afterpulses from the main pulse. Another explanation is that the new metal package is less permeable than a glass bulb for atmospheric helium, and helium diffusion is known to be one of the main reasons for afterpulses.

## 4. Results and Discussion

Raman lidar measurements were performed both from the EPFL site (46° 31′N; 6° 38′E) in March–April 1999 and during a field campaign in Crete, Greece, in May 1999. The different results are discussed here and will help to underline the advantages and the limitations of our instrument.

The first results were obtained with the idea of achieving a time series of Raman lidar measurements in daytime and nighttime conditions for both ozone and water-vapor vertical profiles simultaneously. During this time series, additional measurements at 8 m AGL of ozone concentration, relative humidity, temperature, and pressure were performed. The ozone concentration was monitored by an UV absorption analyzer (Dasibi 1008 AH) with a precision of ±2 ppbv.

The Raman-shifted nitrogen and oxygen backscattered signals were acquired in the analog mode by use of a 12-bit, 20-MHz ADC whereas the photon-counting method of detection was used for the water-vapor signal. The signals were acquired with LabVIEW-based software with a real-time display of the preliminary results and with posttreatment by Matlab software. The time series in Fig. 6 shows the

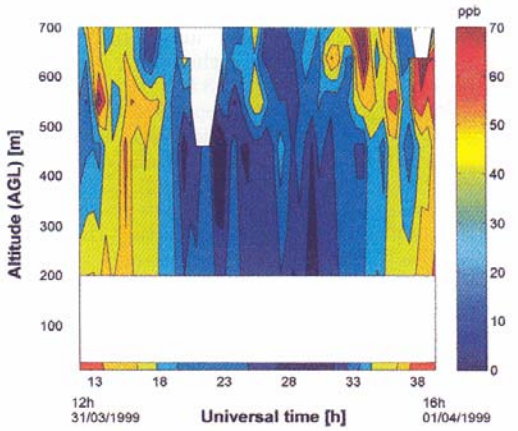


Fig. 6. Ozone Raman DIAL obtained in March 1999 for a time series of 28 h. The ozone concentrations measured at the ground are given by an UV absorption detector. They are measured by Raman DIAL from altitudes of 200 to 700 m AGL. The spatial resolution is 90 m, and the time resolution is 30 min.

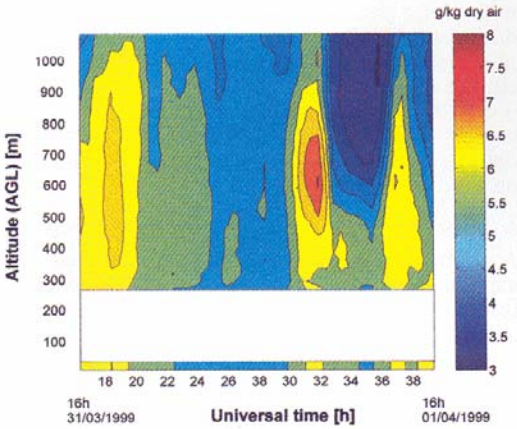


Fig. 7. Water-vapor mixing ratio retrieved by Raman lidar obtained in March 1999 for a time series of 24 h from altitudes of 200–1200 m AGL. The water vapor relative humidity measured at the ground is given by a standard meteorological station. The latter values are also used at 270 m AGL as reference values for the first altitude range of the Raman lidar profile. The spatial resolution is 22.5 m, and the time resolution is 30 min.

ozone vertical profile measured continuously over a period of 28 h. Based on the statistical noise analysis presented in Section 2, we set the lidar vertical resolution at 90 m and the time resolution at 30 min. A sliding average was applied both for the altitude range and for the time scale. The white rectangle at the bottom of Fig. 6 indicates the spatial range where ozone cannot be retrieved by lidar because of the incomplete overlap between the laser beam and the telescope's field of view. The ground-level ozone concentrations measured by the point monitor are also shown in the figure for comparison with the lidar data.

In this time series the ozone's diurnal cycle was clearly seen, with higher values during the period of high solar radiation and lower values at nighttime. Note also that this time series was taken in the humid conditions that are associated with formation of thin water cloud layers at night. But, even so, essentially no data rejection in the ozone retrieval was needed, with the exception of some data at 20–22 UT at an altitude range higher than 500 m AGL. Furthermore, during this period of observation of more than 1 day, a strong variation in the height of the inversion layer was observed. The combined optical interference of cloud layers and the change in aerosol gradient caused by the change in height of the top of the planetary boundary layer would certainly affect or even make impossible any elastic DIAL ozone measurements in similar conditions. Such effects have often been reported[9,10] but did not affect this ozone time series.

The water-vapor time series following the data treatment in Eq. (10) with the three (nitrogen, oxygen, and water-vapor) Raman signals is presented in Fig. 7. These measurements were taken simultaneously with the ozone measurements, but because of technical problems with the photoncounting photomultiplier the water-vapor results are shown after 16 h UT. As indicated above, as the instrument constant $K_{cal}$ is unknown, an absolute profile of the water-vapor mixing ratio in air may be obtained only if an absolute reference is available at a given altitude. As such is not the case here, we used the absolute water-vapor mixing ratio measured at ground level as the reference value of the first altitude achieved by the lidar, namely, ~270 m AGL. In a manner similar to that for the ozone time series in Fig. 6, the white rectangle in Fig. 7 covers the spatial range where the water-vapor mixing ratio cannot be retrieved by lidar. But in this case the values measured close to the ground are equivalent to the reference values at 270 m AGL. This means that the present water-vapor mixing ratio time series should be regarded as a time series with relative numbers; below, we shall compare an absolute water-vapor mixing-ratio vertical profile with balloon measurement.

The measurements are presented with a vertical resolution of 22.5 m and a time resolution of 30 min. It is important to note that, even under daytime conditions, with a water-vapor Raman-shifted wavelength at 294.6 nm close to the solar-blind border, the solar background essentially did not perturb the photon-counting signal detection. This result indicates good rejection of the solar background achieved by the combination of the polychromator and the bandpass and solar-blind filters. This water-vapor time series shows the characteristic daytime–nighttime behavior of the water-vapor content in the atmosphere, with convection at daytime lifting upward air masses with higher water-vapor content.

In deriving the result in Fig. 7 we accounted for the

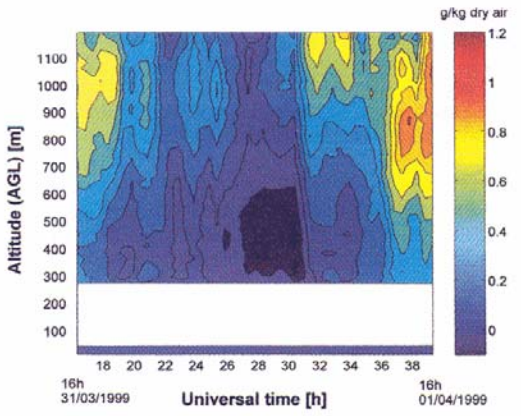


Fig. 8. Difference in the water-vapor mixing-ratio retrieval $\Delta H_2O$ uncorrected for the ozone differential absorption effect compared with the corrected time series. Small values of $\Delta H_2O$ along the entire vertical range are associated with low ozone content in the atmosphere. Note that negative $\Delta H_2O$ values ($>-0.1$ g of $H_2O$/kg of dry air) are also indicative of the limit of precision of the method ($\pm 2\%$).

ozone differential absorption effect described by Eq. (10). In this formalism we used the three Raman backscattered signals and were able to correct the water-vapor mixing-ratio retrieval for the ozone effect without having to retrieve explicitly the vertical ozone profile. Whereas ozone was explicitly retrieved up to 700 m AGL, as shown in Fig. 6, the water-vapor mixing ratio corrected for the ozone absorption can be retrieved up to 1200 m AGL. Based on this formalism it is furthermore possible to express the systematic shift in the water-vapor time series that is due to ozone differential absorption. Figure 8 illustrates the difference $\Delta H_2O$ between the water-vapor mixing-ratio retrieval uncorrected for the ozone differential absorption effect and the same time series but corrected. As has already been shown as a model result in Fig. 2, higher ozone content leads to larger water-vapor corrections with an additive effect that is due to the integral term in Eq. (3). In this sense Fig. 8 gives additional information about the ozone content in the air because low $\Delta H_2O$ values will be associated directly with low ozone concentration. This correlation is nicely confirmed if we compare Figs. 6 and 8 for an altitude range up to 700 m AGL, while it is now possible to gain a first estimate up to an altitude of 1200 m AGL of the ozone contribution. See, for example, the $\Delta H_2O$ vertical profile at 4 a.m. (28 h UT in Fig. 8) with values that are essentially near zero. The values are confirmed by the low ozone concentration in Fig. 6 up to 700 m AGL measured at the same time. They are also indicative of low ozone concentration for the rest of the altitude range to 1200 m AGL, where ozone was no longer retrieved by Raman DIAL. This information was gained because in this case the ozone contribution is integrated along the profile and is not range resolved. Values of $\Delta H_2O$ up to 1.2 g of $H_2O$/kg of dry air are indicative of higher ozone content, as is the case at 4 p.m. (40 h UT in Fig. 8) on the second day of continuous measurement. This shift in the water-vapor retrieval corresponds to an effect of $\sim 15\%$ for ozone values typically below 60 ppbv, as partially shown in Fig. 6, and would be even worse for atmospheric conditions with higher ozone concentrations. Finally, one should note that some negative values for $\Delta H_2O$ were obtained with magnitudes to as low as $-0.1$ g of $H_2O$/kg of dry air in the worst cases. These negative values correspond to less than 2% of the effective water-vapor mixing ratio. They are directly associated with the limit of precision of our determination of the water-vapor mixing-ratio retrieval and are slightly higher than the predicted statistical error defined by the model study.

Later in the year, the same lidar instrument was mounted upon a movable platform and transported to Crete, Greece, to participate in the Photochemical Activity and Ultraviolet Radiation Modulation Factors II (PAUR II) program.[29] The measuring site was situated in the northwest part of the island of Crete in Nopigia (35° 51′N 23° 72′E), and the lidar was placed 5 m above sea level (ASL). Whereas the system most of the time operated in the ozone elastic DIAL mode, the chance for additional Raman water-vapor measurements was offered for a short period of time by direct comparison with an absolute water-vapor profile measured by balloon. The balloon ozone and temperature profiles were determined with an electrochemical concentration cell ozonesonde in combination with a Vaisala RS-80 radiosonde, H-type Humicap sensor. This widely used sensor measures water-vapor mixing ratios with an accuracy of $\pm 5\%$ in the lower troposphere. Procedures for sonde preparation and data acquisition are similar to those developed by the National Oceanic and Atmospheric Administration/Climate Diagnostics and Monitoring Laboratories.[30] Data of 1-s duration were recorded and processed as described by Thompson *et al.*[31] The balloon was launched from essentially the same place as was the EPFL lidar trailer.

Figure 9 shows a comparison of the vertical water-vapor profile obtained by Raman lidar and the balloon measurements. During this experiment the lidar system measured only the Raman nitrogen and water-vapor channels. Thus we used the ozone data from the balloon directly to correct for the ozone interference effect on water vapor according to Eq. (3). We used the water-vapor mixing ratio measured by balloon to determine the lidar calibration constant $K_{cal}$ at 210 m ASL, where a full overlap between the laser beam and the telescope's field of view was achieved. This absolute water-vapor mixing-ratio vertical profile retrieved by Raman lidar was obtained by averaging over five files of 4000 laser shots (total integration time of 30 min, from 5 to 5.30 a.m. UT) with a vertical resolution of 22.5 m and appeared to be in good agreement with the balloon data. The difference $\Delta H_2O$ shown in Fig. 9 between the water-

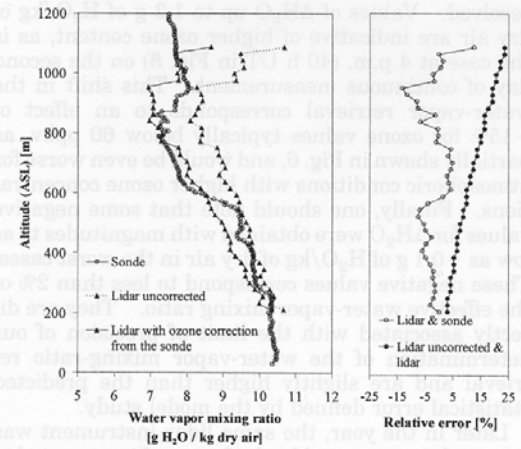


Fig. 9. Raman lidar water-vapor measurements compared with balloon soundings. The lidar data are shown with a spatial resolution of 22.5 m and a time resolution of 30 min. They are compared with 1-s balloon data recorded at an ascent speed of ~5 m/s. The water-vapor balloon measurement at 210 m ASL is used as an absolute calibration for the lidar signal. The water-vapor mixing-ratio vertical profile retrieved by Raman lidar is shown with the ozone concentration profile measured simultaneously by balloon taken into account (Lidar with ozone correction). The same lidar profile is also shown without this correction (Lidar uncorrected). The corresponding difference (Lidar uncorrected & lidar) may be compared with results presented in Fig. 8. The relative difference (Lidar & sonde) indicates values below 15% over the entire range of measurement. This comparison was made in May 1999 in Crete during the PAUR II experiment with the Raman lidar on board the EPFL lidar trailer.

vapor profile obtained by lidar and that by balloon was typically below 1 g of $H_2O$/kg of dry air over the entire range (or less than 15% in relative units), with the highest discrepancy observed at the height of the inversion layer. This transition layer was observed between 850 and 950 m ASL in the balloon data, whereas for the lidar data it was defined above 950 m ASL. This difference could well be explained by the difference in time and air volume sampled by the two methods. In particular, averaged values obtained by lidar over a period of 30 min were compared with instantaneous values measured by balloon that could in turn be influenced by highly local air masses. In this example the balloon was launched at 5:11 a.m. UT with a vertical speed of ~5 m/s and 1/data point/s.

In Fig. 9 the water-vapor content obtained without consideration of the ozone correction (labeled Lidar uncorrected) is also shown. This profile was calculated with the instrument constant determined as previously without consideration of the integral factor in Eq. (3). In this case the error estimate $\Delta H_2O_{\text{Lidar–lidar uncorrected}}$ reached differences as high as 15% for ozone concentrations of ~70 ppbv; this is an integrative effect and therefore the highest discrepancy is reached at a long range. This difference is greater than the largest discrepancy between balloon and water-vapor lidar measurements corrected for the ozone effect. Note that at the calibration height at 210 m ASL $\Delta H_2O_{\text{Lidar–lidar uncorrected}}$ is not zero because the water-vapor shift that is due to the ozone absorption between the ground and this height has already been taken into account.

## 5. Conclusion

The principle and design of a single-wavelength excitation Raman–DIAL instrument for daytime and nighttime ozone and water-vapor measurements in the planetary boundary layer have been demonstrated. Our objective was to perform measurements at low altitude in the PBL, an atmospheric layer characterized by a high and inhomogeneous aerosol load, where elastic DIAL observations cannot in some cases be used because of unpredictable Mie interference.

An error analysis based on the influence of the instrumental and atmospheric effects that could decrease the Raman lidar performance was made. It concerned the influence of the aerosol content on the ozone retrieval and of the ozone concentration on the water-vapor retrieval, the statistical noise, the afterpulse effect, the cross talk between Raman channels, and the influence of the residual laser light on Raman signals. The results of this study were confirmed by Raman lidar results obtained for the measurements of ozone and water-vapor vertical profiles in the PBL. The error induced in the water-vapor mixing-ratio retrieval by the ozone differential absorption effect revealed that, if three Raman signals (namely, oxygen, nitrogen, and water vapor) are measured simultaneously, it is possible to extend the water-vapor retrieval range corrected for the ozone effect.

This lidar development is important because ozone and water-vapor measurements are key criteria for control and quality testing of the predictive results obtained by atmospheric transport chemical modeling. These Raman lidar measurements were furthermore obtained with a resolution that fit both the time and the space model resolution. A future combination of the powerful elastic DIAL technique applied at higher altitude or in more-homogeneous aerosol conditions with the Raman DIAL method at low altitude will essentially be able to encompass an altitude range in full agreement with the vertical grid resolution of the model.

This study was supported by the Swiss National Science Foundation under contract 21-50861.97 and the Swiss Federal Office for Science and Education under contract 97.0377. The balloon sounding was provided by NASA's (Total Ozone Mapping Spectrometer (TOMS) project. The authors thank the organizers of the PAUR II project for logistical support in Crete and are grateful to Ed Browell and his team at NASA Langley for stimulating discussions.

## References

1. B. J. Finlayson-Pitts and J. N. Pitts, Jr., *Chemistry of the Upper and Lower Atmosphere: theory, Experiments, and Applications* (Academic, San Diego, Calif., 1999).

2. A. Clappier, A. Martilli, P. Gross, P. Thunis, F. Pasi, B. C. Krueger, B. Calpini, G. Graziani, and H. van den Bergh, "Effect of sea breeze on air pollution in the Greater Athens area. I. Numerical simulations and field observations," J. Appl. Meteorol. **39,** 563–575 (1999).
3. P. Grossi, P. Thunis, A. Martilli, and A. Clappier, "Effect of sea breeze on air pollution in the Greater Athens area. II. Analysis of different emission scenarios," J. Appl. Meteorol. **39,** 546–562 (1999).
4. S. Perego, "A numerical mesoscale model for simulation of regional photosmog in complex terrain: model description and application during POLLUMET 1993 (Switzerland)," Meteorol. Atmos. Phys. **70,** 43–69 (1999).
5. B. Calpini, V. Simeonov, F. Jeanneret, J. Kuebler, V. Sathya, and H. van den Bergh, "Ozone LIDAR as an analytical tool in effective air pollution management: the Geneva 96 campaign," Chimia **51,** 700–704 (1997).
6. L. Fiorani, B. Calpini, L. Jaquet, H. van den Bergh, and E. Durieux, "A combined determination of wind velocities and ozone concentrations for a first measurement of ozone fluxes with a DIAL instrument during the Medcaphot Trace campaign," Atmos. Environ. **32,** 2151–2159 (1998).
7. L. Schoulepnikoff, H. van den Bergh, B. Calpini, and V. Mitev, "Tropospheric air pollution monitoring lidar," in *Encyclopedia of Environmental Analysis and Remediation*, R. A. Meyers, ed. (Wiley, New York, 1998), pp. 4873–4909.
8. E. V. Browell, S. Ismail, and T. Shipley, "UV DIAL measurements of $O_3$ profiles in regions of spatially inhomogeneous aerosols," Appl. Opt. **24,** 2827–2836 (1985).
9. P. Quaglia, G. Larcheveque, R. Jimenez, V. Simeonov, G. Ancellet, H. van den Bergh, and B. Calpini, "Planetary boundary layer ozone fluxes from combined airborne, ground based lidars and wind profiler measurements," Eur. J. Anal. Chem. **27,** 305–313 (1999).
10. P. Völger, J. Bösenberg, and I. Schult, "Scattering properties of selected model aerosol calculated at uv-Wavelengths: implications for DIAL measurements of tropospheric ozone," Beitr. Phys. Atmos. **69,** 177–187 (1996).
11. S. H. Melfi, J. D. Lawrence, Jr., and M. P. Mc Cormick, "Observation of Raman scattering by water vapor in the atmosphere," Appl. Phys. Lett. **15,** 295–297 (1969).
12. D. Renault, J. C. Pourny, and R. Capitini, "Daytime Raman-lidar measurements of water vapor," Opt. Lett. **5,** 233–235 (1980).
13. A. J. Sedlacek and M. D. Ray, "Raman DIAL: application to areas characterized by varying aerosol burden," presented at the 19th International Laser Radar Conference, Annapolis, Md., July 1998.
14. D. Renault, and R. Capitini, "Boundary-layer water vapor probing with a solar-blind Raman lidar: validation, meteorological observation and prospects," J. Atmos. Oceanic Technol. **5,** 585–601 (1988).
15. T. J. Mc Gee, M. Gross, R. Ferrare, W. Heaps, and U. Singh, "Raman DIAL measurements of stratospheric ozone in the presence of volcanic aerosols," J. Geophys. Res. Lett. **20,** 955–958 (1983).
16. R. T. H. Collis and P. B. Russell, "Lidar measurement of particles and gases by elastic backscattering and differential absorption," in *Laser Monitoring of the Atmosphere*, E. D. Hinkley, ed. (Springer-Verlag, Berlin, 1976), p. 89.
17. J. A. Sunesson, "Differential absorption lidar system, for routine measurement of tropospheric ozone," Appl. Opt. **33,** 7045–7058 (1994).
18. W. K. Bishel and G. Black, "Wavelength dependence of Raman scattering cross-sections from 200–600 nm," in American Institute of Physics Conference Proceedings No. 100: Excimer Lasers, C. K. Rhodes, H. Egger, and H. Pummer, eds. (American Institute of Physics, New York, 1983), pp. 181–194.
19. L. T. Molina and M. J. Molina, "Absolute absorption cross sections of ozone in the 185 to 350 nm wavelength range," J. Geophys. Res. **91,** 14,501–14,508 (1986).
20. A. C. Vandaele, P. C. Simon, J. M. Guilmot, M. Carleer, and R. Colin, "$SO_2$ absorption cross-section in the UV using a Fourier transform spectrometer," J. Geophys. Res. **99,** 25,599–25,605 (1994).
21. W. Schneider, G. K. Moortgat, G. S. Tyndall, and J. P. Burrows, "Absorption cross-sections of $NO_2$ in the UV and visible region (200–700 nm) at 298 K," J. Photochem. Photobiol. A **40,** 195–217 (1987).
22. G. P. Anderson, S. A. Clough, F. X. Kneizys, J. H. Chetwynd, and E. P. Shettle, "AFGL atmospheric constituent profiles (0–120 km)," Tech. Rep. AFGL-TR-86-0110 (U.S. Air Force Geophysics Laboratory, Hanscom Air Force Base, Mass., 1986).
23. P. B. Coates, "A theory of afterpulse formation in photomultipliers and the prepulse height distribution," J. Phys. D **6,** 1862–1869 (1973).
24. T. Antonioly and P. Benetti, "Study of afterpulse effects in photomultipliers," Rev. Sci. Instrum. **54,** 1777–1780 (1983).
25. P. B. Coates, "The origins of afterpulses in photomultipliers," J. Phys. D **6,** 1159–1166 (1973).
26. B. Lazzarotto, V. Simeonov, P. Quaglia, G. Larchevêque, H. van den Bergh, and B. Calpini, "A Raman differential absorption lidar for ozone and water vapor measurement in the lower troposphere," Int. J. Env. Anal. Chem. **74,** 255–261 (1999).
27. V. Simeonov, G. Larchevêque, P. Quaglia, H. van den Bergh, and B. Calpini, "The influence of the photomultiplier tube spatial uniformity on lidar signals," Appl. Opt. **38,** 5186–5190 (1999).
28. H. Kyushima, Y. Hasegawa, A. Atsumi, K. Nagura, H. Yokota, M. Ito, J. Takeuchi, K. Oba, H. Matsuura, and S. Suzuki, "Photomultiplier tube of new dynode configuration," IEEE Trans. Nucl. Sci. **41,** 725–729 (1994).
29. A. Kylling, A. F. Bais, M. Blumenthaler, J. Schreder, C. Zerefos, and E. Kosmidis, "The effect of aerosols on solar UV irradiances during the PAUR campaign," J. Geophys. Res. **103,** 26,151–26,060 (1998).
30. W. D. Komhyr, S. J. Oltmans, P. R. Franchois, W. F. J. Evans, and W. A. Matthews, "The latitudinal distribution of ozone to 35 km altitude from ECC observations, 1985–1987," in *Proceedings of the Quadrennial Ozone Symposium and Tropospheric Ozone Workshop*, R. D. Bojkov and P. Fabian, eds. (Deepak, Hampton, Va., 1989), pp. 147–150.
31. A. M. Thompson, B. G. Doddridge, J. C. Witte, R. D. Hudson, W. T. Luke, J. E. Johnson, B. J. Johnson, S. J. Oltmans, and R. Weller, "A Tropical Atlantic paradox: shipboard and satellite views of a tropospheric ozone maximum and wave-one in January–February 1999," Geophys. Res. Lett. **27,** 3317–3320 (2000).

# References

## Chapter 1 Introduction to Atmospheric Backscatter Lidar


[*Ackermann*, 1998] Ackermann J., "The Extinction-to-Backscatter Ratio of Tropospheric Aerosol : A Numerical Study", Journal of. Atmospheric and Oceanic Technology **15**, 1043-1050 (1998).

[*Anderson et al.*, 1986] Anderson G.P., S.A. Clough, F.X. Kneizys, J.H. Chetwynd and E.P. Shettle, "Atmospheric Constituents Profiles (0-120 km)", AFGL-TR-86-0110 (1986).

[*Bates*, 1984] Bates D.R., "Rayleigh scattering bay air", Planetary Space Science **32**, 785-790 (1984).

[*Baxter*, 1991] Baxter R.A., "Determination nof mixing heights from data collected during the 1985 SCCCAMP field program", Journal of Applied Meteorology **30**, 598-606 (1991).

[*Bodhaine et al.*, 1999] Bodhaine B.A., N.B. Wood, E.G. Dutton, J.R. Slusser, "On Rayleigh Optical Depth Calculations", American Meterorlogical Society **16**, 1854-1861 (1999).

[*Bohren and Huffman*, 1983] Bohren C.F. and Donald R. Huffman, "Absorption and scattering of light by small particles", Wiley, New York (1983).

[*Bösenberg*, 1998] Bösenberg J., "Ground-based differential absorption Lidar for water vapor and temperature profiling: methodology", Applied Optics **37** (18), 3828-3834 (1998).

[*Coulter*, 1979] Coulter R.L., "A comparison of three methods for measuring mixing layer height", Journal of Applied Meteorology **18**, 1495-1499 (1979).

[*d'Almeida et al.*, 1991] d'Almeida G.A., P. Koepke and E.P. Shettle, "Atmospheric Aerosols: Global Climatology and Radiative Characteristics", A. Deepak Publishers (1991).

[*Deardorff et al.*, 1980] Deardorff J.W., G.E. Willis and B.H. Stockton, "Laboratory studies of the entrainment zone of a convectively mixed layer", J. Fluid. Mech. **100**, 41-64 (1980).

[*Edlen*, 1966] Edlen B., "The refractive Index of Air", Metrologia **2**, 71-80 (1966).

[*Eltermann*, 1968] Eltermann L., "UV, visible and IR attenuation for altitudes to 50 km", Air Force Cambridge Research Laboratories (1968).

[*Fenn*, 1966] Fenn R.V., "Correlation between atmospheric backscattering and meteorological visual range", Applied Optics **5**, 615-616 (1966).

[*Fernald et al.*, 1972] Fernald F.G., B.M. Hermann and J.A. Raegan, "Determination of Aerosol Height Distributions by Lidar", J. Applied Meteorology **11**, 482-489 (1972).

[*Fernald*, 1984] Fernald F.G., "Analysis of atmospheric Lidar observations: some comments", Applied Optics **23** (5), 652-653 (1984).

[*Flamant et al.*, 1997] Flamant C., J. Pelon, P.H. Flamant and P. Durand, "Lidar determination of the entrainment zone thickness at the top of the unstable marine atmospheric boundary layer", Boundary-Layer Meteorology **83**, 247-284 (1997).

[*Garratt*, 1987] Garrat J.R., "The stably stratified internal boundary layer for steady and diurnal varying offshore flow", Boundary Layer Meteorology **38**, 369-394 (1987).

[*Garratt*, 1992] Garratt J.R., "The Atmospheric Boundary Layer", University Press, Cambridge (1992).

[*Godish*, 1991] Godish T., "Air Quality", Lewis Publishers, Michigan (1991).

[*Hartmann*, 1994] Hartmann D.L., "Global Physical Climatology", Academic Press (1994).

[*Hooper and Eloranta*, 1986] Hooper W.P. and E. Eloranta, "Lidar measurements of wind in the planetary boundary layer: the method, accuracy and results from joint measurements with radiosondes and kytoon", Journal of Climate and Applied Meteorology **25**, 990-1001 (1986).

[*Klett*, 1981] Klett J.D., "Stable Analytical Inversion Solution for Processing Lidar Returns", Applied Optics **20** (2) 211-220 (1981).

[*Klett*, 1985] Klett J.D., "Lidar inversion with variable backscattering to extinction ratios", Applied Optics **24** (11), 1638-1643 (1985).

[*Kunz et al.*, 1993] Kunz G.J. and G. de Leeuw, "Inversion of Lidar signals with the slope method", Applied Optics **32** (18), 3249-3256 (1993).

[*Lyons*, 1975] Lyons W.A., "Turbulent diffusion and pollutant transport in shorelines environments", Lectures on Air Pollution and Environmental Impact Analysis, D.A. Haugen, American Meterorlogical Society **136**, 208 (1975).

[*Measures*, 1984] Measures R.M., "Laser remote sensing, fundamentals and applications", John Wiley&Sons (1984).

[*Melfi et al.*, 1985] Melfi S.H., J.D. Spinhire, S.H. Chou, and S.P. Palm, "Lidar observation of vertically organized convection in the planetary boundary layer over the ocean", Journal of Climate and Applied Meteorology **24**, 806-821 (1985).

[*Menut et al.*, 1999] Menut L., C. Flamant, J. Pelon and P.H. Flamant, "Urban boundary-layer height determination from Lidar measurements over the Paris area", Applied Optics **38**, 945-954 (1999).

[*Peck and Reeder*, 1972] Peck E.R. and K. Reeder, "Dispersion of Air", Journal of the Optical Society of America **62**, 958-962 (1972).

[*Penndorf*, 1957] Penndorf R., "Tables of refractive index for standard air and the Rayleigh scattering coefficient for the spectral region 0.2 to 20 μm and their application to atmospheric optics", Journal of the Optical Society of America **47**, 176-182 (1957).

[*Readings et al.*, 1973] Readings C.J., E. Golton and K.A. Browning, "Fine scale structure and mixing within an inversion", Boundary-Layer Meteorology **4**, 275-287 (1973).

[*Rocadenbosch et al.*, 1998] Rocadenbosch F., A. Comeron and D. Pineda, "Assessment of Lidar inversion errors for homogeneous atmospheres", Applied Optics **37** (12), 2199-2206 (1998).

[*Rocadenbosch et al.*, 2000] Rocadenbosch F., A. Comeron and L. Albiol, "Statistics of the slope-method estimator", Applied Optics **39** (33), 6049-6057 (2000).

[*Russell et al.*,1974] Russell P.B., E.E. Uthe, F.L. Ludwig and N.A. Shaw, "A comparison of atmospheric structure as observed with monostatic acoustic sounder and Lidar techniques", Journal of Geophysical Research **79**, 5555-5566 (1974).

[*Seibert et al.*, 1998] Seibert P., F. Beyrich, S.E: Gryning, S. Joffre, A. Rasmussen and P. Tercier, "Mixing layer depth determination for dispersion modelling", in COST Action 710-Final Report (1998).

[*Seibert et al.*, 2000] Seibert P., F. Beyrich, S.E: Gryning, S. Joffre, A. Rasmussen and P. Tercier, "Review and intercomparison of operational methods for the determination of the mixing height", Atmospheric Environment **34**, 1001-1027 (2000).

[*Steyn et al.*, 1998] Steyn D.G., M. Baldi and R.M. Hoff, "A New Technique to Derive Mixed Layer Depth and Entrainment Zone Thickness from Lidar Profiles", Abstracts of Papers of the 19th International Laser Radar Conference (ILRC), Annapolis - USA, 6-10 July 1998, 461-464 (1998).

[*Stull*, 1988] Stull R.B., "An introduction to Boundary Layer Meteorology", Kluwer Academic Press (1988).

[*Sunesson et al.*, 1994] Sunesson J.A., A Apituley and D.P.J. Swart, "Differential absorption Lidar system for routine monitoroing of tropospheric ozone", Applied Optics **33**, 7045-7058 (1994).

[*Twomey et al.*, 1965] Twomey H. and H.B. Howell, "Relative merit of white and monochromatic light for the determination of visibility by backscattering measurements", Applied Optics **4**, 501-506 (1965).

[*Young*, 1981] Young A.T., "On the Rayleigh-scattering optical depth of the atmosphere", Journal of applied Meteorology **20**, 328-330 (1981).

## Chapter 2 Numerical Simulations of Atmospheric Backscatter Lidar

[*Ansmann et al.*, 1992] Ansmann A., U. Wandinger, M. Riebesell, C. Weitkamp and W. Michaelis, "Independent measurement of the extinction and backscatter profiles in cirrus clouds by using a combined Raman elastic-Backscatter Lidar", Applied Optics **31** (33), 7113-, (1992).

[*Böckmann et al.*, 2001] Böckmann C., U. Wandinger, A. Ansmann, J. Bösenberg, V. Amiridis, A. Boselli, A. Delaval, F. De Tomasi, M. Frioud, M. Iarlori, L. Komguem, S. Kreipl, G. Larchevêque, V. Matthias, A. Papayannis, F. Rocadenbosch, J. Schneider, V. Scherbakov and M. Wiegner, "EARLINET – Lidar Algortihm Intercomparison", Abstracts of the European Aerosol Conference 2001, Journal of Aerosol Science **32** , sup. 1, Sept. 2001, 433-434 (2001).

[*Bösenberg*, 1998] Bösenberg J., "Ground-based differential absorption Lidar for water vapor and temperature profiling: methodology", Applied Optics **37** (18), (1998).

[*Coates*, 1973 A] Coates P.B., "A theory of afterpulse effects in photomultipliers and the prepulse height distribution", Applied Physics **6**, 1862-1869 (1973)

[*Coates*, 1973 B] Coates P.B., "The origins of afterpulses in photomultipliers", Applied Physics **6**, 1159-1166 (1973)

[*Iqbal*, 1983] Iqbal M., "An Introduction to Solar Radiation", Academic Press, New York (1983).

[*Lazzarotto et al.*, 2001] Lazzarotto B, M. Frioud, G. Larchevêque, V. Mitev, P. Quaglia, V. Simeonov, A. Thompson, H. van den Bergh and B. Calpini, "Ozone and water-vapor measurements by Raman Lidar in the planetary boundary layer: error sources and field measurements", Applied Optics **40** (18), 2985-2997 (2001).

[*Matthias et al.*, 2002] Matthias V., C. Böckmann, V. Freudenthaler, G. Pappalardo, J. Bösenberg, V. Amiridis, A. Amodeo, A. Ansmann, D. Balis, A. Boselli, A. Chaykovski, G. Chourdakis, A. Comeron, A. Delaval, F. De Tomasi, R. Eixmann, M. Frioud, A. Hagard, M. Iarlori, L. Komguem, S. Kreipl, G. Larchevêque, H. Linné, R. Matthey, I. Mattis, A. Papayannis, J. Pelon, R.M. Perrone, R. Persson, D.P. Resendes, V. Rizi, F. Rocadenbosch, J.A. Rodriguez, L. Sauvage, J. Schneider, R. Schumacher, V. Shcherbakov, V. Simeonov, U. Wandinger, X. Wang, M. Wiegner and C. Zerefos, "Lidar Intercomparisons on algorithm and system level in the frame of EARLINET", Max-Planck Institut für Meteorologie, Hamburg (2002).

[*Measures*, 1984] Measures R.M., "Laser remote sensing, fundamentals and applications", John Wiley&Sons (1984).

[*Renault et al.*, 1980] Renault D., J.C. Pourny and R. Capitini, "Daytime Raman-Lidar measurements of water-vapor", Optics Letter **5** (6), 233-235 (1980)

[*Schoulepnikoff*, 1996] Schoulepnikoff, "High-power single-pass Raman cells in the ultraviolet: numerical and experimental study, with applications in the differential absorption Lidar measurement of tropospheric ozone", Thesis presented at the LPAS / EPFL (1996)

[*Sunesson et al.*, 1994] Sunesson J.A., A Apituley and D.P.J. Swart, "Differential absorption Lidar system for routine monitoroing of tropospheric ozone", Applied Optics **33**, 7045-7058 (1994).

[*Theopold and Bösenberg, 1988*] Theopold F. and J. Bosenberg, "Evaluation of DIAL measurements in presence of signal noise", Proceedings of the 14th ILRC (1988).

[*Whiteman*, 2000] Whiteman D., "Raman Lidar measurements of water vapor and cirrus clouds during the passage of hurricane Bonnie", accepted at Journal of Geophysical Research (2000).

## Chapter 3 Elevated aerosol stratification above Rhine Valley in strong anticyclonic conditions

[*Ackermann*, 1998] Ackermann J., "The Extinction-to-Backscatter Ratio of Tropospheric Aerosol : A Numerical Study", Journal of. Atmospheric and Oceanic Technology **15**, 1043-1050 (1998).

[*Arrit and Young*, 1990] Arritt R.W. and G.S. Young, "Elevated stable layers generated by mesoscale boundary-layer dynamics over complex terrain", Proceedings of the 5th Conference on Mountain Meteorology, American Meteorological Society, 114-117 (1990).

[*Baltensperger et al.*, 1997] Baltensperger U., H.W. Gäggeler, D.T. Jost, M. Lugauer, M. Schwikowski, E. Weingartner and P. Siebert, "Aerosol climatology at the high-alpine site Jungfraujoch, Switzerland", Journal of Geophysical Research **102**, 19707-19715 (1997).

[*Blumen*, 1990] Blumen W., "Atmospheric processes over complex terrain", Blumen W., editor. Publ. by the American Meteorological Society (1990).

[*Bauer-Pfundstein*, 1999] Bauer-Pfundstein M., "Bestimmung von Turbulenzparametern und der Schallabsorbtion mit einem Wind-Temperatur-RADAR", Wissenschaftliche Berichte FZKA 6281, Forschungszentrum Karlsruhe (1999).

[*Bougeault et al.*, 2001] Bougeault, P., P. Binder, A. Buzzi, R. Dirks, R. Houze, J. Kuettner, R.B. Smith, R. Steinacker, H. Volkert and all MAP scientists, "The MAP Special Observation Period", Bulletin of the American Meteorological Society **82**, 433-462 (2001).

[*Carnuth and Trickl*, 2000] Carnuth W. and T. Trickl, "Transport studies with the IFU three-wavelength aerosol Lidar during the VOTALP Mesolcina experiment", Atmospheric Environment **34**, 1425-1434 (2000).

[*Dupont et al.*, 1994] Dupont, E., J. Pelon, and C. Flamant, "Study of the moist convective boundary-layer structure by Backscatter Lidar", Boundary-Layer Meteorology **69**, 1-25 (1994).

[*Furger et al.*, 2000] Furger, M., Dommen, J., Graber, W.K., Pioglio, l., Prévôt, A., Emeis, S., Greil, G., Trickl, T., Gomiscek, B., Neininger, B., Wotawa, G., "The VOTALP Mesoclina valley campaign 1996 – concept, background and some highlights", Atmospheric Environment **34**, 1395-1412 (2000).

[*Häberli et al.*, 2001] Häberli, Ch., Drobinski, P., Dabas, A.M.,Beffrey, G., "Statistical characterization of the Foehn flow in and above the Rhine valley during MAP-SOP using rawinsonde ascents", MAP Newsletter 15, 36-39 (www.map.ethz.ch/NL15/haeberli.pdf), (2001).

[*Hägeli et al.*, 2000] Hägeli P., D.G. Steyn, D.G., and K.B. Strawbridge, "Spatial and temporal variability of mixed-layer depth and entrainment zone thickness", Boundary-Layer Meteorology **97**, 47-71 (2000).

[*Henning et al.*, 2002] Henning, S., Weingartner, E., Schnidt, S., Wendisch, M., Gäggeler, H.W., Baltensberger, U., "Size-dependent aerosol activation at the high-alpine site Jungfraujoch (3580 m asl)", Tellus 54B, 82-95 (2002).

[*Hindman*, 1973] Hindman, E.E.,. "Air currents in a mountain valley deduced from the breakup of a stratus deck", Monthly Weather Research **101**, 195-200 (1973)

[*Hoff et al.*, 1997] Hoff, R.M., Harwood, M., Sheppard A., Froude, F., Martin, J.B., Strapp, W., "Use of airborne Lidar to determine aerosol sources and movement in the Lower Fraser Valley, BC", Atmospheric Environment **31**, 2123-2134 (1997).

[*Kossmann et al.*, 1999] Kossmann, M., Corsmeier, U., Wekker, S.F.J., Fiedler, F., Vögtlin, R., Kalthoff, N., Güsten H., Neininger, B., "Observations of Handover Processes between the Atmospheric Boundary Layer and the Free Troposphere over Mountainous Terrain", Contribution to Atmospheric Physics **72**, 329-350 (1999).

[*Kreipl et al.*, 2000] Kreipl, S., Mücke, R., Jäger H., Trickl, T., "Spectacular Cases of Vertical Transport and Long Range Ozone and Aerosol Transport", Advances of Laser Remote Sensing. In : Selected Papers at 20th International Laser Radar Conference, Vichy, France, edit.: Dabas A., Claude L. and Pelon J.,10-14 July 2000, 455-459 (2000).

[*Lugauer et al.*, 1998] Lugauer, M., U. Baltensperger, M. Furger, H.W. Gäggeler, D.T., Jost, M. Schwikowski and H. Wanner, "Aerosol transport to the high alpine site Jungfraujoch (3454 m asl) and Colle Gnifetti (4452 m asl)", Tellus **50B**, 76-92 (1998)

[*McKendry et al.*, 1997] McKendry, I.G., Steyn, D.G., Lundgren, J., Hoff, R.M., Strapp, W., Anlauf, K., Froude, F., Martin, J.B., Banta, R.M., Olivier, L.D., 1997. Elevated ozone layers and vertical down-mixing over the Lower Frased Valley, BC. Atmospheric Environment **31**, 2135-2146 (1997).

[*Nyeki et al.*, 2000] Nyeki S., M. Kalberer, I. Colbeck, S. De Wekker, M. Furger, H.W. Gäggeler, M. Kossmann, M. Lugauer, D. Steyn, H. Weingarten, M. Wirt, and U. Baltensperger, "Convective Boundary Layer Evolution to 4 km asl over High-Alpine Terrain: Airborne Lidar Observation in the Alps", Geophysical Research Letters **27**, 689-692 (2000).

[*Seibert et al.*, 1998] Seibert P., H. Kromp-Kolb, A. Kasper, M. Kalina, H. Puxbaum, D.T. Jost, M. Schwikowski and U. Baltensperger, "Transport of polluted boundary layer air from Po valley to high-alpine sites", Atmospheric Environment **32**, 3953-3965 (1998).

[*Stensrud*, 1993] Stenstrud D.J., "Elevated Residual Layers and Their Influence on Surface Boundary-Layer Evolution", Journal of the Atmospheric Sciences **50**, 2284-2293 (1993).

[*Steyn et al.*, 1998] Steyn D.G., M. Baldi and R.M. Hoff, "A New Technique to Derive Mixed Layer Depth and Entrainment Zone Thickness from Lidar Profiles", Abstracts of Papers of the 19th International Laser Radar Conference (ILRC), Annapolis - USA, 6-10 July 1998, 461-464 (1998).

[*Stewart et al.*, 2001] Stewart, J.Q., C.D. Whiteman, W.J. Steenburgh, and X. Bian. "A climatological study of thermally driven wind systems of the U.S. Intermountain West", Bulletin of the American Meteorological Society **83**, 1233-1242 (2001).

[*Stull*, 1988] Stull R.B., "An introduction to Boundary Layer Meteorology", Kluwer Academic Press (1988).

[*Vogt et al.*, 1998] Vogt S., M. Bauer, U. Corsmeier and P. Thomas, "Virtual heat flux measurements from a boundary-layer profiler-RASS", in : Proc. of the 14th Internat. Symp. on Tropospheric Profiling, Snowmass, Colorado, Sept. 22-26, 1998, CIRES, Boulder, 320-321 (1998).

[*Wakimoto and McElroy*, 1986] Wakimoto, R.M., and J.L. McElroy, "Lidar observation of elevated pollution layers over Los Angeles", Journal of Climate and Applied Meteorology **25**, 1583-1599 (1986).

[*Werner*, 1998] Werner, R., "Zur Auflösung von Inversionen im Vorarlberger Rheintal", Oberland **4**, 193-197 (1988).

[*Whiteman*, 2000] Whiteman C.D., "Mountain Meteorology: Fundamentals and Applications", Oxford University Press (2000).

## Chapter 4 Aerosol stratification above Rhine Valley in Foehnic conditions


[*Baines*, 1987] Baines P.G., "Upstream blocking and airflow over mountains", Ann. Rev. Fluid Mech. **19**, 75-97 (1987).

[*Beffrey et al.*, 2002] Beffrey G., A. Dabas, and G. Jaubert, "Foehn and stable air mass in the Rhine valley", 10th Conference on Mountain Meteorology and MAP Meeting 2002, Park City, Utah, American Meteorological Society, 437-440 (2002).

[*Brinkmann*, 1971] Brinkmann W.A.R., "What is a Foehn?", Weather **26** (6), 230-239 (1971).

[*Drobinski et al.*, 2002] Drobinski P., C. Haeberli, E. Richard, M. Lothon, A.M. Dabas, P.H. Flamant, M. Furger and R. Steinacker, "Scale interaction processes during MAP-IOP 12 south Foehn event in the Rhine valley", Quarterly Journal of the Royal Meteorological Society **128** (2002).

[*Egger and Hoinka*, 1992] Egger J. and K.P. Hoinka,. "Fronts and Orography", Meteorology and Atmospheric Physics **42**, 3-36 (1992).

[*Furger*, 2000] Furger M., "Crosswind measurements with scintillometers at 500 m above valley floor during Foehn", 9th Conference on Mountain Meteororolgy, Aspen, Colorado, American Meteorological Society, 75-78 (2000).

[*Furger et al.*, 2002] Furger M., P. Drobinski, H. Prévôt, R.O. Weber, W.K. Graber and B. Neininger, "Comparison of horizontal and vertical scintillometer crosswinds during strong Foehn with Lidar and aircraft measurements", Journal of Atmospheric and Oceanic Technolology **18**, 1975-1988 (2002).

[*Hack*, 1994] Hack K.H., "Situations météorologiques typiques dans les Alpes", SPL - Pool Suisse d'Assurance contres les risques d'Aviation, C.P. 357, CH-8401 Winterthur (1994).

[*Hoinka et al.*, 1987] Hoinka K.P. and F. Rösler, "The surface layer on the leeside of the Alps during Foehn", Meteorology and Atmospheric Physics **37**, 245-258 (1987).

[*Hoinka*, 1985] Hoinka K.P., "What is a Foehn Clearance", Bulletin American Meteorogical Society **66**, 1123-1132 (1985).

[*McIlveen*, 1992] McIlveen R., "Fundamentals of weather and climate", Chapman&Hall (1992).

[*Menut et al.*, 1999] Menut L., C. Flamant, J. Pelon, and P.H. Flamant, "Urban boundary-layer height determination from Lidar measurements over the Paris area", Applied Optics **38**, 945-954 (1999).

[*Seibert*, 1990] Seibert P., "South Foehn Studies Since ALPEX Experiment", Meteorology and Atmospheric Physics **43**, 91-103 (1990).

[*Steinacker et al.*, 2001] Steinacker R., Ch. Häberli, K. Baumann, S. Gubser, M. Lothon, M. Furger and Th. Gutermann, "Unstationary Aspects of Foehn in a Large Valley: Scientific Objectives and selected Results of the MAP subprogramm FORM", Meteorol. Atmos. Phys., submitted (2001).

[*Stensrud*, 1993] Stenstrud D.J., "Elevated Residual Layers and Their Influence on Surface Boundary-Layer Evolution", Journal of the Atmospheric Sciences **50**, 2284-2293 (1993).

## Chapter 5 Aerosols statistics in the PBL and lower troposphere above Neuchâtel: two years of routine observations


[*Ackermann*, 1998] Ackermann J., "The Extinction-to-Backscatter Ratio of Tropospheric Aerosol: A Numerical Study", Journal of. Atmospheric and Oceanic Technology **15**, 1043-1050 (1998).

[*Ansmann*, 2001] Ansmann A., "Lindenberg Aerosol Characterization Experiment (LACE'98): Overview and main results", J Geophys Res. **106**, Accepted for publication (2001).

[*Bates et al.*, 1998] Bates T., B. Huebert , J. Gras, F. Griffiths and P. Durkee, "International Global Atmosphere Chemistry (IGAC) Project's first aerosol characterization experiment (ACE-1): Overview", J. Geophys. Reserach **103** (1998).

[*Bösenberg et al.*, 1998] Bösenberg J, C. Böckmann, R. Eixmann, V. Matthias, I. Mattis, T. Trickl and M. Weigner, "Lidar network to establish an aerosol climatology", Proceedings of 19th Int Laser Radar Conference, Annapolis, USA, 23-24 (1998).

[*Bösenberg et al.*, 2000] Bösenberg J., A. Ansmann, J.M. Baldasano, D. Balis, C. Böckmann, B. Calpini, A. Chaikovsky, P. Flamant, A. Hagard, V. Mitev, A. Papayannis, J. Pelon, D. Resendes, J. Schneider, N. Spinelli, T. Trickl, G. Vaughan, G. Visconti and M. Weigner, "EARLINET: A European Aerosol Research Lidar Network", Proceedings of the 20th International Laser Radar Conference, Vichy (2000).

[*Dupont et al.*, 1994] Dupont, E., J. Pelon, and C. Flamant, "Study of the moist convective boundary-layer structure by Backscatter Lidar", Boundary-Layer Meteorology **69**, 1-25 (1994).

[*Franke et al*., 2003] Franke K., A. Ansmann, D. Muller, D. Altheusen, C. Venkataraman, M. S. Reddy, F. Wagner and R. Scheele, "Optical properties of the Indo-Asian haze layer over the tropical Indian Ocean", Journal of Geophysical Research. **108** (D2), 4059 (2003).

[*Furger et al.*, 1989] Furger M., H. Wanner, J. Engel, X. Troxler and A. Valsangiacomo, "Zur durchluftung der taler und Vorlandsenken der Schweiz", Geogr. Bersensia P **20**, 185 (1989)

[*Herman et al.*, 1997] Herman J R, Bhartia P, Torres O, Hsu C, Seftor C and Celarier E, 1997, "Global distribution of UV- absorbing aerosols from Nimbus 7/TOMS data'", J. Geophys. Res. **201** (D14), 16911-16922 (1997).

[*Holben et al.*, 1998] Holben B.N., T.F. Eck, I. Slutsker, D. Tarne, J.P. Buis, A. Setzer, E. Vermote, J.A. Reagan, Y.J. Kaufman, T. Nakajima , F. Lavenu, I. Jankoviak and A. Smirnov, "AERONET, A Fererated Instrument Network and Data Archive for Aerosol Characterization", Remote Sensing Environment **66**, 1-16 (1998).

[*IPCC*, 2001] IPCC Climate Change, "The science of climate change, Technical summary of the working group", I report, WMO, Geneva (2001).

[*Kaufman et al.*, 1997] Kaufman Y.J., D. Tanre, H. Gordon, T. Nakajima, J. Lenoble, R. Frouine, H. Grabl, B. Herman, M. King and P.M. Teillet, "Passive remote sensing of tropospheric aerosol and atmospheric correction for aerosol effect", J. Geophys. Res. **102** (D14), 16815-16830 (1997).

[*Kaufman et al.*, 2002] Kaufman Y.J., D. Tanre and O. Boucher, "A satellite view of aerosols in the climate system", Nature **419**, 215-223 (2002).

[*Matthias and Bösenberg*, 2002] Matthias V. and J. Bösenberg, "Aerosol climatology for the planatery boundary layer derived from regular Lidar measurements", Atmospheric Research **63**, 221-245 (2002).

[*Matthias et al.*, 2002] Matthias V. et al. (42 authors), "Lidar intercomparisons on algorithm and system level in the frame of EARLINET"', Max Plank Institute For Meteorology, Report No 337, Hamburg, Germany (2002).

[*Mattis et al.*, 2000] Mattis I., J. Volker, D. Müller, K. Franke and A. Ansmann, "Classification of particle Extinction Profiles derived within the framwork of the German Lidar Network by the use of cluster analysis of backtrajectories", Advances in Laser Remote Sensing, (Eds), A Dabas, C Loth and J Pelon, Publ: Ecole Polytechnique- 91128 Palaiseau Cedex. France, pp 211-214 (2000).

[*Papayanis et al.*, 2002] Papayanis A. et al. (20 Authors), "Two years of continuons observations of Saharan dust events over the European continent using a coordinated LIDAR Network in the frame of the EARLINET Project", Proc. of Lidar Remote Sensing in Atmospheric and Earth Sciences, (Eds) L Bissonette, G Roy, G Vallèe, Publ: DRDC, Canada, 309-312 (2002).

[*Russell et al.*, 1999] Russell P.B., P.V. Hobbs and L. Stove, "Aerosol properties and radiative effects in the United States east coast haze plume: An overview of the tropospheric aerosol radiative forcing observational experiment (TARFOX)", J. Geophys. Res. **104** (D2), 2213-2222 (1999).

[*Schneider and Eixmann*, 2002] Schneider J and R. Eixmann, "Three years of routine Raman Lidar measurements of tropospheric aerosols: Backscattering, extinction, and residual layer height", Atmos. Chem. Phys. **2**, 313-323 (2002) (Web: www.atmos-chem-phys.org/acp/2/313).

[*Schneider et al.*, 2000] Schneider J., D. Balis, C. Böckmann, J. Bösenberg, B. Calpini, A. Chaikovsky, A. Comeron, P. Flamant, V. Freudenthaler, V. Hågård, I. Mattis, V. Mitev, A. Papayannis, G. Pappalardo, J. Pelon, M.R. Perrone, D.P. Resendes, N. Spinelli, T. Trickl, T.G. Vaughan and G. Visconti, "A European Aerosol Research Lidar Network To Establish An Aerosol Climatology (Earlinet)", Journal of Aerosol Science **31**, 592-593 (2000).

[*Travis et al.*, 2002] Travis J.T., A.M. Carleton and R.G. Lauritsen, "Contrails reduce daily temperature range", Nature **418**, 601 (2002).

[*Wandinger et al.*, 2002] Wandinger U, I. Mattis, L. Komguem, G. Vaughan, V. Mattias and J. Bösenberg, "Air-mass modification over Europe observaed with the European Aerosol Research Lidar Network (EARLINET)", Proc. of Lidar Remote Sensing in Atmospheric and Earth Sciences, (Eds) L Bissonette, G Roy, G Vallèe, Publ: DRDC, Canada, 317-320 (2002).

[*Wanner and Furger*, 1990] Wanner H. and M. Furger, "The Bise-Climatology of a regional wind north of the Alps", Meteorol. Atmos. Phys. **43**, 105-115 (1990).

[*Weber and Furger*, 2001] Weber R.O. and M. Furger, "Climatology of near-surface wind patterns over Switzerland", Int. J. Climatol. **21**, 809-827 (2001).

# Publications


Frioud M., V. Mitev and R. Matthey, "Determination of the critical system and data processing parametere for Raman-DIAL O3 and H2O measurements: numerical simulations", in the SPIE Proceedings Vol. 3821 of the EUROPTO Conference on Environmental Sensing and Applications, June 14-17, 1999, Munich (Germany), pp 35-45.

Lazzarotto B., M. Frioud, G. Larchevêque, V. Mitev, P. Quaglia, V. Simeonov, A. Thompson, H. van den Bergh and B. Calpini, "Ozone and water-vapor measurements by Raman Lidar in the planetary boundary layer: error sources and field measurements", Applied Optics 40 (18), 2985-2997 (2001).

Frioud M., V. Mitev, R. Matthey, H. Richner, S. Gubser, and M. Furger "Backscatter Lidar detection of the evolution of the aerosol stratification in the PBL during Foehn events in FORM", MAP Meeting 2001 in Schliersee-Germany, 14-16 May, 2001; MAP Newsletter 15, pp. 179-182, http://www.map.ethz.ch/NL15/Frioud1.pdf.

Frioud M., V. Mitev, R. Matthey, C. Häberli, H. Richner, and R. Werner, "PBL elevation to 3.5 km over Rhine Valley: Backscatter Lidar observation in FORM", MAP Meeting 2001 in Schliersee-Germany, 14-16 May 2001; MAP Newsletter, 15, pp. 175-178, http://www.map.ethz.ch/NL15/Frioud2.pdf.

Papayannis A., A. Boselli, B. Calpini, A. Chaikovsky, G. Chourdakis, V. Cuomo, M. Frioud, M. Iarlori, S. Kreipl, G. Larchevêque, R. Matthey, G. Pappalardo, J. Pelon, M.R. Perrone, V. Rizi, F. Rocadenbosch, L. Sauvage, P. Sobolewski, C. Soriano, N. Spinelli, F. De Tomasi, V. Amoiridis, D. Balis and T. Trickl, "Simultaneous Observations of free tropospheric Saharan dust layers over Europe monitored by a co-ordinated ground-based Lidar network in the frame of the EARLINET Project", Abstracts of the European Aerosol Conference 2001, Journal of Aerosol Science 32 , sup. 1, Sept. 2001, 389-390 (2001).

Böckmann C., U. Wandinger, A. Ansmann, J. Bösenberg, V. Amoiridis, A. Boselli, A. Delaval, F. De Tomasi, M. Frioud, M. Iarlori, L. Komguem, S. Kreipl, G. Larchevêque, V. Matthias, A. Papayannis, F. Rocadenbosch, J. Schneider, V. Scherbakov and M. Wiegner, "EARLINET – Lidar Algortihm Intercomparison", Abstracts of the European Aerosol Conference 2001, Journal of Aerosol Science 32 , sup. 1, Sept. 2001, 433-434 (2001).

Frioud M., V. Mitev, R. Matthey, Ch. Haeberli, H. Richner, R. Werner and S. Vogt, "Backscatter Lidar Observation of the Aerosol Stratification over Rhine Valley during a 'hot-wave' in September 1999", in the Proceedings of the 9th International Symposium on Remote Sensing of Clouds and the Atmosphere, September 23-27, 2002, Crete (Greece), in press (2002).

Amodeo A., G. Pappalardo, U. Wandinger, V. Matthias, J. Bösenberg, M. Alpers, V. Amiridis, F. De Tomasi, M. Frioud, M. Iarlori, L. Komguem, G. Larchevêque, A. Papayannis, X. Wang, "Raman Lidar algorithm intercomparison in the frame of EARLINET", in the Proceedings of the 21th International Laser Radar Conference, July 8-12, 2002, Quebec (Canada), pp 349-352 (2002).

Böckmann C., U. Wandinger, A. Ansmann, J. Bösenberg, V. Amiridis, A. Boselli, A. Delaval, F. De Tomasi, M. Frioud, A. Hagard, M. Iarlori, L. Komguem, S. Kreipl, G. Larchevêque, V.Matthias, A. Papayannis, G. Pappalardo, F. Rocadenbosch, J. Schneider, V. Shcherbakov and M. Wiegner, "EARLINET – Backscatter Lidar Algorithm Intercomparison", in the Proceedings of the 21th International Laser Radar Conference, July 8-12, 2002, Quebec (Canada), pp 353-356 (2002).

Frioud M., V. Mitev, R. Matthey, Ch. Haeberli, H. Richner, R. Werner and S. Vogt, "Elevated Aerosol Stratification Above Rhine Valley in Strong Anticyclonic Conditions", Atmospheric Environment **37** (13), 1785-1797 (2003).

Srivastava M.K., M. Frioud, R. Matthey and V. Mitev, "Backscatter Lidar study of planetary boundary layer and stratified aerosol layers above Neuchâtel (Switzerland) during winter Bise wind", submitted (2002).